Second-order correlation analysis of multifrequency dephasing in single-particle interferometry

Dissertation

der Mathematisch-Naturwissenschaftlichen Fakultät
der Eberhard Karls Universität Tübingen
zur Erlangung des Grades eines
Doktors der Naturwissenschaften
(Dr. rer. nat.)

vorgelegt von
Alexander Rembold
aus Ulm

Tübingen
2017

Gedruckt mit Genehmigung der Mathematisch-Naturwissenschaftlichen Fakultät der Eberhard Karls Universität Tübingen.

Tag der mündlichen Qualifikation:	13.12.2017
Dekan:	Prof. Dr. Wolfgang Rosenstiel
1. Berichterstatter:	Dr. Alexander Stibor
2. Berichterstatter:	Prof. Dr. Claus Zimmermann

Abstract

Single-particle interferometers became a remarkable tool in many fields of fundamental research and technical applications, such as sensor technology. Due to their high phase sensitivity, these interferometers are susceptible to dephasing which originates typically from electromagnetic fields, mechanical vibrations or temperature drifts, leading to a reduced contrast in the spatial signal. In opposition to decoherence, where the contrast is reduced due to the entanglement of the quantum state to the environment, dephasing is a collective phase shift of the interference pattern. Therefore, it can in principle be reversed after the measurement if the spatial and temporal information about the particle events in the detection plane is available. Using two-particle correlations, it is possible to reveal the properties of the unperturbed interference pattern, such as contrast and spatial periodicity, and the dephasing characteristics. In this thesis, the second-order correlation analysis of multifrequency dephasing is discussed theoretically and demonstrated experimentally. The second-order correlation theory is derived and the equations are explained in detail. Additionally, the numerical correlation function used to extract the experimental data is provided and it is explained how the discretization influences the accuracy of the obtained parameters. Using an electron biprism interferometer, the validity of our correlation analysis is verified experimentally by applying artificially an external time-varying magnetic field dephasing the temporally integrated interference pattern. It is demonstrated successfully that the parameters of the unperturbed interference pattern can be revealed even if the contrast in the spatial signal is nearly vanished. Furthermore, the characteristics of single- and multifrequency dephasing can be identified and used for the reconstruction of the unperturbed interference pattern. The applicability of our correlation analysis is also investigated by applying external mechanical vibrations in a broad frequency range to the electron biprism interferometer. Here, the amplitude spectrum of the correlation function is used together with a numerical algorithm to identify the unknown dephasing frequencies, amplitudes, and phases. In this way, the vibrational response spectrum of the biprism interferometer including the mechanical resonances could be determined. Our correlation analysis can be applied in principle in all interferometers generating a spatial interference pattern on a detector with high spatial and temporal single-particle resolution. Such detectors are available for electrons, ions, atoms, neutrons, molecules, and photons which enables the application of our method in a wide range of interferometric experiments. In fundamental research, the second-order correlation analysis can be used to distinguish between dephasing and decoherence in experiments where the contrast of the interference pattern has to be determined. This is e.g. relevant for studying the mechanisms of decoherence and testing the limits of quantum mechanical superposition. Our method can also be a useful tool in technical applications to optimize the electromagnetic shielding and vibrational damping of the interferometer by measuring its response spectra. As the correlation analysis is suitable

to identify unknown dephasing frequencies and the corresponding amplitudes, it can be applied in sensor technology. At the end of this thesis, a compact sensor for the measurement of time-varying electromagnetic fields based on an electron biprism interferometer is proposed. Due to the wide application possibilities of the described correlation analysis, it is of significant relevance in various fields of single-particle interferometry.

Zusammenfassung

In vielen Bereichen der Grundlagenforschung und technischen Anwendungen, wie der Sensortechnik, eignen sich Interferometer mit einzelnen Teilchen zu einem präzisen Messinstrument. Auf Grund ihrer hohen Phasenempfindlichkeit sind diese Interferometer anfällig für Dephasierungen, die typischerweise von elektromagnetischen Feldern, mechanischen Vibrationen oder Temperaturdrifts stammen. Dies führt zu einem reduzierten Kontrast im räumlichen Signal. Im Gegensatz zur Dekohärenz, bei welcher der Kontrast auf Grund der Verschränkung des Quantenzustands mit der Umgebung verringert wird, ist Dephasierung eine kollektive Phasenverschiebung des Interferenzmusters. Deshalb ist diese im Prinzip reversibel, wenn die räumliche und zeitliche Information der Teilchenereignisse in der Detektionsebene zur Verfügung steht. Durch die Verwendung von Zwei-Teilchen Korrelationen ist es möglich die Eigenschaften des ungestörten Interferenzmusters, wie Kontrast und Streifenabstand, und die Charakteristika der Dephasierung zu bestimmen. In dieser Arbeit wird die Korrelationsanalyse zweiter Ordnung von Mehrfrequenz-Dephasierung theoretisch diskutiert und experimentell demonstriert. Die Korrelationstheorie zweiter Ordnung wird hergeleitet und die Gleichungen werden im Detail erläutert. Zusätzlich wird die numerische Korrelationsfunktion bereitgestellt, um die experimentellen Daten zu extrahieren, und erläutert, wie die Diskretisierung die Genauigkeit der ermittelten Parameter beeinflusst. Mit einem Elektronen Biprisma Interferometer wird die Gültigkeit unserer Korrelationsanalyse nachgewiesen. Dafür wird künstlich ein externes zeitlich-variierendes Magnetfeld angelegt, welches das zeitlich aufsummierte Interferenzmuster dephasiert. Es wird erfolgreich gezeigt, dass die Parameter des ungestörten Interferenzmusters bestimmt werden können, auch wenn der Kontrast im räumlichen Signal beinahe verschwunden ist. Des Weiteren können die Eigenschaften der Ein- und Mehrfrequenz-Dephasierung identifiziert und für die Rekonstruktion des ungestörten Interferenzmusters verwendet werden. Die Anwendung unserer Korrelationsanalyse wird ebenfalls untersucht, indem externe mechanische Vibrationen in einem weiten Frequenzbereich an das Elektronen Biprisma Interferometer angelegt werden. Hierbei wird das Amplitudenspektrum der Korrelationsfunktion zusammen mit einem numerischen Algorithmus verwendet, um die unbekannten Frequenzen, Amplituden und Phasen der Dephasierung zu identifizieren. Auf diese Weise kann das Antwortspektrum des Biprisma Interferometers auf Vibrationen bestimmt werden, welches die mechanischen Resonanzen enthält. Unsere Korrelationsanalyse kann im Prinzip in allen Interferometern angewendet werden, die ein räumliches Interferenzmuster auf einem Detektor mit hoher räumlicher und zeitlicher Einzelteilchen Auflösung erzeugen. Diese Art von Detektor ist verfügbar für Elektronen, Ionen, Atome, Neutronen, Moleküle und Photonen, was die Anwendung unserer Methode in einem weiten Bereich von interferometrischen Experimenten ermöglicht. In der Grundlagenforschung kann die Korrelationsanalyse zweiter Ordnung dazu verwendet werden um in Experimenten, in denen der Kontrast des Interferenzmus-

ters bestimmt werden muss, zwischen Dephasierung und Dekohärenz zu unterscheiden. Dies ist z.B. zur Untersuchung von Dekohärenz-Mechanismen und der Grenzen der quantenmechanischen Superposition relevant. Unsere Methode ist auch in technischen Anwendungen ein nützliches Werkzeug um durch die Vermessung der Antwortspektren die elektromagnetische Abschirmung und das Vibrations-Dämpfungssystem eines Interferometers optimieren zu können. Auf Grund der Möglichkeit unbekannte Frequenzen und die dazugehörenden Amplituden der Dephasierung zu identifizieren, eignet sich die dargestellte Korrelationsanalyse für die Anwendung in der Sensortechnik. Am Ende der Arbeit wird daher ein kompakter Sensor für die Messung von zeitlich-variierenden elektromagnetischen Feldern vorgeschlagen, welcher auf einem Elektronen Biprisma Interferometer basiert. Auf Grund der breiten Anwendungsmöglichkeiten der beschriebenen Korrelationsanalyse ist diese von signifikanter Relevanz in verschiedensten Bereichen der Interferometrie mit einzelnen Teilchen.

List of Publications

This cumulative thesis is based on the publications listed below. They are thematically ordered as discussed in the thesis and appended at the end.

Publications

Publication [1] **A. Rembold**, R. Röpke, G. Schütz, J. Fortágh, A. Stibor, and A. Günther,
Second-order correlations in single-particle interferometry,
New Journal of Physics **19**, 103029 (2017),
doi: 10.1088/1367-2630/aa88f9.

Publication [2] **A. Rembold**, G. Schütz, W. T. Chang, A. Stefanov, A. Pooch, I. S. Hwang, A. Günther, and A. Stibor,
Correction of dephasing oscillations in matter-wave interferometry,
Physical Review A **89**, 033635 (2014),
doi: 10.1103/PhysRevA.89.033635.

Publication [3] A. Günther, **A. Rembold**, G. Schütz, and A. Stibor,
Multifrequency perturbations in matter-wave interferometry,
Physical Review A **92**, 053607 (2015),
doi: 10.1103/PhysRevA.92.053607.

Publication [4] **A. Rembold**, G. Schütz, R. Röpke, W. T. Chang, I. S. Hwang, A. Günther, and A. Stibor,
Vibrational dephasing in matter-wave interferometers,
New Journal of Physics **19**, 033009 (2017),
doi: 10.1088/1367-2630/aa60a1.

Publications (not included in this thesis)

Publication [5] G. Schütz, **A. Rembold**, A. Pooch, S. Meier, P. Schneeweiss, A. Rauschenbeutel, A. Günther, W. T. Chang, I. S. Hwang, and A. Stibor,
Biprism electron interferometry with a single atom tip source,
Ultramicroscopy **141**, 9 (2014),
doi: 10.1016/j.ultramic.2014.02.003.

Publication [6] G. Schütz, **A. Rembold**, A. Pooch, H. Prochel, and A. Stibor,
Effective beam separation schemes for the measurement of the electric Aharonov–Bohm effect in an ion interferometer,
Ultramicroscopy **158**, 65 (2015),
doi: 10.1016/j.ultramic.2015.06.016.

Publication [7] G. Schütz, **A. Rembold**, A. Pooch, W. T. Chang, and A. Stibor,
Electron matter wave interferences at high vacuum pressures,
Measurement **68**, 201 (2015),
doi: 10.1016/j.measurement.2015.02.022.

Publication [8] A. Pooch, M. Seidling, M. Layer, **A. Rembold**, and A. Stibor,
A compact electron matter wave interferometer for sensor technology,
Applied Physics Letters **110**, 223108 (2017),
doi: 10.1063/1.4984839.

Publication [9] A. Pooch, M. Seidling, N. Kerker, R. Röpke, **A. Rembold**, W. T. Chang, I. S. Hwang, and A. Stibor,
Coherent properties of a tunable low-energy electron-matter-wave source,
accepted for publication in Physical Review A (2018),
arXiv:1705.10383.

Contributions

The contributions to the manuscripts of this thesis are outlined below. Alexander Stibor and Andreas Günther proposed and supervised the experiments and theoretical calculations. All authors participated in the revision of the manuscripts.

- **Publication [1]**

  The second-order correlation theory for single-particle interferometry was calculated by Andreas Günther, with several contributions by myself. The implementation of the numerical calculations of the deduced theory was done by myself. The simulations made to investigate the properties of the theory and the data evaluation have been done by Robin Röpke and myself. All authors discussed the theoretical predictions and results. The manuscript was mainly written by myself, with contributions by Andreas Günther and Alexander Stibor.

- **Publication [2]**

  The experimental setup was assembled by Georg Schütz, Andreas Pooch, and myself. Our co-operation partners Wei-Tse Chang and Ing-Shouh Hwang fabricated the electron source used in the experiment. The measurements of magnetically perturbed electron interferences were performed by Georg Schütz and myself. André Stefanov proposed the use of the additional time information of the detected particles to identify the pattern periodicity of the perturbed interference pattern. Andreas Günther advanced this idea, using second-order correlation theory. The experimental data was evaluated by Andreas Günther, with some contributions by myself. The manuscript was written by Andreas Günther, Alexander Stibor, and myself.

- **Publication [3]**

  The measurements have been taken by Georg Schütz and myself. The numerical implementation of the second-order correlation theory and the evaluation of the experimental data were made by myself. Andreas Günther calculated the theory used for the description of the results. All authors discussed the experimental results. The manuscript was written by myself, with some contributions by Andreas Günther and Alexander Stibor.

- **Publication [4]**

  The assembly of the experimental setup was made by Georg Schütz and myself. Our co-operation partners Wei-Tse Chang and Ing-Shouh Hwang produced the electron source installed in the experiment. The measurements of vibrationally perturbed electron interference patterns were mainly performed by Georg Schütz, with contributions by myself. The experimental data was evaluated by Robin Röpke and myself. The search algorithm used for the identification of unknown perturbation frequencies and the reconstruction process of unperturbed interference patterns were developed by Robin Röpke and myself. The applied theory was calculated by Andreas Günther and myself. All authors discussed the experimental results. The manuscript was mainly written by myself, with contributions by Andreas Günther and Alexander Stibor.

Contents

1. Introduction

The famous double-slit experiment of Young proved the wave nature of light in 1802 [10]. Using the wave property of light, a large number of interferometers have been realized in the following century by Jamin (1856) [11], Michelson and Morley (1887) [12], Zehnder and Mach (1891-92) [13, 14], and Fabry and Pérot (1899) [15]. At this time, the idea of light consisting of particles proposed originally in 1671 by Newton [16] was outdated due to the large number of interferometric experiments. The first reference for the quantization of light was given by Planck in 1901 [17], who postulated that energy can be absorbed or emitted by a black body only in a quantized manner. This energy is given by $E = h\nu$, with the Planck constant h and the frequency ν. In 1905, Einstein described theoretically the photoelectric effect [18] with the assumption that light itself is quantized. The energy of each "light quanta", later called photon, is again determined by the product of the Planck constant and the frequency. Another evidence for the particle nature of light was realized by Compton in 1923 demonstrating the scattering of x-rays at graphite [19].

One year later, de Broglie formulated his famous hypothesis that also particles carrying mass and momentum exhibit wave properties [20], with a wavelength given by $\lambda = h/p$, where h and p denote the Planck constant and the momentum. By the revolutionary work of Heisenberg (1925) [21], Schrödinger (1926) [22], and Dirac (1928) [23], the quantum mechanical theory of the microscopic world was established. The first successful experiments verifying de Broglie's hypothesis were performed in 1927 by Davisson and Germer [24], and Thomson and Reid [25]. They proved the wave nature of particles by diffraction of electrons at a single crystal of nickel atoms [24] and at a thin celluloid film [25]. In 1930, Estermann and Stern realized diffraction of a beam of helium atoms and hydrogen molecules at a lithium fluoride crystal [26] and in 1940 Boersch demonstrated successfully Fresnel electron diffraction at the edge of aluminium oxide [27]. Möllenstedt and Düker accomplished in 1955 electron interferences with an electrostatic biprism [28, 29], which became the standard instrument for variable wave splitting in electron interferometers [30] and electron holography [31]. In the group of Möllenstedt, electron interferences were measured by Jönsson in 1961 using miniaturized double- and multiple-slit systems [32]. His double-slit electron interference experiment was awarded in 2002 by *PhysicsWorld* as the most beautiful experiment ever made in physics [33].

Based on the ideas for the x-ray interferometer [34] Rauch *et al.* realized in 1974 an interferometer for neutrons using a perfect silicon-crystal [35] and in 1975 Colella *et al.* measured a quantum-mechanical phase shift in a neutron interferometer due to the gravitational field of the earth [36]. In 1988, Zeilinger *et al.* achieved diffraction of cold neutrons in a single- and double-slit experiment [37].

Diffraction experiments with neutral atoms have been carried out by Leavitt and Bills using a potassium beam diffracted at a single-slit (1969) [38], by Moskowitz *et*

al. with a sodium beam diffracted at a standing light wave (1983) [39], and by Keith *et al.* observing diffraction of sodium atoms at a transmission grating (1988) [40]. In 1991, Carnal and Mlynek realized Young's double-slit experiment with neutral atoms [41]. In the following years, interferometers for coherent atoms [42, 43] were used to measure inertial forces [44], fundamental constants [45, 46], the earth's rotation rate [47], and gravitation [48].

Two years after the first observation of Bose-Einstein condensation [49–51], Andrews *et al.* achieved interference between two condensates of sodium atoms released from a double-well potential [52].

In 1994, Schöllkopf and Toennies proved the wave nature of clusters of He, H_2, and D_2 by diffraction at a transmission grating [53]. Interferences with C_{60} molecules have been realized in 1999 by Arndt *et al.* using a diffraction grating [54]. Three years later, Brezger *et al.* measured interferences of C_{70} fullerene molecules in a near-field Talbot-Lau interferometer [55].

Based on these pioneering experiments, single-particle interferometers have become a remarkable tool in many fields of fundamental research [56] and technical applications [57], such as sensor technology [58], due to their high phase sensitivity. Highly sensitive laser interferometers are used for the measurement of gravitational waves [59, 60] and rotation with high accuracy [61]. With atom interferometers [62], the nature of time is investigated [63, 64] and the universality of free-fall in microgravity is tested [65]. With a large wave path separation [66], the sensitivity for the measurement of inertial forces [67] can be increased. In neutron interferometry [68], the use of a larger beam path separation [69] enables higher sensitivity in fundamental research [70]. The wave nature of Bose-Einstein condensates [71], observed also in a chip based double-well potential [72] and with weakly bound Feshbach molecules [73], is used in a Mach-Zehnder interferometer for Bose-Einstein condensates [74] to measure fundamental concepts of quantum mechanics and general relativity in microgravity [75]. Molecule interferometers [62, 76, 77] test the limits of quantum mechanical superposition [78] by proving the wave nature of large molecules [79, 80] with masses beyond 10,000 amu [81]. The mechanisms of decoherence [82] by collisions [83, 84], thermal emission of radiation [85], molecule temperature [86], and photon absorption [87] are investigated in interferometers for molecules and clusters [88, 89]. Furthermore, the scalar polarizability of molecules is measured in a near-field interferometer [90] and interferences of molecular clusters are realized with optical ionization gratings in the time domain [91].

Large progress was made in electron microscopy and holography of fragile biological samples. Using interfering single particles, the amount of destructive particle deposition can potentially be decreased [92, 93]. The development of new electron sources [94] and the possibility to emit electrons by laser induced photoemission [95, 96] enabled the generation of low-energy electrons for time-resolved microscopy using electron diffraction [97], microscopy with a divergent electron beam [98], and holography reaching a resolution of 1 nm [99].

Interferometry with charged particles [30], such as electrons [5, 7, 8, 100] and ions [101, 102], opened the door for the observation of the magnetic Aharonov-Bohm effect [103, 104]. This could be realized by implementing a large beam path separation [6, 105] in an electron biprism interferometer. A micro magnetic coil was installed between the two paths to detect the phase shift of the electron interference pattern depending on

the enclosed magnetic flux [106–110]. Another experimental verification of the magnetic Aharonov-Bohm effect was realized in an electron interferometer using a toroidal magnet with superconducting cladding for the shielding of magnetic fields [111]. The Sagnac effect was measured successfully in an electron interferometer rotated around the axis perpendicular to the enclosed area of a large beam path separation resulting in a phase shift of the interference pattern [112, 113]. With electron interferences above a silicon wafer [114, 115], the influence of Coulomb-induced decoherence [82, 116, 117] was studied. At a standing light wave forming a periodic grating the diffraction of electrons was observed [118] demonstrating the Kapitza-Dirac effect in electron matter optics [119, 120]. An interferometer for electrons based on the Talbot-Lau effect [121, 122] was realized for the measurement of magnetic fields [123].

In recent years, new interferometric experiments with charged particles were enabled by novel developments concerning the beam source [94, 96], precise beam guiding [124, 125], coherent beam separation [96, 126], and single-particle detection with high spatial and temporal resolution [127]. New beam sources were realized such as single-atom tips, noble-metal covered tungsten tips [128, 129], multi-wall carbon nanotubes for electron emission [130, 131], and laser-induced photoemission of electrons from a tungsten tip [132–134]. Coherent beam separation was demonstrated successfully with electron interferences at a single-wall carbon nanotube [135] used also in a low-energy point projection microscope [136] and for interferences of a laser-pulsed electron source [96].

Due to their high phase sensitivity, all these single-particle interferometers are susceptible to dephasing, resulting in a contrast reduction of the temporally integrated interference pattern. Dephasing originates typically from external electromagnetic oscillations [2, 3, 8, 9], mechanical vibrations [4, 137] or temperature drifts. This is especially an obstacle for precision measurements, experiments in a perturbing environment, and mobile interferometers [138]. In opposition to decoherence [82, 84, 117, 139], where the contrast is reduced due to the entanglement of the quantum state to the environment, dephasing is a collective phase shift of the interference pattern. Unlike decoherence, dephasing can therefore in principle be reversed after the measurement. Using the temporal and spatial information about the particle impacts in the detection plane, two-particle correlations can be calculated. They reveal the wave properties of the unperturbed interference pattern and the dephasing characteristics. In this thesis, the second-order correlation analysis of multifrequency dephasing will be described theoretically and demonstrated experimentally in an electron biprism interferometer.

In particular, to test the limits of quantum mechanical superposition [78], e.g. with large molecules [79, 80] and other macroscopic objects with small de Broglie wavelengths, it is necessary to distinguish between decoherence and dephasing. In many experiments the influence of decoherence is studied with ions [140–143], electrons [115, 144, 145], atoms [146], molecules [83, 85, 86, 147], and in solid state physics [148, 149]. The understanding of decoherence mechanisms is of major importance in electron microscopy [93, 97, 98], electron holography [99], and a variety of hybrid quantum devices for the realization of long coherence times [150–155].

Dephasing also disturbs sensitive phase measurements, as performed in Aharonov-Bohm physics [103, 104]. Here, the phase of the particle wave is shifted in the field-free region due to the vector potential of the magnetic field and the scalar potential of the electric field. The Aharonov-Bohm effect was observed in diverse experiments with

electrons in a biprism interferometer [110, 111] and a two-dimensional electron gas [156], photons interacting with phonons in an acousto-optical crystal [157], and atoms in a graphene-like hexagonal optical lattice [158].

The influence of dephasing caused by vibrations was analyzed and decreased in various fields of research, e.g. in a Mach-Zehnder interferometer for thermal lithium atoms [159]. Vibrations induce an arbitrary phase shift to the interfering particles in the interferometry with ultracold atoms used for precise measurements of gravity [138] and inertial effects [160]. As atoms require a large time of flight in the interferometer a passive and active damping is required to suppress vibrations [161]. In atom interferometry vibrational phase shifts are compensated by a seismometer attached to the beam mirror [162] or by the conjugation of two simultaneous operating atom interferometers [163, 164]. For precise measurements of the equivalence principle the reduction of vibrational noise is also a main challenge to achieve high accuracy [165–167].

For interferometers creating a spatial interference pattern in the detection plane, the second-order correlation analysis discussed in this thesis can be used to reveal the characteristics of an interference pattern dephased by an external mechanical vibration. This is demonstrated experimentally in an electron biprism interferometer by introducing artificially external mechanical vibrations in a broad frequency range to dephase the electron interference pattern [4]. The interference characteristics, such as contrast and spatial periodicity, are determined successfully over the complete frequency region. Additionally, the properties of the mechanical vibration are identified and the unperturbed interference pattern is reconstructed [4]. This correlation analysis is also applied in an experiment with an interference pattern dephased by an external time-varying magnetic field with one and multiple perturbation frequencies [2, 3]. The measurements demonstrate that this method can in principle reduce the requirements for vibrational damping and electromagnetic shielding.

Since the famous experiment of Hanbury Brown and Twiss [168–170], second-order correlations became a remarkable tool in many fields of research. In particular, noise correlations enable a direct access to the quantum nature of a source, which is the basis for modern quantum optics [171] and allows to prove the quantum nature of bosons [172] and fermions [173]. Nowadays, noise correlation analysis is applied in modern astrophysics [174], solid state physics [175], quantum atom optics [176–178], and particle physics [179–181]. The counting statistic of lasers [182], atom lasers [183], and the coherent transfer of magnetic field fluctuations onto an atom laser [184] have been analyzed by temporal correlations of single particle events. On the other hand, spatial correlations have been used for the investigation of atoms in an optical lattice [185] and for the study of complex many body states in cold atom optics, such as the Mott insulator state [186, 187].

The second-order correlation analysis of multifrequency dephasing deduced theoretically and demonstrated experimentally in this thesis uses spatial and temporal correlations of particle events. If an external perturbation dephases an interference pattern during data acquisition, the contrast is reduced or vanished in the spatial signal. If the flight time of the particles through the area of dephasing is smaller than the periodic time of the perturbation, the interference pattern is always present. Otherwise, the perturbation is averaged out as the particles traverse many periods of the perturbation. If the requirement for the flight time of the particles is fulfilled, the spatial

differences of the particle impacts on the detector reveal the interference characteristics of the unperturbed interference pattern, such as contrast K and spatial periodicity λ. Taking additionally into account the temporal differences, the perturbation parameters, such as frequency ω, amplitude (peak phase deviation) φ, and phase ϕ, can be obtained. The structure in the correlation function can be seen as a finger print of the underlying perturbation [2, 3]. For certain correlation times, the contrast of the unperturbed interference pattern is directly linked to the correlation function and recovers with a temporal periodicity given by the perturbation frequencies. For particles arriving in the detection plane with temporal differences corresponding to this temporal periodicity, the resulting interference pattern is stationary and shows the same contrast and spatial periodicity as the unperturbed interference pattern. This can be interpreted as a stroboscope effect. Although the correlation function is unique for each external perturbation, it is difficult to identify unknown perturbation frequencies if more than one frequency is involved. Therefore, the amplitude spectrum of the correlation function has to be applied for the identification of unknown perturbation frequencies and corresponding amplitudes [4]. This is possible as, according to the Wiener-Khintchine theorem [188, 189], the Fourier transform of the correlation function is equal to the power spectrum of the perturbed measurement signal. Using the obtained perturbation parameters, the unperturbed interference pattern can be reconstructed from the spatial and temporal coordinates of the perturbed interference pattern.

Our method is a useful tool to prove the wave nature of single particles even if the interference pattern is vanished. It can be used in an interferometer generating a spatial interference pattern in the detection plane dephased by a time-varying perturbation. Especially, for precise measurements investigating the mechanisms of decoherence [115] and testing the limits of quantum mechanical superposition [79] it is necessary to distinguish between dephasing and decoherence which can be realized using our correlation analysis. In these experiments the interference characteristics, such as contrast and spatial periodicity, have to be determined to measure the influence of decoherence and to prove the quantum mechanical superposition of a macroscopic object. Additionally, our correlation analysis reduces the requirements for vibrational damping and electromagnetic shielding in a broad frequency range for interferometric experiments identifying the contrast and spatial periodicity of an interference pattern. For experiments measuring a constant phase shift of an interference pattern our correlation analysis can not be applied. Nevertheless, a time-varying phase shift acts like an external perturbation and therefore, can be identified using our correlation analysis to determine the oscillation frequency and amplitude of the phase shift. For technical applications measuring a constant phase shift of the interference pattern, our correlation analysis can be used for the determination of the electromagnetic and vibrational response spectrum of the used interferometer [3, 4] allowing the optimization of damping and shielding techniques. Unwanted perturbations originating from laboratory equipment or power supply can be identified and eliminated. Our second-order correlation analysis has the potential for the application in sensor technology as unknown perturbation frequencies and amplitudes can be identified in a broad range. Using the possibility to reconstruct the unperturbed interference pattern, the accuracy of the parameters obtained from the correlation analysis can be increased. Our method can be

applied in all single-particle interferometers generating a spatial interference pattern on a detector with high spatial and temporal single-particle resolution. Such detectors are available for electrons and ions [127], atoms [172], neutrons [190], molecules [191], and photons [192–194]. Due to the wide applicability of our method, it is of significant relevance in various fields of single-particle interferometry.

In this cumulative thesis, the publications [1–4] on our theoretical and experimental work concerning the second-order correlation analysis for multifrequency dephasing in single-particle interferometry are summarized in the following chapters. First, the principle function of a biprism interferometer and the influence of dephasing are discussed. Furthermore, the experimental setup used for the verification of our correlation analysis is explained and the basic principles of the first- and second-order correlation theory are outlined. The second-order correlation function and corresponding amplitude spectrum are discussed in chapter 2 and the important equations used in the subsequent chapters are provided. Furthermore, the numerical correlation function used for the evaluation of the experimental data is derived and the influence of the discretization of the numerical correlation function on the obtained parameters is discussed. In chapter 3, the validity of the correlation theory for one perturbation frequency is investigated experimentally in an electron biprism interferometer by applying an external oscillating magnetic field that dephases the interference pattern. The same experiment is performed in chapter 4 with an oscillating magnetic field consisting of a superposition of multiple perturbation frequencies. In chapter 5, the application of our second-order correlation analysis is demonstrated by dephasing an electron interference pattern with mechanical vibrations in a broad frequency range. It is shown that the matter-wave characteristics can be determined over the complete perturbation spectrum. Additionally, the vibrational response spectrum of the used biprism interferometer including the mechanical resonances is measured, which demonstrates the applicability of our second-order correlation analysis. Based on an electron biprism interferometer and the correlation analysis a compact sensor for the measurement of oscillating electromagnetic fields is proposed in the outlook. At the end of this thesis, the publications [1–4] are appended.

1.1. Electron biprism interferometry in the presence of dephasing

In this section, the principle operation of an electron biprism interferometer is explained and the necessary equations are discussed. Furthermore, it is outlined, how dephasing influences the interference pattern and which informations can be obtained from the correlation analysis discussed in this thesis. Afterwards, the experimental setup used to investigate the validity and applicability of the correlation analysis is explained.

In figure 1.1, a schematic illustration of an electron biprism interferometer is presented [28, 29]. Emitted from an electron source under the angle α, the coherent matter-wave is separated by an electrostatic biprism placed between two grounded electrodes. For electrons the two partial matter-waves are deflected toward each other by applying a positive voltage to the biprism. Each electron path is deflected by the same angle and superposed under the angle Θ in the interference plane. There, the

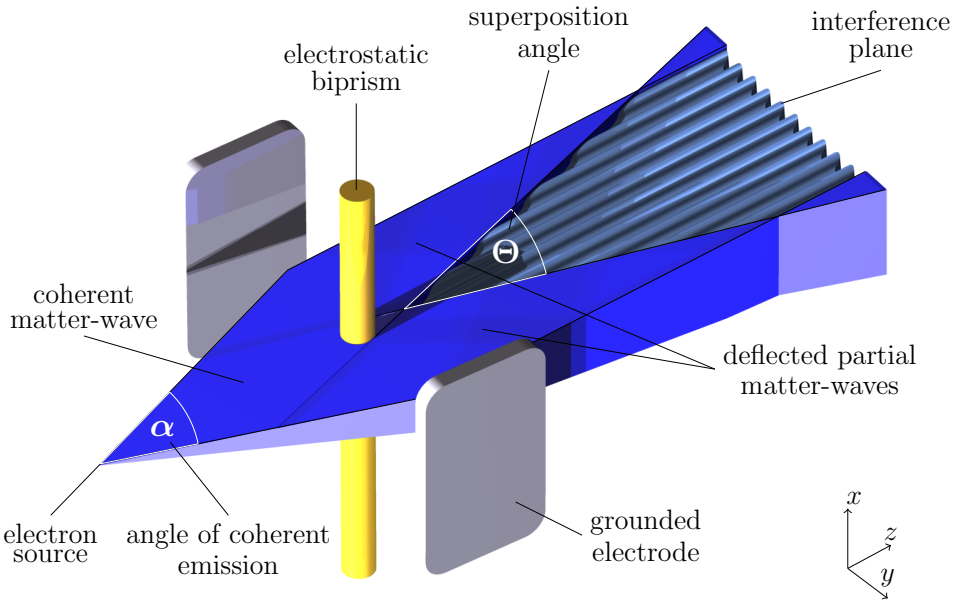

Figure 1.1.: Schematic illustration (not to scale) of the principle operation of an electron biprism interferometer. The coherent matter-wave emitted under the angle of coherent emission α from an electron source is separated and recombined by the electrostatic biprism installed between two grounded electrodes. For electrons a positive voltage has to be applied to the biprism. Each electron path is deflected by the same angle and superposed in the interference plane under the angle Θ. The two deflected partial matter-waves overlap in the interference plane and form the interference pattern given by equation (1.1).

two overlapping partial matter-waves form the interference pattern described by

$$I(y) = I_0\big(1 + K\cos\left(ky\right)\big) \ . \tag{1.1}$$

Here, the mean intensity is denoted by I_0, the contrast by K, and the wave number by $k = 2\pi/\lambda$, with the spatial periodicity λ. The contrast of the interference pattern depends on the spatial size and spectral bandwidth of the electron source [195]. For a perfectly monochromatic, point-like source the contrast would be equal to 1.

For the realization of interferences the angular coherence constraint [29]

$$\alpha \ll \frac{\lambda_{\mathrm{dB}}}{2d_{\mathrm{s}}} \tag{1.2}$$

has to be fulfilled. Here, α denotes the opening angle of the coherent emission (figure 1.1), d_{s} the diameter of the source, and λ_{dB} the de Broglie wavelength of the particles [101]

$$\lambda_{\mathrm{dB}} = \frac{h}{mv} = \frac{h}{\sqrt{2qmU_{\mathrm{acc}}}} \ , \tag{1.3}$$

where h is the Planck constant, m the particle mass, $v = \sqrt{2q/m \cdot U_{\mathrm{acc}}}$ the particle velocity, q the electric charge of the particle, and U_{acc} the acceleration voltage. With the opening angle of coherent emission α satisfying the constraint in equation (1.2),

the diameter s of the coherent illuminated area at the position of the biprism can be calculated by

$$s = 2a \tan\left(\frac{\alpha}{2}\right) , \tag{1.4}$$

with the distance a between electron source and biprism. For different wavelengths λ_{dB} and therefore, different angles of coherent emission α fulfilling the angular coherence constraint in equation (1.2), the diameter s of the coherent illuminated area can be adjusted by varying the distance a.

As explained in figure 1.1, the coherent electron matter-wave is separated and recombined by applying a positive voltage to the biprism. All electron paths are deflected by the same angle and overlapped in the interference plane under the superposition angle Θ given by [29, 195]

$$\Theta = \frac{a\gamma_0}{l}\frac{U_{\mathrm{bp}}}{U_{\mathrm{acc}}} , \tag{1.5}$$

where l is the distance between emission source and interference plane, U_{bp} the voltage applied to the biprism, and γ_0 is defined by

$$\gamma_0 = \frac{\pi}{2\ln\left(\frac{R}{r_{\mathrm{bp}}}\right)} , \tag{1.6}$$

with R denoting the distance between grounded electrode and biprism and r_{bp} the radius of the biprism. Using equation (1.3) and (1.5), the spatial periodicity λ of the pattern in the interference plane can be calculated by

$$\lambda = \frac{\lambda_{\mathrm{dB}}}{\Theta} = \frac{h}{\sqrt{2qm}}\frac{l}{a\gamma_0}\frac{\sqrt{U_{\mathrm{acc}}}}{U_{\mathrm{bp}}} . \tag{1.7}$$

In figure 1.2, an exemplary interference pattern $I(y)$ is plotted (red dashed line). It is calculated according to equation (1.1) for a mean intensity of $I_0 = 1$, a contrast of $K = 1$, and a spatial periodicity of $\lambda = 557\,\mathrm{nm}$, determined with equation (1.7) for an acceleration voltage of $U_{\mathrm{acc}} = -1.5\,\mathrm{kV}$ and a biprism voltage of $U_{\mathrm{bp}} = 0.5\,\mathrm{V}$. Using equation (1.3), the wavelength of the electrons can be calculated, yielding $\lambda_{\mathrm{dB}} = 32\,\mathrm{pm}$. These are typical experimental parameters realized in an electron biprism interferometer.

Assuming a constant perturbation, the interference pattern $I(y)$ is shifted along the y-direction by the amount of Δy which corresponds to a phase shift φ_1 of the interference pattern in equation (1.1), yielding

$$I(y) = I_0\big(1 + K\cos\left(ky + \varphi_1\right)\big) , \tag{1.8}$$

with the phase shift

$$\varphi_1 = k\Delta y = 2\pi\frac{\Delta y}{\lambda} . \tag{1.9}$$

In figure 1.2, a shifted interference pattern (blue solid line) calculated according to equation (1.8) with the same values as the non-shifted pattern (red dashed line) but phase shifted by $\varphi_1 = -0.65\,\pi$ is plotted. Here, the spatial periodicity λ given by equation (1.7) remains unchanged by the shift as the superposition angle Θ is not influenced by the perturbation. As a constant perturbation does not change the contrast of the

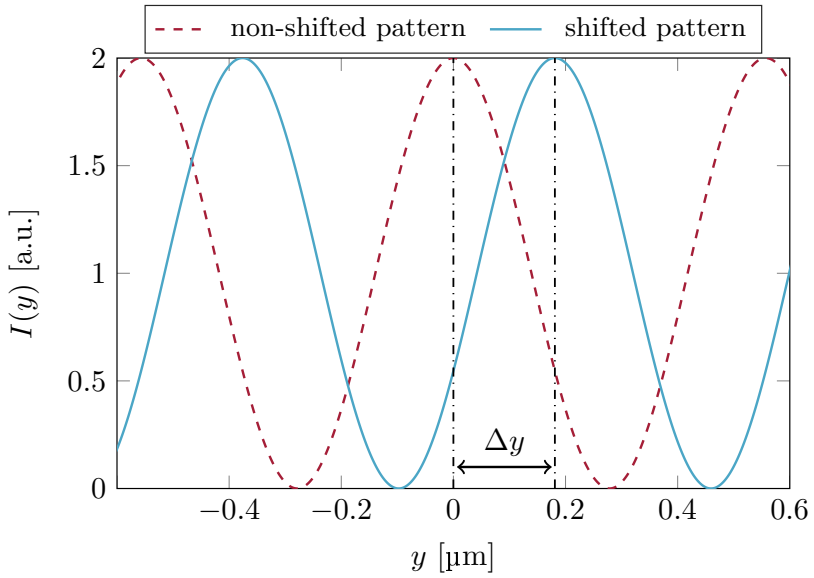

Figure 1.2.: Non-shifted interference pattern (red dashed line) calculated according to equation (1.1) with $I_0 = 1$, $K = 1$, and $\lambda = 557\,\mathrm{nm}$. The spatial periodicity was determined with equation (1.7) for $U_{\mathrm{acc}} = -1.5\,\mathrm{kV}$ and $U_{\mathrm{bp}} = 0.5\,\mathrm{V}$. According to equation (1.8), the shifted interference pattern (blue solid line) is calculated for the same values as the non-shifted pattern but phase shifted by $\varphi_1 = -0.65\,\pi$. The values used in equation (1.7) concerning the dimensions of the interferometer are: distance source to biprism $a = 12\,\mathrm{cm}$, distance source to interference plane $l = 24\,\mathrm{cm}$, and $\gamma_0 \approx 0.17$ (equation (1.6) with $R = 2\,\mathrm{mm}$ and $r_{\mathrm{bp}} = 200\,\mathrm{nm}$).

temporally integrated interference pattern, the case of a time-varying perturbation, which reduces the contrast, is discussed in the following.

For a time-dependent shift $\Delta y(t) = \Delta y \cos(\omega_1 t + \phi_1)$ of the interference pattern due to an oscillating perturbation with the spatial amplitude Δy, frequency ω_1, and phase ϕ_1, the phase shift in equation (1.9) becomes

$$\varphi(t) = k\Delta y(t) = \varphi_1 \cos(\omega_1 t + \phi_1) \ , \tag{1.10}$$

with the perturbation amplitude (peak phase deviation) φ_1 given by equation (1.9). During the measurement of an electron interference pattern this time-dependent perturbation dephases the temporally integrated pattern and therefore, the contrast in the spatial signal is reduced or vanished (see section 2.1.1). In figure 1.3, an exemplary measurement of a temporally integrated electron interference pattern detected without (figure 1.3(a)) and with external perturbation (figure 1.3(b)) is shown. For this purpose, a time-varying magnetic field with a frequency of 50 Hz was applied during the measurement [2]. As a consequence, the electron interference pattern in figure 1.3(b) is nearly vanished in the spatial signal. However, using the second-order correlation analysis presented in this thesis it is possible to determine the interference characteristics of the unperturbed interference pattern, such as contrast K and spatial periodicity λ, as well as the perturbation properties (φ_1, ω_1, and ϕ_1). In equation (1.9), the peak phase deviation φ_1 obtained from the correlation analysis is directly linked to the spatial amplitude Δy. Therefore, it can be used to determine the strength of

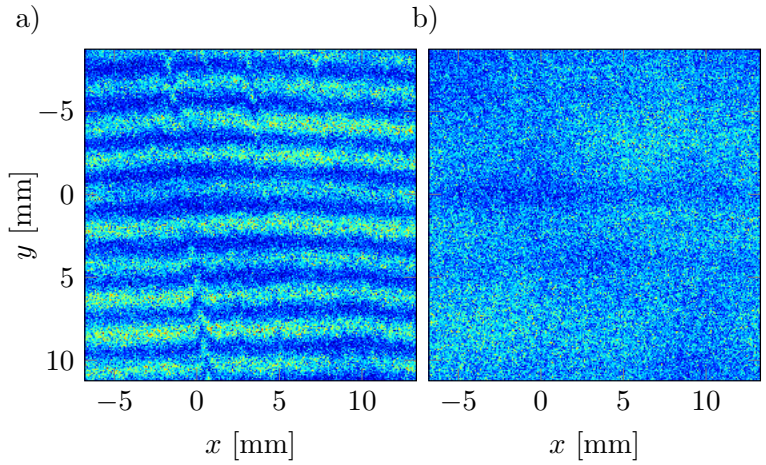

Figure 1.3.: a) Electron interference pattern with a contrast of $K \approx 35\,\%$ and a spatial periodicity of $\lambda \approx 2\,\mathrm{mm}$ in the detection plane after magnification ($M \approx 3 \cdot 10^3$) was measured in a biprism interferometer without external perturbation. b) Temporally integrated interference pattern dephased by a time-varying magnetic field with a frequency of 50 Hz. The contrast of the pattern is nearly vanished in the spatial signal. Figure from [2]. Reprints with permission of the American Physical Society (AIP).

the underlying perturbation, e.g. the amplitude of a mechanical vibration [4] or the electromagnetic field strengths (see appendix A.4).

For a time-dependent perturbation $\varphi(t)$ consisting of a superposition of N harmonic frequencies ω_j equation (1.10) yields

$$\varphi(t) = \sum_{j=1}^{N} \varphi_j \cos\left(\omega_j t + \phi_j\right) \ . \tag{1.11}$$

This equation is used together with equation (1.8) to describe the probability distribution $f(y,t)$ of particle impacts in the detection plane

$$f(y,t) = f_0\Big(1 + K\cos\big(ky + \varphi(t)\big)\Big) \ , \tag{1.12}$$

with f_0 ensuring normalization. The second-order correlation analysis of multifrequency dephasing which is the topic of this thesis is derived in [1] using equation (1.11) and (1.12).

In the following, the experimental setup of the electron biprism interferometer is explained in detail which is used to verify the validity of our correlation analysis [2, 3] and to demonstrate the applicability of our method for the identification of unknown perturbation parameters [4].

In figure 1.4, the biprism interferometer is illustrated schematically. It is based on the interferometer originally constructed by Hasselbach *et al.* for electrons and ions [30, 101, 102] equipped with a new particle source as well as a detector with high spatial and temporal single-particle resolution. Furthermore, a new fabrication method for the biprism was applied to assure a certain known diameter [5, 196, 197]. A detailed characterization of the interferometer is made in publication [5].

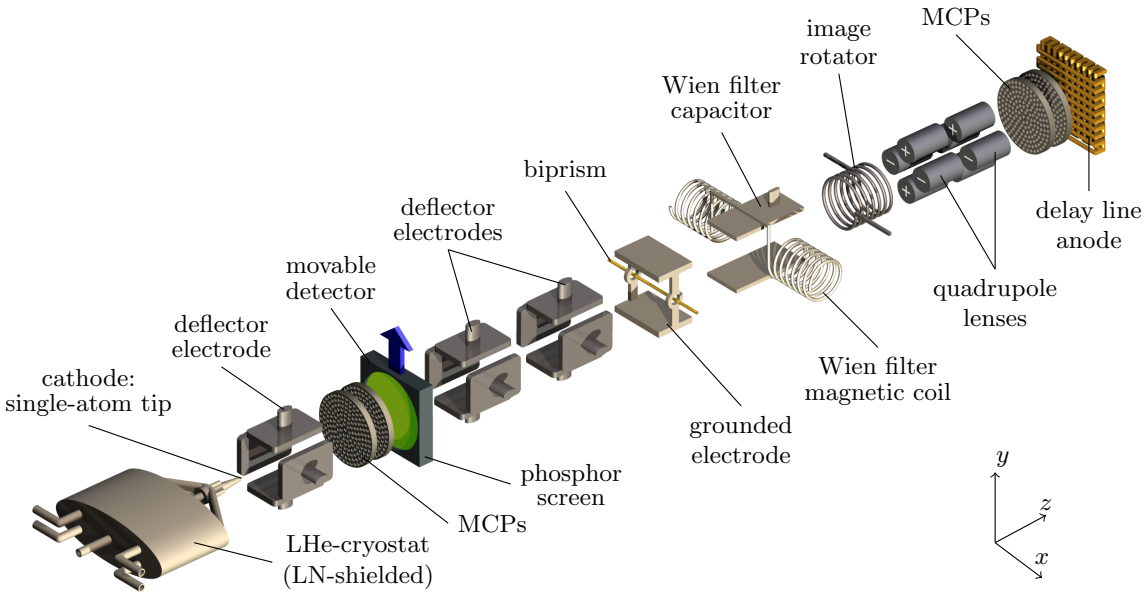

Figure 1.4.: Schematic illustration (not to scale) of the used biprism interferometer. The electrons are field-emitted from a single-atom tip (SAT) [94, 129] mounted on a continuous-flow liquid helium cryostat which is shielded by a liquid nitrogen shield. Therefore, it could also be used for the creation of ions. Followed by the first deflector electrode for beam alignment, the movable detector is used to characterize the shape of the electron emission after annealing of the SAT. After moving the detector out of the beam path the electrons are adjusted with the deflector electrodes (x- and y-direction) onto the optical axis and the biprism, a thin gold-palladium-coated glass-fibre with a diameter of $\sim 400\,\mathrm{nm}$ [5, 196, 197]. It separates and recombines the electron matter-wave by applying a positive voltage [28, 29] (figure 1.1). A possible longitudinal phase shift of the electron matter-wave-packets is corrected by the Wien filter [198] creating a magnetic (x-direction) and electric field (y-direction) perpendicular to each other. It consists of two magnetic coils in Helmholtz configuration and a capacitor. The electron interference pattern is magnified along the y-direction by two quadrupole lenses and detected with a delay line detector [127] consisting of two MCPs and a delay line anode. Possible misalignment of the biprism in the x-y-plane is corrected by the image rotator installed between Wien filter and quadrupole lens. The elements of the interferometer are mounted on two rigid ceramic rods to avoid mechanical vibrations and the complete interferometer is shielded by a mu-metal shield against oscillating electromagnetic fields. The length of the interferometer between SAT and delay line detector amounts to about $55\,\mathrm{cm}$. At a pressure of $5 \cdot 10^{-10}\,\mathrm{mbar}$, the experimental setup is placed inside of a vacuum chamber.

Surrounded by a mu-metal shield to suppress external oscillating electromagnetic radiation the interferometer is placed inside of a vacuum chamber at a pressure of about $5 \cdot 10^{-10}$ mbar. To avoid mechanical vibrations all elements of the interferometer are mounted on two rigid ceramic rods except the single-atom tip (SAT) [94, 129] which is installed on a cryostat. The SAT consists of an etched tungsten tip covered with a monolayer of iridium. A three-sided pyramid of iridium atoms with one single atom on top is formed by annealing the tip to about 1100 K. Mounted on a continuous-flow liquid helium cryostat shielded against thermal radiation by a nitrogen shield, the SAT can be cooled to about 17 K for the generation of ions by applying a positive voltage. For this purpose, helium or hydrogen gas is introduced to the vacuum chamber, ionized at the top most atom of the SAT, and accelerated away from the tip. As the interferometric experiments discussed in this thesis were performed with electrons, the focus is placed on them in the following.

Electrons are field-emitted from the SAT by applying a negative voltage and adjusted onto the movable detector by the first deflector electrode. This detector composed of two multichannel plates (MCPs) in conjunction with a phosphor screen is used for the characterization of the electron emission after the annealing process. Each electron that impacts at the MCPs (first +1 kV, second +2 kV) creates an electron avalanche inducing a light pulse on the phosphor screen (+7 kV). This light pulse is guided outside of the vacuum chamber trough a window with the help of a 45° mirror. With this field electron/ion microscope [199], the emission pattern of the electron beam is detected after annealing of the SAT. The formation process is repeated until only one electron emission spot with a round shape is created. Then, the detector is moved out of the interferometer. Using the two successive deflector electrodes, the electron beam is adjusted in horizontal (x) and vertical direction (y) onto the electrostatic biprism installed between two grounded electrodes which separates and recombines the electron matter-wave by applying a positive voltage (figure 1.1). It consists of a thin gold-palladium-coated glass-fibre with a diameter of ~ 400 nm [5, 196, 197]. Placed behind the biprism, the Wien filter [198] consists of two magnetic coils in Helmholtz configuration and a capacitor creating a magnetic (x-direction) and electric field (y-direction) perpendicular to each other. It is used to correct possible longitudinal shifts of the electron matter-wave-packet due to the electrostatic potential of the deflector electrodes. The electrons form wave packets according to the quantum mechanical superposition principle and due to the finite emission energy bandwidth of the source. These matter-wave-packets traverse regions of different electrostatic potential inside of the deflector electrodes. The two partial matter-waves-packets get deflected at the biprism and shifted with respect to each other longitudinally resulting in different group velocities. Therefore, they overlap less and the contrast of the resulting interference pattern is reduced. This has to be corrected by the electrostatic potential created by the Wien filter. To avoid deflection of the electron beam due to the electrostatic potential, the magnetic field is applied to generate a Lorentz force that compensates the electric force. Using two quadrupole lenses as illustrated in figure 1.4, the created electron interference pattern is magnified along the y-direction up to a magnification of $M \approx 3 \cdot 10^4$. It remains nearly unmagnified along the x-direction ($M \approx 0 - 100$) which is favorable to preserve the signal strength. Due to possible misalignment of the biprism in the x-y-plane, an image rotator is installed ahead of the quadrupole lenses

to adjust the interference fringes perpendicular to the magnifying axis. It consists of a magnetic coil creating a homogeneous field along the z-direction. The magnetic field and the transversal velocity of the electrons result in a Lorentz force that rotates the interference pattern around the optical axis. After a distance of about 30 cm from the exit of the second quadrupole lens, the interference pattern is measured at a delay line detector [127] consisting of two MCPs in conjunction with a delay line anode. This detector is essential for the application of the correlation analysis as it provides the temporal and spatial information of the particle impacts in the detection plane used for the calculation of the correlation function as explained in this thesis.

In figure 1.5, a schematic illustration of the principle operation of the used delay line detector DLD40 from the company RoentDek GmbH is shown. It is build up of two MCPs and two meandering delay lines oriented perpendicular to each other (x- and y-direction). The MCPs have an active area of 47 mm, a pore size of 25 µm, and a centre-to-centre spacing of 32 µm [200], which limits the spatial resolution of the detector to $2 \cdot 32$ µm, according to the Nyquist-Shannon sampling theorem [201, 202]. The delay line detector achieves a temporal accuracy below 1 ns with a dead time of 10 to 20 ns between two successive events [200].

The electron beam is directed along the z-direction onto the first MCP of the detector. An incident electron impacts on the first grounded MCP and creates an electron avalanche amplified by the second MCP set on a voltage of +2.14 kV. The pulse at the first MCP caused by the incident electron is used as a trigger for the measurement of the spatial coordinates determined by the delay lines. Additionally, this pulse defines the arrival time t of the electron in the detection plane. After the second MCP the electron avalanche is accelerated onto the delay lines set on a voltage of +2.4 kV. Passing through the delay lines the electron avalanche causes a voltage drop in each delay line that creates a signal pulse propagating in both directions along the wire. Measuring the arrival times of the signal at the end of each wire (t_{x_1}, t_{x_2} and t_{y_1}, t_{y_2}), the two-dimensional spatial position (x- and y-coordinate) of the impact of the electron avalanche can be calculated using the temporal differences. For a real signal the sum of the arrival times has to be equal in both wires ($t_{x_1} + t_{x_2} = t_{y_1} + t_{y_2}$) as the time of a signal pulse propagating from one end of the delay line to the other is constant. With the propagation velocity $v_\perp = \frac{1}{0.73} \frac{\text{mm}}{\text{ns}}$ [200] of the signal perpendicular to the straight lines of the delay line anode, the spatial coordinates (x and y) of the particle impacts in the detection plane can be calculated with regard to the center of the detector by

$$x = \frac{(t_{x_1} - t_{x_2} + O_x) v_\perp}{2} \qquad \text{and} \qquad y = \frac{(t_{y_1} - t_{y_2} + O_y) v_\perp}{2} \,, \tag{1.13}$$

with offsets O_x and O_y. After the measurement of an electron interference pattern the delay line detector provides a set of N detected electrons with arrival times $t_i, i = 1 \ldots N$ determined by the impact of electron i at the first MCP and spatial coordinates (x_i and y_i) obtained according to equation (1.13) with the temporal differences of the signal pulses at the end of the two delay lines (t_{x_1}, t_{x_2} and t_{y_1}, t_{y_2}). These temporal and spatial coordinates of particle events in the detection plane are necessary to calculate the numerical two-dimensional second-order correlation function used for the determination of the interference characteristics, such as contrast K and spatial periodicity λ, and for the identification of the perturbation characteristics (am-

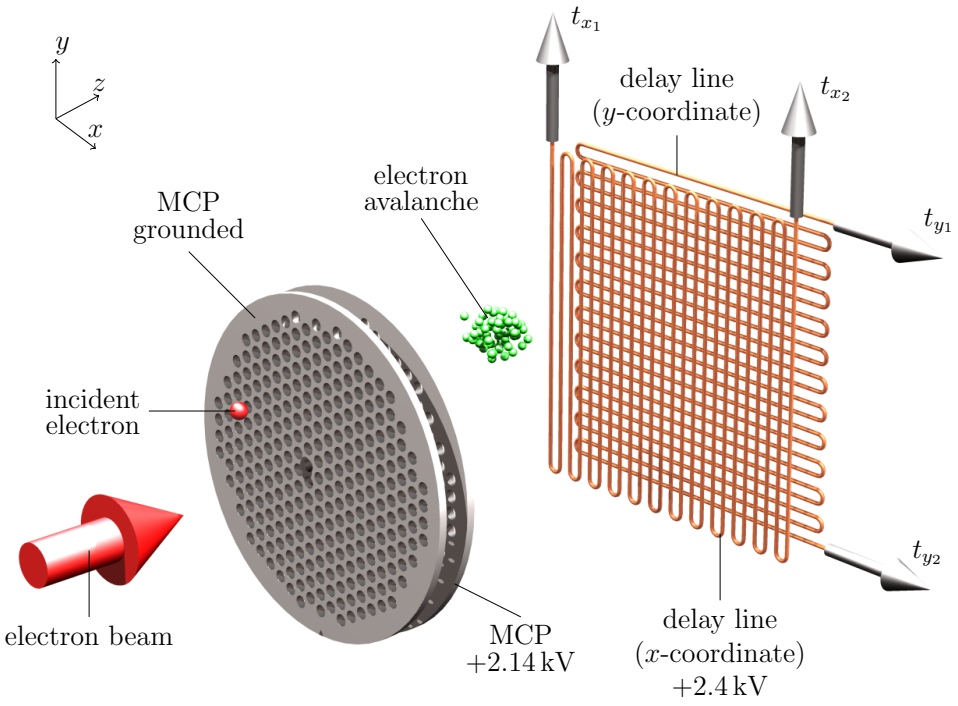

Figure 1.5.: Schematic illustration (not to scale) of the used delay line detector which provides the temporal and spatial coordinates of the particle events in the detection plane. It consists of two MCPs and two meandering delay lines oriented perpendicular to each other (x- and y-direction). The incident electron hits the first grounded MCP and creates an electron avalanche amplified by the second MCP set on +2.14 kV. Between second MCP and delay line (+2.4 kV) the electron avalanche is accelerated. It passes through the delay lines and initiates a signal pulse in each delay line which propagates in both directions along the wire. Using the differences of the arrival times at both ends of the delay line for the x- and y-direction (t_{x_1}, t_{x_2} and t_{y_1}, t_{y_2}), the spatial position of the incident electron can be calculated with equation (1.13). Here, the propagation velocity $v_\perp$ of the signal is oriented perpendicular to the straight lines of the delay line anode.

plitude φ, frequency ω, and phase ϕ) which is explained theoretically and demonstrated experimentally in this thesis.

1.2. First- and second-order correlation function

The characteristics of the first- and second-order correlation function are discussed in this section. Afterwards, the application of the two-dimensional second-order correlation function for the correlation analysis discussed in this thesis is explained for electron interferences.

The normalized first-order correlation function defined by

$$g^{(1)}(\mathbf{r}_1, \mathbf{r}_2, \tau) := \frac{\left\langle E^*(\mathbf{r}_1, t) E(\mathbf{r}_2, t+\tau) \right\rangle_t}{\sqrt{\left\langle \left| E(\mathbf{r}_1, t) \right|^2 \right\rangle_t \left\langle \left| E(\mathbf{r}_2, t+\tau) \right|^2 \right\rangle_t}} , \tag{1.14}$$

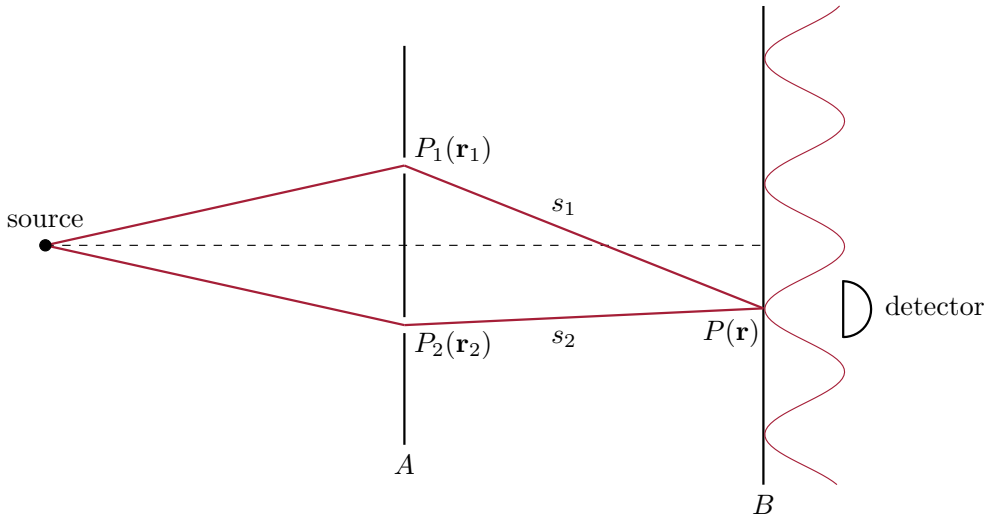

Figure 1.6.: Illustration of Young's double-slit interference experiment. Light emitted from a source illuminates the two slits in the plane A. The two elementary waves originating from $P_1(\mathbf{r}_1)$ and $P_2(\mathbf{r}_2)$ superpose in the observation plane B creating an interference pattern. The intensity of the resulting light field is measured with a detector at the position $P(\mathbf{r})$. Interferences can be observed if the path difference between s_1 and s_2 is $\Delta s = |s_1 - s_2| \leq c/\Delta\omega$, with the speed of light c and the frequency bandwidth of the source $\Delta\omega$.

where $\langle\cdot\rangle_t$ denotes the time-average

$$\left\langle f(\mathbf{r},t)\right\rangle_t \coloneqq \lim_{T\to\infty}\frac{1}{T}\int_0^T f(\mathbf{r},t)\,\mathrm{d}t\ , \tag{1.15}$$

is a measure for the phase fluctuations of the field and therefore, a measure for the capability of interference. It shall be motivated in the following with Young's double-slit experiment [10], as illustrated in figure 1.6. Two slits in the plane A are illuminated by a light source generating to elementary waves at $P_1(\mathbf{r}_1)$ and $P_2(\mathbf{r}_2)$ that are superposed in the observation plane B creating an interference pattern. At the position $P(\mathbf{r})$ the intensity of the resulting light field is measured by a detector. For a light source with a frequency bandwidth of $\Delta\omega$ interferences can occur if the difference between the two paths s_1 and s_2 is $\Delta s = |s_1 - s_2| \leq c/\Delta\omega$, with the speed of light c. The quantity $l_c = c/\Delta\omega$ is called the coherence length and $\tau_c = l_c/c = 1/\Delta\omega$ the coherence time (also referred to as longitudinal coherence). For $\tau_c\Delta\omega \simeq 1$ interferences can be created. The coherence time and length define the time duration and spatial length in which the phase of the wave train remains stable.

For the position $P(\mathbf{r})$ in the observation plane the field at a time t is given by a superposition of the two fields originating from $P_1(\mathbf{r}_1)$ and $P_2(\mathbf{r}_2)$ for earlier times $t_1 = t - s_1/c$ and $t_2 = t - s_2/c$, yielding [203, 204]

$$\begin{aligned} E\left(\mathbf{r},t\right) &= E\left(\mathbf{r}_1, t-\frac{s_1}{c}\right) + E\left(\mathbf{r}_2, t-\frac{s_2}{c}\right) \\ &= E\left(\mathbf{r}_1,t\right) + E\left(\mathbf{r}_2, t+\tau\right)\ , \end{aligned} \tag{1.16}$$

with the correlation time $\tau = t_1 - t_2 = \left(s_2 - s_1\right)/c$. Using a detector acquiring the signal for a time T, the averaged light intensity can be measured which is described

theoretically by

$$I(\mathbf{r}) = \big\langle I(\mathbf{r},t)\big\rangle_t = \Big\langle \big|E(\mathbf{r},t)\big|^2 \Big\rangle_t \,, \tag{1.17}$$

with $\langle\cdot\rangle_t$ indicating the time-average (equation (1.15)). With equation (1.16) and (1.17) the intensity of the light field on the detector can be calculated by

$$I(\mathbf{r}) = \Big\langle \big|E(\mathbf{r}_1,t)\big|^2 \Big\rangle_t + \Big\langle \big|E(\mathbf{r}_2,t+\tau)\big|^2 \Big\rangle_t + 2\,\Re\Big(\big\langle E^*(\mathbf{r}_1,t)E(\mathbf{r}_2,t+\tau)\big\rangle_t \Big) \,. \tag{1.18}$$

Here, the first two terms correspond to the intensities originating from the two slits at $P_1(\mathbf{r}_1)$ and $P_2(\mathbf{r}_2)$, and the third term describes the interferences. With

$$I(\mathbf{r}_1) = \big\langle I(\mathbf{r}_1,t)\big\rangle_t = \Big\langle \big|E(\mathbf{r}_1,t)\big|^2 \Big\rangle_t \,, \tag{1.19}$$

$$I(\mathbf{r}_2) = \big\langle I(\mathbf{r}_2,t+\tau)\big\rangle_t = \Big\langle \big|E(\mathbf{r}_2,t+\tau)\big|^2 \Big\rangle_t \,, \tag{1.20}$$

and the definition of the normalized first-order correlation function in equation (1.14), equation (1.18) becomes

$$I(\mathbf{r}) = I(\mathbf{r}_1) + I(\mathbf{r}_2) + 2\sqrt{I(\mathbf{r}_1)I(\mathbf{r}_2)}\,\Re\Big(g^{(1)}(\mathbf{r}_1,\mathbf{r}_2,\tau) \Big) \,, \tag{1.21}$$

where $\Re(\cdot)$ denotes the real part of $g^{(1)}(\mathbf{r}_1,\mathbf{r}_2,\tau)$. The complex number $g^{(1)}(\mathbf{r}_1,\mathbf{r}_2,\tau)$ can be written as

$$g^{(1)}(\mathbf{r}_1,\mathbf{r}_2,\tau) = \big|g^{(1)}(\mathbf{r}_1,\mathbf{r}_2,\tau)\big|\, \mathrm{e}^{i\Psi(\mathbf{r}_1,\mathbf{r}_2,\tau)} \,, \tag{1.22}$$

with its absolute value $\big|g^{(1)}(\mathbf{r}_1,\mathbf{r}_2,\tau)\big|$ and phase $\Psi(\mathbf{r}_1,\mathbf{r}_2,\tau)$. For correlation times $\tau < \tau_c$ and lengths $(s_2 - s_1) < l_c$ the phase is approximately given by $\Psi(\mathbf{r}_1,\mathbf{r}_2,\tau) = \omega_0\tau = k_0\,(s_2 - s_1)$, with the central frequency of the light field $\omega_0/2\pi$ and the corresponding wave number $k_0 = 2\pi/\lambda_0$, where λ_0 denotes the wavelength. Thus, the interference term in equation (1.21) only depends on the difference of the path lengths s_1 and s_2, resulting in

$$I(\mathbf{r}) = I(\mathbf{r}_1) + I(\mathbf{r}_2) + 2\sqrt{I(\mathbf{r}_1)I(\mathbf{r}_2)}\;\big|g^{(1)}(\mathbf{r}_1,\mathbf{r}_2,\tau)\big| \cos\big(k_0\,(s_2 - s_1)\big) \,. \tag{1.23}$$

Hence, interferences can be observed for $\big|g^{(1)}(\mathbf{r}_1,\mathbf{r}_2,\tau)\big| \neq 0$ and three types of coherence can be distinguished

$$\begin{aligned} &\big|g^{(1)}(\mathbf{r}_1,\mathbf{r}_2,\tau)\big| = 1 && \text{full coherence} \\ 0 < &\big|g^{(1)}(\mathbf{r}_1,\mathbf{r}_2,\tau)\big| < 1 && \text{partial coherence} \\ &\big|g^{(1)}(\mathbf{r}_1,\mathbf{r}_2,\tau)\big| = 0 && \text{incoherence} \,. \end{aligned} \tag{1.24}$$

With the definition of the contrast

$$K = \frac{I_{\max} - I_{\min}}{I_{\max} + I_{\min}} \tag{1.25}$$

and the maximum and minimum value of equation (1.23)

$$I(\mathbf{r})_{\min}^{\max} = I(\mathbf{r}_1) + I(\mathbf{r}_2) \pm 2\sqrt{I(\mathbf{r}_1)I(\mathbf{r}_2)}\;\big|g^{(1)}(\mathbf{r}_1,\mathbf{r}_2,\tau)\big| \tag{1.26}$$

the contrast of the interference pattern results in

$$K = \frac{2\sqrt{I(\mathbf{r}_1)I(\mathbf{r}_2)}\ \left|g^{(1)}(\mathbf{r}_1, \mathbf{r}_2, \tau)\right|}{I(\mathbf{r}_1) + I(\mathbf{r}_2)}\ . \tag{1.27}$$

If the intensities of the light fields originating from the two slits in figure 1.6 at $P_1(\mathbf{r}_1)$ and $P_2(\mathbf{r}_2)$ are equal $I(\mathbf{r}_1) = I(\mathbf{r}_2)$, equation (1.27) yields

$$K = \left|g^{(1)}(\mathbf{r}_1, \mathbf{r}_2, \tau)\right|\ . \tag{1.28}$$

Thus, the contrast is directly given by the absolute value of the first-order correlation function indicating the degree of coherence (equation (1.24)). For $I(\mathbf{r}_1) = I(\mathbf{r}_2)$ the first-order correlation function in equation (1.14) becomes

$$g^{(1)}(\mathbf{r}_1, \mathbf{r}_2, \tau) := \frac{\left\langle E^*(\mathbf{r}_1, t)E(\mathbf{r}_2, t+\tau)\right\rangle_t}{\left\langle \left|E(\mathbf{r}_1, t)\right|^2\right\rangle_t}\ . \tag{1.29}$$

It is a measure for the phase stability of the electric field at two spatial positions $\mathbf{r}_1$ and $\mathbf{r}_2$ with a time difference $\tau = t_1 - t_2$. For $\tau = 0$ the coherence of the electric field for two different positions can be determined with the so called *spatial* first-order correlation function $g^{(1)}(\mathbf{r}_1, \mathbf{r}_2)$. Measuring the contrast of the interference pattern as a function of the slit separation $\mathbf{r}_1 - \mathbf{r}_2$, the spatial coherence (transverse coherence) of a source can be determined with the spatial correlation function. This was used to measure the transverse coherence length with a Michelson stellar interferometer [205] to determine the angular diameter of stars. With the analysis of intensity fluctuations corresponding to the *second-order* correlation function discussed later, Hanbury Brown and Twiss could improve this method [168–170].

If the coherence of the electric field is determined for the same spatial position $\mathbf{r}_1 = \mathbf{r}_2$ but different correlation times τ, equation (1.29) is referred as the *temporal* first-order correlation function denoted in the following by $g^{(1)}(\tau)$. It is used to quantify the temporal coherence (longitudinal coherence) of the source. For a perfectly monochromatic light source with a frequency bandwidth $\Delta\omega = 0$, the coherence time τ_c is infinite and therefore, the correlation function is $\left|g^{(1)}(\tau)\right| = 1$ for all correlation times τ. In contrast, the coherence time $\tau_c = 1/\Delta\omega$ of a chaotic light source is finite due to the non-vanishing frequency bandwidth $\Delta\omega$ originating from the chaotic light emission process, e.g. Doppler or lifetime broadened emission of light from excited atoms [206]. As a consequence, the temporal first-order correlation function is equal to unity for $\tau = 0$ and remains close to unity for $0 < \tau \ll \tau_c$. It decreases for increasing τ as the probability of phase randomness of the electric field rises and therefore, $0 < \left|g^{(1)}(\tau)\right| < 1$. For correlation times $\tau \gg \tau_c$ the correlation function is $\left|g^{(1)}(\tau)\right| = 0$ as the phases of the electric fields are totally uncorrelated. Using the Wiener-Khintchine theorem [188, 189], the normalized frequency spectrum of the source can be determined as it is equal to the Fourier transform $\mathcal{F}\left(g^{(1)}(\tau)\right)(\omega)$ of the temporal first-order correlation function

$$\mathcal{F}\left(g^{(1)}(\tau)\right)(\omega) = \frac{1}{\sqrt{2\pi}}\int_{-\infty}^{\infty} g^{(1)}(\tau)\,\mathrm{e}^{i\omega\tau}\,\mathrm{d}\tau = \frac{|E(\omega)|^2}{\int_{-\infty}^{\infty}|E(\omega)|^2\,\mathrm{d}\omega}\ . \tag{1.30}$$

From the normalized frequency spectrum, the spectral width of the source can be determined which is inverse proportional to the coherence time τ_c. For a perfectly monochromatic light source with $\Delta\omega = 0$ the spectrum consists of one δ-peak at the position of the frequency of the light field $\omega_0/2\pi$. The spectrum of a chaotic light source has for example a Gaussian shape for Doppler broadened light emission or a Lorentzian shape for lifetime broadened light emission [206].

To analyze the statistic of the intensity fluctuations of the light source at a fixed detector position the normalized temporal second-order correlation function is used [171, 203]

$$g^{(2)}(\tau) \coloneqq \frac{\left\langle E^*(t)E^*(t+\tau)E(t+\tau)E(t)\right\rangle_t}{\left\langle \left|E(t)\right|^2\right\rangle_t \left\langle \left|E(t+\tau)\right|^2\right\rangle_t} = \frac{\left\langle I(t)I(t+\tau)\right\rangle_t}{\left\langle I(t)\right\rangle_t \left\langle I(t+\tau)\right\rangle_t} \,, \tag{1.31}$$

with the electric field $E(t)$ and intensity $I(t)$ of the light source at the time t. The time-average of the intensity acquired for a time T with a detector is indicated by $\langle\cdot\rangle_t$ (equation (1.15)). Compared to the first-order correlation function which determines the contrast of the light field the second-order correlation function is its intensity analogue. $g^{(2)}(\tau)$ is a measure for the fluctuations of the intensity whereas $g^{(1)}(\tau)$ is a measure for the field fluctuations (compare equation (1.29) for $\mathbf{r}_1 = \mathbf{r}_2$ and equation (1.31)). For the analysis of the statistic of the emitted photons, a detector with single-photon resolution can be used and equation (1.31) is rewritten for a single mode of the light field

$$g^{(2)}(\tau) \coloneqq \frac{\left\langle \hat{a}^\dagger(t)\hat{a}^\dagger(t+\tau)\hat{a}(t+\tau)\hat{a}(t)\right\rangle}{\left\langle \hat{a}^\dagger(t)\hat{a}(t)\right\rangle \left\langle \hat{a}^\dagger(t+\tau)\hat{a}(t+\tau)\right\rangle} \,, \tag{1.32}$$

with the photon creation $\hat{a}^\dagger$ and annihilation operator $\hat{a}$. Here, the time-average $\langle\cdot\rangle_t$ is replaced by the expectation value of the respective operator in the state $|\Psi\rangle$. $g^{(2)}(\tau)$ is the conditional probability to detect a photon at the time $t+\tau$ after detecting a photon at the time t. For a coherent state $|\alpha\rangle$, defined as the eigenstate of the annihilation operator $\hat{a}|\alpha\rangle = \alpha|\alpha\rangle$, the correlation function is normalized so that $g^{(2)}(\tau) = 1$. For $\tau = 0$ in equation (1.32) the statistic of the photons can be related to the average photon number $\langle\hat{n}\rangle$ and the variance $(\Delta n)^2 = \left\langle \left(\hat{n} - \langle\hat{n}\rangle\right)^2 \right\rangle$, yielding [204]

$$g^{(2)}(0) = \frac{\left\langle \hat{a}^\dagger\hat{a}^\dagger\hat{a}\hat{a}\right\rangle}{\left\langle \hat{a}^\dagger\hat{a}\right\rangle^2} = 1 + \frac{\left\langle (\Delta n)^2\right\rangle - \langle\hat{n}\rangle}{\langle\hat{n}\rangle^2} \,, \tag{1.33}$$

with the photon number operator $\hat{n} = \hat{a}^\dagger\hat{a}$. Here, the commutator $\left[\hat{a}, \hat{a}^\dagger\right] = 1$ was used. With equation (1.33) three different types of photon statistics can be distinguished

$$\left\langle (\Delta n)^2\right\rangle > \langle\hat{n}\rangle \;\rightarrow\; g^{(2)}(0) > 1 \qquad \text{super-Poissonian statistic} \tag{1.34}$$

$$\left\langle (\Delta n)^2\right\rangle = \langle\hat{n}\rangle \;\rightarrow\; g^{(2)}(0) = 1 \qquad \text{Poissonian statistic} \tag{1.35}$$

$$\left\langle (\Delta n)^2\right\rangle < \langle\hat{n}\rangle \;\rightarrow\; g^{(2)}(0) < 1 \qquad \text{sub-Poissonian statistic .} \tag{1.36}$$

The super-Poissonian and Poissonian statistic are known from classical light sources, such as chaotic and coherent, whereas the sub-Poissonian statistic is related to a non-classical light source generated for example by a single-photon source.

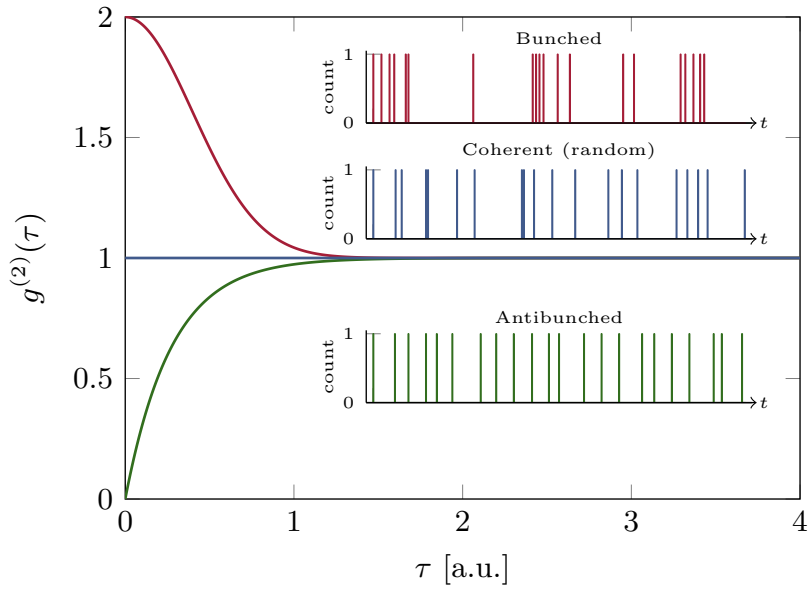

Figure 1.7.: Illustration of the normalized temporal second-order correlation function for three different light sources. In the insets, the corresponding single-photon detector signals are shown. For a coherent light source the correlation function (blue line) is equal to unity as the detected photons (see inset blue bars) follow a Poissonian statistic (equation (1.35)) and are therefore uncorrelated for all correlation times τ. For a chaotic light source the conditional probability to detect two photons with the time difference $\tau < \tau_c$ is increased named bunching and decreases to unity for $\tau > \tau_c$ (red line). The detected photons (see inset red bars) show a super-Poissonian statistic (equation (1.34)). If the conditional probability is decreased for small correlation times τ (green line) it is called antibunching which can only be observed for a non-classical source, e.g. a single-photon source. The detected photons (see inset green bars) follow a sub-Poissonian statistic (equation (1.36)).

In figure 1.7, the normalized temporal second-order correlation function $g^{(2)}(\tau)$ is illustrated for three different light sources together with the corresponding single-photon detector signal (see insets). The detected photons of a coherent light source (see inset blue bars) follow a Poissonian statistic (equation (1.35)) and are therefore uncorrelated for all correlation times τ resulting in a correlation function equal to unity (blue line). For a chaotic light source with a coherence time τ_c the conditional probability of detecting two photons with a time difference τ is increased for correlation times $\tau < \tau_c$ and drops down to unity for $\tau > \tau_c$ (red line). This behaviour for $\tau < \tau_c$ is named bunching as the probability to detect two photons with a small time difference (see inset red bars) is increased compared to a coherent source (blue line). As $g^{(2)}(0) > 1$ this case is related to a super-Poissonian statistic of the detected photons (equation (1.34)). If the conditional probability is decreased for small correlation times it is named antibunching (green line). Here, the detected particles (see inset green bars) follow a sub-Poissonian statistic as $g^{(2)}(0) < 1$ (equation (1.36)). The effect of antibunching can only be observed for non-classical sources and was measured with single-photon sources [207, 208] and electrons [173]. This demonstrates that it is possible to analyze the statistics of the detected particles using a detector with single-particle resolution.

In this thesis, the validity and applicability of our second-order correlation analysis

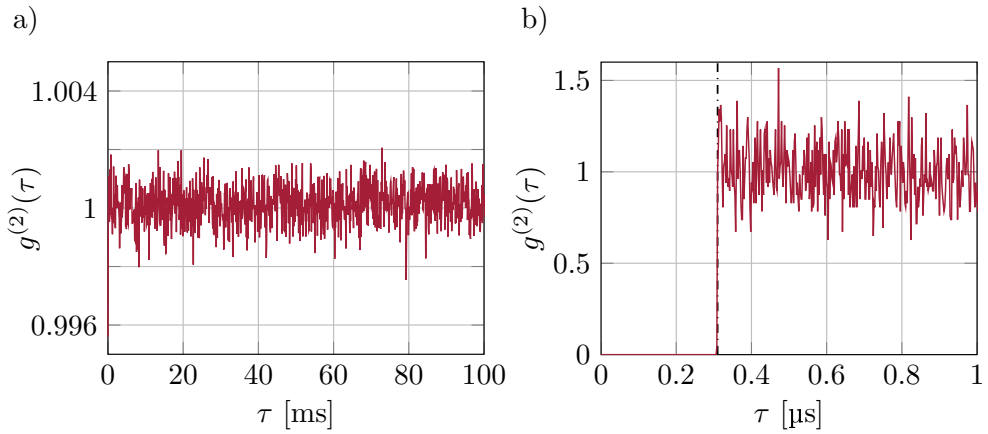

Figure 1.8.: a) Normalized temporal second-order correlation function of the perturbed electron interference pattern illustrated in figure 1.3(b). The detected electrons follow a Poissonian statistic (equation (1.35)) and therefore, the correlation function is $g^{(2)}(\tau) \approx 1$ (compare figure 1.7 blue line). b) The correlation function is equal to zero between 0 and 310 ns as the dead time of the detector was set to 310 ns for the measurement. This corresponds to antibunching (compare figure 1.7 green line) but does not originate from the source. Here, the noise of the correlation function is increased compared to a) as the temporal discretization step size $\Delta\tau$ is five orders of magnitude smaller.

is investigated in an electron biprism interferometer as explained in section 1.1. Using a delay line detector (figure 1.5) the temporal and spatial coordinates of the electrons arriving in the detection plane are provided. With this informations the temporal and spatial second-order correlation function $g^{(2)}(u,\tau)$ can be calculated. In figure 1.8(a), the normalized temporal second-order correlation function $g^{(2)}(\tau)$ of the perturbed electron interference pattern illustrated in figure 1.3(b) is shown. As the detected electrons follow the Poissonian statistic in equation (1.35) the resulting correlation function is $g^{(2)}(\tau) \approx 1$ for correlation times larger than 310 ns which corresponds to a coherent electron source and uncorrelated electrons (compare figure 1.7 blue line). Due to the limited acquisition time T of the measurement, $g^{(2)}(\tau)$ varies around unity. In the experiment, the dead time of the delay line detector between two detected electrons was set to 310 ns which can be identified in figure 1.8(b) for correlation times between 0 and 310 ns. Here, the second-order correlation function is equal to zero corresponding to antibunching of the detected electrons (compare figure 1.7 green line), which is not a property of the electron source but originates from the chosen detector dead time. Therefore, only electrons with a time difference of $\tau \geq 310$ ns could be detected. The noise of the correlation function in figure 1.8(b) is increased compared to figure 1.8(a) due to the five orders of magnitude smaller temporal discretization step size $\Delta\tau$.

For the derivation of the theory explained in this thesis, the following normalized two-dimensional second-order correlation function is used

$$g^{(2)}(u,\tau) \coloneqq \frac{\left\langle\!\left\langle f(y+u,t+\tau)f(y,t)\right\rangle\!\right\rangle_{y,t}}{\left\langle\!\left\langle f(y+u,t+\tau)\right\rangle\!\right\rangle_{y,t}\left\langle\!\left\langle f(y,t)\right\rangle\!\right\rangle_{y,t}}\,, \tag{1.37}$$

with the probability distribution of particle impacts in the detection plane $f(y,t)$ in

equation (1.12) and $\langle\!\langle \cdot \rangle\!\rangle_{y,t}$ indicating the average over position and time

$$\langle\!\langle f(y,t) \rangle\!\rangle_{y,t} := \lim_{Y,T\to\infty} \frac{1}{TY} \int_0^T \int_{-Y/2}^{Y/2} f(y,t)\,\mathrm{d}y\mathrm{d}t \ . \tag{1.38}$$

In equation (1.37), u denotes the spatial distance in y-direction between two particles in the detection plane with a temporal difference of τ. $g^{(2)}(u,\tau)$ is the conditional probability to detect a particle at the time $t+\tau$ and spatial position $y+u$ after detecting a particle at the time t and spatial position y.

In the following, the second-order correlation function of three different cases shall be discussed concerning the case of no present interference pattern ($K=0$), an unperturbed interference pattern ($K>0$, $\varphi(t)=0$), and a perturbed interference pattern ($K>0$, $\varphi(t)\neq 0$).

If no interference pattern is present, meaning the contrast K in equation (1.12) is equal to zero, the correlation function in equation (1.37) is $g^{(2)}(u,\tau)=1$ for all correlation times τ and lengths u. The reason for this is that the conditional probability to detect two particles with a certain temporal and spatial difference is identical for all possible correlation times and lengths as the probability distribution of the particles in equation (1.12) shows no periodic structure.

In figure 1.9(a), the correlation function of the unperturbed interference pattern illustrated in figure 1.3(a) is shown. It demonstrates the case of a temporal stationary interference pattern ($K>0$ and $\varphi(t)=0$ in equation (1.12)). Along the u-direction the characteristics of the interference pattern can be identified for all correlation times τ. For spatial distances u corresponding to multiples of the spatial periodicity $u=n\lambda, n\in\mathbb{Z}$, the correlation function is $g^{(2)}(u,\tau)>1$. The reason is that the conditional probability to detect two particles with this spatial difference is raised due to the probability distribution of the particles in equation (1.12), e.g. detecting one particle in a maximum of the interference pattern and afterwards another one in a maximum. For spatial distances $u=(2n+1)\lambda/2$ corresponding to odd multiples of half of the spatial periodicity, the correlation function is $g^{(2)}(u,\tau)<1$ due to the reduced conditional probability of detecting two particles with this spatial difference, e.g. detecting one particle in a maximum of the interference pattern and afterwards one particle in a minimum. The second-order correlation function in equation (1.37) for this case is given by [1]

$$g^{(2)}(u,\tau) = 1 + \frac{K^2}{2}\cos(ku) \ , \tag{1.39}$$

which is independent of the correlation time τ as the interference pattern is stationary in time. Equation (1.39) shows that the characteristics of the interference pattern, such as contrast K and spatial periodicity λ, are included in the second-order correlation function via its contrast $K^2/2$ and wave number $k=2\pi/\lambda$. As discussed before, if no interference pattern is present, the correlation function is equal to one for all correlation times and lengths which can be seen from equation (1.39) for $K=0$.

In figure 1.9(b), the correlation function of the perturbed interference pattern in figure 1.3(b) is plotted illustrating the case of an interference pattern dephased by a single-frequency perturbation (equation (1.11) and (1.12) for $N=1$). Comparing figure 1.9(a) and (b), it can be seen that the correlation function in figure 1.9(b) is modified

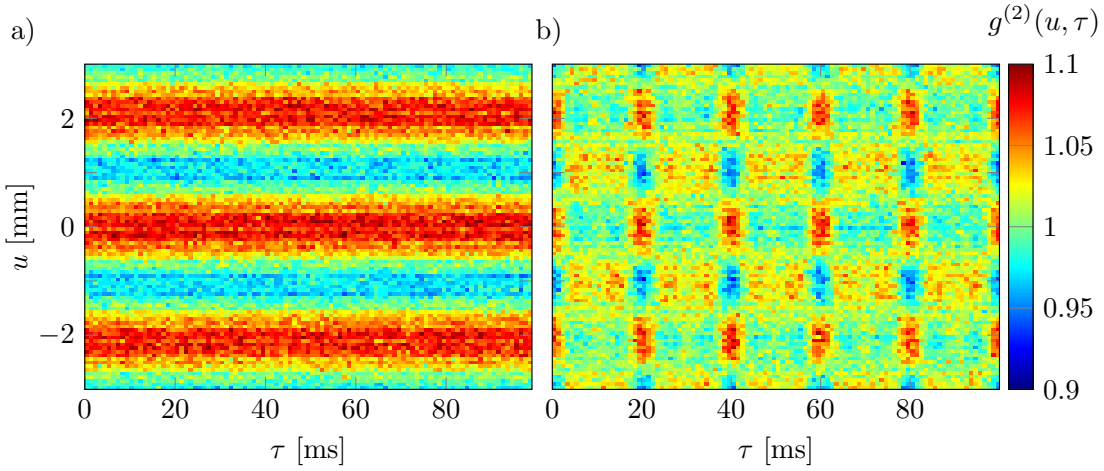

Figure 1.9.: a) Two-dimensional second-order correlation function $g^{(2)}(u,\tau)$ of the unperturbed interference pattern illustrated in figure 1.3(a). Along the u-direction the characteristics of the interference pattern can be identified for all correlation times τ. The positions of the maxima in the correlation function correspond to multiples of the spatial periodicity $u = n\lambda, n \in \mathbb{Z}$ and the minima $u = (2n+1)\lambda/2$ to odd multiples of half of the spatial periodicity. The correlation function can be described theoretically by equation (1.39). b) Correlation function of the perturbed interference pattern illustrated in figure 1.3(b). Due to the time-varying perturbation with a frequency of $\omega_1/2\pi = 50\,\text{Hz}$, the correlation function is modified along the τ-direction compared to a). The characteristics of the unperturbed interference pattern can be identified at correlation times corresponding to the reciprocal value of the applied perturbation frequency $\tau = M_\tau \cdot 2\pi/\omega_1 = M_\tau \cdot 20\,\text{ms}, M_\tau \in \mathbb{N}_0$. For correlation times $\tau \neq M_\tau \cdot 20\,\text{ms}$ the amplitude of the correlation function is reduced as $|A(\tau)| < 1$ (equation (1.40)).

along the τ-direction due to the time-varying perturbation $\varphi(t)$ with a frequency of $\omega_1/2\pi = 50\,\text{Hz}$. The characteristics of the unperturbed interference pattern can be identified in the correlation function for correlation times τ corresponding to multiples of the reciprocal value of the applied perturbation frequency $\tau = M_\tau \cdot 2\pi/\omega_1 = M_\tau \cdot 20\,\text{ms}, M_\tau \in \mathbb{N}_0$. For two particles arriving in the detection plane with a temporal difference of $\tau = t_1 - t_2 = M_\tau \cdot 2\pi/\omega_1$ the interference pattern has the same spatial position on the detector although it oscillates with the time t. This can be seen for the particle arrival times $t_1 = t + M_\tau \cdot 2\pi/\omega_1$ and $t_2 = t$ used in equation (1.11) and (1.12) for $N = 1$, resulting in $f(y,t_1) = f(y,t_2) = f(y,t)$ for all times t. Therefore, the interference pattern is stationary for the two particles and the spatial difference u reveals the characteristics of the unperturbed interference pattern, as explained before for the case of an unperturbed interference pattern ($K > 0$, $\varphi(t) = 0$). Equation (1.39) is valid for correlation times $\tau = M_\tau \cdot 2\pi/\omega_1$ and can be used to determine the characteristics of the unperturbed interference pattern. In contrast, for a temporal difference of $\tau \neq M_\tau \cdot 2\pi/\omega_1$ between two particles detected at the time $t_1 = t + \tau$ and $t_2 = t$ the spatial interference pattern has a different position in the detection plane for the one particle with respect to the position of the spatial interference pattern for the other particle, meaning $f(y,t_1) \neq f(y,t_2)$. Therefore, the spatial difference u of these particles does not reveal the characteristics of the unperturbed interference

pattern and the amplitude of the correlation function is reduced (see figure 1.9(b) for $\tau \neq M_\tau \cdot 20\,\mathrm{ms}$). The second-order correlation function in equation (1.37) for an interference pattern dephased by a time-varying perturbation is given by [1]

$$g^{(2)}(u,\tau) = 1 + \frac{K^2}{2} \cdot A(\tau)\cos(ku) \ , \tag{1.40}$$

with the amplitude $A(\tau)$ depending on the correlation time and the specific perturbation characteristics. Comparing equation (1.39) and (1.40), it can be seen that the correlation function of the unperturbed interference pattern is modified by $A(\tau)$. The correlation function of an unperturbed interference pattern (figure 1.9(a)) results from equation (1.40) for the maximum value of the amplitude $A(\tau) = 1$ for all correlation times τ. In figure 1.9(b), at the temporal positions given by $\tau = M_\tau \cdot 2\pi/\omega_1 = M_\tau \cdot 20\,\mathrm{ms}$ the amplitude in equation (1.40) reaches its maximum value of $A(\tau) = 1$ resulting in equation (1.39) which is suitable to determine the characteristics of the unperturbed interference pattern, such as contrast K and spatial periodicity λ. For correlation times $\tau \neq M_\tau \cdot 2\pi/\omega_1$ the amplitude of the correlation function is reduced $|A(\tau)| < 1$. A detailed theoretical description and discussion of $A(\tau)$ is given in the next chapter for single- and multifrequency perturbations.

The descriptive explanations of the used second-order correlation function made here shows that the temporal differences τ of particle arrival times in the detection plane reveal the parameters of the time-varying perturbation $\varphi(t)$, such as amplitude φ, frequency ω, and phase ϕ. Therefore, it is possible to determine the properties of the unperturbed interference pattern as well as the perturbation characteristics with the second-order correlation analysis of multifrequency dephasing discussed theoretically and demonstrated experimentally in this thesis.

2. Second-order correlations in single-particle interferometry

Publication [1] provides a comprehensive derivation of the two-dimensional second-order correlation theory for multifrequency dephasing in single-particle interferometry. It is the fundament for the experimental implementation in the dephasing experiments in publications [2–4].

In the following, the properties of the second-order correlation function for single- and multifrequency dephasing are discussed. It is explained how the characteristics of the unperturbed interference pattern, such as contrast K and spatial periodicity λ, can be determined from the correlation function. Furthermore, the amplitude spectrum of the correlation function which is applied in publication [4] for the identification of unknown perturbation parameters is calculated. The numerical correlation function used to extract the measurement data is derived and the effects resulting from the discretization of the correlation function are outlined.

The significant equations and results will be summarized and discussed in the following sections. Publication [1] is appended at the end of this thesis including more details of the calculations and discussions.

2.1. Theory of second-order correlations

In this section, the analytic solution of the second-order correlation function and the corresponding amplitude spectrum are provided and the difference between explicit and approximate solution is discussed. The determination of contrast and spatial periodicity of the unperturbed interference pattern from the correlation function is explained. Furthermore, the identification of the perturbation characteristics is outlined.

2.1.1. Time-averaged interference pattern

In many single-particle interferometry experiments [30, 100, 102, 113, 115] phosphor screens in conjunction with multichannel plates (MCPs) are used to detect the interference pattern. Light pulses on the phosphor screen are generated by particle impacts and integrated with a charge-coupled device camera (CCD-camera). If the interference pattern is dephased by a time-dependent perturbation, the contrast is reduced or vanished in the temporally integrated signal. It is demonstrated below how this contrast reduction depends on the perturbation amplitude.

As discussed in section 1.1, the time-dependent perturbation $\varphi(t)$ in equation (1.11) "washes-out" the temporally integrated interference pattern [2–4]. Using the time-

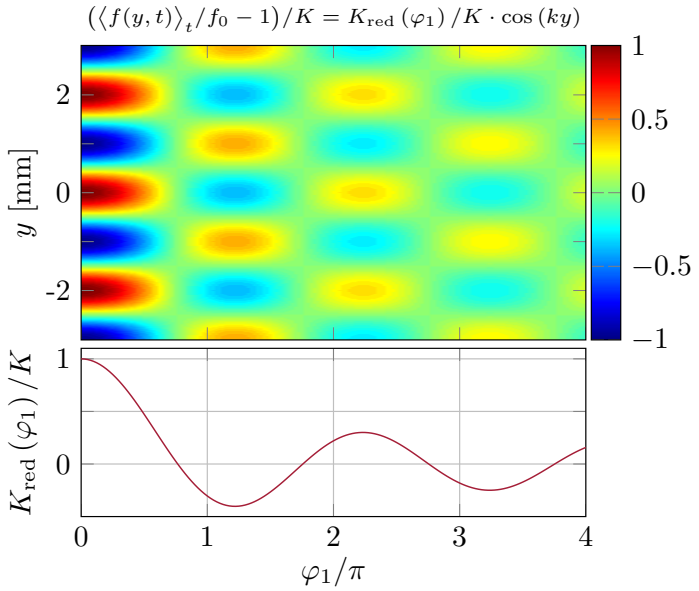

Figure 2.1.: Top: Time-averaged interference pattern (equation (2.2)) with a spatial periodicity $\lambda = 2\,\mathrm{mm}$ along the y-direction depending on the peak phase deviation φ_1. Bottom: Dependence of the relative contrast reduction $K_{\mathrm{red}}(\varphi_1)/K$ on the peak phase deviation φ_1. The contrast is equal to zero at $\varphi_1 = 0.76\,\pi$, which corresponds to the first zero of $J_0(\varphi_1)$. Figure from [1].

average

$$\big\langle f(y,t)\big\rangle_t \coloneqq \lim_{T\to\infty} \frac{1}{T}\int_0^T f(y,t)\,\mathrm{d}t\ , \tag{2.1}$$

of the probability distribution of particle impacts in the detection plane (equation (1.12)), the dephased interference pattern can be calculated for one perturbation frequency ($N = 1$ in equation (1.11)), yielding

$$\big\langle f(y,t)\big\rangle_t = f_0\big(1 + \underbrace{K J_0(\varphi_1)}_{=K_{\mathrm{red}}(\varphi_1)}\cos(ky)\big)\ , \tag{2.2}$$

with the zeroth order Bessel function of first kind J_0. This interference pattern shows a reduced contrast compared to the unperturbed interference pattern (equation (1.12)). The contrast reduction is given by the perturbation amplitude via the zeroth order Bessel function: $K_{\mathrm{red}}(\varphi_1) = K J_0(\varphi_1)$, with $|J_0(\varphi_1)| \leq 1$. A detailed derivation of equation (2.2) can be found in section 2.1 of publication [1].

In figure 2.1 at the top, the time-averaged interference pattern calculated with equation (2.2) depending on the peak phase deviation φ_1 is illustrated. The spatial periodicity of the interference pattern $\lambda = 2\,\mathrm{mm}$ can be identified along the y-direction. In figure 2.1 at the bottom, the relative contrast reduction $K_{\mathrm{red}}(\varphi_1)/K$ is plotted. For a peak phase deviation of $\varphi_1 = 0.76\,\pi$, the contrast vanishes and returns for larger φ_1, but not completely. The first position of zero contrast corresponds to the first zero of $J_0(\varphi_1)$. Due to the changing sign of $J_0(\varphi_1)$ from positive to negative, the interference pattern is phase shifted by π. This cycle goes on for higher peak phase deviations and the contrast is further reduced.

For a perturbation consisting of multiple frequencies ($N > 1$) with peak phase deviations $\varphi_j < 1$, equation (2.2) becomes

$$\left\langle f(y,t)\right\rangle_t = f_0\big(1 + \underbrace{K\prod_{j=1}^{N} J_0(\varphi_j)}_{=K_{\mathrm{red}}\left(\varphi_{j=1\ldots N}\right)}\cos(ky)\big)\ . \tag{2.3}$$

The reduced contrast $K_{\mathrm{red}}\left(\varphi_{j=1\ldots N}\right)$ now depends on all peak phase deviations φ_j and is therefore typically stronger reduced as compared to the case of one perturbation frequency.

2.1.2. Approximate solution of the second-order correlation function

In contrast to the temporally integrated interference pattern, the correlation function uses spatial and temporal differences of the detected particles. The interference pattern is still present and not influenced by the perturbation on timescales below the periodic time of the oscillation. As discussed in section 1.2, the spatial differences unveil the contrast K and spatial periodicity λ of the unperturbed interference pattern in the correlation function. Using the temporal differences additionally, the perturbation properties (ω_j, φ_j, and ϕ_j) can be identified.

An explicit solution of the second-order correlation function for multifrequency dephasing can be derived from equation (1.37) using the probability distribution in equation (1.12) and the average over position and time in equation (1.38). For perturbation frequencies ω_j (equation (1.11)) which are small compared to the acquisition time $T \gg 2\pi/\omega_j$ and for a spatial periodicity λ which is small compared to the acquisition length $Y \gg \lambda$, equation (1.37) can be solved analytically, yielding the explicit solution of the correlation function provided in appendix A.1. A detailed derivation is given in section 2.2 of publication [1].

In the following, the approximate solution of the correlation function given by equation (1.40) is discussed as it typically constitutes the main contribution to the explicit solution in equation (A.1) and is usually suitable to describe multifrequency perturbations ($N > 1$ in equation (1.11)). The exceptional cases for which the explicit solution has to be used are discussed at the end of this section.

In section 1.2, the formation of the correlation function from an interference pattern dephased by one perturbation frequency ω_1 ($N = 1$ in equation (1.11)) was explained and the approximate solution of the correlation function in equation (1.40) was discussed. For this case the explicit and approximate solutions are identical, yielding equation (1.40) with the time-dependent amplitude $A(\tau)$ given by

$$A(\tau) = \sum_{m_1=-\infty}^{\infty} J_{m_1}(\varphi_1)^2 \cos\left(m_1\omega_1\tau\right)\ , \tag{2.4}$$

with the Bessel function of first kind J_{m_1} and the perturbation amplitude (peak phase deviation) φ_1. $A(\tau)$ is composed of a superposition of cosines with the periodicity determined by the perturbation frequency ω_1 and its harmonics $m_1\omega_1$, with $m_1 \in \mathbb{Z}$. The

amplitude of each cosine is determined by the peak phase deviation φ_1 via the square of the Bessel function $J_{m_1}(\varphi_1)^2$. As discussed in section 1.2, the amplitude reaches its maximum value of $A(\tau) = 1$ for correlation times given by the reciprocal value of the perturbation frequency $\tau = M_\tau \cdot 2\pi/\omega_1$ with $M_\tau \in \mathbb{N}_0$. Only for these correlation times, the cosines in equation (2.4) are in phase with respect to each other and can sum up to a maximum. Then, the characteristics of the unperturbed interference pattern can be identified in the correlation function along the u-direction and equation (1.40) turns into equation (1.39). Here, the contrast of the correlation function $K^2/2$ is directly linked to the contrast of the unperturbed interference pattern K and therefore, equation (1.39) is used to determine the contrast and spatial periodicity. For all other correlation times the absolute value of the amplitude is $|A(\tau)| < 1$ and therefore, the contrast of the correlation function in equation (1.40) is reduced $K^2/2 \cdot A(\tau)$. In principle, the sum in equation (2.4) has to be evaluated for an infinite number of addends. However, for large values of m_1 the contribution to the sum is suppressed due to the strong decay of the Bessel function $J_{m_1}(\varphi_1)$ for $m_1 > \varphi_1$, which can be seen in the asymptotic form of the Bessel function for $0 < \varphi \ll \sqrt{m+1}$ [209]

$$J_m(\varphi) \approx \frac{1}{\Gamma(m+1)} \left(\frac{\varphi}{2}\right)^m , \tag{2.5}$$

where $\Gamma(m+1) = m!$ denotes the gamma function. Thus, the number of addends in equation (2.4) is limited and the maximum frequency component included in the correlation function is approximately given by $m_{1,\max}\omega_1$, with $m_{1,\max} \approx \varphi_1$. This shows that for a larger perturbation amplitude φ_1 higher orders of the Bessel function has to be taken into account for the calculation of the amplitude in equation (2.4). In section 2.1.4, an exemplary correlation function for the single-frequency case is explained in detail.

For a multifrequency perturbation ($N > 1$ in equation (1.11)) the time-dependent amplitude in equation (1.40) is given by

$$A(\tau) = \prod_{j=1}^{N} \left(\sum_{m_j=-\infty}^{\infty} J_{m_j}(\varphi_j)^2 \cos(m_j \omega_j \tau) \right) . \tag{2.6}$$

Compared to equation (2.4), the amplitude for the multifrequency case is determined by the product of the sums of the individual frequencies ω_j. Therefore, it is composed of a superposition of the perturbation frequencies and their harmonics $m_j\omega_j$ as well as the sums and differences of the involved perturbation frequencies (intermodulation terms). Due to the strong decay of the Bessel function (equation (2.5)), the maximum frequency component of all underlying perturbation frequencies included in the correlation function is approximately given by $\max\{\varphi_j\omega_j\}$. The amplitude $A(\tau)$ reveals a periodic structure in τ-direction with the periodicity defined by the involved perturbation frequencies ω_j (see section 2.1.3). It has to be mentioned that the phases of the perturbation ϕ_j can not be determined with the approximate correlation function. However, using the possibility to reconstruct the unperturbed interference pattern the phases can be identified which is discussed in section 2.1.6.2. A detailed derivation of equation (1.40) and (2.6) is given in section 2.3 of publication [1].

Compared to the approximate solution in equation (1.40), the explicit solution of the correlation function explained detailed in appendix A.1 and section 2.2 of publication

[1] is modified by a temporal $\tilde{\Phi}(\tau)$ and spatial phase $\psi(\tau)$ depending on the correlation time

$$g^{(2)}(u,\tau) = 1 + \frac{K^2}{2} \cdot A\big(\tau, \tilde{\Phi}(\tau)\big) \cos\big(ku + \psi(\tau)\big) \ . \tag{2.7}$$

For correlation times τ that are multiples of the temporal periodicity of the amplitude given by the involved perturbation frequencies (see section 2.1.3), the time-dependent phases are $\tilde{\Phi}(\tau) = 0$ and $\psi(\tau) = 0$. Thus, the explicit and approximate solution are identical for these correlation times. Due to the non-vanishing phases $\tilde{\Phi}(\tau)$ and $\psi(\tau)$ for other correlation times, the explicit correlation function is modified compared to the approximate one.

As mentioned before, the approximate correlation function is usually suitable to describe multifrequency perturbations ($N > 1$). However, in the case of few perturbation frequencies that are multiples of each other, e.g. ω_1 and $\omega_2 = 2\omega_1$, the explicit solution in equation (2.7) has to be applied. An example for the case of two frequencies that are multiples of each other is explained in detail in section 2.1.4. For three perturbation frequencies that are separated by the same frequency $\Delta\omega$, e.g. $\omega_1 = \omega_2 - \Delta\omega$, ω_2, and $\omega_3 = \omega_2 + \Delta\omega$, the explicit solution also has to be used. This demonstrates that it depends on the involved perturbation frequencies which solution of the second-order correlation function has to be applied to achieve a good agreement between experiment and theory. In publication [1] and appendix A.1, this is discussed more detailed.

2.1.3. Determination of contrast and spatial periodicity

Only at certain correlation times τ, the contrast K and the spatial periodicity λ of the unperturbed interference pattern can be determined correctly in the correlation function, which is discussed below.

The explicit and approximate correlation function (equation (2.7) and (1.40)) show a periodic modulation in u-direction with the same spatial periodicity λ as the unperturbed interference pattern. The amplitude of this modulation depends on the correlation time τ and the specific perturbation characteristics. Only at correlation times τ, for which the resulting amplitude reaches its maximum value of 1, the contrast of the correlation function $K^2/2$ is directly linked to the contrast K of the unperturbed interference pattern. As mentioned in section 2.1.2, the explicit and approximate solution of the correlation function are identical at these correlation times $\tau = M_\tau \tau_s$, with $M_\tau \in \mathbb{N}_0$. Here, the so called superperiod $\tau_s = 2\pi/\omega_{gcd}$ of the modulation in τ-direction is defined by the greatest common divisor of all perturbation frequencies $gcd(\omega_1, \ldots, \omega_N) = \omega_{gcd}$. Each frequency ω_j has an integer value $s_j \in \mathbb{N}$, for which $\omega_{gcd} = \omega_j / s_j$. Using $\tau = M_\tau \tau_s$ in equation (1.40) and (2.6), the correlation function yields

$$\begin{aligned} g^{(2)}(u, M_\tau \tau_s) &= 1 + \frac{K^2}{2} \cos(ku) \cdot \underbrace{\prod_{j=1}^{N} \left(\sum_{m_j=-\infty}^{\infty} J_{m_j}(\varphi_j)^2 \underbrace{\cos(2\pi M_\tau m_j s_j)}_{=1} \right)}_{=1} \\ &= 1 + \frac{K^2}{2} \cos(ku) \ , \end{aligned} \tag{2.8}$$

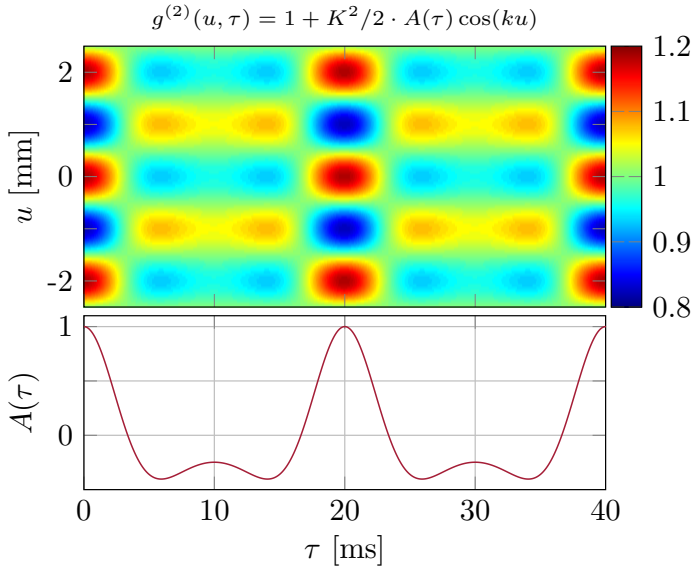

Figure 2.2.: Top: Correlation function of an interference pattern with $K = 0.6$, $\lambda = 2\,\mathrm{mm}$ perturbed by $\omega_1/2\pi = 50\,\mathrm{Hz}$, $\varphi_1 = 0.76\,\pi$, calculated according to equation (1.40) and (2.4). The spatial periodicity λ can be identified in the modulation along u. In τ-direction, the periodicity is given by the specific perturbation spectrum. Bottom: Amplitude $A(\tau)$ of the correlation function calculated with equation (2.4). Its maximum value of 1 is reached at correlation times that are multiples of the superperiod $\tau_s = 2\pi/\omega_1 = 20\,\mathrm{ms}$. At these correlation times, the contrast of the correlation function $K^2/2$ is directly given by the contrast of the unperturbed interference pattern K. For all other correlation times the contrast of the correlation function is reduced to $K^2/2 \cdot A(\tau)$ as $|A(\tau)| < 1$. Figure from [1].

which is used for the determination of the contrast K and spatial periodicity λ of the unperturbed interference pattern. Equation (2.8) is identical to equation (1.39) describing the correlation function of an interference pattern that was not dephased by a perturbation ($\varphi(t) = 0$ in equation (1.12)). Thus, for correlation times $\tau = M_\tau \tau_s$ it seems as if the interference pattern was not dephased by the applied perturbation. If the involved perturbation frequencies do not have a greatest common divisor ω_{gcd}, the superperiod τ_s is infinite and the only correlation time, where the amplitude has its maximum value of 1, is $\tau = 0$. Therefore, the contrast and spatial periodicity are always determined at $\tau = 0$ using equation (2.8).

2.1.4. Correlation function of a single- and two-frequency perturbation

The characteristics of the explicit and approximate correlation function, explained in section 2.1.2 and appendix A.1, are illustrated in the following for the case of a single- and two-frequency perturbation.

As mentioned in section 2.1.2, the explicit and approximate solution are identical for one perturbation frequency ω_1. Therefore, this case is explained in detail in the following. Using equation (1.40) and (2.4), a correlation function $g^{(2)}(u,\tau)$ is calculated for an interference pattern perturbed by a single-frequency perturbation $\omega_1/2\pi = 50\,\mathrm{Hz}$,

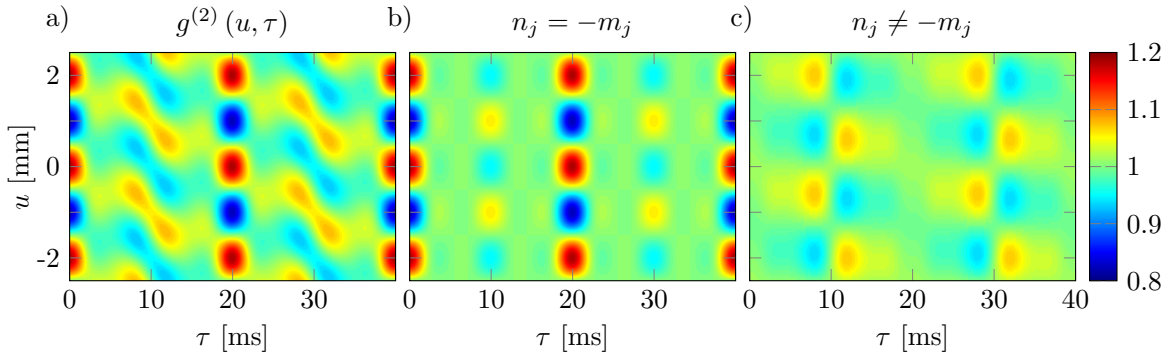

Figure 2.3.: a) Correlation function $g^{(2)}(u,\tau)$ calculated with the explicit solution in equation (A.1) for an interference pattern with $K = 0.6$ and $\lambda = 2\,\mathrm{mm}$ perturbed by two frequencies $\omega_1/2\pi = 50\,\mathrm{Hz}, \varphi_1 = 0.5\,\pi, \phi_1 = 0.25\,\pi$ and $\omega_2/2\pi = 100\,\mathrm{Hz}, \varphi_2 = 0.5\,\pi, \phi_2 = -0.25\,\pi$. b) Approximate correlation function calculated with equation (1.40) and (2.6). c) Difference between a) and b) containing the terms that are only included in the explicit solution. Figure from [1].

$\varphi_1 = 0.76\,\pi$ and plotted at the top of figure 2.2. Here, a contrast $K = 0.6$ and spatial periodicity $\lambda = 2\,\mathrm{mm}$ were chosen as these are typical experimental values. The periodic structure in u- and τ-direction is clearly visible. According to equation (1.40), the spatial periodicity of the unperturbed interference pattern is included in the correlation function in the modulation along u. The contrast of the correlation function, however, is reduced for each τ to $K^2/2 \cdot A(\tau)$. According to equation (2.4) and illustrated in figure 2.2 at the bottom, the maximum of the amplitude $A(\tau) = 1$ is achieved for correlation times that are multiples of the superperiod $\tau_s = 2\pi/\omega_1 = 20\,\mathrm{ms}$ (see section 2.1.3). At these correlation times, the contrast of the correlation function $K^2/2$ is directly given by the contrast of the unperturbed interference pattern K. For the above perturbation parameters, the time-averaged interference pattern would be vanished according to equation (2.2) and the illustration in figure 2.1. However, it is possible to determine the contrast and spatial periodicity using correlation analysis as discussed in section 2.1.3.

If the perturbation consists of frequencies that are multiples of each other, the explicit correlation function (equation (2.7)) has to be used. This case is discussed below for two perturbation frequencies with $\omega_2 = 2\omega_1$. Then, additional terms contribute to the correlation function generating a temporal $\tilde{\Phi}(\tau)$ and spatial phase $\psi(\tau)$ depending on the correlation time τ (equation (2.7)) that are not included in the approximate solution (equation (1.40)). A correlation function $g^{(2)}(u,\tau)$ calculated according to equation (A.1) is shown in figure 2.3(a) for an interference pattern with contrast $K = 0.6$ and spatial periodicity $\lambda = 2\,\mathrm{mm}$ perturbed with two frequencies $\omega_1/2\pi = 50\,\mathrm{Hz}, \varphi_1 = 0.5\,\pi, \phi_1 = 0.25\,\pi$ and $\omega_2/2\pi = 100\,\mathrm{Hz}, \varphi_2 = 0.5\,\pi, \phi_2 = -0.25\,\pi$. In figure 2.3(b), the result for the approximate correlation function (equation (1.40) and (2.6)) can be seen. The periodic modulation in u-direction can be identified in both correlation functions, figure 2.3(a) and (b), and reveals the same spatial periodicity as the unperturbed interference pattern. As discussed in section 2.1.3, the periodicity in τ-direction, which is also present in both correlation functions, is given by the superperiod $\tau_s = 2\pi/\omega_{gcd} = 20\,\mathrm{ms}$ via the greatest common divisor of the involved perturbation

frequencies $\omega_{gcd}/2\pi = 50\,\mathrm{Hz}$. For correlation times that are multiples of the superperiod, the modulation amplitude reaches its maximum value of 1 and the explicit and approximate correlation function are identical. In figure 2.3(c), the difference between them, solely given by the terms that are only included in the explicit solution, is shown. The contribution of these terms to the correlation function in figure 2.3(a) results in a temporal $\tilde{\Phi}(\tau)$ and spatial phase $\psi(\tau)$ modifying the explicit solution compared to the approximate one (equation (1.40) and (2.7)).

Under certain conditions, the approximate solution can also be used to describe the case of frequencies that are multiples of each other. The transition between explicit and approximate solution is discussed in detail in section 2.6 of publication [1].

2.1.5. Amplitude spectrum of the approximate solution

For multifrequency dephasing, it is difficult to determine the perturbation spectrum from the correlation function (c.f. figure 2.3). Therefore, its amplitude spectrum is used for the identification of the unknown perturbation characteristics [4] as it enables better access to the involved frequencies. Here, the equivalence between the power spectrum of the perturbed measurement signal and the Fourier transform of the correlation function is utilized, according to the Wiener-Khintchine theorem [188, 189].

With the temporal Fourier transform $\mathcal{F}\left(g^{(2)}(u,\tau)\right)(u,\omega) = \frac{1}{\sqrt{2\pi}}\int_{-\infty}^{\infty} g^{(2)}(u,\tau)\mathrm{e}^{i\omega\tau}\,\mathrm{d}\tau$ of equation (1.40) and (2.4) the amplitude spectrum $\left|\mathcal{F}\left(g^{(2)}(u,\tau)\right)(u,\omega)\right|$ of the approximate correlation function for a single-frequency perturbation can be calculated, yielding

$$\frac{1}{2\pi}\left|\mathcal{F}\left(g^{(2)}(u,\tau)\right)(u,\omega)\right|^2 = \delta(\omega)^2 + \left(\frac{K^2}{2}\cdot\hat{A}(\omega)\cos\left(ku\right)\right)^2, \tag{2.9}$$

with the frequency-dependent amplitude

$$\hat{A}(\omega) = \sum_{m_1=-\infty}^{\infty} J_{m_1}(\varphi_1)^2\cdot\Big(\delta(\omega+m_1\omega_1)+\delta(\omega-m_1\omega_1)\Big) \tag{2.10}$$

and the Dirac delta function $\delta(\omega)$. The modulation along the u-direction given by the spatial periodicity of the unperturbed interference pattern λ remains unchanged in the amplitude spectrum (compare equation (1.40) and (2.9)). As discussed in section 2.1.2, the amplitude in equation (2.4) consists of a superposition of the perturbation frequency ω_1 and its harmonics $m_1\omega_1$, with $m_1 \in \mathbb{Z}$. These frequency components can be identified in the argument of the Dirac delta function $\delta(\omega\pm m_1\omega_1)$ in equation (2.10). The amplitude of each frequency component is given by the peak phase deviation φ_1 via the square of the Bessel function $J_{m_1}(\varphi_1)^2$. According to equation (2.5), the maximum frequency component included in the amplitude spectrum is approximately given by $m_{1,\max}\omega_1$, with $m_{1,\max} \approx \varphi_1$.

For a multifrequency perturbation the frequency-dependent amplitude $\hat{A}(\omega)$ of the approximate solution can be found in equation (A.12) in appendix A.2 together with the amplitude spectrum of the explicit solution of the correlation function (equation (A.9)). The amplitude spectrum of the approximate solution in equation (A.12) can be interpreted as a convolution of the single-frequency spectra given by equation (2.10).

Thus, not only the perturbation frequencies and their harmonics are included in the amplitude spectrum but also their sum and difference frequencies (intermodulation terms). A detailed derivation of the explicit and approximate solution of the amplitude spectrum can be found in section 2.7 of publication [1].

As the frequency components included in the amplitude spectrum are specific for the applied perturbation characteristics, they are used for the identification of unknown perturbation frequencies [4].

2.1.6. Determination of perturbation characteristics

For multifrequency perturbations, the identification of unknown frequencies directly from the structure of the correlation function is difficult (c.f. figure 2.3). Its amplitude spectrum provides a better access to the included frequency components. In publication [4], a numerical algorithm has been developed which can identify unknown perturbation frequencies using the amplitude spectrum. With the obtained frequencies ω_j, the amplitude spectrum of the explicit solution (equation (A.9)) or approximate solution (equation (2.9) and (A.12)) is used to determine the corresponding peak phase deviations φ_j and phases ϕ_j. Due to the invariance of the correlation function, the phases ϕ_j are not determined uniquely. Nevertheless, using the possibility to reconstruct the unperturbed interference pattern the original phases can be identified.

2.1.6.1. Invariance of the correlation function

In section 2.1.3, the determination of the contrast and spatial periodicity from the second-order correlation function was discussed. Using the amplitude spectrum, the perturbation frequencies, amplitudes, and phases can be identified. However, the phases of the perturbation can not be determined uniquely. In the case of a single perturbation frequency ($N = 1$) the phase information is completely lost. Though, for multifrequency perturbations ($N > 1$) relative phase informations can be revealed with the correlation analysis. Therefore, it is necessary to understand the invariance of the correlation function under specific transformations.

The correlation function is invariant under position shifts $y \to y + y_0$ and time transformations $t \to t + t_0$, as only position and time differences between particles are taken into account. Using equation (1.11) and (1.12), this time transformation and position shift is equal to the transformations

$$y \to y + y_0 \quad \widehat{=} \quad \varphi(t) \to \varphi(t) + k y_0 \ , \tag{2.11}$$

$$t \to t + t_0 \quad \widehat{=} \quad \phi_j \to \phi_j + \omega_j t_0 \ . \tag{2.12}$$

Additionally, the correlation function is invariant under simultaneous time and space reversal: $t \to -t\,,\ y \to -y$. According to equation (1.11) and (1.12), this transformation equals a phase transformation

$$t \to -t\,,\ y \to -y \quad \widehat{=} \quad \phi_j \to -\phi_j + \pi \ . \tag{2.13}$$

As the correlation function is not modified under phase transformations mentioned above (equation (2.12) and (2.13)), it is identical for different phase multiplets.

This invariance is calculated exemplarily for a two-frequency perturbation ($N = 2$) with phases ϕ_1 and ϕ_2 in section 2.8.1 of publication [1]. The two resulting linear equations for the phase duplets $\{\hat{\phi}_1, \hat{\phi}_2\}$ and $\{\tilde{\phi}_1, \tilde{\phi}_2\}$ describe the same correlation function. Therefore, it is not possible to determine the original phases ϕ_1 and ϕ_2 uniquely from the correlation analysis.

2.1.6.2. Determination of perturbation phases

Using the possibility to reconstruct the unperturbed interference pattern, the original phases ϕ_j can be determined. With the obtained perturbation parameters from the correlation analysis ω_j and φ_j, the spatial coordinates of the reconstructed interference pattern $y_{i,\mathrm{new}}$ are given by [4]

$$y_{i,\mathrm{new}} = y_i - \frac{\lambda}{2\pi}\varphi(t_i) = y_i - \frac{\lambda}{2\pi}\sum_{j=1}^{N}\varphi_j \cos\left(\omega_j t_i + \phi_j\right) \ , \tag{2.14}$$

with $\varphi(t_i)$ denoting the time-dependent perturbation (equation (1.11)) and y_i, t_i the spatial and temporal coordinate of particle i of the perturbed interference pattern. For the original phases ϕ_j the maximum contrast of the reconstructed pattern is reached. The free parameter space for the phases ϕ_j can be reduced by one dimension if one linear equation for the phase duplets $\{\hat{\phi}_j\}$ and $\{\tilde{\phi}_j\}$ (section 2.1.6.1) is used in the reconstruction process for one of the phases ϕ_j.

2.2. Numerical second-order correlation function

In this section, the numerical correlation function used for the evaluation of the experimental data is derived and the influence of discretization on the obtained parameters is discussed.

2.2.1. Correlation function for discrete signals

Until now, the analytic probability distribution of particle impacts at the detector in equation (1.12) was used for the calculation of the correlation function. However, the real detector provides a discrete signal of particle impacts with a finite acquisition time T and length Y. This detector signal $f(y,t)$ used to extract the correlation function consists of N particles with arrival times t_i and coordinates y_i ($i = 1 \ldots N$). The particle impacts in the detection plane are given by the Dirac delta function, which is an appropriate approximation due to the much smaller pulse width at the detector compared to the mean time distance between particle impacts. This definition is used for the calculation of the correlation function in equation (1.37), yielding the discrete second-order correlation function

$$g^{(2)}(u,\tau) = \frac{TY}{N^2}\sum_{i,j=1}^{N}\delta\left(\tau + t_i - t_j\right)\delta\left(u + y_i - y_j\right) \ . \tag{2.15}$$

In section 3.1 of publication [1], a detailed derivation of equation (2.15) is given. For an appropriate correlation function that can be compared with the analytic theory,

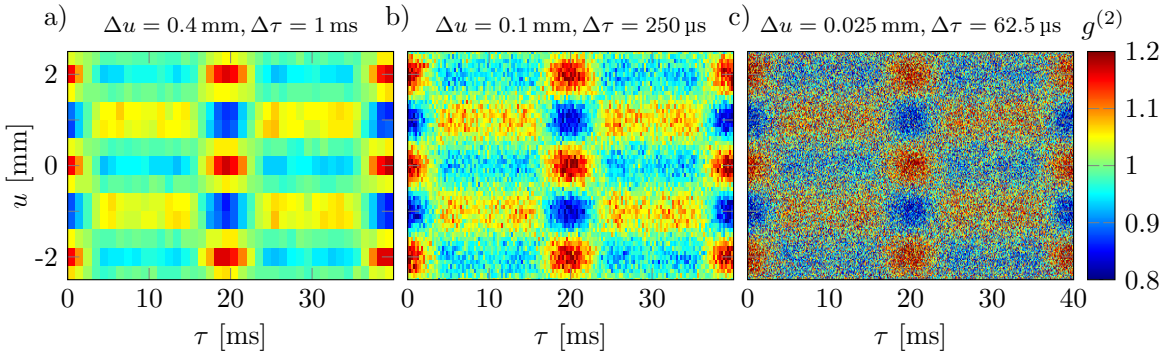

Figure 2.4.: Correlation functions with different temporal and spatial discretization step sizes Δu and $\Delta\tau$ extracted according to equation (2.17) from a single-particle simulation of a perturbed interference pattern. The interference pattern has a contrast of $K = 0.6$ and a spatial periodicity $\lambda = 2\,\mathrm{mm}$ and was perturbed by $\omega_1/2\pi = 50\,\mathrm{Hz}$ and $\varphi_1 = 0.75\,\pi$. a) For large Δu and $\Delta\tau$, the structure is "smeared-out". b) The structure is clearly visible compared to a), but the noise is increased for smaller discretization step size. c) The noise grows larger for even smaller Δu and $\Delta\tau$. Figure from [1].

a temporal and spatial discretization step size $\Delta\tau$ and Δu has to be implemented in equation (2.15), resulting in

$$g^{(2)}(u,\tau) = \frac{TY}{N^2}\frac{1}{\Delta\tau\Delta u}\underbrace{\int_{\tau-\frac{\Delta\tau}{2}}^{\tau+\frac{\Delta\tau}{2}}\int_{u-\frac{\Delta u}{2}}^{u+\frac{\Delta u}{2}}\sum_{i,j=1}^{N}\delta\left(\tau+t_i-t_j\right)\delta\left(u+y_i-y_j\right)\,\mathrm{d}u\mathrm{d}\tau}_{=N_{u,\tau}}$$
$$= \frac{TY}{N^2\Delta\tau\Delta u}N_{u,\tau}\ . \tag{2.16}$$

Here, $N_{u,\tau}$ is the number of particle pairs (i,j) with spatial distances $(y_i - y_j) \in [u - \Delta u/2, u + \Delta u/2]$ and temporal separations $(t_i - t_j) \in [\tau - \Delta\tau/2, \tau + \Delta\tau/2]$.

Due to the finite acquisition time T and length Y, the detection probability of particle impacts with large temporal and spatial differences is decreased by a factor of $(1 - \tau/T)$ and $(1 - |u|/Y)$, respectively. To correct this effect, the number $N_{u,\tau}$ in equation (2.16) has to be modified, yielding the numerical correlation function

$$g^{(2)}(u,\tau) = \frac{TY}{N^2\Delta\tau\Delta u}\frac{N_{u,\tau}}{\left(1-\frac{\tau}{T}\right)\left(1-\frac{|u|}{Y}\right)}\ , \tag{2.17}$$

which is also normalized to one as the analytic correlation function.

Three correlation functions with different spatial and temporal discretization step sizes are extracted according to equation (2.17) from a single-particle simulation of a perturbed interference pattern and shown in figure 2.4. In section 3.3 of publication [1], the simulation using the acceptance-rejection method [210] is explained in detail. The interference pattern with a contrast $K = 0.6$ and a spatial periodicity $\lambda = 2\,\mathrm{mm}$ was perturbed by $\omega_1/2\pi = 50\,\mathrm{Hz}$ and $\varphi_1 = 0.75\,\pi$. In figure 2.4(a), the structure of the correlation function is "smeared-out" due to the large values of Δu and $\Delta\tau$, whereas it is clearly visible in figure 2.4(b). However, the noise in the correlation function is

increased in comparison to figure 2.4(a). For a even smaller discretization step size, the noise increases further which can be seen in figure 2.4(c). Both effects influence the correlation function and the parameters obtained from the correlation analysis. Therefore, the effects of discretization have to be understood to choose Δu and $\Delta\tau$ in an appropriate way which is derived theoretically for one perturbation frequency in appendix A.3 and section 3.2 of publication [1].

2.2.2. Application limits of the second-order correlation analysis

The perturbation frequency can not be resolved if the particles spend longer times in the area of dephasing compared to the cycle time of the oscillation. Then, the particles traverse many periods of the perturbation and therefore, it is averaged out. In this case, the application of the correlation analysis is not possible.

In general, if the perturbation is a periodic oscillation, the correlation analysis can be applied, even if the perturbation frequency is much larger than the mean particle count rate, due to the infinite coherence of such a perturbation. As discussed in section 2.1.2, the maximum frequency component of all involved perturbation frequencies is given by $\max(\varphi_j\omega_j)$. For the determination of slow and random perturbations with large peak phase deviations, this maximum sets a lower threshold for the mean particle count rate for a good agreement between experiment and theory.

2.3. Conclusion

The contrast reduction of a temporally integrated interference pattern dephased by a time-varying perturbation depends on the perturbation amplitude. However, it is possible to reveal the contrast and spatial periodicity of the unperturbed interference pattern using the second-order correlation function for multifrequency perturbations. Additionally, the perturbation frequencies, amplitudes, and phases can be obtained using the amplitude spectrum of the explicit or approximate correlation function. Due to the invariance of the correlation function under time and space transformations, the perturbation phases are not uniquely determined from the correlation analysis. Nevertheless, with the possibility to reconstruct the unperturbed interference pattern the phases can be identified.

To evaluate the experimental data the numerical correlation function is applied. Here, the parameters extracted from the correlation function, such as contrast and perturbation amplitude, depend on the spatial and temporal discretization step size which have to be chosen in an appropriate way to obtain the correct results.

3. Correction of dephasing oscillations in matter-wave interferometry

In **publication [2]**, the case of a single-frequency perturbation is demonstrated in an electron biprism interferometer. For this purpose, an external time-varying magnetic field shifts the interference pattern perpendicular to the fringes and therefore, the contrast in the spatial signal is reduced. As mentioned in section 2.1.2, the explicit (equation (2.7)) and approximate correlation function (equation (1.40) and (2.4)) are identical for one perturbation frequency ($N = 1$). This special case is investigated in detail.

The experimental setup is explained and it is demonstrated, how the contrast and spatial periodicity can be revealed using the spatial distances of temporal successive particle events. For one perturbation frequency, the applied second-order correlation theory is explained in detail in section 2.1.2. Fitting the theory to the numerical correlation function extracted from the experimental data, the matter-wave characteristics, such as contrast K and spatial periodicity λ, and the perturbation properties (ω_1 and φ_1) are determined. Using the obtained perturbation parameters, the reconstruction of the unperturbed interference pattern is demonstrated. A good agreement between experiment and theory can be shown.

In the following sections the experiment and results are summarized and discussed. Publication [2] is appended at the end of this thesis including more details of the experiment and results.

3.1. Experiment

Based on the biprism interferometer constructed originally by Hasselbach *et al.* for electrons and ions [30, 101, 102], the experimental setup has been equipped with a new beam source as well as a detector with high spatial and temporal single-particle resolution. A detailed description of the used biprism interferometer is made in section 1.1 and publication [5]. In the following, a short explanation of the essential elements of the interferometer is given.

In figure 3.1, a schematic representation of the interferometer assembled inside a vacuum chamber at a pressure of $5 \cdot 10^{-9}$ mbar is shown. A mu-metal shield (not illustrated in figure 3.1) is placed inside of the chamber around the interferometer to suppress external electromagnetic fields. Coherent electrons are field-emitted by applying a voltage of -1.53 kV to a single-atom tip (SAT) [94, 129] consisting of an etched tungsten (111) wire covered with iridium. Using deflector electrodes, the electron beam is adjusted in horizontal (x) and vertical direction (y) onto the optical axis and the electrostatic biprism, a gold-palladium-coated glass-fibre with a diameter of ~ 400 nm [5, 196, 197]. The electron matter-wave is separated by the biprism into two

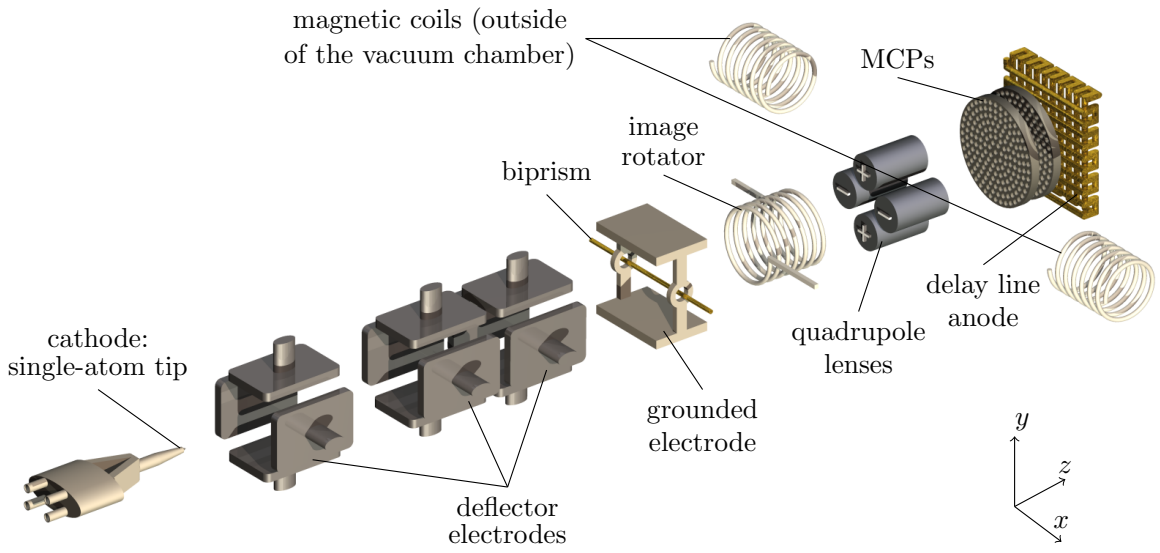

Figure 3.1.: Schematic representation of the used electron biprism interferometer assembled in a vacuum chamber (not to scale). From the single-atom tip (SAT) [94, 129] the electrons are field-emitted and aligned onto the biprism [5, 196, 197] by the deflector electrodes. The electron matter-wave is separated and recombined by applying a positive voltage to the biprism [29]. Magnified by the quadrupole lenses, the created interference pattern is detected with the delay line detector [127]. It is artificially dephased by a time-varying external magnetic field produced by two magnetic coils in Helmholtz configuration outside of the vacuum chamber. A mu-metal shield (not illustrated) is placed inside of the chamber between interferometer and magnetic coils. Figure from [2]. Reprints with permission of the American Physical Society (AIP).

partial waves. Subsequently, they are overlapped by applying a positive potential of a few 100 mV to the biprism, leading to an electron interference pattern (figure 1.1). Perpendicular to the interference fringes the electrostatic quadrupole lenses magnify the pattern along the y-direction. It almost remains unmagnified along the x-direction to preserve the signal strength. Using the magnetic coil installed after the biprism, the interference pattern can be rotated to adjust the fringes along the x-direction to compensate possible misalignment between the biprism and the direction of magnification. The electrons are amplified by two multichannel plates (MCPs) and the resulting pulses are detected with a delay line anode consisting of two meandering wires oriented perpendicular to each other in x- and y-direction (figure 1.5). It achieves a spatial resolution below 100 µm and a temporal accuracy below 1 ns, which sets an upper threshold of about 1 GHz for the perturbation frequency, that can be identified with the correlation analysis. The dead time between two events of 310 ns limits the maximum detectable count rate to a few MHz. A detailed description of the used delay line detector is given in section 1.1. For the application of the second-order correlation analysis the high spatial and temporal single-particle resolution of the detector is essential.

Figure 3.2(a) shows an electron interference pattern acquired in about 100 s with $5 \cdot 10^5$ particles together with the line profile averaged along the x-direction. The spatial periodicity of the interference pattern is $\lambda \approx 2$ mm and the contrast amounts

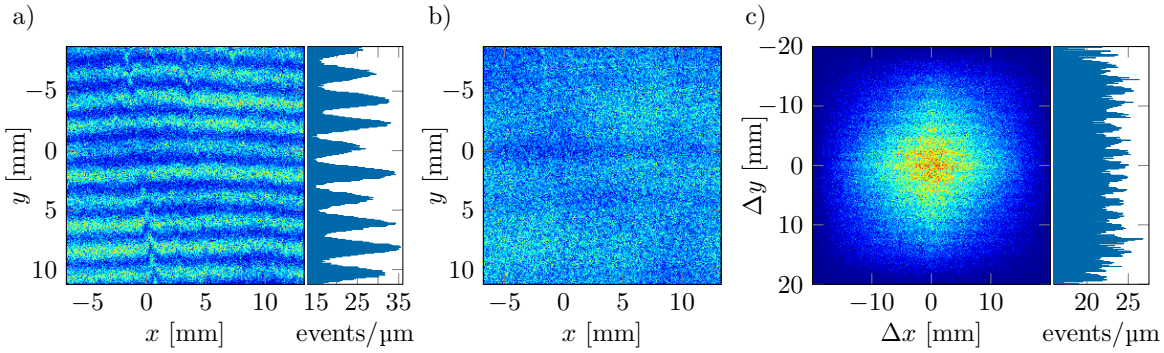

Figure 3.2.: a) Electron interference pattern plotted together with the line profile averaged along the x-direction. Here, a spatial periodicity $\lambda \approx 2\,\mathrm{mm}$ and contrast $K \approx 35\,\%$ can be determined. b) Interference pattern dephased by an external time-varying magnetic field with a frequency of $\omega_1/2\pi = 50\,\mathrm{Hz}$ resulting in an almost vanished contrast (see section 2.1.1). c) Two-dimensional histogram of spatial distances (Δx and Δy) between temporal successive particle events. It is illustrated together with the line profile averaged along Δx and corrected by the factor $(1 - |\Delta y|/Y)^{-1}$, due to the finite acquisition length $Y = 20\,\mathrm{mm}$. Figure from [2]. Reprints with permission of the American Physical Society (AIP).

to $K \approx 35\,\%$. Two magnetic coils in Helmholtz configuration installed outside of the vacuum chamber generate a time-varying magnetic field that dephases the interference pattern. Oriented along the x-direction this magnetic field generates a Lorentz force that shifts the interference pattern perpendicular to the fringes along the y-direction. With an applied perturbation frequency of $\omega_1/2\pi = 50\,\mathrm{Hz}$, an interference pattern with $N_\mathrm{part} \approx 5 \cdot 10^5$ particles is recorded and plotted in figure 3.2(b). The perturbation amplitude was set to a maximum deflection of the pattern of $\pm 2\,\mathrm{mm}$ for a constant current which corresponds to a peak phase deviation of $\varphi = 2\,\pi$. In section 2.1.1, it is discussed that the contrast in the spatial signal is reduced or vanished due to the applied perturbation. Using the possibility to calculate the spatial differences in x- and y-direction between temporal successive particles $(i, i+1)$, $i = 1 \ldots N_\mathrm{part} - 1$ ($\Delta x = x_i - x_{i+1}$ and $\Delta y = y_i - y_{i+1}$), the spatial periodicity of the unperturbed interference pattern can be revealed, which is shown in figure 3.2(c) together with the line profile averaged along Δx. As the probability to detect large particle distances is decreased, the line profile has to be corrected for the finite acquisition length Y by the factor $(1 - |\Delta y|/Y)^{-1}$. Along the Δy-direction a spatial periodicity of $\sim 2\,\mathrm{mm}$ and a contrast of $\sim 34\,\%$ can be identified.

3.2. Results

The correlation function of the dephased interference pattern in figure 3.2(b) is extracted from the measurement data using equation (2.17) and illustrated in figure 3.3(a). As discussed in section 2.1.3, the contrast K and spatial periodicity λ of the unperturbed interference pattern can be identified along the correlation length u. In the direction of the correlation time τ, the superperiod τ_s for one perturbation frequency is given by $\tau_s = 2\pi/\omega_1 = 20\,\mathrm{ms}$.

To the experimental correlation function $g^{(2)}_\mathrm{expt}(u, \tau)$ in figure 3.3(a) the approxi-

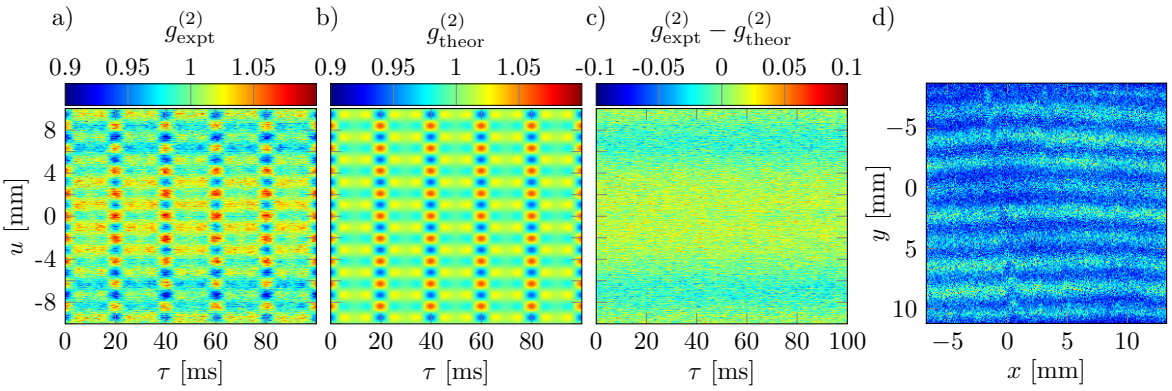

Figure 3.3.: a) Correlation function of the dephased interference pattern in figure 3.2(b) extracted from the experimental data using equation (2.17). b) Theoretical correlation function resulting from the fit of equation (1.40) and (2.4) to $g^{(2)}_{\mathrm{expt}}$. c) Residuum of the experimental and theoretical correlation function. The remaining structure is possibly related to diffraction at the biprism. d) Interference pattern with a contrast of $K_{\mathrm{rec}} \approx 30\,\%$ reconstructed from the measurement data of the perturbed pattern using the obtained parameters in equation (2.14) for $N = 1$. Figure from [2]. Reprints with permission of the American Physical Society (AIP).

mate solution in equation (1.40) and (2.4) is fitted and the result $g^{(2)}_{\mathrm{theor}}(u, \tau)$ is plotted in figure 3.3(b). A good agreement between experiment and theory is indicated by the remaining residuum in figure 3.3(c). The extracted parameters describing the unperturbed interference pattern and applied perturbation are: contrast $K_{\mathrm{g}^{(2)}} = (34.5 \pm 0.2)\,\%$, spatial periodicity $\lambda_{\mathrm{g}^{(2)}} = (2.089 \pm 0.001)\,\mathrm{mm}$, perturbation frequency $\omega_1/2\pi = (49.996 \pm 0.018)\,\mathrm{Hz}$ and perturbation amplitude (peak phase deviation) $\varphi_1 = (0.802 \pm 0.004)\,\pi$. They agree well with the parameters of the unperturbed interference pattern ($K \approx 35\,\%$, $\lambda \approx 2\,\mathrm{mm}$) in figure 3.2(a) and the applied perturbation frequency of $\omega_1/2\pi = 50\,\mathrm{Hz}$. As the mu-metal shield installed inside of the vacuum chamber around the interferometer attenuates the amplitude for oscillating magnetic fields more as compared to a DC field, the peak phase deviation resulting from the fit is lower than the applied amplitude for constant current of $\varphi = 2\,\pi$. According to equation (2.2) and figure 2.1, the contrast of the temporally integrated interference pattern nearly vanishes for a peak phase deviation of $\varphi_1 = 0.8\,\pi$. However, using correlation analysis, the contrast and spatial periodicity of the unperturbed interference pattern can be revealed.

With the parameters obtained from the correlation analysis, the unperturbed interference pattern can be reconstructed with equation (2.14) for $N = 1$. As discussed in section 2.1.6.1, the phase information of the applied perturbation is completely lost in the case of one frequency, but can be determined in the reconstruction process. Therefore, ϕ_1 is varied between 0 and 2π to achieve the maximum contrast of the reconstructed interference pattern. The result with a contrast of $K_{\mathrm{rec}} \approx 30\,\%$ is illustrated in figure 3.3(d) and agrees well with the unperturbed interference pattern in figure 3.2(a). Even phase shifts due to charged dust on the biprism can be seen.

3.3. Conclusion

Using an external time-varying magnetic field applied to an electron biprism interferometer, the validity of the second-order correlation theory for a single-frequency perturbation was demonstrated. Here, the contrast of the temporally integrated interference pattern was vanished almost completely. However, using the correlation analysis the contrast and spatial periodicity could be revealed. Additionally, fitting the theoretical correlation function for one perturbation frequency to the experimental one, the perturbation characteristics could be determined. A good agreement between experiment and theory was achieved. With the obtained perturbation parameters the unperturbed interference pattern could be reconstructed and the phase of the perturbation was identified.

Here, it is possible to use the correlation analysis, as the periodic time of the perturbation (20 ms) is much larger than the time that the electrons spend in the region of dephasing ($t = s/\sqrt{2q/m \cdot U_{\mathrm{acc}}} \approx 0.3\,\mathrm{m}/2.3{\cdot}10^7\,\frac{\mathrm{m}}{\mathrm{s}} \approx 13\,\mathrm{ns}$, with the length of the interaction region s). Therefore, the interference pattern is still present on timescales below the periodic time of the perturbation. As demonstrated experimentally, the contrast and spatial periodicity of the unperturbed interference pattern can be unveiled in the spatial differences of the particle events. Using the temporal differences additionally, the correlation analysis can be applied to determine the perturbation characteristics.

4. Multifrequency perturbations in matter-wave interferometry

After verifying experimentally the validity of the second-order correlation analysis for a single-frequency perturbation, the theory is further investigated by performing the experiment with a perturbation composed of many frequencies.

In **publication [3]**, the case of multifrequency perturbations as well as a perturbation consisting of a broad frequency spectrum is demonstrated. As discussed in section 2.1.2, the application of the explicit (equation (2.7)) or approximate solution of the correlation function (equation (1.40) and (2.6)) depends on the specific perturbation frequencies. Here, the difference between the two solutions is investigated experimentally in an electron biprism interferometer.

The measurements were performed with the same apparatus as described in publication [2] and chapter 3. To demonstrate the difference between explicit and approximate correlation function, the electron interference pattern is dephased artificially by a time-varying external magnetic field consisting of several superposed frequencies. For this purpose, two and three perturbation frequencies are applied as well as a broad-band noise spectrum. A good agreement between experiment and theory can be presented for all measurements.

Below, the results of the correlation analysis of multifrequency perturbations are summarized and discussed. In chapter 2 and appendix A.1, the used equations are provided. Publication [3], appended at the end of this thesis, includes more details of the measurements and results.

4.1. Experiment

As explained in chapter 3 and figure 3.1, the electron interference pattern is dephased by an oscillating magnetic field generated with two coils in Helmholtz configuration installed outside of the vacuum chamber. Oriented along the x-direction (figure 3.1) the magnetic field shifts the interference pattern due to the generated Lorentz force perpendicular to the interference fringes along the y-direction. The time-varying magnetic field is attenuated by the mu-metal shield installed inside of the vacuum chamber around the interferometer. Before applying multifrequency perturbations, the transmission characteristics of the mu-metal shield is determined. For this purpose, the interference pattern is dephased by a single-frequency perturbation applied stepwise from 0 to 500 Hz to the external magnetic coils. For each measurement, the theory for one perturbation frequency in equation (1.40) and (2.4) is fitted to the experimental correlation function extracted according to equation (2.17) to obtain the perturbation amplitude $\varphi_1(\omega_1)$. To determine the transmission of the mu-metal shield, $\varphi_1(\omega_1)$ is compared to the amplitude of a DC magnetic field $\varphi_1(0)$, which is determined

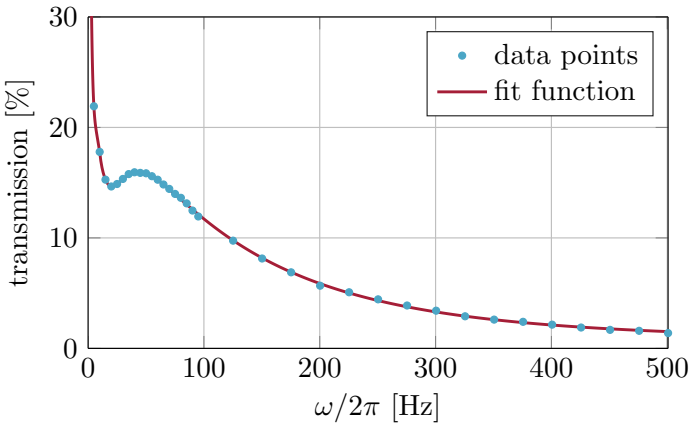

Figure 4.1.: Normalized frequency-dependent transmission of the mu-metal shield installed inside of the vacuum chamber around the interferometer. For each single-frequency perturbation, applied stepwise from 0 to 500 Hz, the correlation function of the dephased interference pattern is extracted according to equation (2.17) and fitted with the theory for one perturbation frequency in equation (1.40) and (2.4) to determine the perturbation amplitude $\varphi_1(\omega_1)$. This is compared to the amplitude of a DC magnetic field $\varphi_1(0)$ to obtain the transmission of the mu-metal shield given by $\varphi_1(\omega_1)/\varphi_1(0)$. Figure from [3]. Reprints with permission of the American Physical Society (AIP).

from the 0 Hz-measurement. Together with an appropriate fit function, the normalized frequency-dependent transmission of the mu-metal shield given by $\varphi_1(\omega_1)/\varphi_1(0)$ is plotted in figure 4.1.

To verify the validity of the second-order correlation theory for multifrequency dephasing, the interference pattern is perturbed by a time-varying magnetic field consisting of several superposed frequencies. The results of these measurements are discussed in the next section.

4.2. Results

For each measurement of a perturbed electron interference pattern, $7 \cdot 10^5$ particles were acquired in about 22 s. To extract the experimental correlation function, equation (2.17) is used. Afterwards, the contrast K and spatial periodicity λ are determined for each measurement at the correlation time $\tau = 0$, according to equation (2.8). Depending on the specific perturbation frequencies, the explicit (equation (A.1)) or approximate correlation function (equation (1.40) and (2.6)) is used for the fit to the experimental data. The perturbation frequencies ω_j, contrast K, and spatial periodicity λ are fixed parameters during the fit.

In the first measurement, the electron interference pattern was dephased by a superposition of two perturbation frequencies $\omega_1/2\pi = 6$ Hz and $\omega_2/2\pi = 40$ Hz. In figure 4.2(a), the extracted correlation function $g^{(2)}_{\text{expt}}(u,\tau)$ is plotted and in figure 4.3(a) the corresponding dephased interference pattern with a remaining contrast of $K_{\text{pert}} = 6.4\,\%$. Using equation (2.8) at $\tau = 0$ ms, the contrast and spatial periodicity are determined, $K_{\text{g}^{(2)}} = 62.9\,\%$ and $\lambda_{\text{g}^{(2)}} = 2.08$ mm. The explicit correlation function in equation (A.1) with $N = 2$ is used for the fit to the experimental correlation function

and the result $g^{(2)}_{\text{theor}}(u,\tau)$ is plotted in figure 4.2(b), yielding the peak phase deviations $\varphi_1 = 1.34\,\pi$ and $\varphi_2 = 0.93\,\pi$. In this case, the approximate correlation function in equation (1.40) and (2.6) would have led to the same result as the time-dependent phases $\tilde{\Phi}(\tau)$ and $\psi(\tau)$ in equation (2.7) vanish for all correlation times τ. Therefore, the perturbation phases ϕ_1 and ϕ_2 can not be determined by the fit of the correlation theory.

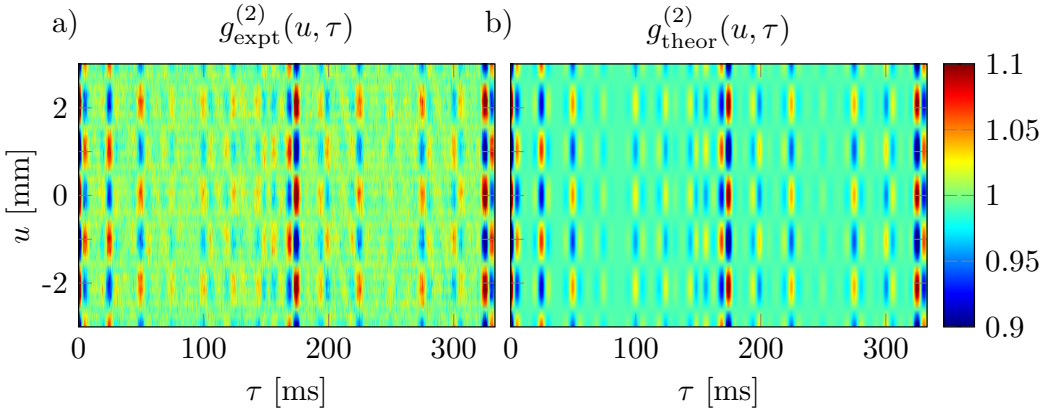

Figure 4.2.: a) Experimental correlation function of an interference pattern dephased by two perturbation frequencies $\omega_1/2\pi = 6\,\text{Hz}$ and $\omega_2/2\pi = 40\,\text{Hz}$. b) Theoretical correlation function fitted to the experimental data according to equation (A.1) with $N = 2$. The approximate solution in equation (1.40) and (2.6) would have led to the same result. Figure from [3]. Reprints with permission of the American Physical Society (AIP).

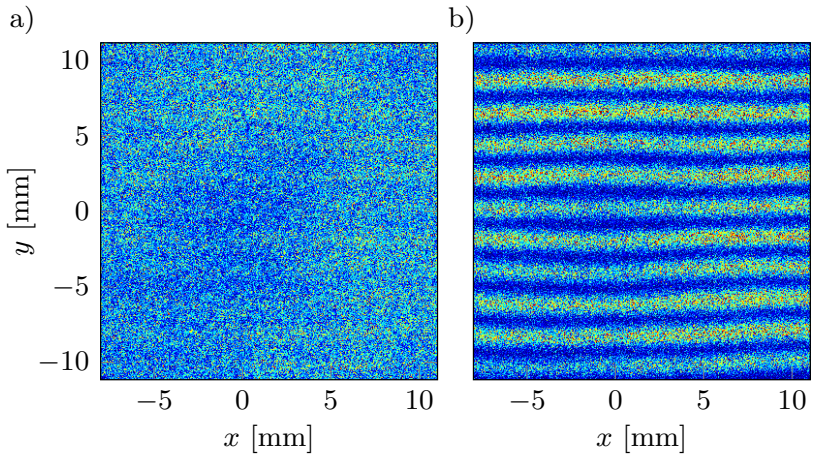

Figure 4.3.: a) Interference pattern dephased with two frequencies $\omega_1/2\pi = 6\,\text{Hz}$ and $\omega_2/2\pi = 40\,\text{Hz}$. The remaining contrast is $K_{\text{pert}} = 6.4\,\%$. b) Using equation (2.14) with $N = 2$, the interference pattern can be reconstructed, yielding a contrast of $K_{\text{rec}} = 62.4\,\%$. Figure from [3]. Reprints with permission of the American Physical Society (AIP).

As discussed in section 2.1.6.2, the perturbation phases can be identified using the obtained perturbation parameters in equation (2.14) ($N = 2$) for the reconstruction of the unperturbed interference pattern. Varying the phases between 0 and $2\,\pi$, the contrast of the reconstructed pattern can be maximized. For the perturbation phases

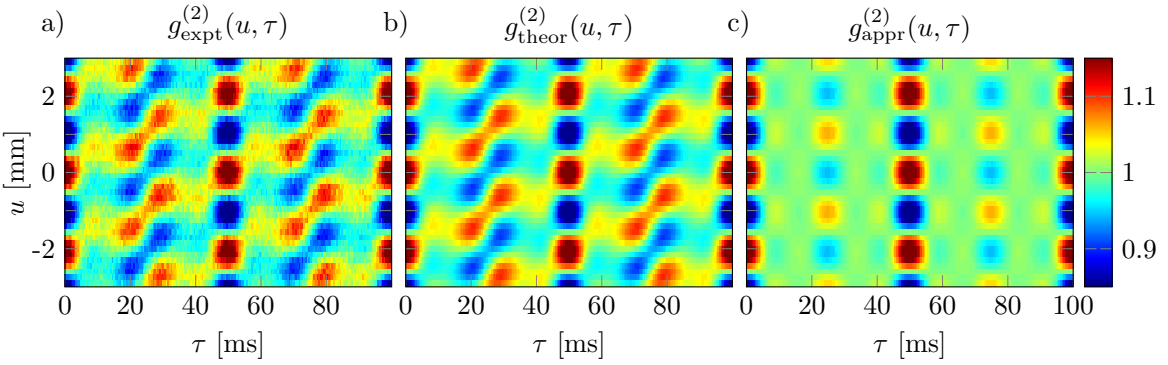

Figure 4.4.: a) Correlation function of an interference pattern perturbed by two frequencies, that are multiples of each other $\omega_1/2\pi = 20\,\mathrm{Hz}$ and $\omega_1/2\pi = 40\,\mathrm{Hz}$. b) Theoretical correlation function resulting from the fit of equation (A.1) with $N = 2$ to the experimental data. c) Approximate solution of the correlation function calculated with equation (1.40) and (2.6) ($N = 2$) using the parameters obtained from the fit of the explicit solution in b). Figure from [3]. Reprints with permission of the American Physical Society (AIP).

$\phi_1 = -0.33\,\pi$ and $\phi_2 = -0.63\,\pi$, the resulting interference pattern with a contrast of $K_{\mathrm{rec}} = 62.4\,\%$ is plotted in figure 4.3(b). The contrast of the reconstructed interference pattern is in good agreement with the contrast $K_{\mathrm{g^{(2)}}}$ extracted from the correlation function.

In a second measurement, the interference pattern is perturbed by two frequencies, that are multiples of each other $\omega_1/2\pi = 20\,\mathrm{Hz}$ and $\omega_2/2\pi = 40\,\mathrm{Hz}$. In figure 4.4(a), the experimental correlation function extracted according to equation (2.17) is plotted. As discussed in section 2.1.4, the explicit correlation function has to be used for this case as additional terms contribute to the explicit solution of the correlation function in equation (2.7). These terms lead to the temporal $\tilde{\Phi}(\tau)$ and spatial phase $\psi(\tau)$ depending on the correlation time τ and the specific perturbation characteristics, as can be seen in figure 4.4(a). A superperiod of $\tau_s = 50\,\mathrm{ms}$ defined by the greatest common divisor of the applied perturbation frequencies $\omega_{gcd}/2\pi = 20\,\mathrm{Hz}$ (see section 2.1.3) can be identified in τ-direction. Using the explicit correlation function in equation (A.1) ($N = 2$) for the fit, the matter-wave properties and perturbation parameters are extracted: $K_{\mathrm{g^{(2)}}} = 62.9\,\%$, $\lambda_{\mathrm{g^{(2)}}} = 2.08\,\mathrm{mm}$, $\varphi_1 = 0.50\,\pi$, $\varphi_2 = 0.52\,\pi$, $\phi_1 = -0.21\,\pi$, and $\phi_2 = 0.24\,\pi$. The resulting theoretical correlation function shown in figure 4.4(b) agrees well with the experiment. In figure 4.4(c), the approximate solution of the correlation function is plotted. It was calculated according to equation (1.40) and (2.6) ($N = 2$) with the parameters obtained from the fit with the explicit solution. Comparing 4.4(b) and (c), the difference between the two solutions can be seen which originates from the additional terms in the explicit correlation function (equation (2.7)) resulting in the non-vanishing phases $\tilde{\Phi}(\tau)$ and $\psi(\tau)$. As discussed in section 2.1.6.1, the phases of the perturbation ϕ_1 and ϕ_2 are not determined uniquely due to the invariance of the correlation function. However, they can be obtained in the reconstruction process of the unperturbed interference pattern using equation (2.14).

The case of three perturbation frequencies is demonstrated with an interference pattern dephased by $\omega_1/2\pi = 6\,\mathrm{Hz}$, $\omega_2/2\pi = 23\,\mathrm{Hz}$, and $\omega_3/2\pi = 40\,\mathrm{Hz}$. In figure 4.5(a), the extracted correlation function is plotted and the corresponding dephased interfer-

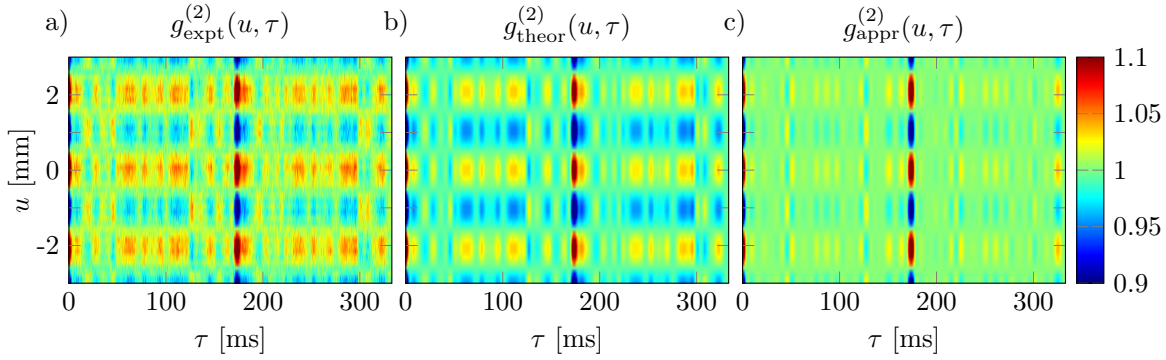

Figure 4.5.: a) Correlation function of an interference pattern dephased by three perturbation frequencies $\omega_1/2\pi = 6\,\mathrm{Hz}$, $\omega_2/2\pi = 23\,\mathrm{Hz}$, and $\omega_3/2\pi = 40\,\mathrm{Hz}$. b) Theoretical correlation function resulting from the fit using the explicit solution of the correlation function in equation (A.1) with $N = 3$. c) With the parameters determined from the fit of the explicit solution in b), the approximate correlation function is calculated according to equation (1.40) and (2.6) with $N = 3$. Figure from [3]. Reprints with permission of the American Physical Society (AIP).

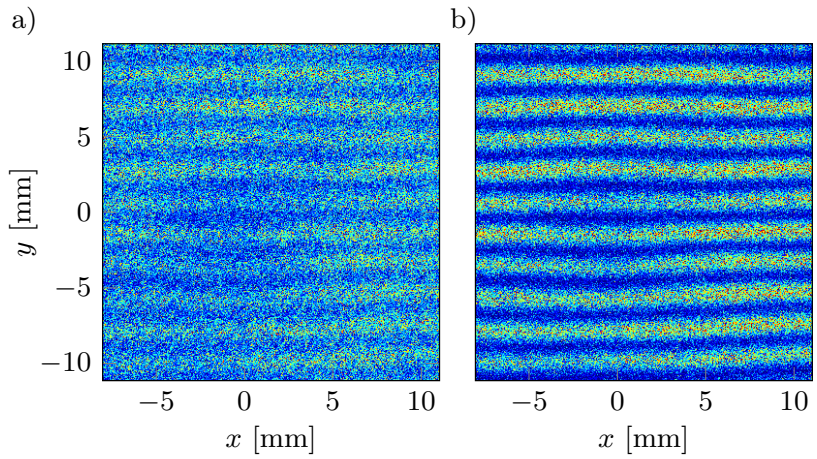

Figure 4.6.: a) Interference pattern with a contrast of $K_{\mathrm{pert}} = 21.1\,\%$ perturbed by three frequencies $\omega_1/2\pi = 6\,\mathrm{Hz}$, $\omega_2/2\pi = 23\,\mathrm{Hz}$, and $\omega_3/2\pi = 40\,\mathrm{Hz}$. b) Reconstructed interference pattern (equation (2.14) with $N = 3$) revealing a contrast of $K_{\mathrm{rec}} = 62.9\,\%$.

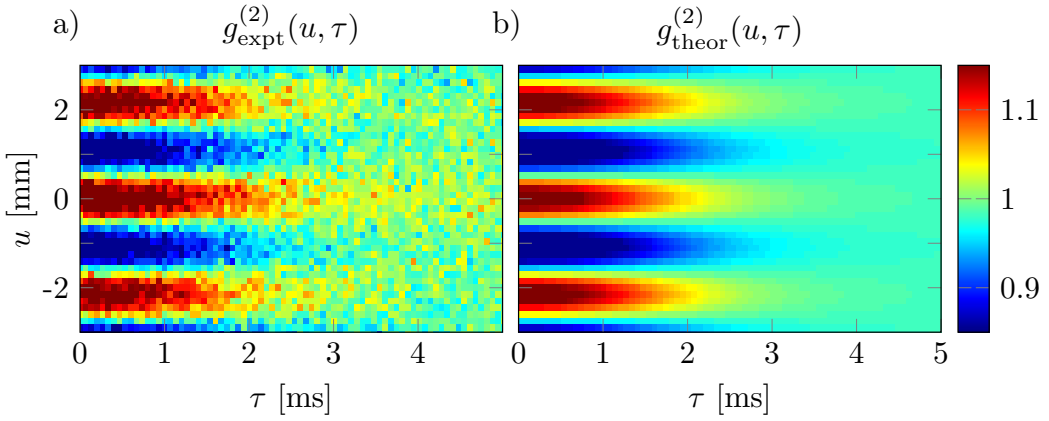

Figure 4.7.: a) Correlation function of an interference pattern perturbed by a broad-band noise spectrum between 0 and 150 Hz. b) Theoretical correlation function calculated with the approximate solution in equation (1.40) and (2.6) using the attenuated values of the applied perturbation signal. Figure from [3]. Reprints with permission of the American Physical Society (AIP).

ence pattern in figure 4.6(a) with a remaining contrast of $K_{\mathrm{pert}} = 21.1\,\%$. As discussed at the end of section 2.1.2 and in appendix A.1, the explicit correlation function has to be used in this case for the fit as the time-dependent phases in equation (2.7) do not vanish, due to the additional terms contributing to the explicit solution of the correlation function. The resulting theoretical fit using equation (A.1) with $N = 3$ is illustrated in figure 4.5(b), yielding $K_{\mathrm{g}^{(2)}} = 61.3\,\%$, $\lambda_{\mathrm{g}^{(2)}} = 2.08\,\mathrm{mm}$, $\varphi_1 = 0.76\,\pi$, $\varphi_2 = 1.01\,\pi$, $\varphi_3 = 0.52\,\pi$, $\phi_1 = 0.01\,\pi$, $\phi_2 = 1.01\,\pi$, and $\phi_3 = 0.01\,\pi$. Using equation (1.40) and (2.6) with $N = 3$, the approximate correlation function is calculated with the parameters obtained from the fit with the explicit solution and plotted in figure 4.5(c). Originating from the non-vanishing phases $\tilde{\Phi}(\tau)$ and $\psi(\tau)$ in equation (2.7), the difference between the two solutions is clearly visible. Therefore, the experimental correlation function could not be described completely using the approximate solution. As discussed before, the phases of the perturbation are not determined uniquely, as the correlation function remains invariant under phase transformations (equation (2.12) and (2.13)). However, using the possibility to reconstruct the unperturbed interference pattern with the parameters determined from the correlation analysis the phases can be identified. In figure 4.6(b), the reconstructed interference pattern is shown calculated according to equation (2.14) with $N = 3$. The contrast of $K_{\mathrm{rec}} = 62.9\,\%$ is in good agreement with the contrast determined from the correlation function $K_{\mathrm{g}^{(2)}}$ and could be achieved for the phases $\phi_1 = -0.13\,\pi$, $\phi_2 = 0.31\,\pi$, and $\phi_3 = -1.29\,\pi$.

In the last measurement, it is demonstrated that the correlation analysis can also be applied for a perturbation consisting of a broad frequency spectrum. Using a broad-band noise spectrum from 0 Hz up to a cutoff frequency of 150 Hz, the interference pattern is perturbed resulting in the experimental correlation function plotted in figure 4.7(a). The contrast $K_{\mathrm{g}^{(2)}} = 63.4\,\%$ and the spatial periodicity $\lambda_{\mathrm{g}^{(2)}} = 2.16\,\mathrm{mm}$ are obtained with equation (2.8) at $\tau = 0\,\mathrm{ms}$. The perturbation spectrum at the position of the particles is determined via a temporal numerical Fourier transformation of the applied perturbation signal detected during the measurement and fitted with an appro-

priate function (see section IV of publication [3]). According to the mu-metal shielding characteristics in figure 4.1, the resulting fit function is attenuated and used for the calculation of the theoretical correlation function with equation (1.40) and (2.6). In figure 4.7(b), the result is shown indicating a good agreement between experiment and theory. Due to the large number of involved frequencies, the approximate solution of the correlation function can be used in this case as the time-dependent phases in equation (2.7) vanish for all correlation times.

4.3. Conclusion

Using an electron biprism interferometer, the validity of the second-order correlation analysis for multifrequency perturbations was demonstrated experimentally. For this purpose, the electron interference pattern was dephased by applying a superposition of two and three frequencies as well as a broad-band frequency spectrum to the magnetic coils generating a time-varying magnetic field. Therefore, the contrast of the temporally integrated interference pattern was reduced or nearly vanished. However, the contrast and spatial periodicity of the unperturbed interference pattern were successfully unveiled for all measurements. Furthermore, a good agreement between experimental and theoretical correlation function could be demonstrated. Using the obtained perturbation parameters the unperturbed interference pattern could be reconstructed for the case of two and three perturbation frequencies and the phases of the perturbation were identified.

These measurements clearly show that the second-order correlation theory in publication [1] is suitable for the analysis of multifrequency perturbations in single-particle interferometry. The matter-wave characteristics and perturbation parameters could be revealed successfully. In the next chapter, the correlation analysis shall be applied to unknown perturbation frequencies originating from an external mechanical vibration dephasing the electron interference pattern.

5. Vibrational dephasing in matter-wave interferometers

In chapter 3 and 4, the validity of the second-order correlation analysis for multifrequency dephasing was proved experimentally in an electron biprism interferometer by applying a time-varying magnetic field. In the following, the correlation analysis will be applied for the identification of unknown perturbation characteristics.

In **publication [4]**, the application of the correlation analysis is demonstrated by introducing external vibrational dephasing to an electron biprism interferometer. Unlike with electromagnetic oscillations (publication [2] and [3]), the perturbation frequencies dephasing the interference pattern are not known *a priori* due to the complexity of the setup with several mechanical resonances and additional frequencies induced from the environment. As explained in section 2.1.6, the amplitude spectrum is used for the identification of unknown perturbation frequencies and corresponding amplitudes in a numerical search algorithm developed for this purpose.

It is demonstrated that the matter-wave characteristics can be revealed over the complete vibrational perturbation spectrum. Additionally, the vibrational response spectrum of the electron biprism interferometer is measured indicating the possible application in sensor technology. Furthermore, it is demonstrated that the reconstruction of the unperturbed interference pattern is realized successfully over a wide range of the perturbation spectrum.

The experiment, data analysis, and results are summarized and discussed in the following. More details can be found in publication [4], which is appended at the end of this thesis.

5.1. Experiment

In figure 5.1, the experimental setup used to demonstrate the identification of vibrational dephasing by the correlation analysis is illustrated. Here, the interference pattern is artificially perturbed by mechanical vibrations produced by a speaker and a piezo element attached to the vacuum chamber. Using a frequency generator with a resolution of 1 µHz and an accuracy of ±10 ppm on the set frequency value, only a single excitation frequency is applied at once. The frequency region amounts 100 to 320 Hz for the speaker and 330 to 1000 Hz for the piezo element.

For each applied frequency, an electron interference pattern was detected with $1.95 \cdot 10^5$ particles at a mean particle count rate of (2.0 ± 0.5) kHz for the speaker measurements and (11 ± 2) kHz for the piezo element. In this way, the complete vibrational response spectrum of the interferometer is measured. The electron energy was set to 1.45 keV, which leads to a velocity of $2.26 \cdot 10^7$ m/s and a flight time of the electrons between source and detector (distance: 0.565 m) of 26 ns. According to section 2.2.2

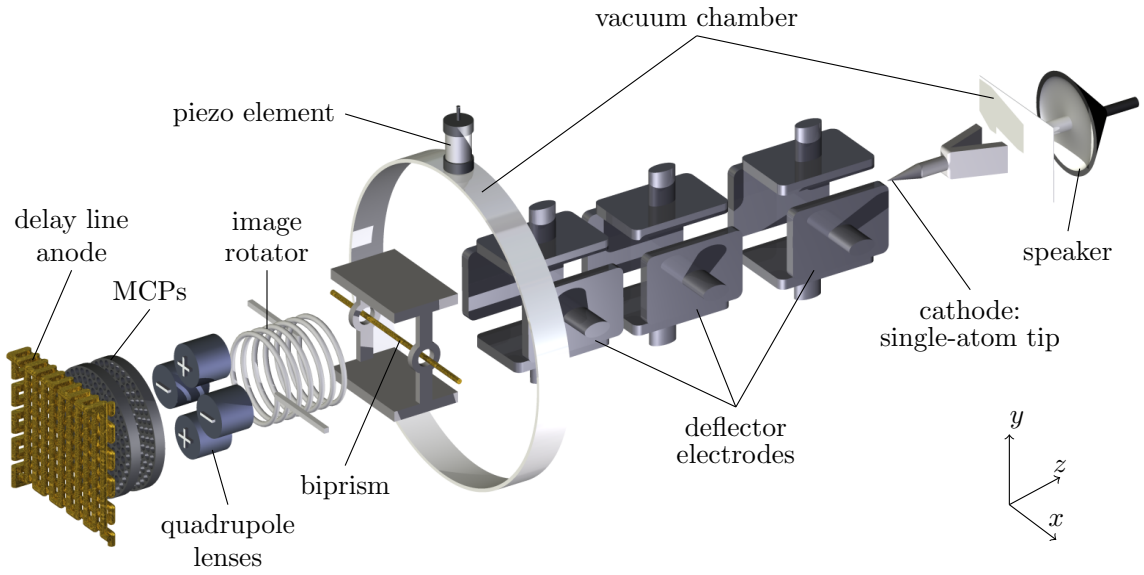

Figure 5.1.: Illustration of the experiment (not to scale) for the measurement of external mechanical vibrations introduced to the electron biprism interferometer by a speaker and a piezo element attached to the vacuum chamber. The electrons are field-emitted from a SAT [94, 129] and adjusted using the deflector electrodes onto the biprism, a $\sim 400\,\mathrm{nm}$ thin gold-palladium-coated glass-fibre [5, 196, 197]. At the biprism the electron matter-wave is separated into two partial waves, that are overlapped afterwards by applying a positive voltage to the biprism (figure 1.1). After the magnification of the generated electron interference pattern by a quadrupole lens, it is measured with a single-particle detector consisting of two MCPs in conjunction with a delay line anode (figure 1.5). Figure from [4]. Reprints with permission of IOP Publishing Limited.

and equation (A.37), this flight time results in a maximum detectable perturbation frequency of about 3.8 MHz.

5.2. Correlation analysis

The method to analyze an interference pattern dephased by mechanical vibrations is demonstrated exemplarily for the measurement with an excitation frequency of $\omega_0/2\pi = 540\,\mathrm{Hz}$ introduced by a piezo element. In the following, the evaluation steps applied to all measurements are outlined.

Using the spatial coordinates of the particles (x_i, y_i), a two-dimensional histogram of the temporally integrated interference pattern is calculated and plotted in figure 5.2(a). To determine the contrast K_{pert} and spatial periodicity λ_{pert} of the perturbed interference pattern the histogram is averaged along the x-direction and a model function is fitted

$$I(y) = I_0\big(1 + K\cos(ky)\big)\ , \tag{5.1}$$

with the mean intensity I_0 and the wave number $k = 2\pi/\lambda$. The averaged interference pattern and fitted model function are plotted in figure 5.2(a) below the histogram, yielding $K_{\mathrm{pert}} = (8.8 \pm 1.6)\,\%$ and $\lambda_{\mathrm{pert}} = (2.62 \pm 0.06)\,\mathrm{mm}$, with the errors indicating the 95 % confidence interval of the fit.

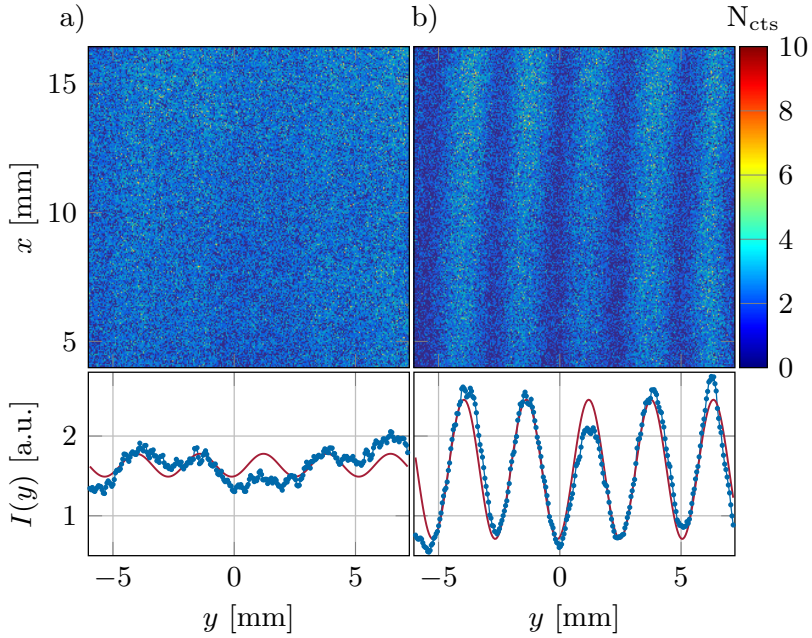

Figure 5.2.: a) Electron interference pattern dephased by a mechanical vibration with an excitation frequency of $\omega_0/2\pi = 540\,\mathrm{Hz}$. The interference pattern averaged along the x-direction (blue dots) is plotted together with the fitted model function (red solid line) of equation (5.1). b) Interference pattern after the reconstruction process using equation (2.14) with the parameters obtained from the correlation analysis and subsequent optimization. Figure from [4]. Reprints with permission of IOP Publishing Limited.

For the determination of the matter-wave characteristics and perturbation properties the correlation function is extracted from the experimental data up to a maximum correlation time of $\tau_{\mathrm{max}} = 10\,\mathrm{s}$ using equation (2.17). Subsequently, the contrast $K_{\mathrm{g}^{(2)}}$ and spatial periodicity $\lambda_{\mathrm{g}^{(2)}}$ of the unperturbed interference pattern are determined from the correlation function using equation (2.8) at the correlation time $\tau = 0\,\mathrm{ms}$. As discussed in appendix A.3.1, the spatial and temporal discretization step size Δu and $\Delta\tau$ has to be taken into account to obtain the correct results. In the inset of figure 5.3, the correlation function with a discretization step size of $\Delta u = 90\,\mu\mathrm{m}$ and $\Delta\tau = 50\,\mu\mathrm{s}$ is shown. The extracted contrast and spatial periodicity are $K_{\mathrm{g}^{(2)}} = (58.5 \pm 3.2)\,\%$ and $\lambda_{\mathrm{g}^{(2)}} = (2.60 \pm 0.02)\,\mathrm{mm}$.

After the determination of the matter-wave characteristics, the amplitude spectrum of the correlation function used for the identification of unknown perturbation properties is calculated via a numerical Fourier transformation at the spatial positions $u = N_u \lambda_{\mathrm{g}^{(2)}}/2$, with $N_u \in \mathbb{Z}$ and subsequent averaging. The result is plotted in figure 5.3 (red solid line). Three peaks can be identified corresponding to the fundamental perturbation frequency and higher harmonics at discrete frequencies $m_1\omega_1$, with $m_1 \in \{1, 2, 3\}$. Using these peaks, the search algorithm identifies the perturbation frequency that describes the amplitude spectrum best. A detailed explanation of the applied algorithm can be found in section 4 of publication [4]. In the example, the resulting perturbation frequency is $\omega_1/2\pi = (540.0 \pm 0.05)\,\mathrm{Hz}$. Afterwards, equation (A.9) is fitted to the experimental amplitude spectrum to determine the perturbation amplitude and phase, yielding $\varphi_1 = (0.5725 \pm 0.0015)\,\pi$. For the fit the contrast, spatial

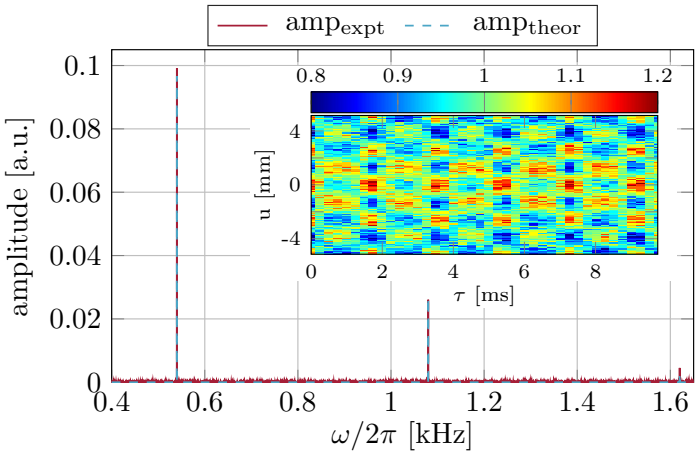

Figure 5.3.: Amplitude spectrum of the $\omega_0/2\pi = 540\,\mathrm{Hz}$ measurement (red solid line) calculated from the correlation function (see inset) via a numerical Fourier transformation at the spatial positions $u = N_u \lambda_{g^{(2)}}/2$, with $N_u \in \mathbb{Z}$ and subsequent averaging. The fundamental perturbation frequency of $\omega_1/2\pi = (540.0 \pm 0.05)\,\mathrm{Hz}$ is identified with the search algorithm. Afterwards, equation (A.9) is fitted (dashed blue line), yielding a perturbation amplitude of $\varphi_1 = (0.5725 \pm 0.0015)\,\pi$. Figure from [4]. Reprints with permission of IOP Publishing Limited.

periodicity, and perturbation frequency are used as fixed parameters. In the case of one perturbation frequency the phase information is lost, as discussed in section 2.1.6. Therefore, ϕ_1 can not be obtained from the fit. In figure 5.3, the resulting theoretical amplitude spectrum is plotted (dashed blue line) indicating a good agreement between experiment and theory.

With the perturbation parameters obtained from the correlation analysis the unperturbed interference pattern can be reconstructed from the perturbed one in figure 5.2(a) using equation (2.14). For this purpose, the phase ϕ_1 is varied from $-\pi$ to $+\pi$ and the perturbation frequency ω_1 and peak phase deviation φ_1 in a narrow region around the obtained values to maximize the contrast of the reconstructed interference pattern. The result of the exemplary measurement is plotted in figure 5.2(b), yielding the perturbation parameters $\omega_1/2\pi = 539.994\,\mathrm{Hz}$, $\varphi_1 = 0.66\,\pi$, and $\phi_1 = 0.59\,\pi$. Using equation (5.1), the contrast and spatial periodicity of the reconstructed interference pattern are determined, $K_{\mathrm{rec}} = (55.5 \pm 2.8)\,\%$ and $\lambda_{\mathrm{rec}} = (2.57 \pm 0.01)\,\mathrm{mm}$. Both are in good agreement with the obtained values from the correlation analysis.

A detailed discussion of the reconstruction process is given in section 4 of publication [4]. For the measurements performed here it can be shown that a frequency accuracy of $\pm 1\,\mathrm{mHz}$ is necessary to reveal the contrast of the reconstructed interference pattern with less than 1 % deviation from the contrast of the unperturbed interference pattern. Therefore, the accuracy of the obtained perturbation parameters can be increased significantly in the reconstruction process.

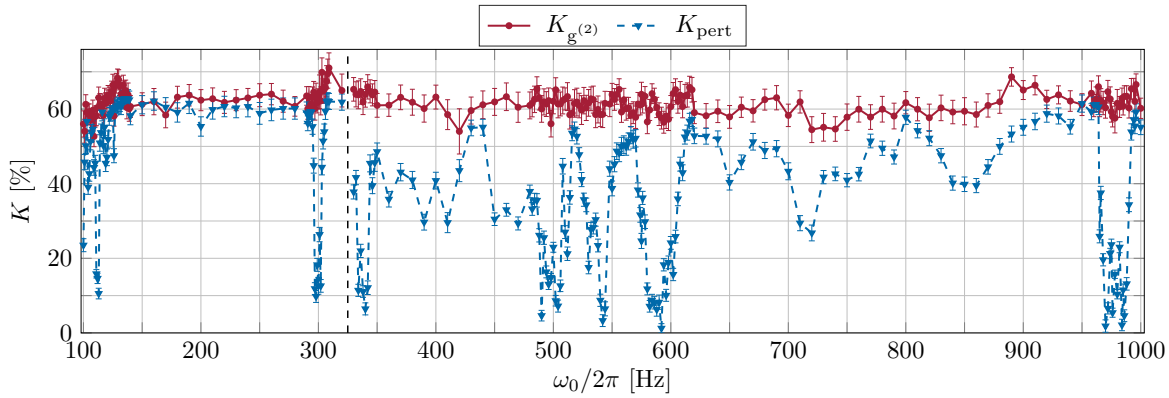

Figure 5.4.: Contrast $K_{g^{(2)}}$ (red dots with solid line) extracted from the correlation function using equation (2.8) at $\tau = 0\,\text{ms}$ and contrast K_{pert} (blue triangles with dashed line) of the perturbed interference pattern determined by the fit of equation (5.1) to the averaged interference pattern. The two data sets of the speaker and piezo excitation are separated by the vertical dashed line at 325 Hz. Figure from [4]. Reprints with permission of IOP Publishing Limited.

5.3. Results of the correlation analysis

All measurements of interference patterns dephased by an external mechanical vibration introduced by a speaker ($\omega_0/2\pi$ between 100 and 320 Hz) and piezo element ($\omega_0/2\pi$ between 330 and 1000 Hz) are evaluated in the same way as described in section 5.2.

In figure 5.4, the results for the contrast $K_{g^{(2)}}$ extracted from the correlation function and the contrast of the perturbed interference pattern K_{pert} are plotted against the excitation frequency $\omega_0/2\pi$. It can be seen that the data of K_{pert} reveals clear resonances, at which the contrast nearly vanishes. However, using the correlation analysis, the contrast $K_{g^{(2)}}$ of the unperturbed interference pattern can be determined over the complete perturbation spectrum.

For the speaker measurement the resulting response spectrum of the biprism interferometer is shown in figure 5.5. To indicate the positions where the identified perturbation frequency ω_j is equal to the excitation frequency ω_0 the red solid line is plotted in the frequency plane. Comparing figure 5.4 with 5.5, it can be seen that the contrast K_{pert} of the perturbed interference pattern is strongly reduced for perturbation frequencies with large amplitudes φ_j, according to equation (2.2). In figure 5.5, the maximum perturbation amplitude in the spectrum is $\varphi_j = 0.99\,\pi$ at $\omega_j/2\pi = 112\,\text{Hz}$. Especially in the region from 100 to 140 Hz higher harmonics of ω_0 denoted by the blue chain lines are visible. For a linear response of the interferometer, the response spectrum should only include the excitation frequencies. However, due to anharmonicities in the excitation process and a possible nonlinear response of the complex interferometer setup, higher harmonics could be included in the spectrum. The green horizontal dashed lines indicate external perturbation frequencies at 150 Hz and 300 Hz that are independent of ω_0. They originate probably from the electrical network frequency at 50 Hz.

In figure 5.6, the resulting response spectrum from the piezo measurement with excitation frequencies from 330 to 1000 Hz is plotted. As before, the frequency positions of

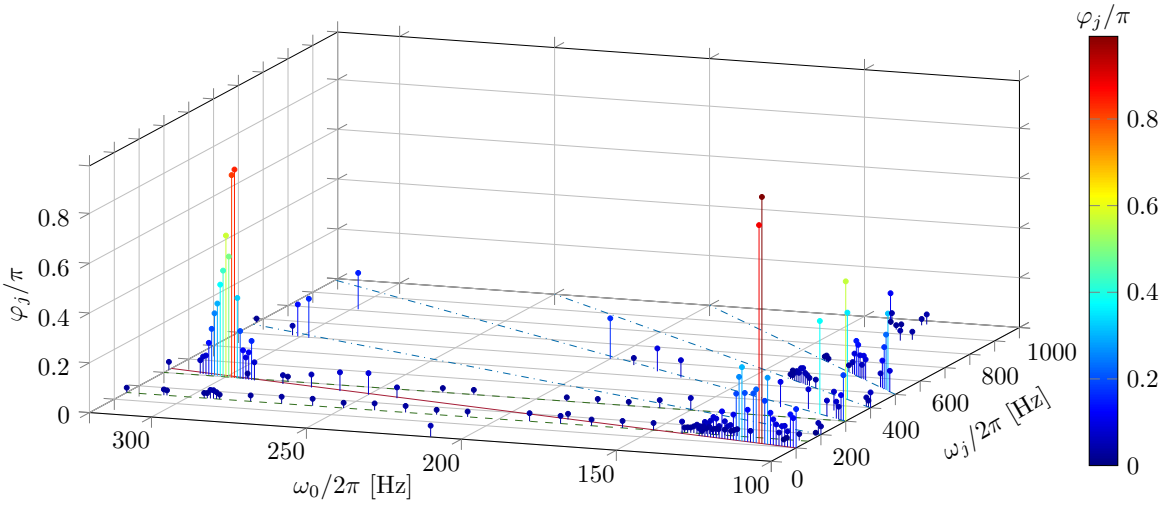

Figure 5.5.: Response spectrum of the biprism interferometer extracted from the speaker measurement. The red solid line in the frequency plane indicates where ω_j equals ω_0. The blue chain lines notify the higher harmonics of ω_0, especially visible in the region from 100 to 140 Hz. The green horizontal dashed lines show constant frequencies at 150 Hz and 300 Hz. Figure from [4]. Reprints with permission of IOP Publishing Limited.

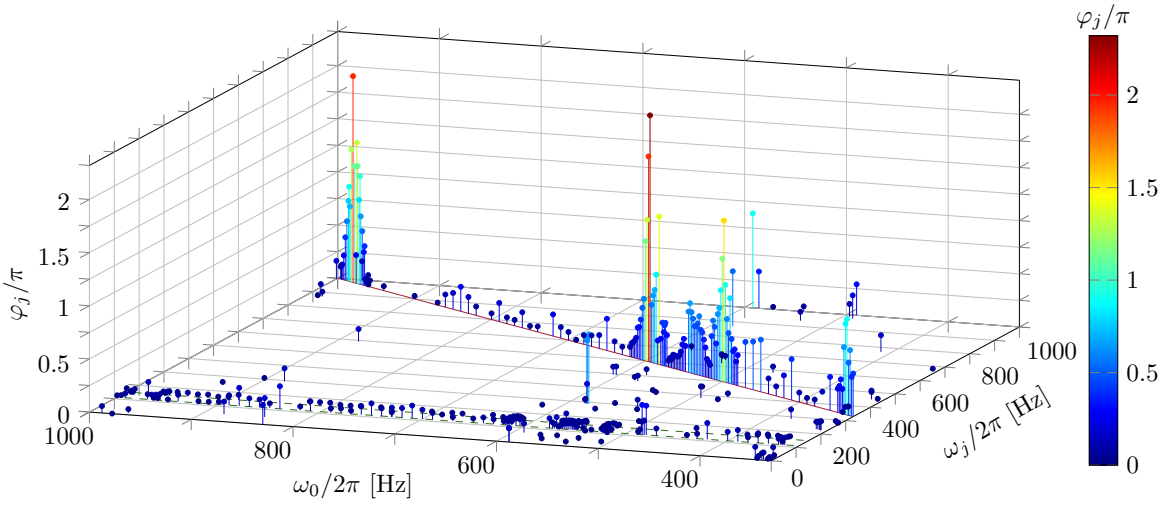

Figure 5.6.: Response spectrum extracted from the piezo measurement. The red solid line indicates where ω_j equals ω_0. The green horizontal dashed lines are at the positions of constant frequencies, 111.4 Hz and 150 Hz. Figure from [4]. Reprints with permission of IOP Publishing Limited.

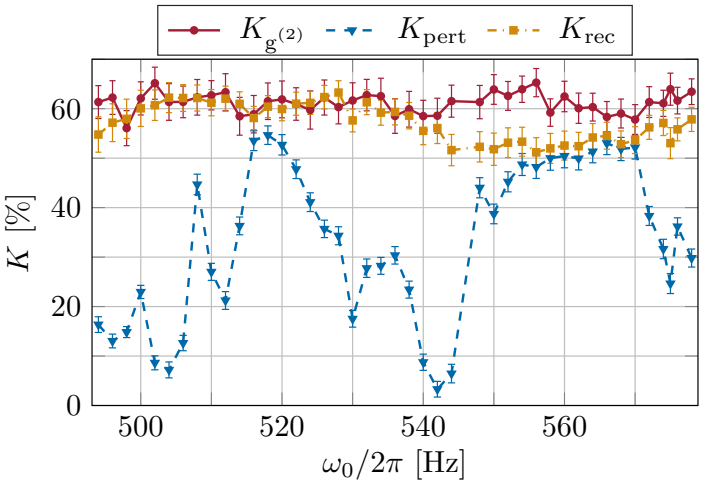

Figure 5.7.: Contrast extracted from the correlation function $K_{g^{(2)}}$ (red dots with solid line), contrast of the perturbed interference pattern K_{pert} (blue triangles with dashed line), and contrast of the reconstructed interference pattern K_{rec} (yellow squares with chain line) for different excitation frequencies ω_0. Figure from [4]. Reprints with permission of IOP Publishing Limited.

large perturbation amplitudes φ_j coincide well with the positions of reduced contrast K_{pert} in figure 5.4, according to equation (2.2). The maximum perturbation amplitude included in the response spectrum is $\varphi_j = 2.32\,\pi$ at $\omega_j/2\pi = 594\,\text{Hz}$. At the positions of 111.4 Hz and 150 Hz the green horizontal dashed lines indicate external perturbation frequencies. The first one could originate from a mechanical vibration or electromagnetic radiation in the laboratory and the latter from the electrical network frequency.

With $A(\varphi_j) = \lambda \cdot \varphi_j/2\pi$ (compare equation (1.9) for $A(\varphi_j) = \Delta y$) the amplitude of the mechanical oscillation can be calculated assuming that the perturbation occurs before magnification. Here, λ is the unmagnified spatial periodicity calculated according to equation (1.7) with the electron emission voltage of $-1.45\,\text{kV}$ and the biprism voltage of 0.3 V, yielding $\lambda = 880\,\text{nm}$. The resulting mechanical amplitudes range from 6 nm ($\varphi_j = 1.4{\cdot}10^{-2}\,\pi$ at $\omega_j/2\pi = 111.4\,\text{Hz}$) up to 1.021 µm ($\varphi_j = 2.32\,\pi$ at $\omega_j/2\pi = 594\,\text{Hz}$). In principle, it is possible to increase the sensitivity for the measurement of mechanical vibrations by decreasing the spatial periodicity λ, which is discussed in appendix A.4 for a time-varying magnetic and electric field. This can be achieved by either decreasing the acceleration voltage or increasing the biprism voltage (equation (1.7)). The sensitivity of the biprism interferometer for the measurement of mechanical vibrations can be calculated using equation (A.40) with the parameters of the measurement. For the speaker measurement a peak phase deviation of $\varphi = 5.2 \cdot 10^{-2}\,\pi/\sqrt{\text{Hz}}$ is determined leading to a sensitivity for the measurement of mechanical oscillation amplitudes of $A(\varphi) = 23\,\text{nm}/\sqrt{\text{Hz}}$. The values for the piezo measurement are $\varphi = 2.2 \cdot 10^{-2}\,\pi/\sqrt{\text{Hz}}$ and $A(\varphi) = 9.7\,\text{nm}/\sqrt{\text{Hz}}$. As mentioned before, decreasing the spatial periodicity λ, the sensitivity can be increased.

With the perturbation parameters obtained from the correlation analysis, the unperturbed interference pattern can be reconstructed from the perturbed one using equation (2.14). Additionally, the accuracy of the perturbation parameters is increased by

maximizing the contrast of the reconstructed interference pattern, which is explained in detail in section 4 of publication [4]. In figure 5.7, the resulting contrast K_{rec} of the reconstructed interference pattern is plotted together with $K_{\mathrm{g}^{(2)}}$ and K_{pert} for the region from 494 to 578 Hz of the piezo measurement. Over the complete region the contrast K_{rec} is larger than K_{pert} and close to $K_{\mathrm{g}^{(2)}}$ marking an upper threshold for the reconstruction process. It has to be mentioned that the contrast could not be reconstructed completely for the full spectrum shown in figure 5.4. However, it was possible to increase the contrast of the reconstructed interference pattern compared to the perturbed pattern for the complete spectrum. One reason could be that the oscillation was not phase stable over the complete measurement time. As discussed in section 5.2, a frequency accuracy of ± 1 mHz is necessary to reveal the contrast of the reconstructed interference pattern with less than 1 % deviation from the contrast of the unperturbed pattern. If the oscillation dephases during data acquisition, the contrast of the reconstructed interference pattern is reduced compared to the contrast of the unperturbed interference pattern.

5.4. Conclusion

The application of the correlation analysis was demonstrated successfully in an electron biprism interferometer. For this purpose, the interference pattern was dephased by external mechanical vibrations in a wide range of excitation frequencies. For certain frequencies the contrast is reduced to almost zero. However, it was shown that the matter-wave characteristics could be revealed for the whole perturbation spectrum. In contrast to former dephasing experiments with magnetic perturbations the involved frequencies are not known *a priori* due to the complexity of the system and possible vibrations from the environment. The developed search algorithm uses the amplitude spectrum of the correlation function for the identification of unknown perturbation frequencies and corresponding amplitudes. Using this algorithm, the vibrational response spectrum of the biprism interferometer including the mechanical resonances was measured. With the obtained perturbation parameters the contrast of the unperturbed interference pattern could be reconstructed over a wide range. Additionally, it was possible to increase the accuracy of the perturbation frequencies, amplitudes, and phases in the reconstruction process. This demonstrates that the correlation analysis is not only suitable to reveal the contrast and spatial periodicity of the unperturbed interference pattern but also to analyze the perturbation response spectrum of an interferometer.

6. Conclusion and Outlook

6.1. Conclusion

The high phase sensitivity of single-particle interferometers enables the wide range of applications of interferometry with charged particles [30], light [59], atoms [62], neutrons [70], and molecules [88] in sensor technology [58], fundamental research [78], and other technical applications [98]. At the same time, due to their high phase sensitivity interferometers are susceptible to dephasing originating typically from electromagnetic fields [2, 3], mechanical vibrations [4, 137, 161] or temperature drifts. Dephasing is an outstanding problem for mobile devices [138], precise interferometric measurements [167] or interferometry in perturbing environments. Such interferometric experiments are difficult to decouple sufficiently from the environment by active and passive vibrational damping and electromagnetic shielding in a broad frequency range. In interferometric experiments investigating the mechanisms of decoherence [85, 114, 143], the influence of dephasing has to be distinguished from the contrast reduction caused solely by decoherence. For the test of the quantum mechanical superposition it is necessary to prove interferences which is difficult in the presence of dephasing.

The contrast of an interference pattern dephased by an external time-varying perturbation, consisting of one or multiple perturbation frequencies, is reduced or vanished in the temporally integrated signal. Using second-order correlation analysis, the spatial distances of particle events in the detection plane reveal the contrast and spatial periodicity of the unperturbed interference pattern. Taking additionally into account the temporal differences, the characteristics of the external perturbation can be determined. One requirement for the applicability of the correlation analysis is that the flight time of the particles in the area of dephasing is smaller than the periodic time of the perturbation. Furthermore, the interferometer has to be equipped with a detector recording the spatial interference pattern with high spatial and temporal single-particle resolution. Such a detector is available for electrons and ions [127], atoms [172], neutrons [190], molecules [191], and photons [192–194]. Therefore, our correlation analysis can in principle be applied in a variety of interferometers.

This cumulative thesis summarized the publications [1–4] on our second-order correlation analysis of multifrequency dephasing in single-particle interferometry including the theoretical and experimental results. We have analyzed theoretically the dependence of the contrast reduction from the perturbation amplitude and derived the correlation function and corresponding amplitude spectrum for multifrequency dephasing. Additionally, it was shown how the characteristics of the unperturbed interference pattern can be determined. We derived the numerical solution of the correlation function used to extract the measurement data and discussed how the discretization influences the obtained parameters.

Using an electron biprism interferometer, the validity of our second-order correla-

tion analysis for one and multiple perturbation frequencies was verified experimentally. For this purpose, the interference pattern was shifted artificially perpendicular to the interference fringes by an external time-varying magnetic field which resulted in a reduction of the interference contrast. We demonstrated successfully that for all measurements the matter-wave characteristics could be determined although the contrast in the spatial signal was nearly vanished. Additionally, the perturbation frequencies and corresponding amplitudes were identified and used for the reconstruction of the unperturbed interference pattern.

The application of our correlation analysis for the identification of unknown perturbation characteristics was demonstrated by introducing artificially external mechanical vibrations in a broad frequency range to an electron biprism interferometer. A numerical search algorithm was developed using the amplitude spectrum of the correlation function for the determination of the perturbation frequencies and corresponding amplitudes. It was shown that the matter-wave characteristics could be identified over the complete excitation spectrum. Furthermore, the vibrational response spectrum of the used interferometer including the mechanical resonances was measured and the unperturbed interference pattern could be reconstructed for a large frequency range whereby the accuracy of the perturbation characteristics could be increased.

6.2. Outlook

We have demonstrated successfully the validity and applicability of our second-order correlation analysis for the identification of interference characteristics and unknown perturbation parameters.

For interferometric experiments in fundamental research our method can be used if the contrast and spatial periodicity of the unperturbed interference pattern have to be determined whereas the phase of the interference pattern is not necessary to be measured. This is in particular interesting for interferometric experiments studying the mechanisms of decoherence. Here, it is necessary to distinguish between contrast reduction due to dephasing and decoherence which can be achieved using our correlation analysis to determine the contrast of the unperturbed interference pattern. Therefore, the extracted contrast give direct access to the reduction of the contrast due to decoherence without any falsifying influence of dephasing. For the measurement of Coulomb induced decoherence in an electron biprism interferometer [114, 115] the interference pattern is guided above a surface with perpendicular oriented interference fringes. Depending on the distance to the surface, the material of the surface, and its temperature, the contrast of the interference pattern is reduced due to decoherence. With this setup, different theories can be tested describing the influence of Coulomb induced decoherence for different materials and temperatures. These theories predict different gradients for the contrast reduction depending on the distance to the surface. Additionally, for conductive materials the expected contrast reduction is smaller compared to semiconductor materials and therefore, it is necessary to avoid dephasing. Using our method to determine the contrast for different distances to the surface, it is possible to eliminate the influence of dephasing and obtain solely the contrast reduction due to decoherence. This advantage of our method reduces additionally the requirements for vibrational damping and electromagnetic shielding in a

broad frequency range for such experiments.

To test the limits of quantum mechanical superposition [78] by realizing interferences of macroscopic objects with small de Broglie wavelengths, e.g. interferometry with large molecules [81], the presence of interferences has to be proved. Here, dephasing could cause a vanished interference pattern and therefore, no contrast and spatial periodicity may be measured. As a consequence, it could be assumed that no quantum mechanical superposition was realized. However, using our correlation analysis it is possible to prove the presence of interferences by the determination of contrast and spatial periodicity even if the spatial interference pattern is vanished. Using a biprism interferometer with ions [101, 102], it is also possible to investigate the limits of quantum mechanical superposition due to the small wavelengths of the ions. In such an experiment long integration times of several minutes are necessary to measure interferences. During data acquisition the interference pattern could dephase due to temperature drifts of the cooled ion-emitter and the fringes vanish in the temporally integrated interference pattern. The application of our method, nevertheless, would verify the presence of ion-interferences and the contrast and spatial periodicity could be determined.

Our correlation analysis can be used for interferometric measurements that have to determine the absolute value of the contrast to characterize for example the coherence properties of an emission source. This was demonstrated successfully in our group for an arrangement of a single-atom tip in combination with two counter electrodes [9]. It could be shown that the electron energy can be adjusted independently from the extraction voltage. Additionally, it was demonstrated that the longitudinal and transversal coherence properties of the source stay unchanged. Due to dephasing of the interference pattern originating from the electrical network frequency of 50 Hz, the resulting contrast was reduced in the spatial signal. Using our method, it was possible to obtain the contrast of the unperturbed interference pattern leading to an accurate result for the coherence length and the energy width of the emission source.

For interferometers used as a sensor measuring phase shifts of the interference pattern, e.g. sensors for inertial forces [112, 113], it is important to suppress external perturbations that could dephase the interference pattern and therefore, falsify the results. In these technical applications our correlation analysis can be applied for the determination of the vibrational and electromagnetic response spectrum of the used interferometer. With these informations active and passive damping systems and electromagnetic shielding could be optimized for the application in a certain frequency range. Therefore, our method is a useful tool for the technical optimization of interferometric sensors.

Another possible application of our correlation analysis could be the use as a lock-in technique for the measurement of certain signals. This idea is explained in the following for the proposed measurement of the electrostatic Aharonov-Bohm effect in [6] using a large beam path separation in a biprism interferometer for hydrogen ions. Here, one metal cylinder is placed in each of the two beam paths to cause a phase shift of the interference pattern due to the difference of the electrostatic potentials inside of the two cylinders. If the interference pattern is dephased by temperature drifts or external perturbations during the data acquisition, the phase shift can not be observed. This problem can be overcome by applying a time-varying potential with a frequency of a few ten mHz to the cylinders that varies the electric potential difference between them

periodically. The maximum amplitude of this oscillation corresponds to the phase shift of the interference pattern for a constant potential difference. After the data acquisition, our method can be used to identify the amplitude and frequency of the applied oscillation indicating the successful measurement of the electrostatic Aharonov-Bohm effect. Therefore, it is possible to realize a lock-in technique in interferometers with our method to measure certain signals that are linked to the phase shift of the interference pattern.

This lock-in technique could also be used in an electron biprism interferometer for the measurement of magnetic flux enclosed in a coil that is installed between the two paths of a large beam path separation [108, 109]. Here, the magnetic Aharonov-Bohm effect leads to a phase shift of the interference pattern depending on the enclosed flux. The interference pattern is artificially dephased in the same way as described before by applying a periodic current with a frequency of a few ten mHz to the magnetic coil. Using our correlation analysis the oscillation frequency can be identified and the corresponding amplitude is determined. This amplitude φ is linked to the magnetic flux Φ enclosed in the coil $\varphi = 2\pi\Phi$. The advantages of this method compared to former measurements of the magnetic Aharanov-Bohm effect, where constant currents were applied, are that the influence of dephasing is suppressed and the phase shift can be determined from the measurement without comparing it to the case for zero magnetic flux.

As our correlation analysis can be used to detect electromagnetic as well as mechanical frequencies and corresponding amplitudes in a broad range [2–4, 8, 9], the application as a sensor is conceivable. For this purpose, a new interferometer setup has to be developed with a compact design including a minimum number of electron-optical parts to be resistant against mechanical vibrations and to avoid possible electromagnetic noise introduced by the elements of the interferometer. According to these requirements, the sensitivity of an electron biprism interferometer used as a sensor for oscillating magnetic and electric fields is estimated in appendix A.4. Based on these calculations an experimental setup is proposed in the following using low-energy electrons (50 eV to 1250 eV) due to their high sensitivity to electromagnetic fields. This enables the measurement of magnetic field strengths with a sensitivity down to about $95\,\mathrm{pT}/\sqrt{\mathrm{Hz}}$ and electric field strengths with a sensitivity down to about $4\,\mu\mathrm{V}/\left(\mathrm{cm}\sqrt{\mathrm{Hz}}\right)$. The sensitivity for the measurement of magnetic flux amounts to about $6\,\mathrm{m}\Phi_0/\sqrt{\mathrm{Hz}}$, with the magnetic flux quantum $\Phi_0 \approx 2.07 \cdot 10^{-15}\,\mathrm{Wb}$. It should be possible to detect frequencies from a few ten mHz up to about 100 MHz with the proposed setup. With quantum sensors for AC magnetic fields comprised of Bose-Einstein condensates (BECs) [184, 211], nitrogen-vacancy (NV) centers [212–214], and superconducting quantum interference devices (SQUIDs) [215, 216], sensitivities from $\mathrm{nT}/\sqrt{\mathrm{Hz}}$ down to a few $\mathrm{pT}/\sqrt{\mathrm{Hz}}$ have been realized. Compared to these, the magnetic field sensitivity of the here proposed sensor is in a similar range. However, due to the limited spatial resolution of the proposed setup, the magnetic flux sensitivity is lower compared to a few $\mu\Phi_0/\sqrt{\mathrm{Hz}}$ [184, 211, 216]. Nevertheless, an electron biprism interferometer used as a sensor for oscillating magnetic and electric fields can be a supplement to the established AC magnetic field sensors due to its compact design, the operation at room temperature, and the wide range of detectable frequencies from a few ten mHz up to about 100 MHz. An overview of DC and AC magnetic quantum

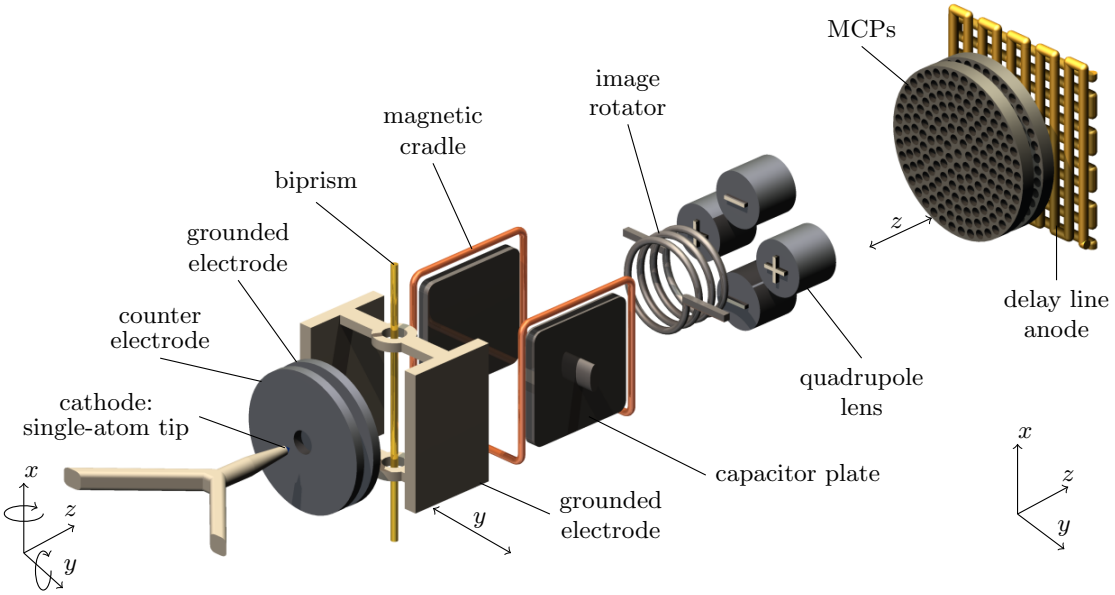

Figure 6.1.: Schematic illustration (not to scale) of the proposed electron biprism interferometer used as a sensor for oscillating magnetic and electric fields. From the single-atom tip (SAT) mounted on a five-axis piezo positioner the electrons are field-emitted and adjusted onto the optical axis. In front of the SAT, the counter electrode can be used to increase the count rate by applying a positive voltage without changing the electron energy. The electron matter-wave is separated and recombined by the biprism which is mounted on a linear piezo positioner to align it onto the optical axis. An oscillating magnetic and electric field can be generated by the magnetic cradle and the capacitor placed behind the biprism shifting the interference pattern along the y-direction perpendicular to the fringes. After the magnification of the interference pattern by the quadrupole lens it is measured with a delay line detector consisting of two MCPs and a delay line anode. The image rotator corrects possible misalignment of the biprism to the axis of the quadrupole lens. The distances between the parts of the interferometer can be found in appendix A.4 and a detailed explanation of the setup in appendix A.5.

sensors can be found in [217].

Based on the realization of a compact electron biprism interferometer [8] and the generation of low-energy electrons down to 50 eV [98, 135, 218] using a single-atom tip (SAT) [94, 129], the proposed electron biprism interferometer for the measurement of oscillating magnetic and electric fields is illustrated in figure 6.1 and explained in detail in appendix A.5. With a total length of 20 cm (see calculations appendix A.4) from single-atom tip to detector, the design of the interferometer is compact and equipped with a minimum number of elements fulfilling the requirements explained before. This design enables the application of the electron biprism interferometer as a sensor with a large range of detectable magnetic and electric field strengths, and oscillation frequencies (appendix A.4).

After investigating the sensitivity of the proposed electron biprism interferometer for the measurement of oscillating magnetic and electric fields, there are two possible applications in sensor technology. First, for the measurement of external fields the magnetic cradle and capacitor plate are taken out and the complete interferometer

is shielded against electromagnetic radiation except the region where they have been installed. In this way, external oscillating fields dephase the interference pattern only in this region. By mounting the interferometer on a stage rotatable around the z-direction the external field can be measured with spatial resolution as the interference pattern is only dephased perpendicular to the fringes. It has to be mentioned that for the measurement of external electromagnetic fields it is not possible to distinguish between the magnetic and electric field component for one set of experimental values, as acceleration voltage U_{acc}, biprism voltage U_{bp}, and peak phase deviation φ extracted from the correlation analysis (equation (A.35) and (A.36)). However, as φ depends on U_{acc} in a different way for the magnetic $\varphi \propto B/\sqrt{U_{\mathrm{acc}}}$ and electric field component $\varphi \propto E/U_{\mathrm{acc}}$ of the electromagnetic radiation (equation (A.30), (A.31) and (A.32)), it can be distinguished between them by varying U_{acc} for a constant U_{bp}. During these measurements obviously the amplitude of the external field must not change. The second sensor application could be the measurement of oscillating currents or voltages. For this purpose, the magnetic cradle and capacitor are replaced by elements which have to be designed in a way that they create magnetic and electric fields with a field strength that can be measured with the proposed electron biprism interferometer. Additionally, the specific design influences the possibility to apply oscillating currents and voltages with a wide frequency spectrum due to their inductance and capacitance. Therefore, it could be interesting to install more than one of these elements into the interferometer to increase the measurement range.

Due to the wide range of detectable frequencies and amplitudes, our second-order correlation analysis is not only an interesting tool for the development of a sensor for oscillating electromagnetic fields as explained before but also for fundamental research. Especially, the possibility to distinguish between dephasing and decoherence is essential for experiments studying the influence of decoherence, e.g. Coulomb induced decoherence, and to test the limits of the quantum mechanical superposition, e.g. interferometry with ions and large molecules. A lock-in technique could be realized in interferometers for the measurement of artificial oscillating phase shifts using our correlation analysis to identify the applied oscillating signal. Furthermore, the mechanical damping and electromagnetic shielding of interferometers used as sensors can be optimized for technical applications by measuring the response spectra for mechanical vibrations and electromagnetic oscillations with our method. Due to the wide range of capabilities discussed here, our correlation analysis is a powerful instrument in interferometric experiments and of significant relevance in various fields of single-particle interferometry.

A. Appendix

A.1. Explicit solution of the second-order correlation function for multifrequency dephasing

The explicit solution of the second-order correlation function for multifrequency dephasing is derived from equation (1.37) using the probability distribution of particle impacts in the detection plane $f(y,t)$ of equation (1.12) and the average over position and time $\langle\!\langle \cdot \rangle\!\rangle_{y,t}$ in equation (1.38). If the perturbation frequencies ω_j (equation (1.11)) and the spatial periodicity λ are small compared to the acquisition time $T \gg 2\pi/\omega_j$ and length $Y \gg \lambda$, respectively, equation (1.37) can be solved analytically, yielding

$$g^{(2)}(u,\tau) = 1 + \frac{K^2}{2} \sum_{\substack{\{n_j,m_j\}\in\ker(c) \\ j=1\ldots N}} A_{\{n_j,m_j\}}\left(\tau, \Phi_{\{n_j,m_j\}}\right) \cos\left(ku + \tilde{\varphi}_{\{n_j,m_j\}}\right) \ . \tag{A.1}$$

Here, the amplitude $A_{\{n_j,m_j\}}\left(\tau, \Phi_{\{n_j,m_j\}}\right)$ depends on the correlation time τ and the specific perturbation characteristics

$$A_{\{n_j,m_j\}}\left(\tau, \Phi_{\{n_j,m_j\}}\right) = \tilde{B}_{\{n_j,m_j\}}\left(\varphi_j\right) \cdot \cos\left(\sum_{j=1}^{N} m_j\omega_j\tau + \Phi_{\{n_j,m_j\}}\right) , \tag{A.2}$$

with the product of the Bessel functions

$$\tilde{B}_{\{n_j,m_j\}}\left(\varphi_j\right) \coloneqq \prod_{j=1}^{N} J_{n_j}\left(\varphi_j\right) J_{m_j}\left(\varphi_j\right) \ . \tag{A.3}$$

The spatial correlation phase $\tilde{\varphi}_{\{n_j,m_j\}}$ and temporal phase $\Phi_{\{n_j,m_j\}}$ in equation (A.1) and (A.2) are given by

$$\tilde{\varphi}_{\{n_j,m_j\}} \coloneqq \frac{\pi}{2} \sum_{j=1}^{N} \left(m_j - n_j\right) \quad , \quad \Phi_{\{n_j,m_j\}} \coloneqq \sum_{j=1}^{N} \phi_j \left(m_j + n_j\right) \ . \tag{A.4}$$

In section 2.2 of publication [1], a detailed derivation of equation (A.1) is given. The sum in equation (A.1) has to be taken over all integer multiplets $\{n_j, m_j\} \in \mathbb{Z}, j = 1\ldots N$ that are contained in the kernel of function c ($\ker(c)$)

$$c : \mathbb{Z}^N \times \mathbb{Z}^N \longrightarrow \mathbb{R} \quad , \quad \left(n_{j=1\ldots N}, m_{j=1\ldots N}\right) \longmapsto \sum_{j=1}^{N} \left(n_j + m_j\right)\omega_j \ , \tag{A.5}$$

so that $c\left(n_{j=1\ldots N}, m_{j=1\ldots N}\right) = 0$. Thus, the integer multiplets $\{n_j, m_j\} \in \ker(c), j = 1 \ldots N$ satisfy the constraint

$$\sum_{j=1}^{N} \left(n_j + m_j\right) \omega_j = 0 \ . \tag{A.6}$$

This is fulfilled trivially for integer multiplets with $n_j = -m_j$. However, depending on the specific perturbation frequencies ω_j, the constraint can also be satisfied for additional integer multiplets with $n_j \neq -m_j$. For example, in the case of two perturbation frequencies that are multiples of each other $\omega_2 = 2\omega_1$ the constraint in equation (A.6) is fulfilled for $n_{1/2} = -m_{1/2}$, but also for $n_{1/2} \neq -m_{1/2}$, e.g. $\{n_1, m_1, n_2, m_2\} = \{0, 2, -1, 0\}$. An exemplary correlation function for this case is shown and discussed in detail in section 2.1.4. Another case for which the explicit solution has to be applied is for three perturbation frequencies having the same frequency difference $\Delta\omega$ between each other, $\omega_1 = \omega_2 - \Delta\omega$, ω_2, and $\omega_3 = \omega_2 + \Delta\omega$. Here, the constraint in equation (A.6) is satisfied for $n_{1/2/3} = -m_{1/2/3}$, but additionally for $n_{1/2/3} \neq -m_{1/2/3}$, e.g. $\{n_1, m_1, n_2, m_2, n_3, m_3\} = \{0, 1, -1, -1, 0, 1\}$.

It has to be noted that for a finite acquisition time T, the constraint in equation (A.6) has to be modified to

$$\left| \sum_{j=1}^{N} \left(n_j + m_j\right) \omega_j \right| < 2\pi/T \ , \tag{A.7}$$

defining the minimum resolvable frequency via $1/T$. In the following equations and discussions equation (A.6) is used as it is assumed that $T \to \infty$.

In equation (A.1), the sum has to be evaluated for all integer multiplets $\{n_j, m_j\} \in \ker(c), j = 1 \ldots N$ that satisfy the constraint in equation (A.6). It is fulfilled, in principle, for an infinite number of multiplets, each contributing to the correlation function with

$$a_{\{n_j,m_j\}}(u,\tau) = A_{\{n_j,m_j\}}\left(\tau, \Phi_{\{n_j,m_j\}}\right) \cos\left(ku + \tilde{\varphi}_{\{n_j,m_j\}}\right) \ , \tag{A.8}$$

where the amplitude is given by equation (A.2). According to equation (2.5), for large values of $\{n_j, m_j\}$ the contribution is suppressed due to the strong decay of the Bessel function (equation (A.3)) for $m_j > \varphi_j$, which limits the number of integer multiplets that have to be evaluated in the sum of equation (A.1).

Each contributing multiplet addend $a_{\{n_j,m_j\}}(u,\tau)$ reveals a periodic modulation with the same spatial periodicity $\lambda = 2\pi/k$ as the unperturbed interference pattern, but shifted by the spatial correlation phase $\tilde{\varphi}_{\{n_j,m_j\}}$ in u-direction. $A_{\{n_j,m_j\}}\left(\tau, \Phi_{\{n_j,m_j\}}\right)$ shows a periodic structure with the periodicity given by the frequency component $\sum_{j=1}^{N} m_j\omega_j$ with the coefficients $\{n_j, m_j\} \in \ker(c)$. The peak phase deviations φ_j in equation (A.3) determine the maximum modulation amplitude. In τ-direction, the periodic structure is shifted by the temporal correlation phase $\Phi_{\{n_j,m_j\}}$.

After evaluating the sum in equation (A.1), the resulting correlation function shows also a periodic modulation in u-direction with the same spatial periodicity λ as the unperturbed interference pattern. The overall amplitude of the resulting correlation function has a maximum value of 1 only at certain correlation times τ defined by the

perturbation frequencies ω_j (see section 2.1.3). Then, the contrast of the correlation function $K^2/2$ is directly linked to the contrast of the unperturbed interference pattern K.

The overall amplitude of the resulting correlation function contains the perturbation frequencies ω_j, their harmonic frequencies as well as their differences and sums (intermodulation terms) given by the frequency components $\sum_{j=1}^{N} m_j\omega_j$ as argument of the cosine in equation (A.2). For each perturbation frequency ω_j, the maximum frequency component included in the correlation function is approximately given by $m_{j,\max}\omega_j$, with $m_{j,\max} \approx \varphi_j$, due to the strong decay of the Bessel function for $m_j > \varphi_j$, according to equation (2.5). Therefore, the maximum frequency component of all underlying perturbation frequencies is approximately determined by $\max\{\varphi_j\omega_j\}$.

An approximate solution of the correlation function can be derived if only the trivial solution $n_j = -m_j$ to the constraint in equation (A.6) is considered. These integer multiplets $\{-m_j, m_j\} \in \ker(c)$ typically constitute the main contribution to the correlation function in equation (A.1). Using $\Phi_{\{-m_j,m_j\}} = 0$, $\tilde{\varphi}_{\{-m_j,m_j\}} = \pi\sum_{j=1}^{N} m_j$ and $J_{-m_j}(\varphi_j) = (-1)^{m_j} J_{m_j}(\varphi_j)$ in equation (A.1) and (A.2), the approximate correlation function in equation (1.40) with the time-dependent amplitude of equation (2.6) can be calculated.

A.2. Amplitude spectrum of the correlation function

The temporal Fourier transform $\mathcal{F}\left(g^{(2)}(u,\tau)\right)(u,\omega) = \frac{1}{\sqrt{2\pi}}\int_{-\infty}^{\infty} g^{(2)}(u,\tau)\mathrm{e}^{i\omega\tau}\,\mathrm{d}\tau$ of equation (A.1) and (A.2) is calculated, yielding the amplitude spectrum $\left|\mathcal{F}\left(g^{(2)}(u,\tau)\right)(u,\omega)\right|$ of the explicit correlation function

$$\frac{1}{2\pi}\left|\mathcal{F}\left(g^{(2)}(u,\tau)\right)(u,\omega)\right|^2 = \delta(\omega)^2 + \tag{A.9}$$
$$+ 2\cdot\left(\frac{K^2}{2}\sum_{\substack{\{n_j,m_j\}\in\ker(c)\\ j=1\ldots N}} \hat{A}_{\{n_j,m_j\}}\left(\omega,\Phi_{\{n_j,m_j\}}\right)\cos\left(ku+\tilde{\varphi}_{\{n_j,m_j\}}\right)\right)^2,$$

where $\hat{A}_{\{n_j,m_j\}}\left(\omega,\Phi_{\{n_j,m_j\}}\right)$ is the amplitude depending on the frequency ω and the perturbation characteristics

$$\hat{A}_{\{n_j,m_j\}}\left(\omega,\Phi_{\{n_j,m_j\}}\right) = \tilde{B}_{\{n_j,m_j\}}(\varphi_j)\cdot\left(\cos\left(\Phi_{\{n_j,m_j\}}-\frac{\pi}{4}\right)\delta(\omega+\omega_{\{m_j\}}) + \right.$$
$$\left. + \cos\left(\Phi_{\{n_j,m_j\}}+\frac{\pi}{4}\right)\delta(\omega-\omega_{\{m_j\}})\right), \tag{A.10}$$

with the Dirac delta function $\delta(\omega)$ and the frequency components $\omega_{\{m_j\}} \coloneqq \sum_{j=1}^{N} m_j\omega_j$. A detailed calculation of equation (A.9) can be found in section 2.7 of publication [1]. In equation (A.9), the sum has to be evaluated for the integer multiplets $\{n_j, m_j\} \in \ker(c), j = 1\ldots N$ fulfilling the constraint of equation (A.6). Each multiplet addend contributes to the amplitude spectrum with

$$\hat{a}_{\{n_j,m_j\}}(u,\omega) = \hat{A}_{\{n_j,m_j\}}\left(\omega,\Phi_{\{n_j,m_j\}}\right)\cos\left(ku+\tilde{\varphi}_{\{n_j,m_j\}}\right), \tag{A.11}$$

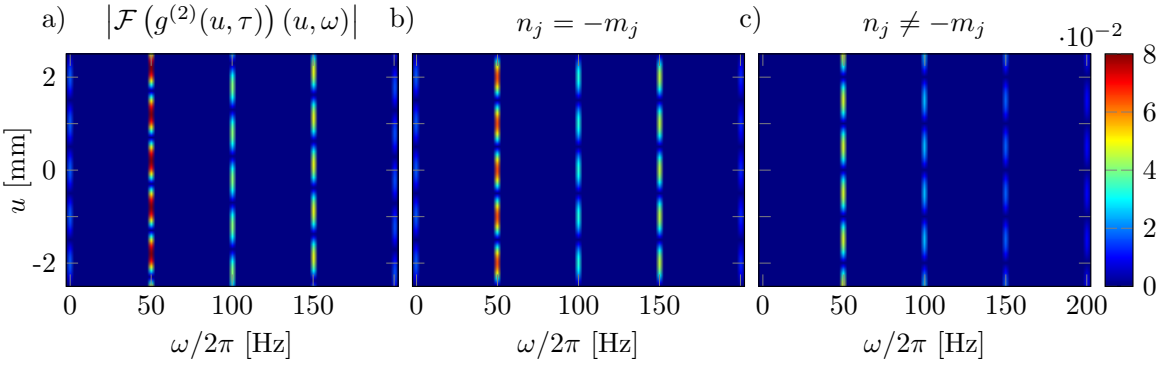

Figure A.1.: a) Amplitude spectrum $\left|\mathcal{F}\left(g^{(2)}(u,\tau)\right)(u,\omega)\right|$ calculated with the explicit solution in equation (A.9) using the same values as for the correlation function in figure 2.3(a) ($K = 0.6$, $\lambda = 2\,\mathrm{mm}$, $\omega_1/2\pi = 50\,\mathrm{Hz}, \varphi_1 = 0.5\,\pi, \phi_1 = 0.25\,\pi$, and $\omega_2/2\pi = 100\,\mathrm{Hz}, \varphi_2 = 0.5\,\pi, \phi_2 = -0.25\,\pi$). b) Approximate solution of the amplitude spectrum calculated according to equation (2.9) and (A.12). c) Contribution of the addends with $n_j \neq -m_j$ to the amplitude spectrum in a). Figure from [1].

revealing a modulation in u-direction with the same spatial periodicity $\lambda = 2\pi/k$ as the unperturbed interference pattern, but phase shifted by $\tilde{\varphi}_{\{n_j,m_j\}}$. The modulation amplitude $\hat{A}_{\{n_j,m_j\}}\left(\omega, \Phi_{\{n_j,m_j\}}\right)$ is given by the peak phase deviations via the product of the Bessel functions in equation (A.3), modified by the cosine of $\Phi_{\{n_j,m_j\}} \mp \pi/4$. By the frequency components $\omega_{\{m_j\}}$ with the coefficients $\{n_j, m_j\} \in \ker(c)$, the position in the frequency space is defined.

After summing up all multiplet addends, the amplitude spectrum shows the same spatial periodicity λ and includes all frequency components up to a maximum frequency of approximately $\max\{\varphi_j\omega_j\}$ (see section 2.1.2).

To calculate the amplitude spectrum of the approximate correlation function in equation (1.40) and (2.6), the trivial solution $n_j = -m_j$ to the constraint in equation (A.6) is applied in equation (A.9) and (A.10), yielding equation (2.9) with the frequency-dependent amplitude

$$\hat{A}(\omega) = \sum_{\substack{\{-m_j,m_j\}\in\ker(c)\\ j=1\ldots N}} \left(\prod_{j=1}^{N} J_{m_j}(\varphi_j)^2\right) \cdot \left(\delta(\omega + \omega_{\{m_j\}}) + \delta(\omega - \omega_{\{m_j\}})\right) . \tag{A.12}$$

The periodicity of the modulation in u-direction is given by the spatial periodicity λ. Furthermore, the maximum modulation amplitude $\hat{A}(\omega)$ is solely defined by the peak phase deviations φ_j via the square of the Bessel functions.

The amplitude spectrum $\left|\mathcal{F}\left(g^{(2)}(u,\tau)\right)(u,\omega)\right|$ of the correlation function shown in figure 2.3(a) of two perturbation frequencies that are multiples of each other, $\omega_1/2\pi = 50\,\mathrm{Hz}$ and $\omega_2/2\pi = 100\,\mathrm{Hz}$, is calculated with equation (A.9) and plotted in figure A.1(a) for positive frequencies. Calculated according to the approximate solution in equation (2.9) and (A.12), the amplitude spectrum of the approximate correlation function (see figure 2.3(b)) is illustrated in figure A.1(b). The contribution of terms with $n_j \neq -m_j$ to the amplitude spectrum in figure A.1(a) is shown in figure A.1(c). Along the u-direction the spatial modulation with the periodicity λ can be identified

for each frequency component given by $m_1\omega_1 + m_2\omega_2$, with $\{n_1, m_1, n_2, m_2\} \in \ker(c)$. In figure A.1(c), the spatial correlation phases $\tilde{\varphi}_{\{n_j,m_j\}}$ cause the shift of the periodic structure in u-direction.

A.3. Discretization effects of the numerical second-order correlation function

The influence of the discretization step size on the correlation analysis and noise in the correlation function is analyzed in this section. For one perturbation frequency, a theory is derived to describe how the discretization affects the determination of the contrast and peak phase deviation. Afterwards, a theory is derived which describes the noise in the correlation function and the corresponding amplitude spectrum. Thereby, an optimum discretization step size is provided to achieve a maximum signal-to-noise ratio. Additionally, the minimum detectable peak phase deviation is estimated.

A.3.1. Influence on correlation analysis

In the following, the approximate correlation function in equation (1.40) and (2.4) is used to investigate the influence of the discretization step size Δu and $\Delta\tau$ on the obtained parameters. Only one perturbation frequency ω_1 is taken into account for simplicity. The analytic correlation function is discretized in spatial and temporal intervals Δu and $\Delta\tau$, yielding

$$\begin{aligned} g^{(2)}(u,\tau)_{\Delta u,\Delta\tau} &= \frac{1}{\Delta\tau\Delta u}\int_{u-\frac{\Delta u}{2}}^{u+\frac{\Delta u}{2}}\int_{\tau-\frac{\Delta\tau}{2}}^{\tau+\frac{\Delta\tau}{2}} g^{(2)}(u,\tau)\,\mathrm{d}\tau\mathrm{d}u \\ &= 1 + \frac{K^2}{2}\cdot A\left(\tau\right)_{\Delta\tau}\operatorname{sinc}\left(k\frac{\Delta u}{2}\right)\cos\left(ku\right)\ , \end{aligned} \tag{A.13}$$

with the sinc-function $\operatorname{sinc}(x) = \sin(x)/x$ and the amplitude $A\left(\tau\right)_{\Delta\tau}$ depending on the correlation time and temporal discretization step size

$$A\left(\tau\right)_{\Delta\tau} = \sum_{m_1=-\infty}^{\infty} J_{m_1}\left(\varphi_1\right)^2 \cdot \operatorname{sinc}\left(m_1\omega_1\frac{\Delta\tau}{2}\right)\cos\left(m_1\omega_1\tau\right)\ . \tag{A.14}$$

For $\Delta u = 0$ and $\Delta\tau = 0$, equation (A.13) and (A.14) are equal to the analytic solution in equation (1.40) and (2.4).

The contrast K and spatial periodicity λ are obtained from the correlation function at the correlation time $\tau = 0$ (see section 2.1.3), for which equation (A.13) and (A.14) results in

$$g^{(2)}(u,0)_{\Delta u,\Delta\tau} = 1 + \frac{K^2}{2}\cdot A\left(0\right)_{\Delta\tau}\operatorname{sinc}\left(k\frac{\Delta u}{2}\right)\cos\left(ku\right)\ , \tag{A.15}$$

with

$$A(0)_{\Delta\tau} = \sum_{m_1=-\infty}^{\infty} J_{m_1}\left(\varphi_1\right)^2 \cdot \operatorname{sinc}\left(m_1\omega_1\frac{\Delta\tau}{2}\right)\ . \tag{A.16}$$

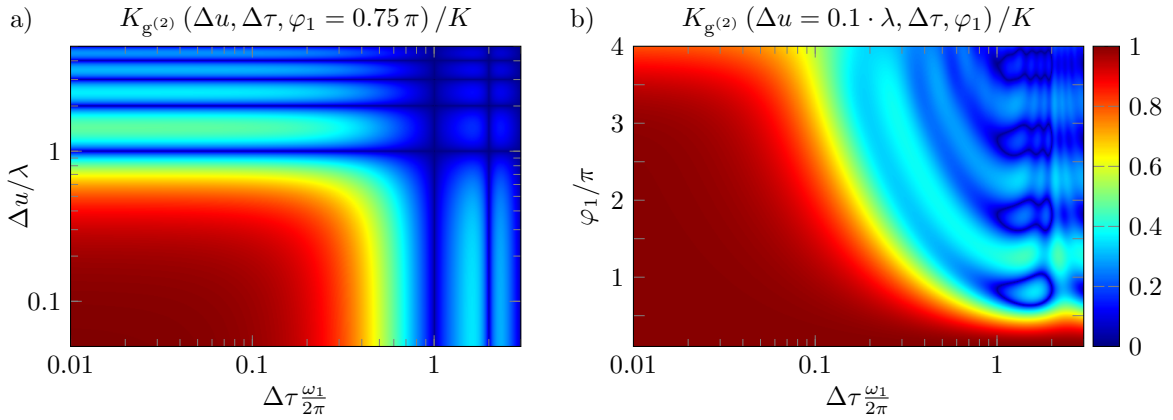

Figure A.2.: a) The extracted contrast $K_{g^{(2)}}(\Delta u, \Delta\tau, \varphi_1 = 0.75\,\pi)/K$ (equation (A.17)) is plotted for one perturbation frequency ω_1, peak phase deviation $\varphi_1 = 0.75\,\pi$, and different Δu and $\Delta\tau$. b) $K_{g^{(2)}}(\Delta u = 0.1\cdot\lambda, \Delta\tau, \varphi_1)/K$ depending on $\Delta\tau$ and φ_1 for $\Delta u/\lambda = 0.1$. Figure from [1].

Here, the spatial periodicity $\lambda = 2\pi/k$ remains unchanged by the discretization, but the extracted contrast $K_{g^{(2)}}$ is modified to

$$K_{g^{(2)}}(\Delta u, \Delta\tau, \varphi_1) = K \cdot \sqrt{\left| A(0)_{\Delta\tau} \cdot \operatorname{sinc}\left(k\frac{\Delta u}{2}\right)\right|}\,. \tag{A.17}$$

For multiples of $\Delta\tau = 2\pi/\omega_1$ and $\Delta u = \lambda$, this contrast is equal to zero, because the sinc-functions become zero. They converge to 1 for $\Delta\tau \to 0$ and $\Delta u \to 0$. The full contrast K is only reached for $\Delta u = \Delta\tau = 0$. In figure A.2(a), the extracted contrast $K_{g^{(2)}}$ (equation (A.17)) depending on $\Delta\tau$ and Δu is shown for a peak phase deviation of $\varphi_1 = 0.75\,\pi$. For $\Delta u/\lambda = 0.1$, the dependence on $\Delta\tau$ and φ_1 is illustrated in figure A.2(b).

The analytic solution of the amplitude spectrum in equation (2.9) and (2.10) is applied for the determination of the perturbation parameters (ω_1 and φ_1). It also depends on Δu and $\Delta\tau$ for discrete signals, and is calculated from equation (A.13) and (A.14) using a temporal Fourier transformation

$$\frac{1}{2\pi}\left|\mathcal{F}\left(g^{(2)}(u,\tau)_{\Delta u,\Delta\tau}\right)(u,\omega)\right|^2 = \delta(\omega)^2 + \\ + \left(\frac{K^2}{2}\cdot\hat{A}(\omega)_{\Delta\tau}\operatorname{sinc}\left(k\frac{\Delta u}{2}\right)\cos(ku)\right)^2, \tag{A.18}$$

where the amplitude $\hat{A}(\omega)_{\Delta\tau}$ depending on the frequency and temporal discretization step size is given by

$$\hat{A}(\omega)_{\Delta\tau} = \sum_{m_1=-\infty}^{\infty} J_{m_1}(\varphi_1)^2 \cdot \operatorname{sinc}\left(m_1\omega_1\frac{\Delta\tau}{2}\right)\Big(\delta(\omega + m_1\omega_1) + \delta(\omega - m_1\omega_1)\Big)\,, \tag{A.19}$$

with the Dirac delta function $\delta(\omega)$ and the frequency components $\pm m_1\omega_1$. Comparing the analytic solution of the amplitude spectrum in equation (2.9) and (2.10) with equation (A.18) and (A.19), it can be seen that the frequency components $\pm m_1\omega_1$ remain

unchanged, whereas their amplitudes $J_{m_1}(\varphi_1)^2$ are varied because of the discretization. The amplitude of the fundamental frequency component ($m_1 = 1$) in equation (A.18) and (A.19) is calculated at the spatial position $u = 0$, yielding

$$\frac{1}{\sqrt{2\pi}}\left|\mathcal{F}\left(g^{(2)}(0,\tau)_{\Delta u,\Delta\tau}\right)(0,\omega_{\{m_1=1\}})\right| = \frac{K^2}{2}\,J_1(\bar{\varphi}_1)^2\ , \tag{A.20}$$

with the modified amplitude

$$J_1(\bar{\varphi}_1)^2 = \operatorname{sinc}\left(k\frac{\Delta u}{2}\right)\operatorname{sinc}\left(\omega_1\frac{\Delta\tau}{2}\right)\cdot J_1(\varphi_1)^2\ . \tag{A.21}$$

To determine the peak phase deviation φ_1 correctly, the factor $\operatorname{sinc}\left(k\frac{\Delta u}{2}\right)\operatorname{sinc}\left(\omega_1\frac{\Delta\tau}{2}\right)$ has to be taken into account, as it reduces the amplitude of the fundamental frequency component $J_1(\varphi_1)^2$. The peak phase deviation $\bar{\varphi}_1$ depends on the discretization, via the square of the Bessel function. For $\Delta u \to 0$ and $\Delta\tau \to 0$ in equation (A.21) the correct amplitude of the fundamental frequency component is directly given by $K^2/2 \cdot J_1(\varphi_1)^2$.

A.3.2. Influence of noise

The correlation function needs to be extracted from a finite number of detection events in a real experiment, as discussed in section 2.2.1. It is calculated from the number of correlated particle pairs $N_{u,\tau}$ within a given window $\Delta\tau$ and Δu. Due to the statistical nature of the particles, $N_{u,\tau}$ is exposed to Poissonian noise, which is transmitted onto the correlation function and corresponding amplitude spectrum. This limits the signal-to-noise ratio and the minimum detectable perturbation amplitude.

This effect is estimated and optimal settings for the discretization step size are found in the following section. For simplicity, the calculation is limited to correlation times $\tau \ll T$ and positions $u \ll Y$. Using the numerical correlation function in equation (2.17), which is normalized to 1, it can be found that

$$g^{(2)}(u,\tau) = \frac{N_{u,\tau}}{\langle N_{u,\tau}\rangle} \quad \text{with} \quad \langle N_{u,\tau}\rangle = \frac{N^2\Delta\tau\Delta u}{TY}\ . \tag{A.22}$$

With $N_{u,\tau}$ following a Poissonian distribution, the variance of the correlation function yields

$$\sigma^2_{g^{(2)}} = \frac{1}{\langle N_{u,\tau}\rangle} = \frac{TY}{N^2\Delta\tau\Delta u} = \frac{N_\tau N_u}{N^2}\ , \tag{A.23}$$

with the number of bins in the temporal and spatial direction $N_\tau = T/\Delta\tau$ and $N_u = Y/\Delta u$. As expected, the variance (noise) of the correlation function depends on the total number of detected particles N. A detailed calculation of equation (A.23) is given in section 3.2.2 of publication [1].

With the assumption that the correlation function consists of an ideal part $g^{(2)}_{id}$ and a part $f(\tau)$ including the noise only, the discrete Fourier transform of the time discrete signal $f(\tau)$ is calculated to

$$\mathcal{F}(\omega) = \frac{1}{\tau_{\max}}\int_0^{\tau_{\max}} f(\tau)e^{i\omega\tau}d\tau = \frac{\Delta\tau}{\tau_{\max}}\sum_{n=1}^{N} f_n e^{i\omega t_n}\ , \tag{A.24}$$

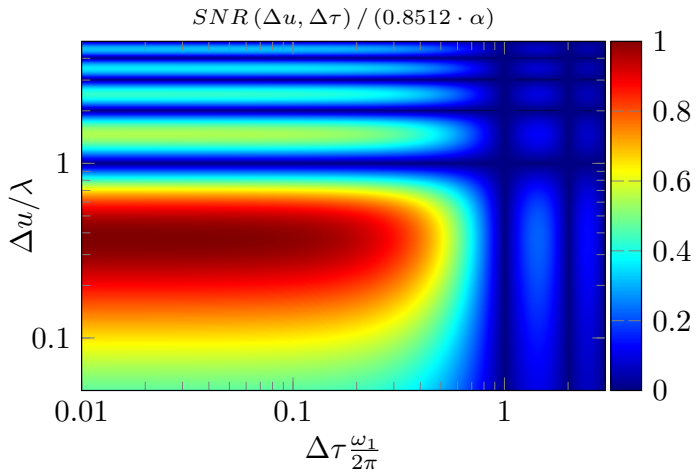

Figure A.3.: Signal-to-noise ratio calculated according to equation (A.26), normalized to α (equation (A.27)) and $f\left(k\frac{\Delta u_{\text{opt}}}{2}\right) = 0.8512$. At $\Delta u/\lambda = 0.371$, the optimum spatial discretization can be seen. Figure from [1].

with the maximum correlation time $\tau_{\max}$ up to which the correlation function is evaluated. The noise in the amplitude spectrum is thus solely included in $|\mathcal{F}(\omega)|$. Applying Parseval's theorem [219] together with $N_{\tau_{\max}} = \tau_{\max}/\Delta\tau$ and equation (A.23), the noise in the power spectrum is given by

$$\sigma^2_{|\mathcal{F}(\omega)|} = \left(1 - \frac{\pi}{4}\right) \frac{\sigma^2_{g^{(2)}}}{N_{\tau_{\max}}} = \left(1 - \frac{\pi}{4}\right) \frac{N_u}{N^2} \frac{T}{\tau_{\max}} \ . \tag{A.25}$$

A detailed derivation of equation (A.25) is given in section 3.2.2 of publication [1].

Using equation (A.20), (A.21), and (A.25), the signal-to-noise ratio $SNR\,(\Delta u, \Delta\tau)$ of the fundamental frequency component in the amplitude spectrum yields

$$SNR\,(\Delta u, \Delta\tau) = \alpha \cdot \frac{\sin\left(k\frac{\Delta u}{2}\right)}{\left(k\frac{\Delta u}{2}\right)^{\frac{1}{2}}} \operatorname{sinc}\left(\omega_1 \frac{\Delta\tau}{2}\right) \ , \tag{A.26}$$

with

$$\alpha = 0.6089 \cdot K^2 J_1(\varphi_1)^2 \cdot \frac{N\sqrt{\tau_{\max}/T}}{\sqrt{Y/\lambda}} \ . \tag{A.27}$$

The factor $\operatorname{sinc}\left(\omega_1\frac{\Delta\tau}{2}\right)$ converges to 1 for $\Delta\tau \to 0$ and the signal-to-noise ratio only depends on Δu. An optimum spatial discretization step size Δu_{opt} can be found at the position $k\frac{\Delta u_{\text{opt}}}{2} = 1.1656$, where the function $f\left(k\frac{\Delta u}{2}\right) = \sin\left(k\frac{\Delta u}{2}\right) / \left(k\frac{\Delta u}{2}\right)^{\frac{1}{2}}$ has a global maximum with the value of $f\left(k\frac{\Delta u_{\text{opt}}}{2}\right) = 0.8512$, yielding

$$\Delta u_{\text{opt}} = 0.371 \cdot \lambda \ . \tag{A.28}$$

The signal-to-noise ratio calculated according to equation (A.26) for different Δu and $\Delta\tau$ is shown in figure A.3. At the position $\Delta u/\lambda = 0.371$, the optimum spatial discretization step size can be identified.

For $\Delta u_{\text{opt}} = 0.371 \cdot \lambda$ and $\Delta\tau \to 0$ the optimum signal-to-noise ratio SNR_{opt} can be derived from equation (A.26) and (A.27). Setting SNR_{opt} equal to 1, a lower limit for

the determination of small peak phase deviations $\varphi_1 \ll 1$ can be found, at which signal and noise have an identical amplitude. With $J_1(\varphi_1)^2 \approx \varphi_1^2/4$, a minimum detectable peak phase deviation can be calculated

$$\varphi_{1,\min} = 0.8842\,\pi \cdot \frac{(Y/\lambda)^{\frac{1}{4}}}{K N^{\frac{1}{2}} (\tau_{\max}/T)^{\frac{1}{4}}} \ . \tag{A.29}$$

Thus, it is favourable to have an interference pattern with large contrast K and spatial periodicity λ for the measurement of small peak phase deviations. Furthermore, acquiring a large number of particles N reduces $\varphi_{1,\min}$.

Using a single-particle simulation of a perturbed interference pattern, the theoretical calculations in this section are numerically cross-checked in section 3.3 of publication [1]. Thereby, it could be shown that the theory and predicted optimum spatial discretization step size are valid.

The correlation analysis can not only be used for the description of discrete perturbation frequencies, but also for broad-band noise spectra. This is demonstrated in section 3.4 of publication [1] using a single-particle simulation of an interference pattern perturbed by a Gaussian distributed noise spectrum with random phases.

A.4. Biprism interferometry in the presence of oscillating magnetic and electric fields

Based on the following theoretical calculations, the design of the proposed electron biprism interferometer for sensor applications explained in appendix A.5 was developed. Here, the deflection of an interference pattern due to oscillating magnetic and electric fields is calculated and the achievable sensitivity for the measurement of small field strengths is estimated.

In figure A.4, the experimental situation is illustrated. The two electron paths (red dashed lines) are deflected by the biprism which is placed at the position $y = 0\,\mu\text{m}$ and $z = 0\,\text{cm}$ and superposed under the angle Θ in the interference plane. In this case no magnetic or electric field is applied ($B = 0$ and $E = 0$) and therefore, the paths are not shifted in the y-direction. The resulting interference pattern calculated with equation (1.1) is plotted on the right side of figure A.4 (red dashed line). These two paths are shifted in the y-direction (blue solid lines) by either a magnetic field with the field strength B oriented perpendicular to the y-z-plane or an electric field with the field strength E directed along the y-direction. Compared to the interference pattern for $B = 0$ and $E = 0$, the interference pattern of the deflected paths (blue solid line) is shifted by Δy. As discussed in section 1.1, this spatial shift corresponds to an interference pattern (equation (1.8)) shifted by the phase

$$\varphi_1 = k\Delta y = 2\pi \frac{\Delta y}{\lambda} \ , \tag{A.30}$$

with the spatial periodicity λ given by equation (1.7). For the magnetic and electric

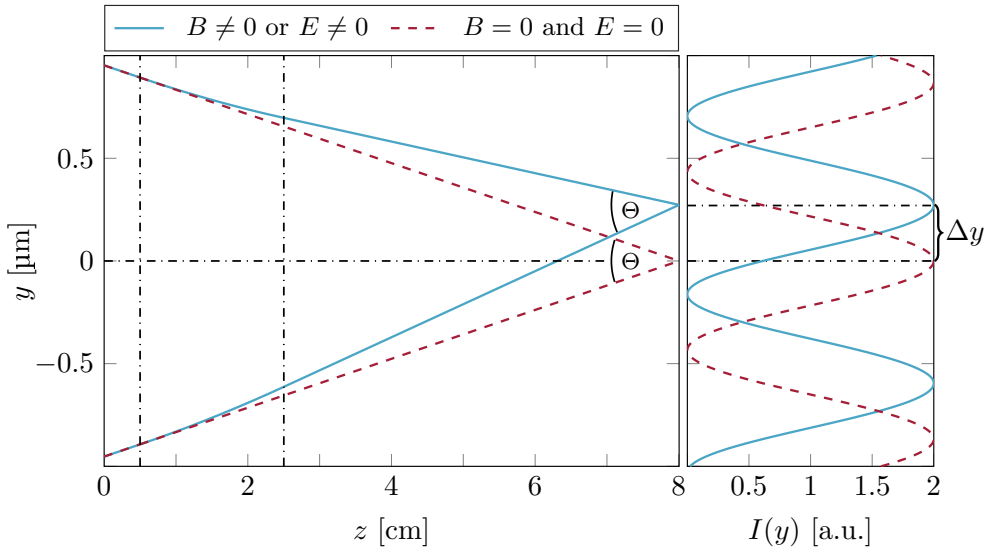

Figure A.4.: Illustration of the two electron paths between biprism (at $y = 0\,\mu\text{m}$ and $z = 0\,\text{cm}$) and interference plane ($z = 8\,\text{cm}$) without applied magnetic $B = 0$ and electric field $E = 0$ (red dashed lines) and for $B \neq 0$ or $E \neq 0$ (blue solid lines). The superposition angle Θ remains unchanged trough the deflection. The magnetic field is oriented perpendicular to the y-z-plane and the electric field along the y-direction. By the two vertical black chain lines the interaction region of the magnetic and electric field is indicated. On the right side the resulting interference patterns are plotted for $B = 0$ and $E = 0$ calculated with equation (1.1) (red dashed line) and $B \neq 0$ or $E \neq 0$ calculated with equation (1.8) (blue solid line). The spatial shift between the two interference patterns Δy corresponds to the phase shift φ_1 in equation (A.30).

field the spatial shift Δy can be calculated, yielding

$$\Delta y = \frac{1}{2}\sqrt{\frac{q}{2m}}\,\eta\,\frac{B}{\sqrt{U_{\text{acc}}}}\,, \tag{A.31}$$

$$\Delta y = \frac{1}{4}\,\eta\,\frac{E}{U_{\text{acc}}}\,, \tag{A.32}$$

with

$$\eta = l_{\text{i.a.}}^2\left(1 + 2\frac{l_{\text{d}}}{l_{\text{i.a.}}}\right)\,, \tag{A.33}$$

where $l_{\text{i.a.}}$ is the length of the interaction region and l_{d} the distance between interaction region and interference plane. For the measurement of small magnetic or electric fields it is therefore favorable to use electrons emitted with a small acceleration voltage U_{acc} to achieve a large spatial shift.

As low-energy electrons are sensitive to magnetic and electric fields, the following calculations are made for acceleration voltages of $U_{\text{acc}} = 50\,\text{V}$ and $U_{\text{acc}} = 1250\,\text{V}$. Using equation (1.3), the de Broglie wavelength of an electron for these voltages can be calculated, yielding $\lambda_{\text{dB}} = 170\,\text{pm}$ and $\lambda_{\text{dB}} = 34\,\text{pm}$, respectively. For this wavelengths the coherent emission angle α fulfilling the constraint in equation (1.2) is determined for a source diameter of $d_{\text{s}} = 5\,\text{nm}$ and one-twentieth of the wavelength: $\alpha = 0.05 \cdot \lambda_{\text{dB}}/2d_{\text{s}}$, resulting in $\alpha_{50\,\text{V}} = 8.5 \cdot 10^{-4}\,\text{rad}$ and $\alpha_{1250\,\text{V}} = 1.7 \cdot 10^{-4}\,\text{rad}$. Here, the factor of one-twentieth was chosen arbitrarily to satisfy the constraint in equation (1.2). With a

distance of $a = 2\,\mathrm{cm}$ between electron source and biprism the diameter of the coherent illuminated area can be determined using equation (1.4), yielding $s_{50\,\mathrm{V}} = 17\,\mu\mathrm{m}$ and $s_{1250\,\mathrm{V}} = 3.4\,\mu\mathrm{m}$ which is sufficiently large to measure electron interferences as the diameter of the biprism is $d_{\mathrm{bp}} = 0.4\,\mu\mathrm{m}$.

For an oscillating field, shifting the interference pattern periodically along the y-direction with $\Delta y(t) = \Delta y \cos(\omega_1 t + \phi_1)$ the phase shift of the interference pattern becomes time-dependent

$$\varphi(t) = k\Delta y(t) = \varphi_1 \cos(\omega_1 t + \phi_1) \ , \tag{A.34}$$

where ω_1 denotes the frequency of the oscillation, ϕ_1 the phase, and φ_1 the amplitude (peak phase deviation) given by equation (A.30). The perturbation parameters (φ_1, ω_1, and ϕ_1) obtained from the second-order correlation analysis discussed in this thesis are given by the properties of the oscillating magnetic and electric field. According to equation (A.30), the extracted perturbation amplitude φ_1 contains the field strength of the magnetic and electric field via Δy (equation (A.31) and (A.32)). For a given spatial shift Δy the peak phase deviation φ_1 in equation (A.30) can be increased by reducing the spatial periodicity λ of the interference pattern. According to equation (1.7), this can be achieved for a constant acceleration voltage, as Δy depends on U_{acc} (equation (A.31) and (A.32)), by increasing the voltage applied to the biprism. A large peak phase deviation φ_1 is favorable as in the correlation function higher orders of the Bessel function are taken into account. As a consequence, the signal in the correlation function and corresponding amplitude spectrum is larger whereby the identification of the perturbation parameters is relieved. Therefore, for the measurement of small field strengths B and E a small spatial periodicity is profitable as it increases the sensitivity of the biprism interferometer.

For a set of U_{acc} and U_{bp} the field strengths B and E can be determined with the perturbation amplitude φ_1 obtained from the correlation analysis using equation (A.30), (A.31), (A.32), and (1.7), yielding

$$B = \frac{h}{q}\frac{l}{a\gamma_0\eta}\frac{U_{\mathrm{acc}}}{U_{\mathrm{bp}}}\frac{\varphi_1}{\pi} \ , \tag{A.35}$$

$$E = \frac{\sqrt{2}h}{\sqrt{qm}}\frac{l}{a\gamma_0\eta}\frac{U_{\mathrm{acc}}^{\frac{3}{2}}}{U_{\mathrm{bp}}}\frac{\varphi_1}{\pi} \ . \tag{A.36}$$

As mentioned before, for a spatial shift of the interference pattern Δy given by the field strength and applied acceleration voltage (equation (A.31) and (A.32)) the peak phase deviation φ_1 in equation (A.30) can be adjusted in principle to any value by varying the spatial periodicity λ. Without changing Δy, which depends on U_{acc}, this can be achieved by varying the voltage applied to the biprism U_{bp} (equation (1.7)). After the determination of the perturbation characteristics by the correlation analysis the obtained peak phase deviation φ_1 is used in equation (A.35) or (A.36) together with the experimental parameters U_{acc} and U_{bp} to determine the field strength of the magnetic or electric field.

The maximum detectable frequency ω_{max} of the oscillating magnetic and electric field is given by one-tenth of the reciprocal value of the time that the particles spend

in the interaction region

$$\omega_{\max} = 2\pi \cdot 0.1 \frac{v}{l_{\text{i.a.}}} = 2\pi \cdot 0.1 \sqrt{\frac{2q}{m}} \frac{\sqrt{U_{\text{acc}}}}{l_{\text{i.a.}}} \ , \tag{A.37}$$

with the particle velocity v, the length of the interaction region $l_{\text{i.a.}}$, and the acceleration voltage U_{acc}. Here, the factor of one-tenth was chosen arbitrarily to satisfy the constraint that the flight time of the particles through the area of the perturbation has to be smaller than the periodic time of the detectable perturbation frequency.

To determine the sensitivity for the measurement of small magnetic and electric field strengths, the minimum detectable peak phase deviation $\varphi_{\min}$ has to be calculated in units of $\pi/\sqrt{\text{Hz}}$. As discussed in section A.3.2, the detectability of the fundamental frequency component in the amplitude spectrum depends on the parameters of the measurement. According to equation (A.26), (A.27), and (A.28), the optimum signal-to-noise ratio of the fundamental frequency component is given by

$$SNR_{\text{opt}} \left(\Delta u_{\text{opt}} = 0.371 \cdot \lambda_{\text{det}}, \Delta\tau \to 0\right) = 0.5183 \cdot K^2 J_1(\varphi)^2 \cdot \frac{N\sqrt{\tau_{\max}/T}}{\sqrt{Y/\lambda_{\text{det}}}} \ , \tag{A.38}$$

with the first order Bessel function of first kind J_1, the number of detected particles N, the maximum correlation time of the numerical correlation function $\tau_{\max}$, the acquisition time T and length Y, and the spatial periodicity of the interference pattern in the detection plane after magnification by the quadrupole lens λ_{det}. For a signal-to-noise ratio of $SNR_{\text{opt}} = 1$, the minimum detectable peak phase deviation can be determined from equation (A.38), yielding

$$J_1(\varphi_{\min}) = 0.4421\,\pi \cdot \frac{\left(Y/\lambda_{\text{det}}\right)^{\frac{1}{4}}}{K\sqrt{N}(\tau_{\max}/T)^{\frac{1}{4}}} \ . \tag{A.39}$$

Under the condition that the correlation function is evaluated for the complete acquisition time $\tau_{\max} = T = 1\,\text{s}$, the minimum detectable peak phase deviation $\varphi_{\min}$ in units of $\pi/\sqrt{\text{Hz}}$ is calculated from equation (A.39), resulting in

$$J_1(\varphi_{\min}) = 0.4421\,\pi \cdot \frac{\left(Y/\lambda_{\text{det}}\right)^{\frac{1}{4}}}{K\sqrt{cr}} \ , \tag{A.40}$$

with the mean particle count rate $cr = N/T$.

The sensitivity for the detection of small magnetic and electric field strengths can be calculated for different acceleration voltages U_{acc} and biprism voltages U_{bp}, according to equation (A.35) and (A.36). To determine $\varphi_{\min}$ from equation (A.40) for this calculation the contrast K and the count rate cr are estimated for each pair of U_{acc} and U_{bp}. For the count rate a model function is used that increases cr for increasing U_{acc}, similar to the Fowler-Nordheim equation [220, 221]. Here, count rates between $cr = 1\,\text{kHZ}$ for $U_{\text{acc}} = 50\,\text{V}$ to $cr = 5\,\text{kHZ}$ for $U_{\text{acc}} = 1250\,\text{V}$ were used for the calculations. As the contrast K depends on the spatial periodicity λ (equation (1.7)) a dependence between contrast K and the experimental parameters U_{acc} and U_{bp} can be found [195]

$$K(U_{\text{acc}}, U_{\text{bp}}) = \mathrm{e}^{-0.5\left(2\pi \frac{(l-a)}{a} \frac{d_s}{\lambda}\right)^2} = \mathrm{e}^{-0.5\left(\frac{\sqrt{2qm}}{\hbar} \frac{(l-a)\gamma_0}{l} d_s \frac{U_{\text{bp}}}{\sqrt{U_{\text{acc}}}}\right)^2} \ , \tag{A.41}$$

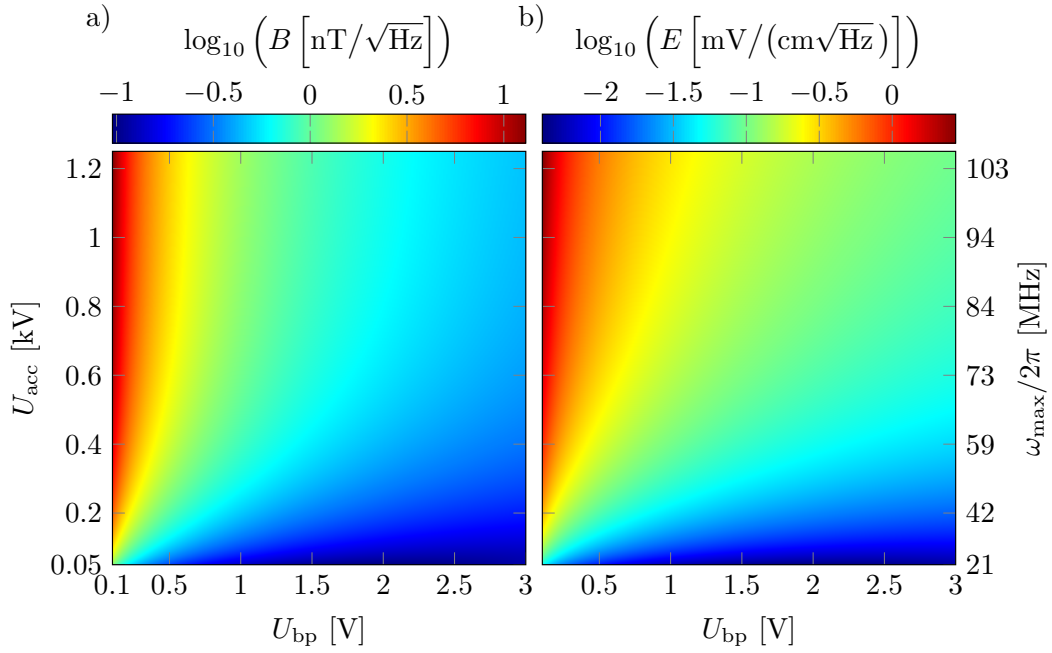

Figure A.5.: a) Sensitivity for the measurement of the minimum detectable magnetic field strengths B. It is calculated according to equation (A.35) for different U_{acc}, U_{bp}, and φ_{min} obtained from equation (A.40) with $Y = 20\,\mathrm{mm}$, $\lambda_{\mathrm{det}} = 2\,\mathrm{mm}$, and the estimated values for cr and K (equation (A.41)). b) Minimum detectable electric field strengths E calculated with equation (A.36) for the same values as in a). On the right side, the values for $\omega_{\mathrm{max}}/2\pi$ calculated with equation (A.37) correspond to U_{acc} on the left side. The parameters in equation (A.35) and (A.36) concerning the distances in the biprism interferometer are: distance source to interference plane: $l = 10\,\mathrm{cm}$, source to biprism: $a = 2\,\mathrm{cm}$, $\gamma_0 \approx 0.17$ (equation (1.6) for $R = 2\,\mathrm{mm}$ and $r_{\mathrm{bp}} = 200\,\mathrm{nm}$), length interaction region: $l_{\mathrm{i.a.}} = 2\,\mathrm{cm}$, and distance interaction region to interference plane: $l_{\mathrm{d}} = 5.5\,\mathrm{cm}$ (equation (A.33)).

with the distance between source and biprism $a = 2\,\mathrm{cm}$, the distance between source and interference plane $l = 10\,\mathrm{cm}$, and the source diameter $d_s = 5\,\mathrm{nm}$. For the calculations the resulting contrast varies between $K = 0.33$ for $U_{\mathrm{acc}} = 50\,\mathrm{V}$ and $U_{\mathrm{bp}} = 3\,\mathrm{V}$ to $K = 1$ for $U_{\mathrm{acc}} = 1250\,\mathrm{V}$ and $U_{\mathrm{bp}} = 0.1\,\mathrm{V}$.

With the obtained values for the minimum detectable peak phase deviation φ_{min} the sensitivity for the measurement of the minimum detectable magnetic field strengths B is calculated with equation (A.35) and plotted in figure A.5(a). The result for the electric field strengths E determined according to equation (A.36) is shown in figure A.5(b). The minimum detectable magnetic field strength B ranges from $95\,\mathrm{pT}/\sqrt{\mathrm{Hz}}$ ($U_{\mathrm{acc}} = 50\,\mathrm{V}$, $U_{\mathrm{bp}} = 3\,\mathrm{V}$, $\varphi_{\mathrm{min}} = 0.15\,\pi/\sqrt{\mathrm{Hz}}$) to $13\,\mathrm{nT}/\sqrt{\mathrm{Hz}}$ ($U_{\mathrm{acc}} = 1250\,\mathrm{V}$, $U_{\mathrm{bp}} = 0.1\,\mathrm{V}$, $\varphi_{\mathrm{min}} = 0.02\,\pi/\sqrt{\mathrm{Hz}}$) and the minimum detectable electric field strength E from $4\,\mu\mathrm{V}/\left(\mathrm{cm}\sqrt{\mathrm{Hz}}\right)$ to $2.7\,\mathrm{mV}/\left(\mathrm{cm}\sqrt{\mathrm{Hz}}\right)$ for the same experimental parameters. These values form the lower limit of the sensitivity for the detection of magnetic and electric field strengths as for each pair of U_{acc} and U_{bp} in figure A.5 also higher peak phase deviations and therefore, larger field strengths can be measured. In principle, there is no upper threshold for the detection of large peak phase deviations, also greater than 2π. On the right side of figure A.5, the values of the maximum detectable frequency

$\omega_{\max}/2\pi$ calculated with equation (A.37) correspond to the acceleration voltages U_{acc} on the left side. It ranges from 21 MHz for $U_{\text{acc}} = 50\,\text{V}$ to 105 MHz for $U_{\text{acc}} = 1250\,\text{V}$. The experimental parameters used here for the estimation of the sensitivity for the measurement of small electromagnetic fields are possible to be realized experimentally as demonstrated in former experiments [4, 9, 135].

To achieve a spatial periodicity of $\lambda_{\text{det}} = 2\,\text{mm}$ in the detection plane for an interference pattern with $\lambda = 85\,\text{nm}$ ($U_{\text{acc}} = 50\,\text{V}$ and $U_{\text{bp}} = 3\,\text{V}$ in equation (1.7)) it has to be magnified by $M = \lambda_{\text{det}}/\lambda \approx 23.5 \cdot 10^3$. This can be realized by applying a voltage of 65 V to a 2 cm long quadrupole lens followed by a 8 cm distance to the detection plane. Therefore, it is also favorable to use low-energy electrons as the created interference patterns can be magnified by one quadrupole lens with voltages that can be realized in an experimental setup. Additionally, the distance between quadrupole lens and detection plane can be reduced compared to other experiments [5, 8].

One interesting feature of the theoretical calculations made here is that the particle velocity v can also be determined in such an experimental setup. This can be shown by calculating the quotient of equation (A.35) and (A.36)

$$v = \sqrt{2\frac{q}{m}U_{\text{acc}}} = \frac{E}{B}\ . \tag{A.42}$$

For fixed experimental parameters U_{acc} and U_{bp} the peak phase deviation φ_1 determined from the correlation analysis has to be equal for the applied magnetic and electric field strength B and E to determine the velocity of the particles with equation (A.42). This means that the field strengths has to be adjusted in a way that the resulting peak phase deviation is identical for both measurements. If the corresponding constant fields would be applied together, the particles would not be deflected in the interaction region as illustrated in figure (A.4) (red dashed lines) as the resulting forces have the same value.

Based on the calculations made here a compact electron biprism interferometer is proposed in the next section using low-energy electrons emitted from a single-atom tip for the measurement of oscillating magnetic and electric fields.

A.5. Sensor for oscillating magnetic and electric fields

The proposed sensor for the measurement of oscillating magnetic and electric fields based on an electron biprism interferometer is illustrated schematically in figure A.6. To create low-energy electrons a very sharp SAT [94, 129] with a low minimum extraction voltage for electron emission is used in combination with two electrodes placed in front of it [9, 218]. The SAT is set on a negative voltage, the first electrode (counter electrode) on a positive voltage, and the second on ground. Between SAT and counter electrode the electrons are accelerated according to the applied voltages and decelerated afterwards between counter electrode and grounded electrode. The resulting electron energy after the grounded electrode is solely given by the applied voltage at the SAT [9]. With this arrangement electron energies lower than the energy defined by the minimum extraction voltage of the SAT can be realized. For this purpose, the SAT is set on a voltage lower than its minimum extraction voltage and the electron emission is initiated by applying a positive voltage to the counter electrode. Without changing

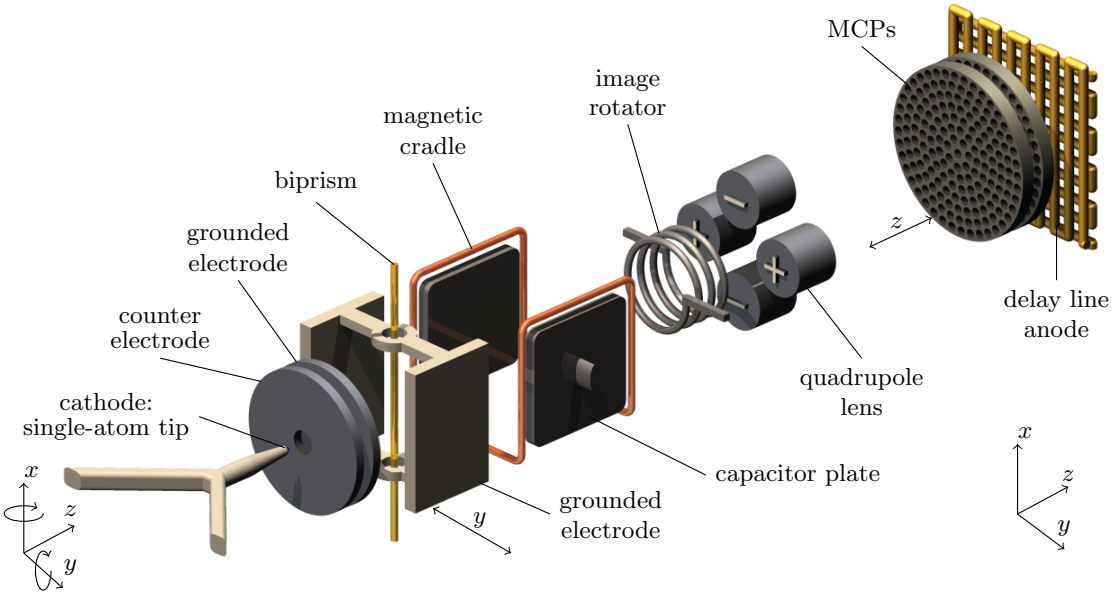

Figure A.6.: Schematic illustration (not to scale) of the proposed electron biprism interferometer used as a sensor for oscillating magnetic and electric fields. From the single-atom tip (SAT) mounted on a five-axis piezo positioner the electrons are field-emitted and adjusted onto the optical axis. In front of the SAT, the counter electrode can be used to increase the count rate by applying a positive voltage without changing the electron energy. The electron matter-wave is separated and recombined by the biprism which is mounted on a linear piezo positioner to align it onto the optical axis. An oscillating magnetic and electric field can be introduced by the magnetic cradle and the capacitor placed behind the biprism shifting the interference pattern along the y-direction perpendicular to the fringes. After the magnification of the interference pattern by the quadrupole lens it is measured with a delay line detector consisting of two MCPs and a delay line anode. The image rotator corrects possible misalignment of the biprism to the axis of the quadrupole lens. The distances between the parts of the interferometer can be found in appendix A.4.

the transversal and longitudinal coherence lengths of the electrons, the particle count rate can be raised by increasing the positive voltage applied to the counter electrode [9]. This is an advantage as the sensitivity for the measurement of small magnetic and electric field strengths depends on the count rate (equation (A.40)).

The SAT is mounted on a five-axis piezo positioner (linear displacement in x-, y- and z-direction, two dimensional tilt around x and y) to align the field-emitted electrons onto the optical axis. Additionally, the electrostatic biprism which separates and recombines the electron matter-wave by applying a positive voltage is placed on a piezo positioner aligning the biprism along the y-direction onto the optical axis. Both positioning systems make the use of deflector electrodes unnecessary. Generally, a Wien filter [198] is placed in a biprism interferometer to correct the longitudinal coherence influenced by the electrostatic potential of the deflector electrodes resulting in a contrast reduction of the interference pattern. Due to the absence of deflector electrodes in the proposed setup, a Wien filter is unnecessary. As discussed in section 1.1, the distance between SAT and biprism can be adjusted to satisfy the angular coherence constraint in equation (1.2) depending on the wavelength of the electrons (equation

(1.3)). Therefore, the proposed biprism interferometer can also be used for electron energies larger than 1250 eV by increasing the distance between SAT and biprism. This enables a more flexible setup used also with electrons emitted at higher acceleration voltages for which it is possible to measure higher perturbation frequencies (equation (A.37)).

The electron interference pattern is magnified by the quadrupole lens perpendicular to the fringes (along the y-direction) and detected with the delay line detector [127]. Possible misalignment of the biprism in the x-y-plane is corrected by the image rotator which aligns the interference pattern to the axis of the quadrupole lens. As explained in appendix A.4, for the measurement of small magnetic and electric field strengths interference patterns with small spatial periodicities have to be realized. To detect these it is necessary to achieve a large magnification with the quadrupole lens which is possible to realize with moderate voltages due to the use of low-energy electrons. Additionally, the distance between the exit of the quadrupole and the detector can be reduced which results in a more compact design of the proposed electron biprism interferometer.

To adjust the electron beam onto the optical axis of the quadrupole lens using the five-axis piezo positioner, it is favorable to use a movable detector that can be shifted along the z-direction [218]. For two displacements of the detector the position of the electron spot in the detection plane has to be identical for optimum adjustment. This is necessary as possible misalignment decreases the resolution of the quadrupole lens for the magnification of small spatial periodicities. After this adjustment, the biprism is moved along the y-direction onto the optical axis using the linear piezo positioner. Another benefit of this system is the variable distance between quadrupole lens and detection plane which can be increased to realize a larger magnification for the same voltage applied to the quadrupole lens. This reduces possible lens aberrations for high applied voltages. Further advantage of this system is that the distance can be increased if electrons with larger energies are used in the interferometer. For the same magnification as with low-energy electrons, higher voltages have to be applied to the quadrupole lens and the distance has to be increased. This makes the proposed setup more flexible to be used also for higher acceleration voltages for which larger perturbation frequencies can be determined (equation (A.37)).

As illustrated in figure A.6, behind the biprism a magnetic cradle and a capacitor are installed in the interferometer to generate the oscillating magnetic and electric fields [123]. The magnetic cradle consists of one wire arranged around a cube with 2 cm long edges. A magnetic field oriented along the x-direction is generated by the segments of the wire that are parallel to the y- and z-direction. On two sides of the cube capacitor plates are placed creating an electric field directed along the y-direction. Both fields shift the electron interference pattern periodically along the y-direction perpendicular to the fringes.

As discussed in section 1.1, the spatial periodicity of the interference pattern depends on the superposition angle (equation (1.7)). The sensitivity of the interferometer for the measurement of small field strengths can be increased by decreasing the spatial periodicity. Based on the large beam path separation in [6], a modified design of the proposed interferometer explained before is illustrated in figure A.7. Here, a second biprism is installed 4.8 cm behind the first one. For the alignment onto the optical

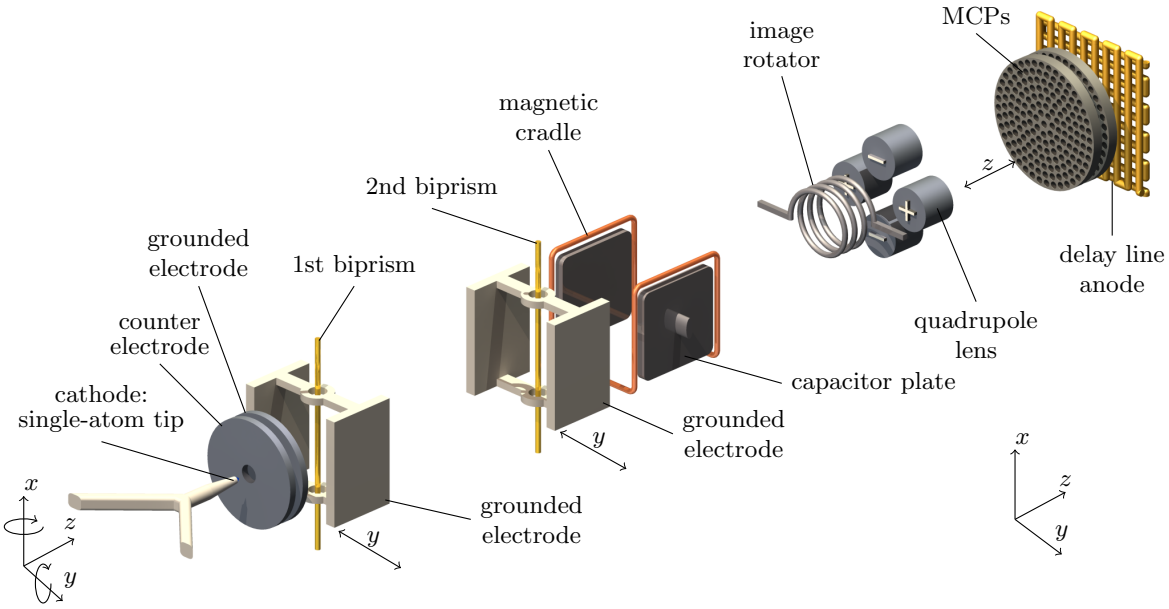

Figure A.7.: Schematic drawing (not to scale) of the modified design of the proposed electron biprism interferometer with a large beam path separation [6]. The second biprism is installed 4.8 cm behind the first one and mounted on a piezo positioner for the alignment onto the optical axis. By applying a negative voltage to the first biprism, the electron matter-wave is split into two partial matter-waves up to a distance of 300 µm at the position of the second biprism. The two partial matter-waves are recombined after the second biprism by applying a positive voltage.

axis it is also placed on a piezo positioner. By applying a negative voltage to the first biprism, the electron matter-wave is split in two partial matter-waves separated up to a distance of 300 µm at the position of the second biprism. The two partial matter-waves are recombined by applying a positive voltage to the second biprism creating the interference pattern. With this setup the superposition angle can be increased by two orders of magnitude and therefore, the spatial periodicity can be decreased by the same magnitude. For electron energies from 50 eV to 1250 eV it could be possible to measure oscillating fields with a sensitivity for magnetic field strengths in the $\mathrm{fT}/\sqrt{\mathrm{Hz}}$-region and for electric field strengths in the $\mathrm{nV}/\left(\mathrm{cm}\sqrt{\mathrm{Hz}}\right)$-region. With low-energy electrons it should be possible to magnify the created interference patterns with spatial periodicities of a few nm.

Bibliography

[1] A. Rembold, R. Röpke, G. Schütz, J. Fortágh, A. Stibor, and A. Günther, "Second-order correlations in single-particle interferometry", New Journal of Physics **19**, 103029 (2017).

[2] A. Rembold, G. Schütz, W. T. Chang, A. Stefanov, A. Pooch, I. S. Hwang, A. Günther, and A. Stibor, "Correction of dephasing oscillations in matter-wave interferometry", Physical Review A **89**, 033635 (2014).

[3] A. Günther, A. Rembold, G. Schütz, and A. Stibor, "Multifrequency perturbations in matter-wave interferometry", Physical Review A **92**, 053607 (2015).

[4] A. Rembold, G. Schütz, R. Röpke, W. T. Chang, I. S. Hwang, A. Günther, and A. Stibor, "Vibrational dephasing in matter-wave interferometers", New Journal of Physics **19**, 033009 (2017).

[5] G. Schütz, A. Rembold, A. Pooch, S. Meier, P. Schneeweiss, A. Rauschenbeutel, A. Günther, W. T. Chang, I. S. Hwang, and A. Stibor, "Biprism electron interferometry with a single atom tip source", Ultramicroscopy **141**, 9 (2014).

[6] G. Schütz, A. Rembold, A. Pooch, H. Prochel, and A. Stibor, "Effective beam separation schemes for the measurement of the electric Aharonov–Bohm effect in an ion interferometer", Ultramicroscopy **158**, 65 (2015).

[7] G. Schütz, A. Rembold, A. Pooch, W. T. Chang, and A. Stibor, "Electron matter wave interferences at high vacuum pressures", Measurement **68**, 201 (2015).

[8] A. Pooch, M. Seidling, M. Layer, A. Rembold, and A. Stibor, "A compact electron matter wave interferometer for sensor technology", Applied Physics Letters **110**, 223108 (2017).

[9] A. Pooch, M. Seidling, N. Kerker, R. Röpke, A. Rembold, W. T. Chang, I. S. Hwang, and A. Stibor, "Coherent properties of a tunable low-energy electron-matter-wave source", arXiv:1705.10383 , accepted for publication in Physical Review A (2018).

[10] T. Young, "Experimental demonstration of the general law of the interference of light", Philosophical Transactions of the Royal Society of London **94**, 1 (1804).

[11] J. C. Jamin, "Neuer Interferential-Refractor", Annalen der Physik und Chemie **98**, 345 (1856).

[12] A. A. Michelson and E. W. Morley, "On the Relative Motion of the Earth and of the Luminiferous Ether", American Journal of Science **34**, 333 (1887).

[13] L. Zehnder, "Ein neuer Interferenzrefraktor", Zeitschrift für Instrumentenkunde **11**, 275 (1891).

[14] L. Mach, "Ueber einen Interferenzrefraktor", Zeitschrift für Instrumentenkunde **12**, 89 (1892).

[15] A. Pérot and C. Fabry, "On the Application of Interference Phenomena to the Solution of Various Problems of Spectroscopy and Metrology", The Astrophysical Journal **9**, 87 (1899).

[16] I. Newton, "New Theory about Light and Colours", Philosophical Transactions (1665-1678) **6**, 3075 (1671).

[17] M. Planck, "Ueber das Gesetz der Energieverteilung im Normalspectrum", Annalen der Physik **309**, 553 (1901).

[18] A. Einstein, "Über einen die Erzeugung und Verwandlung des Lichtes betreffenden heuristischen Gesichtspunkt", Annalen der Physik **17**, 132 (1905).

[19] A. H. Compton, "A Quantum Theory of the Scattering of X-rays by Light Elements", Physical Review **21**, 483 (1923).

[20] L. de Broglie, "A Tentative Theory of Light Quanta", Philosophical Magazine **47**, 446 (1924).

[21] W. Heisenberg, "Über quantentheoretische Umdeutung kinematischer und mechanischer Beziehungen", Zeitschrift für Physik **33**, 879 (1925).

[22] E. Schrödinger, "Quantisierung als Eigenwertproblem", Annalen der Physik **79**, 361 (1926).

[23] P. A. M. Dirac, "The quantum theory of the electron", in *Proceedings of the Royal Society of London A: Mathematical, Physical and Engineering Sciences*, Vol. 117 (The Royal Society, 1928) pp. 610–624.

[24] C. J. Davisson and L. H. Germer, "The scattering of electrons by a single crystal of nickel", Nature **119**, 558 (1927).

[25] G. P. Thomson and A. Reid, "Diffraction of cathode rays by a thin film", Nature **119**, 890 (1927).

[26] I. Estermann and O. Stern, "Beugung von Molekularstrahlen", Zeitschrift für Physik A Hadrons and Nuclei **61**, 95 (1930).

[27] H. Boersch, "Fresnelsche Elektronenbeugung", Naturwissenschaften **28**, 709 (1940).

[28] G. Möllenstedt and H. Düker, "Fresnelscher Interferenzversuch mit einem Biprisma für Elektronenwellen", Naturwissenschaften **42**, 41 (1955).

[29] G. Möllenstedt and H. Düker, "Beobachtungen und Messungen an Biprisma-Interferenzen mit Elektronenwellen", Zeitschrift für Physik **145**, 377 (1956).

[30] F. Hasselbach, "Progress in electron- and ion-interferometry", Reports on Progress in Physics **73**, 016101 (2009).

[31] A. Tonomura, "Applications of electron holography", Reviews of Modern Physics **59**, 639 (1987).

[32] C. Jönsson, "Elektroneninterferenzen an mehreren künstlich hergestellten Feinspalten", Zeitschrift für Physik **161**, 454 (1961).

[33] "The most beautiful experiment", PhysicsWorld **September**, 15 (2002).

[34] U. Bonse and M. Hart, "An x-ray interferometer with long separated interfering beam paths", Applied Physics Letters **7**, 99 (1965).

[35] H. Rauch, W. Treimer, and U. Bonse, "Test of a single crystal neutron interferometer", Physics Letters A **47**, 369 (1974).

[36] R. Colella, A. W. Overhauser, and S. A. Werner, "Observation of Gravitationally Induced Quantum Interference", Physical Review Letters **34**, 1472 (1975).

[37] A. Zeilinger, R. Gähler, C. G. Shull, W. Treimer, and W. Mampe, "Single- and double-slit diffraction of neutrons", Reviews of Modern Physics **60**, 1067 (1988).

[38] J. A. Leavitt and F. A. Bills, "Single-slit diffraction pattern of a thermal atomic potassium beam", American Journal of Physics **37**, 905 (1969).

[39] P. E. Moskowitz, P. L. Gould, S. R. Atlas, and D. E. Pritchard, "Diffraction of an Atomic Beam by Standing-Wave Radiation", Physical Review Letters **51**, 370 (1983).

[40] D. W. Keith, M. L. Schattenburg, H. I. Smith, and D. E. Pritchard, "Diffraction of Atoms by a Transmission Grating", Physical Review Letters **61**, 1580 (1988).

[41] O. Carnal and J. Mlynek, "Young's double-slit experiment with atoms: A simple atom interferometer", Physical Review Letters **66**, 2689 (1991).

[42] J. F. Clauser, "Ultra-high sensitivity accelerometers and gyroscopes using neutral atom matter-wave interferometry", Physica B **151**, 262 (1988).

[43] D. W. Keith, C. R. Ekstrom, Q. A. Turchette, and D. E. Pritchard, "An Interferometer for Atoms", Physical Review Letters **66**, 2693 (1991).

[44] M. Kasevich and S. Chu, "Atomic Interferometry Using Stimulated Raman Transitions", Physical Review Letters **67**, 181 (1991).

[45] D. S. Weiss, B. C. Young, and S. Chu, "Precision Measurement of the Photon Recoil of an Atom Using Atomic Interferometry", Physical Review Letters **70**, 2706 (1993).

[46] C. R. Ekstrom, J. Schmiedmayer, M. S. Chapman, T. D. Hammond, and D. E. Pritchard, "Measurement of the electric polarizability of sodium with an atom interferometer", Physical Review A **51**, 3883 (1995).

[47] T. L. Gustavson, P. Bouyer, and M. A. Kasevich, "Precision Rotation Measurements with an Atom Interferometer Gyroscope", Physical Review Letters **78**, 2046 (1997).

[48] A. Peters, K. Y. Chung, and S. Chu, "Measurement of gravitational acceleration by dropping atoms", Nature **400**, 849 (1999).

[49] M. H. Anderson, J. R. Ensher, M. R. Matthews, C. E. Wieman, and E. A. Cornell, "Observation of Bose-Einstein Condensation in a Dilute Atomic Vapor", Science **269**, 198 (1995).

[50] K. B. Davis, M.-O. Mewes, M. R. Andrews, N. J. van Druten, D. S. Durfee, D. M. Kurn, and W. Ketterle, "Bose-Einstein Condensation in a Gas of Sodium Atoms", Physical Review Letters **75**, 3969 (1995).

[51] C. C. Bradley, C. A. Sackett, J. J. Tollett, and R. G. Hulet, "Evidence of Bose-Einstein Condensation in an Atomic Gas with Attractive Interactions", Physical Review Letters **75**, 1687 (1995).

[52] M. R. Andrews, C. G. Townsend, H.-J. Miesner, D. S. Durfee, D. M. Kurn, and W. Ketterle, "Observation of Interference Between Two Bose Condensates", Science **275**, 637 (1997).

[53] W. Schöllkopf and J. P. Toennies, "Nondestructive Mass Selection of Small van der Waals Clusters", Science **266**, 1345 (1994).

[54] M. Arndt, O. Nairz, J. Vos-Andreae, C. Keller, G. Van der Zouw, and A. Zeilinger, "Wave–particle duality of C_{60} molecules", Nature **401**, 680 (1999).

[55] B. Brezger, L. Hackermüller, S. Uttenthaler, J. Petschinka, M. Arndt, and A. Zeilinger, "Matter-Wave Interferometer for Large Molecules", Physical Review Letters **88**, 100404 (2002).

[56] P. W. Graham, J. M. Hogan, M. A. Kasevich, and S. Rajendran, "New Method for Gravitational Wave Detection with Atomic Sensors", Physical Review Letters **110**, 171102 (2013).

[57] J. Rodewald, P. Haslinger, N. Dörre, B. A. Stickler, A. Shayeghi, K. Hornberger, and M. Arndt, "New avenues for matter-wave-enhanced spectroscopy", Applied Physics B **123**, 3 (2017).

[58] K. S. Hardman, P. J. Everitt, G. D. McDonald, P. Manju, P. B. Wigley, M. A. Sooriyabandara, C. C. N. Kuhn, J. E. Debs, J. D. Close, and N. P. Robins, "Simultaneous Precision Gravimetry and Magnetic Gradiometry with a Bose-Einstein Condensate: A High Precision, Quantum Sensor", Physical Review Letters **117**, 138501 (2016).

[59] B. P. Abbott, R. Abbott, T. D. Abbott, M. R. Abernathy, F. Acernese, K. Ackley, C. Adams, T. Adams, P. Addesso, R. X. Adhikari, *et al.*, "Observation of Gravitational Waves from a Binary Black Hole Merger", Physical Review Letters **116**, 061102 (2016).

[60] M. Armano, H. Audley, G. Auger, J. T. Baird, M. Bassan, P. Binetruy, M. Born, D. Bortoluzzi, N. Brandt, M. Caleno, *et al.*, "Sub-Femto-g Free Fall for Space-Based Gravitational Wave Observatories: LISA Pathfinder Results", Physical Review Letters **116**, 231101 (2016).

[61] R. B. Hurst, M. Mayerbacher, A. Gebauer, K. U. Schreiber, and J.-P. R. Wells, "High-accuracy absolute rotation rate measurements with a large ring laser gyro: establishing the scale factor", Applied Optics **56**, 1124 (2017).

[62] A. D. Cronin, J. Schmiedmayer, and D. E. Pritchard, "Optics and interferometry with atoms and molecules", Reviews of Modern Physics **81**, 1051 (2009).

[63] Y. Margalit, Z. Zhou, S. Machluf, D. Rohrlich, Y. Japha, and R. Folman, "A self-interfering clock as a "which path" witness", Science **349**, 1205 (2015).

[64] M. Arndt and C. Brand, "Interference of atomic clocks", Science **349**, 1168 (2015).

[65] B. Barrett, L. Antoni-Micollier, L. Chichet, B. Battelier, T. Lévèque, A. Landragin, and P. Bouyer, "Dual matter-wave inertial sensors in weightlessness", Nature Communications **7**, 13786 (2016).

[66] T. Kovachy, P. Asenbaum, C. Overstreet, C. A. Donnelly, S. M. Dickerson, A. Sugarbaker, J. M. Hogan, and M. A. Kasevich, "Quantum superposition at the half-metre scale", Nature **528**, 530 (2015).

[67] S. M. Dickerson, J. M. Hogan, A. Sugarbaker, D. M. S. Johnson, and M. A. Kasevich, "Multiaxis Inertial Sensing with Long-Time Point Source Atom Interferometry", Physical Review Letters **111**, 083001 (2013).

[68] H. Rauch and S. A. Werner, *Neutron Interferometry: Lessons in Experimental Quantum Mechanics, Wave-Particle Duality, and Entanglement* (Oxford University Press, USA, 2015).

[69] M. Zawisky, M. Baron, R. Loidl, and H. Rauch, "Testing the world's largest monolithic perfect crystal neutron interferometer", Nuclear Instruments and Methods in Physics Research Section A: Accelerators, Spectrometers, Detectors and Associated Equipment **481**, 406 (2002).

[70] J. Klepp, S. Sponar, and Y. Hasegawa, "Fundamental phenomena of quantum mechanics explored with neutron interferometers", Progress of Theoretical and Experimental Physics **2014**, 082A01 (2014).

[71] J. R. Anglin and W. Ketterle, "Bose–Einstein condensation of atomic gases", Nature **416**, 211 (2002).

[72] T. Schumm, S. Hofferberth, L. M. Andersson, S. Wildermuth, S. Groth, I. Bar-Joseph, J. Schmiedmayer, and P. Krüger, "Matter-wave interferometry in a double well on an atom chip", Nature Physics **1**, 57 (2005).

[73] C. Kohstall, S. Riedl, E. R. S. Guajardo, L. A. Sidorenkov, J. Hecker Denschlag, and R. Grimm, "Observation of interference between two molecular Bose–Einstein condensates", New Journal of Physics **13**, 065027 (2011).

[74] T. Berrada, S. van Frank, R. Bücker, T. Schumm, J.-F. Schaff, and J. Schmiedmayer, "Integrated Mach–Zehnder interferometer for Bose–Einstein condensates", Nature Communications **4**, 2077 (2013).

[75] H. Müntinga, H. Ahlers, M. Krutzik, A. Wenzlawski, S. Arnold, D. Becker, K. Bongs, H. Dittus, H. Duncker, N. Gaaloul, *et al.*, "Interferometry with Bose-Einstein Condensates in Microgravity", Physical Review Letters **110**, 093602 (2013).

[76] R. E. Grisenti, W. Schöllkopf, J. P. Toennies, G. C. Hegerfeldt, T. Köhler, and M. Stoll, "Determination of the Bond Length and Binding Energy of the Helium Dimer by Diffraction from a Transmission Grating", Physical Review Letters **85**, 2284 (2000).

[77] S. Gerlich, L. Hackermüller, K. Hornberger, A. Stibor, H. Ulbricht, M. Gring, F. Goldfarb, T. Savas, M. Müri, M. Mayor, *et al.*, "A Kapitza–Dirac–Talbot–Lau interferometer for highly polarizable molecules", Nature Physics **3**, 711 (2007).

[78] M. Arndt and K. Hornberger, "Testing the limits of quantum mechanical superpositions", Nature Physics **10**, 271 (2014).

[79] S. Gerlich, S. Eibenberger, M. Tomandl, S. Nimmrichter, K. Hornberger, P. J. Fagan, J. Tüxen, M. Mayor, and M. Arndt, "Quantum interference of large organic molecules", Nature Communications **2**, 263 (2011).

[80] T. Juffmann, A. Milic, M. Müllneritsch, P. Asenbaum, A. Tsukernik, J. Tüxen, M. Mayor, O. Cheshnovsky, and M. Arndt, "Real-time single-molecule imaging of quantum interference", Nature Nanotechnology **7**, 297 (2012).

[81] S. Eibenberger, S. Gerlich, M. Arndt, M. Mayor, and J. Tüxen, "Matter–wave interference of particles selected from a molecular library with masses exceeding 10000 amu", Physical Chemistry Chemical Physics **15**, 14696 (2013).

[82] W. H. Zurek, "Decoherence, einselection, and the quantum origins of the classical", Reviews of Modern Physics **75**, 715 (2003).

[83] K. Hornberger, S. Uttenthaler, B. Brezger, L. Hackermüller, M. Arndt, and A. Zeilinger, "Collisional Decoherence Observed in Matter Wave Interferometry", Physical Review Letters **90**, 160401 (2003).

[84] K. Walter, B. A. Stickler, and K. Hornberger, "Collisional decoherence of polar molecules", Physical Review A **93**, 063612 (2016).

[85] L. Hackermüller, K. Hornberger, B. Brezger, A. Zeilinger, and M. Arndt, "Decoherence of matter waves by thermal emission of radiation", Nature **427**, 711 (2004).

[86] K. Hornberger, L. Hackermüller, and M. Arndt, "Influence of molecular temperature on the coherence of fullerenes in a near-field interferometer", Physical Review A **71**, 023601 (2005).

[87] J. P. Cotter, S. Eibenberger, L. Mairhofer, X. Cheng, P. Asenbaum, M. Arndt, K. Walter, S. Nimmrichter, and K. Hornberger, "Coherence in the presence of absorption and heating in a molecule interferometer", Nature Communications **6**, 7336 (2015).

[88] K. Hornberger, S. Gerlich, P. Haslinger, S. Nimmrichter, and M. Arndt, "*Colloquium*: Quantum interference of clusters and molecules", Review of Modern Physics **84**, 157 (2012).

[89] T. Juffmann, H. Ulbricht, and M. Arndt, "Experimental methods of molecular matter-wave optics", Reports on Progress in Physics **76**, 086402 (2013).

[90] M. Berninger, A. Stefanov, S. Deachapunya, and M. Arndt, "Polarizability measurements of a molecule via a near-field matter-wave interferometer", Physical Review A **76**, 013607 (2007).

[91] P. Haslinger, N. Dörre, P. Geyer, J. Rodewald, S. Nimmrichter, and M. Arndt, "A universal matter-wave interferometer with optical ionization gratings in the time domain", Nature Physics **9**, 144 (2013).

[92] W. P. Putnam and M. F. Yanik, "Noninvasive electron microscopy with interaction-free quantum measurements", Physical Review A **80**, 040902 (2009).

[93] P. Kruit, R. G. Hobbs, C.-S. Kim, Y. Yang, V. R. Manfrinato, J. Hammer, S. Thomas, P. Weber, B. Klopfer, C. Kohstall, *et al.*, "Designs for a quantum electron microscope", Ultramicroscopy **164**, 31 (2016).

[94] H.-S. Kuo, I.-S. Hwang, T.-Y. Fu, Y.-C. Lin, C.-C. Chang, and T. T. Tsong, "Noble metal/W (111) single-atom tips and their field electron and ion emission characteristics", Japanese Journal of Applied Physics **45**, 8972 (2006).

[95] G. Herink, D. R. Solli, M. Gulde, and C. Ropers, "Field-driven photoemission from nanostructures quenches the quiver motion", Nature **483**, 190 (2012).

[96] D. Ehberger, J. Hammer, M. Eisele, M. Krüger, J. Noe, A. Högele, and P. Hommelhoff, "Highly Coherent Electron Beam from a Laser-Triggered Tungsten Needle Tip", Physical Review Letters **114**, 227601 (2015).

[97] M. Gulde, S. Schweda, G. Storeck, M. Maiti, H. K. Yu, A. M. Wodtke, S. Schäfer, and C. Ropers, "Ultrafast low-energy electron diffraction in transmission resolves polymer/graphene superstructure dynamics", Science **345**, 200 (2014).

[98] T. Latychevskaia, W.-H. Hsu, W.-T. Chang, C.-Y. Lin, and I.-S. Hwang, "Three-dimensional surface topography of graphene by divergent beam electron diffraction", Nature Communications **8**, 14440 (2017).

[99] J.-N. Longchamp, T. Latychevskaia, C. Escher, and H.-W. Fink, "Low-energy electron holographic imaging of individual tobacco mosaic virions", Applied Physics Letters **107**, 133101 (2015).

[100] F. Hasselbach, "A ruggedized miniature UHV electron biprism interferometer for new fundamental experiments and applications", Zeitschrift für Physik B Condensed Matter **71**, 443 (1988).

[101] U. Maier, *Ein Biprisma-Interferometer für Ionen*, Ph.D. thesis, Universität Tübingen (1997).

[102] F. Hasselbach and U. Maier, "Quantum Coherence and Decoherence", ISQM-Tokyo 98 ed Y. Y. Ono and K. Fujikawa (Amsterdam: Elsevier) , 299 (1999).

[103] Y. Aharonov and D. Bohm, "Significance of Electromagnetic Potentials in the Quantum Theory", Physical Review **115**, 485 (1959).

[104] H. Batelaan and A. Tonomura, "The Aharonov–Bohm effects: Variations on a subtle theme", Physics Today **62**, 38 (2009).

[105] G. Möllenstedt and W. Bayh, "Elektronen-Biprisma-Interferenzen mit weit getrennten kohärenten Teilbündeln", Naturwissenschaften **48**, 400 (1961).

[106] R. G. Chambers, "Shift of an Electron Interference Pattern by Enclosed Magnetic Flux", Physical Review Letters **5**, 3 (1960).

[107] W. Bayh, *Messung der kontinuierlichen Phasenschiebung von Elektronenwellen im kraftfreien Raum durch das magnetische Vektorpotential einer Wolfram-Wendel*, Ph.D. thesis, Universität Tübingen (1962).

[108] G. Möllenstedt and W. Bayh, "Messung der kontinuierlichen Phasenschiebung von Elektronenwellen im kraftfeldfreien Raum durch das magnetische Vektorpotential einer Luftspule", Naturwissenschaften **49**, 81 (1962).

[109] G. Möllenstedt and W. Bayh, "Kontinuierliche Phasenschiebung von Elektronenwellen im kraftfeldfreien Raum durch das magnetische Vektorpotential eines Solenoids", Physikalische Blätter **18**, 299 (1962).

[110] H. Schmid, *Ein Elektronen-Interferometer mit 300 µm weit getrennten kohärenten Teilbündeln zur Erzeugung hoher Gangunterschiede und Messung der Phasenschiebung durch das magnetische Vektorpotential bei metallisch abgeschirmtem Magnetfluss*, Ph.D. thesis, Universität Tübingen (1985).

[111] A. Tonomura, N. Osakabe, T. Matsuda, T. Kawasaki, J. Endo, S. Yano, and H. Yamada, "Evidence for Aharonov-Bohm effect with magnetic field completely shielded from electron wave", Physical Review Letters **56**, 792 (1986).

[112] M. Nicklaus, *Ein Sagnac-Experiment mit Elektronenwellen*, Ph.D. thesis, Universität Tübingen (1989).

[113] F. Hasselbach and M. Nicklaus, "Sagnac experiment with electrons: Observation of the rotational phase shift of electron waves in vacuum", Physical Review A **48**, 143 (1993).

[114] P. Sonnentag, *Ein Experiment zur kontrollierten Dekohärenz in einem Elektronen-Biprisma-Interferometer*, Ph.D. thesis, Universität Tübingen (2006).

[115] P. Sonnentag and F. Hasselbach, "Measurement of Decoherence of Electron Waves and Visualization of the Quantum-Classical Transition", Physical Review Letters **98**, 200402 (2007).

[116] J. R. Anglin, J. P. Paz, and W. H. Zurek, "Deconstructing decoherence", Physical Review A **55**, 4041 (1997).

[117] S. Scheel and S. Y. Buhmann, "Path decoherence of charged and neutral particles near surfaces", Physical Review A **85**, 030101 (2012).

[118] D. L. Freimund, K. Aflatooni, and H. Batelaan, "Observation of the Kapitza–Dirac effect", Nature **413**, 142 (2001).

[119] P. L. Kapitza and P. A. M. Dirac, "The reflection of electrons from standing light waves", Mathematical Proceedings of the Cambridge Philosophical Society **29**, 297 (1933).

[120] H. Batelaan, "*Colloquium*: Illuminating the Kapitza-Dirac effect with electron matter optics", Reviews of Modern Physics **79**, 929 (2007).

[121] H. F. Talbot, "Facts relating to optical science", The London and Edinburgh Philosophical Magazine and Journal of Science **9**, 401 (1836).

[122] E. Lau, "Beugungserscheinungen an Doppelrastern", Annalen der Physik **6**, 417 (1948).

[123] R. Bach, G. Gronniger, and H. Batelaan, "An electron Talbot-Lau interferometer and magnetic field sensing", Applied Physics Letters **103**, 254102 (2013).

[124] J. Hammer, J. Hoffrogge, S. Heinrich, and P. Hommelhoff, "Phase-Resolved Electron Guiding in Optimized Chip-Based Microwave Potentials", Physical Review Applied **2**, 044015 (2014).

[125] J. Hammer, S. Thomas, P. Weber, and P. Hommelhoff, "Microwave Chip-Based Beam Splitter for Low-Energy Guided Electrons", Physical Review Letters **114**, 254801 (2015).

[126] B. Cho, T. Ichimura, R. Shimizu, and C. Oshima, "Quantitative Evaluation of Spatial Coherence of the Electron Beam from Low Temperature Field Emitters", Physical Review Letters **92**, 246103 (2004).

[127] O. Jagutzki, V. Mergel, K. Ullmann-Pfleger, L. Spielberger, U. Spillmann, R. Dörner, and H. Schmidt-Böcking, "A broad-application microchannel-plate

detector system for advanced particle or photon detection tasks: large area imaging, precise multi-hit timing information and high detection rate", Nuclear Instruments and Methods in Physics Research Section A: Accelerators, Spectrometers, Detectors and Associated Equipment **477**, 244 (2002).

[128] T.-Y. Fu, L.-C. Cheng, C.-H. Nien, and T. T. Tsong, "Method of creating a Pd-covered single-atom sharp W pyramidal tip: Mechanism and energetics of its formation", Physical Review B **64**, 113401 (2001).

[129] H.-S. Kuo, I.-S. Hwang, T.-Y. Fu, Y.-H. Lu, C.-Y. Lin, and T. T. Tsong, "Gas field ion source from an Ir/ W⟨111⟩ single-atom tip", Applied Physics Letters **92**, 063106 (2008).

[130] N. de Jonge, Y. Lamy, K. Schoots, and T. H. Oosterkamp, "High brightness electron beam from a multi-walled carbon nanotube", Nature **420**, 393 (2002).

[131] N. de Jonge, M. Allioux, J. T. Oostveen, K. B. K. Teo, and W. I. Milne, "Optical Performance of Carbon-Nanotube Electron Sources", Physical Review Letters **94**, 186807 (2005).

[132] P. Hommelhoff, Y. Sortais, A. Aghajani-Talesh, and M. A. Kasevich, "Field Emission Tip as a Nanometer Source of Free Electron Femtosecond Pulses", Physical Review Letters **96**, 077401 (2006).

[133] P. Hommelhoff, C. Kealhofer, and M. A. Kasevich, "Ultrafast Electron Pulses from a Tungsten Tip Triggered by Low-Power Femtosecond Laser Pulses", Physical Review Letters **97**, 247402 (2006).

[134] M. Krüger, M. Schenk, and P. Hommelhoff, "Attosecond control of electrons emitted from a nanoscale metal tip", Nature **475**, 78 (2011).

[135] C.-C. Chang, H.-S. Kuo, I.-S. Hwang, and T. T. Tsong, "A fully coherent electron beam from a noble-metal covered W(111) single-atom emitter", Nanotechnology **20**, 115401 (2009).

[136] I.-S. Hwang, C.-C. Chang, C.-H. Lu, S.-C. Liu, Y.-C. Chang, T.-K. Lee, H.-T. Jeng, H.-S. Kuo, C.-Y. Lin, C.-S. Chang, *et al.*, "Investigation of single-walled carbon nanotubes with a low-energy electron point projection microscope", New Journal of Physics **15**, 043015 (2013).

[137] A. Stibor, K. Hornberger, L. Hackermüller, A. Zeilinger, and M. Arndt, "Talbot-Lau interferometry with fullerenes: Sensitivity to inertial forces and vibrational dephasing", Laser Physics **15**, 10 (2005).

[138] M. Hauth, C. Freier, V. Schkolnik, A. Senger, M. Schmidt, and A. Peters, "First gravity measurements using the mobile atom interferometer GAIN", Applied Physics B **113**, 49 (2013).

[139] I. Pikovski, M. Zych, F. Costa, and Č. Brukner, "Universal decoherence due to gravitational time dilation", Nature Physics **11**, 668 (2015).

[140] C. Monroe, D. M. Meekhof, B. E. King, and D. J. Wineland, "A "Schrödinger Cat" Superposition State of an Atom", Science **272**, 1131 (1996).

[141] C. J. Myatt, B. E. King, Q. A. Turchette, C. A. Sackett, D. Kielpinski, W. M. Itano, C. Monroe, and D. J. Wineland, "Decoherence of quantum superpositions through coupling to engineered reservoirs", Nature **403**, 269 (2000).

[142] H. Uys, M. J. Biercuk, A. P. VanDevender, C. Ospelkaus, D. Meiser, R. Ozeri, and J. J. Bollinger, "Decoherence due to Elastic Rayleigh Scattering", Physical Review Letters **105**, 200401 (2010).

[143] J. T. Barreiro, P. Schindler, O. Gühne, T. Monz, M. Chwalla, C. F. Roos, M. Hennrich, and R. Blatt, "Experimental multiparticle entanglement dynamics induced by decoherence", Nature Physics **6**, 943 (2010).

[144] E. Buks, R. Schuster, M. Heiblum, D. Mahalu, and V. Umansky, "Dephasing in electron interference by a 'which-path' detector", Nature **391**, 871 (1998).

[145] Y. Ji, Y. Chung, D. Sprinzak, M. Heiblum, D. Mahalu, and H. Shtrikman, "An electronic Mach–Zehnder interferometer", Nature **422**, 415 (2003).

[146] D. A. Kokorowski, A. D. Cronin, T. D. Roberts, and D. E. Pritchard, "From Single- to Multiple-Photon Decoherence in an Atom Interferometer", Physical Review Letters **86**, 2191 (2001).

[147] S. Ballmann, R. Härtle, P. B. Coto, M. Elbing, M. Mayor, M. R. Bryce, M. Thoss, and H. B. Weber, "Experimental Evidence for Quantum Interference and Vibrationally Induced Decoherence in Single-Molecule Junctions", Physical Review Letters **109**, 056801 (2012).

[148] P. Roulleau, F. Portier, P. Roche, A. Cavanna, G. Faini, U. Gennser, and D. Mailly, "Tuning Decoherence with a Voltage Probe", Physical Review Letters **102**, 236802 (2009).

[149] F. Chiarello, E. Paladino, M. G. Castellano, C. Cosmelli, A. D'Arrigo, G. Torrioli, and G. Falci, "Superconducting qubit manipulated by fast pulses: experimental observation of distinct decoherence regimes", New Journal of Physics **14**, 023031 (2012).

[150] M. Wallquist, K. Hammerer, P. Rabl, M. Lukin, and P. Zoller, "Hybrid quantum devices and quantum engineering", Physica Scripta **2009**, 014001 (2009).

[151] D. Hunger, S. Camerer, T. W. Hänsch, D. König, J. P. Kotthaus, J. Reichel, and P. Treutlein, "Resonant Coupling of a Bose-Einstein Condensate to a Micromechanical Oscillator", Physical Review Letters **104**, 143002 (2010).

[152] J. Chan, T. P. Mayer Alegre, A. H. Safavi-Naeini, J. T. Hill, A. Krause, S. Gröblacher, M. Aspelmeyer, and O. Painter, "Laser cooling of a nanomechanical oscillator into its quantum ground state", Nature **478**, 89 (2011).

[153] S. Bernon, H. Hattermann, D. Bothner, M. Knufinke, P. Weiss, F. Jessen, D. Cano, M. Kemmler, R. Kleiner, D. Koelle, *et al.*, "Manipulation and coherence of ultra-cold atoms on a superconducting atom chip", Nature Communications **4**, 2380 (2013).

[154] P. Lodahl, S. Mahmoodian, S. Stobbe, A. Rauschenbeutel, P. Schneeweiss, J. Volz, H. Pichler, and P. Zoller, "Chiral quantum optics", Nature **541**, 473 (2017).

[155] B. Vermersch, P.-O. Guimond, H. Pichler, and P. Zoller, "Quantum State Transfer via Noisy Photonic and Phononic Waveguides", Physical Review Letters **118**, 133601 (2017).

[156] P. Khatua, B. Bansal, and D. Shahar, "Single-Slit Electron Diffraction with Aharonov-Bohm Phase: Feynman's Thought Experiment with Quantum Point Contacts", Physical Review Letters **112**, 010403 (2014).

[157] E. Li, B. J. Eggleton, K. Fang, and S. Fan, "Photonic Aharonov–Bohm effect in photon–phonon interactions", Nature Communications **5**, 3225 (2014).

[158] L. Duca, T. Li, M. Reitter, I. Bloch, M. Schleier-Smith, and U. Schneider, "An Aharonov-Bohm interferometer for determining Bloch band topology", Science **347**, 288 (2015).

[159] A. Miffre, M. Jacquey, M. Büchner, G. Trénec, and J. Vigué, "Vibration-induced phase noise in Mach–Zehnder atom interferometers", Applied Physics B **84**, 617 (2006).

[160] R. Geiger, V. Ménoret, G. Stern, N. Zahzam, P. Cheinet, B. Battelier, A. Villing, F. Moron, M. Lours, Y. Bidel, *et al.*, "Detecting inertial effects with airborne matter-wave interferometry", Nature Communications **2**, 474 (2011).

[161] J. M. Hensley, A. Peters, and S. Chu, "Active low frequency vertical vibration isolation", Review of Scientific Instruments **70**, 2735 (1999).

[162] J. Le Gouët, T. E. Mehlstäubler, J. Kim, S. Merlet, A. Clairon, A. Landragin, and F. Pereira Dos Santos, "Limits to the sensitivity of a low noise compact atomic gravimeter", Applied Physics B: Lasers and Optics **92**, 133 (2008).

[163] S.-w. Chiow, S. Herrmann, S. Chu, and H. Müller, "Noise-Immune Conjugate Large-Area Atom Interferometers", Physical Review Letters **103**, 050402 (2009).

[164] S.-w. Chiow, T. Kovachy, H.-C. Chien, and M. A. Kasevich, "102$\hbar k$ Large Area Atom Interferometers", Physical Review Letters **107**, 130403 (2011).

[165] S. Fray, C. A. Diez, T. W. Hänsch, and M. Weitz, "Atomic Interferometer with Amplitude Gratings of Light and Its Applications to Atom Based Tests of the Equivalence Principle", Physical Review Letters **93**, 240404 (2004).

[166] X. Chen, J. Zhong, H. Song, L. Zhu, J. Wang, and M. Zhan, "Proportional-scanning-phase method to suppress the vibrational noise in nonisotope dual-atom-interferometer-based weak-equivalence-principle-test experiments", Physical Review A **90**, 023609 (2014).

[167] B. Barrett, L. Antoni-Micollier, L. Chichet, B. Battelier, P. A. Gominet, A. Bertoldi, P. Bouyer, and A. Landragin, "Correlative methods for dual-species quantum tests of the weak equivalence principle", New Journal of Physics **17**, 085010 (2015).

[168] R. Hanbury Brown and R. Q. Twiss, "A New Type of Interferometer for Use in Radio Astronomy", The London, Edinburgh, and Dublin Philosophical Magazine and Journal of Science **45**, 663 (1954).

[169] R. Hanbury Brown and R. Q. Twiss, "Correlation between Photons in two Coherent Beams of Light", Nature **177**, 27 (1956).

[170] R. Hanbury Brown and R. Q. Twiss, "A Test of a New Type of Stellar Interferometer on Sirius", Nature **178**, 1046 (1956).

[171] R. J. Glauber, "The Quantum Theory of Optical Coherence", Physical Review **130**, 2529 (1963).

[172] M. Schellekens, R. Hoppeler, A. Perrin, J. V. Gomes, D. Boiron, A. Aspect, and C. I. Westbrook, "Hanbury Brown Twiss Effect for Ultracold Quantum Gases", Science **310**, 648 (2005).

[173] H. Kiesel, A. Renz, and F. Hasselbach, "Observation of Hanbury Brown–Twiss anticorrelations for free electrons", Nature **418**, 392 (2002).

[174] C. Foellmi, "Intensity interferometry and the second-order correlation function $g^{(2)}$ in astrophysics", Astronomy & Astrophysics **507**, 1719 (2009).

[175] M. Aßmann, F. Veit, M. Bayer, M. van der Poel, and J. M. Hvam, "Higher-Order Photon Bunching in a Semiconductor Microcavity", Science **325**, 297 (2009).

[176] J. Simon, W. S. Bakr, R. Ma, M. E. Tai, P. M. Preiss, and M. Greiner, "Quantum simulation of antiferromagnetic spin chains in an optical lattice", Nature **472**, 307 (2011).

[177] S. S. Hodgman, R. G. Dall, A. G. Manning, K. G. H. Baldwin, and A. G. Truscott, "Direct Measurement of Long-Range Third-Order Coherence in Bose-Einstein Condensates", Science **331**, 1046 (2011).

[178] A. Perrin, R. Bücker, S. Manz, T. Betz, C. Koller, T. Plisson, T. Schumm, and J. Schmiedmayer, "Hanbury Brown and Twiss correlations across the Bose-Einstein condensation threshold", Nature Physics **8**, 195 (2012).

[179] G. Baym, "The physics of Hanbury Brown–Twiss intensity interferometry: from stars to nuclear collisions", Acta Physica Polonica B **29**, 1839 (1998).

[180] G. Agakishiev, A. Balanda, B. Bannier, R. Bassini, D. Belver, A. V. Belyaev, A. Blanco, M. Böhmer, J. L. Boyard, P. Cabanelas, *et al.*, "pp and $\pi\pi$ intensity interferometry in collisions of Ar+KCl at 1.76A GeV", The European Physical Journal A-Hadrons and Nuclei **47**, 63 (2011).

[181] A. Singer, U. Lorenz, F. Sorgenfrei, N. Gerasimova, J. Gulden, O. M. Yefanov, R. P. Kurta, A. Shabalin, R. Dronyak, R. Treusch, *et al.*, "Hanbury Brown–Twiss Interferometry at a Free-Electron Laser", Physical Review Letters **111**, 034802 (2013).

[182] F. T. Arecchi, E. Gatti, and A. Sona, "Time distribution of photons from coherent and Gaussian sources", Physics Letters **20**, 27 (1966).

[183] A. Öttl, S. Ritter, M. Köhl, and T. Esslinger, "Correlations and Counting Statistics of an Atom Laser", Physical Review Letters **95**, 090404 (2005).

[184] P. Federsel, C. Rogulj, T. Menold, Z. Darázs, P. Domokos, A. Günther, and J. Fortágh, "Noise spectroscopy with a quantum gas", Physical Review A **95**, 043603 (2017).

[185] J. Grondalski, P. M. Alsing, and I. H. Deutsch, "Spatial correlation diagnostics for atoms in optical lattices", Optics Express **5**, 249 (1999).

[186] E. Altman, E. Demler, and M. D. Lukin, "Probing many-body states of ultracold atoms via noise correlations", Physical Review A **70**, 013603 (2004).

[187] S. Fölling, F. Gerbier, A. Widera, O. Mandel, T. Gericke, and I. Bloch, "Spatial quantum noise interferometry in expanding ultracold atom clouds", Nature **434**, 481 (2005).

[188] N. Wiener, "Generalized harmonic analysis", Acta Mathematica **55**, 117 (1930).

[189] A. Khintchine, "Korrelationstheorie der stationären stochastischen Prozesse", Mathematische Annalen **109**, 604 (1934).

[190] O. H. Siegmund, J. V. Vallerga, A. S. Tremsin, J. McPhate, and B. Feller, "High spatial resolution neutron sensing microchannel plate detectors", Nuclear Instruments and Methods in Physics Research Section A: Accelerators, Spectrometers, Detectors and Associated Equipment **576**, 178 (2007).

[191] X. Zhou, P. Ranitovic, C. W. Hogle, J. H. D. Eland, H. C. Kapteyn, and M. M. Murnane, "Probing and controlling non-Born-Oppenheimer dynamics in highly excited molecular ions", Nature Physics **8**, 232 (2012).

[192] O. Siegmund, A. Tremsin, J. Vallerga, and J. McPhate, "Microchannel plate cross-strip detectors with high spatial and temporal resolution", Nuclear Instruments and Methods in Physics Research Section A: Accelerators, Spectrometers, Detectors and Associated Equipment **610**, 118 (2009).

[193] G. Bonanno, D. Marano, G. Romeo, S. Garozzo, A. Grillo, M. C. Timpanaro, O. Catalano, S. Giarrusso, D. Impiombato, G. La Rosa, *et al.*, "Advances in Multi-Pixel Photon Counter technology: First characterization results", Nuclear Instruments and Methods in Physics Research Section A: Accelerators, Spectrometers, Detectors and Associated Equipment **806**, 383 (2016).

[194] Q.-Y. Zhao, D. Zhu, N. Calandri, A. E. Dane, A. N. McCaughan, F. Bellei, H.-Z. Wang, D. F. Santavicca, and K. K. Berggren, "Single-photon imager based on a superconducting nanowire delay line", Nature Photonics **11**, 247 (2017).

[195] F. Lenz and G. Wohland, "Effect of chromatic aberration and partial coherence on the interference pattern of an electron biprism interferometer", Optik **67**, 315 (1984).

[196] F. Warken, E. Vetsch, D. Meschede, M. Sokolowski, and A. Rauschenbeutel, "Ultra-sensitive surface absorption spectroscopy using sub-wavelength diameter optical fibers", Optics Express **15**, 11952 (2007).

[197] F. Warken, A. Rauschenbeutel, and T. Bartholomäus, "Fiber Pulling Profits from Precise Positioning-Precise motion control improves manufacturing of fiber optical resonators.", Photonics Spectra **42**, 73 (2008).

[198] M. Nicklaus and F. Hasselbach, "Wien filter: A wave-packet-shifting device for restoring longitudinal coherence in charged-matter-wave interferometers", Physical Review A **48**, 152 (1993).

[199] T. T. Tsong, *Atom-Probe Field Ion Microscopy: Field Ion Emission, and Surfaces and Interfaces at Atomic Resolution* (Cambridge University Press, 2005).

[200] RoentDek, *MCP Delay Line Detector Manual* (RoentDek Handels GmbH, version: 9.20.907.2).

[201] H. Nyquist, "Certain Topics in Telegraph Transmission Theory", Transactions of the American Institute of Electrical Engineers **47**, 617 (1928).

[202] C. E. Shannon, "Communication in the Presence of Noise", Proceedings of the Institute of Radio Engineers **37**, 10 (1949).

[203] L. Mandel and E. Wolf, "Coherence Properties of Optical Fields", Reviews of Modern Physics **37**, 231 (1965).

[204] P. L. Knight and C. C. Gerry, *Introductory Quantum Optics* (Cambridge University Press, 2005).

[205] A. A. Michelson and F. G. Pease, "Measurement of the diameter of Alpha-Orionis by the interferometer", Proceedings of the National Academy of Sciences **7**, 143 (1921).

[206] M. Fox, *Quantum Optics: An Introduction*, Vol. 15 (OUP Oxford, 2006).

[207] J. McKeever, A. Boca, A. D. Boozer, J. R. Buck, and H. J. Kimble, "Experimental realization of a one-atom laser in the regime of strong coupling", Nature **425**, 268 (2003).

[208] Z. Yuan, B. E. Kardynal, R. M. Stevenson, A. J. Shields, C. J. Lobo, K. Cooper, N. S. Beattie, D. A. Ritchie, and M. Pepper, "Electrically Driven Single-Photon Source", Science **295**, 102 (2002).

[209] M. Abramowitz and I. A. Stegun, *Handbook of mathematical functions: with formulas, graphs, and mathematical tables*, Vol. 55 (New York: Dover Publications, 1964) p. 360.

[210] G. Casella, C. P. Robert, and M. T. Wells, "Generalized accept-reject sampling schemes", Lecture Notes-Monograph Series **45**, 342 (2004).

[211] M. Vengalattore, J. M. Higbie, S. R. Leslie, J. Guzman, L. E. Sadler, and D. M. Stamper-Kurn, "High-Resolution Magnetometry with a Spinor Bose-Einstein Condensate", Physical Review Letters **98**, 200801 (2007).

[212] M. S. Grinolds, S. Hong, P. Maletinsky, L. Luan, M. D. Lukin, R. L. Walsworth, and A. Yacoby, "Nanoscale magnetic imaging of a single electron spin under ambient conditions", Nature Physics **9**, 215 (2013).

[213] B. J. Shields, Q. P. Unterreithmeier, N. P. de Leon, H. Park, and M. D. Lukin, "Efficient Readout of a Single Spin State in Diamond via Spin-to-Charge Conversion", Physical Review Letters **114**, 136402 (2015).

[214] I. Lovchinsky, A. O. Sushkov, E. Urbach, N. P. de Leon, S. Choi, K. De Greve, R. Evans, R. Gertner, E. Bersin, C. Müller, *et al.*, "Nuclear magnetic resonance detection and spectroscopy of single proteins using quantum logic", Science **351**, 836 (2016).

[215] D. Vasyukov, Y. Anahory, L. Embon, D. Halbertal, J. Cuppens, L. Neeman, A. Finkler, Y. Segev, Y. Myasoedov, M. L. Rappaport, *et al.*, "A scanning superconducting quantum interference device with single electron spin sensitivity", Nature Nanotechnology **8**, 639 (2013).

[216] J. R. Kirtley, L. Paulius, A. J. Rosenberg, J. C. Palmstrom, C. M. Holland, E. M. Spanton, D. Schiessl, C. L. Jermain, J. Gibbons, Y.-K.-K. Fung, *et al.*, "Scanning SQUID susceptometers with sub-micron spatial resolution", Review of Scientific Instruments **87**, 093702 (2016).

[217] F. Yang, A. J. Kollár, S. F. Taylor, R. W. Turner, and B. L. Lev, "Scanning Quantum Cryogenic Atom Microscope", Physical Review Applied **7**, 034026 (2017).

[218] W.-T. Chang, C.-Y. Lin, W.-H. Hsu, M.-T. Chang, Y.-S. Chen, E.-T. Hwu, and I.-S. Hwang, "Low-voltage coherent electron imaging based on a single-atom electron source", arXiv:1512.08371 (2015).

[219] G. B. Arfken and H. J. Weber, *Mathematical Methods for Physicists* (Oxford: Elsevier, 2005).

[220] R. H. Fowler and L. Nordheim, "Electron Emission in Intense Electric Fields", Proceedings of the Royal Society of London A: Mathematical, Physical and Engineering Sciences **119**, 173 (1928).

[221] R. G. Forbes, "Refining the application of Fowler–Nordheim theory", Ultramicroscopy **79**, 11 (1999).

Appended publications

Publication 1

A. Rembold, R. Röpke, G. Schütz, J. Fortágh, A. Stibor, and A. Günther,
Second-order correlations in single-particle interferometry,
New Journal of Physics **19**, 103029 (2017).

New Journal of Physics
The open access journal at the forefront of physics

Deutsche Physikalische Gesellschaft DPG
IOP Institute of Physics

Published in partnership with: Deutsche Physikalische Gesellschaft and the Institute of Physics

OPEN ACCESS

RECEIVED
22 March 2017

REVISED
27 July 2017

ACCEPTED FOR PUBLICATION
29 August 2017

PUBLISHED
25 October 2017

PAPER

Second-order correlations in single-particle interferometry

A Rembold[1], R Röpke[1], G Schütz[1], J Fortágh[2], A Stibor[1] and A Günther[2,3]

[1] Institute of Physics and Center for Collective Quantum Phenomena in LISA, University of Tübingen, Auf der Morgenstelle 15, D-72076 Tübingen, Germany
[2] Institute of Physics and Center for Collective Quantum Phenomena in LISA, University of Tübingen, Auf der Morgenstelle 14, D-72076 Tübingen, Germany
[3] Author to whom any correspondence should be addressed.

E-mail: alexander.stibor@uni-tuebingen.de **and** a.guenther@uni-tuebingen.de

Keywords: single-particle interferometry, second-order correlation analysis, dephasing, sensor technology

Abstract

Interferometers with single particles are susceptible for dephasing perturbations from the environment, such as electromagnetic oscillations or mechanical vibrations. On the one hand, this limits sensitive quantum phase measurements as it reduces the interference contrast in the signal. On the other hand, it enables single-particle interferometers to be used as sensitive sensors for electromagnetic and mechanical perturbations. Recently, it was demonstrated experimentally, that a second-order correlation analysis of the spatial and temporal detection signal can decrease the electromagnetic shielding and vibrational damping requirements significantly. Thereby, the relevant matter-wave characteristics and the perturbation parameters could be extracted from the correlation analysis of a spatially 'washed-out' interference pattern and the original undisturbed interferogram could be reconstructed. This method can be applied to all interferometers that produce a spatial fringe pattern on a detector with high spatial and temporal single-particle resolution. In this article, we present and discuss in detail the used two-dimensional second-order correlation theory for multifrequency perturbations. The derivations of an explicit and approximate solution of the correlation function and corresponding amplitude spectra are provided. It is explained, how the numerical correlation function is extracted from the measurement data. Thereby, the influence of the temporal and spatial discretization step size on the extracted parameters, as contrast and perturbation amplitude, is analyzed. The influence of noise on the correlation function and corresponding amplitude spectrum is calculated and numerically cross-checked by a comparison of our theory with numerical single-particle simulations of a perturbed interference pattern. Thereby, an optimum spatial discretization step size is determined to achieve a maximum signal-to-noise ratio, which was used in former experiments to identify the perturbation caused by the electrical network. Our method can also be applied for the analysis of broad-band frequency noise, dephasing the interference pattern. Using Gaussian distributed noise in the simulations, we demonstrate that the relevant matter-wave parameters and the applied perturbation spectrum can be revealed by our correlation analysis.

1. Introduction

Single-particle interferometry became a remarkable tool in various fields of quantum physics and sensor technology. Interferometers for coherent atoms [1–3] recently investigated the nature of time [4, 5] and measured inertial forces [6] and gravitational acceleration [7]. Molecule interferometers [1, 8] proved the wave nature of large particles [9–12] and contributed to the understanding of quantum decoherence [13–15]. In neutron interferometers [16], the quantum-mechanical phase shift due to the Earth's gravitational field was observed [17]. Moreover, remarkable progress was achieved in the field of matter-wave interferometry with charged particles such as electrons and ions [18–20] based on new developments concerning the beam source [21–23], the precise electron guiding [24, 25], the coherent beam path separation by nanostructures [22, 26–28]

and highly resolved spatial and temporal single-particle detection [29]. This advance opened the door for experiments in Aharonov–Bohm physics [30–32] and Coulomb-induced decoherence [13, 33, 34]. Technical devices with interfering single particles can decrease the amount of destructive particle deposition in electron microscopy for the analysis of fragile biological specimen [35, 36].

All these technical [37] and fundamental applications [38, 39] of single-particle interferometers are based on the high phase sensitivity and are therefore susceptible to dephasing, which can be caused by external electromagnetic oscillations, mechanical vibrations or temperature drifts. In contrast to decoherence [33, 34], where actual information of the quantum state is lost to the environment, dephasing is a collective, time-dependent phase shift of the interference pattern. Both, decoherence and dephasing, cause a reduction of the contrast of the time-averaged interference pattern on the detector. However, in opposite to decoherence, dephasing can in principle be corrected after the measurement, if the temporal and spatial information of the single-particle events are known. Then, two-particle correlations may be used to study the dephasing process and to reveal the undisturbed interference pattern.

Ever since the famous Hanbury Brown and Twiss experiment [40], second-order correlations are successfully used in many research areas. Thereby, noise correlations play a key role, as they give direct access to the quantum nature of the source. This understanding has not only set the fundament for modern quantum optics [41], but also helped to prove the quantum nature of fermions [42] and bosons [43]. Today, noise correlation analysis is widely used in modern astrophysics [44], quantum atom optics [45] and particle physics [46]. For matter-waves, temporal correlations have been used to analyze the counting statistics of atom lasers [47] and to demonstrate the coherent transfer of magnetic field fluctuations onto an atom laser [48]. Spatial correlations, on the other hand, have been used to analyze atoms in optical lattices [49] or to study many-body states, such as the Mott insulator state, in cold atom physics [50, 51].

In previous publications [52–54] we have demonstrated experimentally in a biprism electron interferometer [18, 26, 55], how multifrequency dephasing caused by electromagnetic [52, 53] and vibrational oscillations [54] can be corrected using second-order correlation analysis in combination with the amplitude spectrum of the correlation function. Latter can be used for the identification of unknown perturbation frequencies [54], as according to the Wiener–Khintchine theorem [56, 57] the Fourier transform of the correlation function is equal to the power spectrum of the perturbed measurement signal. For the measurements, an interference pattern was shifted artificially by external perturbations leading to a contrast reduction of the temporally integrated pattern on the detector. Using the time and position information of particle impacts at the detector, the numerical second-order correlation function was extracted. With this, we were able to reveal the unknown perturbation frequencies, corresponding amplitudes and the characteristics of the matter-wave, such as contrast and pattern periodicity. The undisturbed interference pattern could be reconstructed with the parameters of the perturbation. Our method is a powerful tool to prove the wave nature of particles, even if the integrated interference pattern is vanished. Therefore, it reduces the requirements for electromagnetic shielding and vibrational damping of the experimental setup, e.g. for mobile interferometers or experiments in a perturbing environment. Furthermore, it can be used to sensitively detect electromagnetic and mechanical perturbations or for the spectroscopy of the electromagnetic and vibrational response spectrum of an interferometer [54]. Therefore, this technique has the potential for the application in sensor technology and can in principle be applied in interferometers for electrons [29], ions [29], atoms [43], neutrons [58] and molecules [59] that generate a spatial fringe pattern in the detection plane. For the application of the correlation analysis, the devices have to be equipped with a detector with high spatial and temporal single-particle resolution, which is available for all above mentioned interferometers. Another requirement is, that the particle flight time is shorter than the cycle time of the perturbation. Otherwise, the particles traverse many periods of the perturbation and therefore the perturbation is averaged out and can not be resolved.

This article provides a comprehensive description of the applied theory, being the base for the experimental application of second-order correlations in single-particle interferometry. In the first chapter, we give a detailed derivation of the two-dimensional second-order correlation theory for multifrequency perturbations leading to the equations applied in former dephasing experiments [52–54]. We deduce the explicit solution for the correlation function and explain under which conditions an approximation can be applied. The characteristics of the explicit and approximate solutions are discussed and the determination of the matter-wave properties is shown. Furthermore, we calculate the analytic solution of the corresponding amplitude spectrum used for the identification of the unknown perturbation frequencies and amplitudes [54]. The invariance of the correlation function under time and space transformations is analyzed in detail and the consequence for the determination of the perturbation parameters is shown.

In the second part of this article, we investigate the general characteristics of numerical correlation functions. They are typically derived from a finite set of measurement data, causing statistics and noise to play an important role. Temporal and spatial discretization, then influences not only the contrast and the amplitude spectrum of the correlation function, but also the corresponding noise levels. This limits the maximal signal-to-noise ratio in the correlation analysis. From our theoretical study, we identify an optimum discretization step size for best

sensitivity, which was used in a previous publication [60] for the identification of the electrical network frequency. With single-particle simulations of a perturbed interference pattern, we cross-check our theoretical description and show, how the correlation theory can be used to identify broad-band frequency noise.

2. Theory of second-order correlations

In this chapter, the theory of second-order correlations in single-particle interferometry is derived and the properties are discussed in detail. First, the contrast reduction of a time-averaged interference pattern dephased by a perturbation is analyzed. Afterwards, the explicit solution of the second-order correlation function is calculated and discussed under which conditions an approximate solution is suitable. The determination of the contrast and spatial periodicity of the unperturbed interference pattern is demonstrated. The corresponding amplitude spectra used for the identification of unknown perturbation frequencies are derived. At the end of the chapter, the invariance of the correlation function under time and space transformations is analyzed in detail and the consequence for the determination of the perturbation phases is discussed.

2.1. Time-averaged interference pattern

In many experiments in single-particle interferometry, the interference pattern is detected using multichannel plates in conjunction with a phosphor screen [18, 19, 24, 33, 61]. The particle impacts generate light pulses on the phosphor screen, that are temporally integrated with a charge-coupled device camera (CCD-camera). An interference pattern, that is dephased by a temporal perturbation, is then irreversibly 'washed-out' in the spatial signal and its contrast is reduced. This behavior shall be calculated in the following.

The probability distribution, that describes the particle impacts in the detection plane forming the interference pattern, is given by

$$f(y,\,t) = f_0(1 + K\cos(ky + \varphi(t))), \tag{1}$$

where f_0 assures normalization, K and $k = 2\pi/\lambda$ indicate the contrast and wave number of the unperturbed interference pattern, with the spatial periodicity λ. The time-dependent perturbation $\varphi(t)$ is described as a superposition of N harmonic frequencies ω_j

$$\varphi(t) = \sum_{j=1}^{N} \varphi_j \cos(\omega_j t + \phi_j), \tag{2}$$

with perturbation amplitudes (peak phase deviations) φ_j and phases ϕ_j. The perturbation leads to a washout of the time-averaged interference pattern. For one perturbation frequency ($N = 1$), this can be easily seen by calculating the time-average of equation (1)

$$\langle f(y,\,t)\rangle_t := \lim_{T\to\infty} \frac{1}{T}\int_0^T f(y,\,t)\,\mathrm{d}t, \tag{3}$$

resulting in

$$\begin{aligned}\langle f(y,\,t)\rangle_t &= \lim_{T\to\infty} \frac{f_0}{T}\int_0^T \left(1 + \frac{K}{2}(\mathrm{e}^{\mathrm{i}(ky+\varphi(t))} + \text{c.c.})\right)\mathrm{d}t \\ &= f_0 + \lim_{T\to\infty} \frac{f_0 K}{2T}\left(\mathrm{e}^{\mathrm{i}ky}\int_0^T \mathrm{e}^{\mathrm{i}\varphi_1\cos(\omega_1 t+\phi_1)}\,\mathrm{d}t + \text{c.c.}\right).\end{aligned} \tag{4}$$

Using Bessel functions of first kind J_n, the exponential function can be rewritten as

$$\mathrm{e}^{\pm\mathrm{i}\phi_1\cos(\omega_1 t+\varphi_1)} = \sum_{n_1=-\infty}^{+\infty} (\pm\mathrm{i})^{n_1} J_{n_1}(\phi_1)\mathrm{e}^{\mathrm{i}n_1(\omega_1 t+\varphi_1)} = \sum_{n_1=-\infty}^{+\infty} J_{n_1}(\phi_1)\mathrm{e}^{\mathrm{i}n_1\left(\omega_1 t+\varphi_1\pm\frac{\pi}{2}\right)}, \tag{5}$$

yielding

$$\begin{aligned}\langle f(y,\,t)\rangle_t = f_0 + \frac{f_0 K}{2}\sum_{n_1=-\infty}^{+\infty} J_{n_1}(\varphi_1)(&\mathrm{e}^{\mathrm{i}ky}\mathrm{e}^{\mathrm{i}n_1\left(\phi_1+\frac{\pi}{2}\right)} \\ &+ \mathrm{e}^{-\mathrm{i}ky}\mathrm{e}^{\mathrm{i}n_1\left(\phi_1-\frac{\pi}{2}\right)})\lim_{T\to\infty}\frac{1}{T}\int_0^T \mathrm{e}^{\mathrm{i}n_1\omega_1 t}\,\mathrm{d}t.\end{aligned} \tag{6}$$

Only for $n_1 = 0$, the limit of the time integral is equal to one. For all other $n_1 \neq 0$, it approaches zero, such that the time-averaged interference pattern becomes

$$\langle f(y,\,t)\rangle_t = f_0(1 + \underbrace{K J_0(\varphi_1)}_{=K_{\mathrm{red}}(\varphi_1)}\cos(ky)). \tag{7}$$

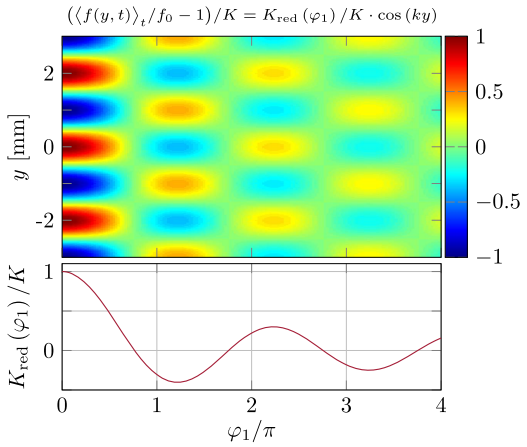

Figure 1. Top: dependence of the time-averaged interference pattern (equation (7)) on the peak phase deviation φ_1 for an interference pattern with a periodicity of $\lambda = 2$ mm along the y-direction. Bottom: dependence of the relative contrast reduction $K_{\mathrm{red}}(\varphi_1)/K$ on the peak phase deviation φ_1. For $\varphi_1 = 0.76\,\pi$, the contrast vanishes due to the first zero of $J_0(\varphi_1)$. The contrast returns for larger peak phase deviations, but not completely. At each sign change of $J_0(\varphi_1)$, the phase of the interference pattern is shifted by π.

The perturbation thus leads to a reduced contrast $K_{\mathrm{red}}(\varphi_1)$ given by the perturbation amplitude: $K_{\mathrm{red}}(\varphi_1) = KJ_0(\varphi_1)$, with $|J_0(\varphi_1)| \leqslant 1$. In figure 1 at the top, the dependence of the time-averaged interference pattern (equation (7)) on the peak phase deviation φ_1 is illustrated. The interference pattern with a spatial periodicity of $\lambda = 2$ mm can be identified in the y-direction. The reduced contrast $K_{\mathrm{red}}(\varphi_1)$ normalized to the contrast of the unperturbed interference pattern K is plotted at the bottom of figure 1. For a peak phase deviation of $\varphi_1 = 0.76\,\pi$, the contrast is zero corresponding to the first zero of $J_0(\varphi_1)$. The contrast returns for larger peak phase deviations, but does not recover completely. Additionally, the interference pattern is phase shifted by π as the sign of $J_0(\varphi_1)$ changes from positive to negative. This behavior is repeated for higher peak phase deviations and the contrast is further reduced.

For multifrequency perturbations ($N > 1$) with peak phase deviations $\varphi_j < 1$, equation (7) becomes

$$\langle f(y,\,t)\rangle_t = f_0\left(1 + \underbrace{K\prod_{j=1}^{N} J_0(\varphi_j)}_{=K_{\mathrm{red}}(\varphi_{j=1\ldots N})}\cos(ky)\right). \tag{8}$$

Here, the reduced contrast $K_{\mathrm{red}}(\varphi_{j=1\ldots N})$ depends on all peak phase deviations φ_j, via the product of the zeroth order Bessel functions. Therefore, the contrast is typically stronger reduced as compared to the single frequency case in figure 1.

2.2. Solution for the analytic second-order correlation function

With the spatial and temporal information of the particles arriving in the detection plane, it is possible to reveal the contrast K and spatial periodicity λ of the unperturbed interference pattern by correlation analysis. This is possible, because in the correlation function the spatial and temporal differences are taken into account in contrast to the temporally integrated interference pattern. Then, on timescales below the perturbation frequency, the interference pattern is still visible and not influenced by the perturbation. Furthermore, the characteristics of the perturbation (frequencies ω_j, peak phase deviations φ_j and phases ϕ_j) can be determined from the correlation analysis.

With the probability distribution in equation (1), the second-order correlation function reads

$$g^{(2)}(u,\,\tau) = \frac{\langle\!\langle f(y+u,\,t+\tau)f(y,\,t)\rangle\!\rangle_{y,t}}{\langle\!\langle f(y+u,\,t+\tau)\rangle\!\rangle_{y,t}\langle\!\langle f(y,\,t)\rangle\!\rangle_{y,t}}, \tag{9}$$

with $\langle\!\langle\cdot\rangle\!\rangle_{y,t}$ denoting the average over position and time

$$\langle\!\langle f(y,\,t)\rangle\!\rangle_{y,t} := \lim_{Y,T\to\infty}\frac{1}{TY}\int_0^T\int_{-Y/2}^{Y/2} f(y,\,t)\,\mathrm{d}y\mathrm{d}t. \tag{10}$$

If the acquisition time T and length Y are large compared to the involved perturbation frequencies $T \gg 2\pi/\omega_j$ and spatial periodicity $Y \gg \lambda$, equation (9) can be solved analytically. First, the term $\langle\!\langle f(y+u,\,t+\tau)\rangle\!\rangle_{y,t}$ in the denominator of equation (9) is calculated, using equations (1) and (10)

$$\begin{aligned}\langle\!\langle f(y+u,\,t+\tau)\rangle\!\rangle_{y,t} &= \lim_{Y,T\to\infty}\frac{f_0}{TY}\int_0^T\int_{-Y/2}^{Y/2}(1+K\cos(k(y+u)+\varphi(t+\tau)))\,\mathrm{d}y\mathrm{d}t\\ &= f_0+\lim_{Y,T\to\infty}\frac{f_0K}{TY}\frac{1}{2}\int_0^T\int_{-Y/2}^{Y/2}(\mathrm{e}^{\mathrm{i}(k(y+u)+\varphi(t+\tau))}+\text{c.c.})\,\mathrm{d}y\mathrm{d}t\\ &= f_0+\lim_{Y,T\to\infty}\frac{f_0K}{TY}\left(\mathrm{e}^{\mathrm{i}ku}\underbrace{\frac{1}{2}\int_{-Y/2}^{Y/2}\mathrm{e}^{\mathrm{i}ky}\mathrm{d}y}_{=\sin\left(k\frac{Y}{2}\right)/k}\int_0^T\mathrm{e}^{\mathrm{i}\varphi(t+\tau)}\mathrm{d}t+\text{c.c.}\right).\end{aligned}\tag{11}$$

In the limit of large acquisition length $Y \gg \lambda$, the spatial limit becomes

$$\lim_{Y\to\infty}\frac{\sin\left(k\frac{Y}{2}\right)}{kY}\to 0,\tag{12}$$

yielding

$$\langle\!\langle f(y+u,\,t+\tau)\rangle\!\rangle_{y,t} = f_0.\tag{13}$$

Using $u = 0$ and $\tau = 0$ in equation (11), the second term in the denominator becomes $\langle\!\langle f(y,\,t)\rangle\!\rangle_{y,t} = f_0$. This is expected, because shifts in time and space should not alter the long time and position average of the probability distribution.

Using equations (1) and (10), the numerator in equation (9) results in

$$\begin{aligned}&\langle\!\langle f(y+u,\,t+\tau)f(y,\,t)\rangle\!\rangle_{y,t}\\ &\quad=\lim_{Y,T\to\infty}\frac{f_0^2}{TY}\int_0^T\int_{-Y/2}^{Y/2}[1+K\cos(k(y+u)\varphi(t+\tau))+K\cos(ky+\varphi(t))\\ &\qquad+K^2\cos(k(y+u)+\varphi(t+\tau))\cdot\cos(ky+\varphi(t))]\,\mathrm{d}y\mathrm{d}t.\end{aligned}\tag{14}$$

Similar as before, the second and third term in equation (14) vanish, leaving

$$\begin{aligned}&\langle\!\langle f(y+u,\,t+\tau)f(y,\,t)\rangle\!\rangle_{y,t}\\ &=f_0^2+\lim_{Y,T\to\infty}\frac{f_0^2}{TY}\frac{K^2}{4}\int_0^T\int_{-Y/2}^{Y/2}(\mathrm{e}^{-\mathrm{i}(k(y+u)+\varphi(t+\tau))}+\text{c.c.})(\mathrm{e}^{-\mathrm{i}(ky+\varphi(t))}+\text{c.c.})\,\mathrm{d}y\mathrm{d}t\\ &=f_0^2+\lim_{Y,T\to\infty}\frac{f_0^2}{TY}\frac{K^2}{4}\left(\mathrm{e}^{-\mathrm{i}ku}\underbrace{\int_{-Y/2}^{Y/2}1\,\mathrm{d}y}_{=Y}\int_0^T\mathrm{e}^{-\mathrm{i}(\varphi(t+\tau)-\varphi(t))}\,\mathrm{d}t+\text{c.c.}\right.\\ &\left.+\,\mathrm{e}^{-\mathrm{i}ku}\underbrace{\int_{-Y/2}^{Y/2}\mathrm{e}^{-2\mathrm{i}ky}\,\mathrm{d}y}_{=\frac{\sin(kY)}{k}}\int_0^T\mathrm{e}^{-\mathrm{i}(\varphi(t+\tau)+\varphi(t))}\,\mathrm{d}t+\text{c.c.}\right).\end{aligned}\tag{15}$$

In the limit $Y \gg \lambda$, again $\lim_{Y\to\infty}\sin(kY)/kY \to 0$, yielding with equation (2)

$$\begin{aligned}\langle\!\langle f(y+u,\,t+\tau)f(y,\,t)\rangle\!\rangle_{y,t} &= f_0^2+\lim_{T\to\infty}\frac{f_0^2}{T}\frac{K^2}{4}\left(\mathrm{e}^{-\mathrm{i}ku}\int_0^T\mathrm{e}^{-\mathrm{i}\sum_{j=1}^N\varphi_j\cos(\omega_j(t+\tau)+\phi_j)}\mathrm{e}^{\mathrm{i}\sum_{j=1}^N\varphi_j\cos(\omega_jt+\phi_j)}\,\mathrm{d}t\right.\\ &\left.+\,\mathrm{e}^{\mathrm{i}ku}\int_0^T\mathrm{e}^{\mathrm{i}\sum_{j=1}^N\varphi_j\cos(\omega_j(t+\tau)+\phi_j)}\mathrm{e}^{-\mathrm{i}\sum_{j=1}^N\varphi_j\cos(\omega_jt+\phi_j)}\,\mathrm{d}t\right).\end{aligned}\tag{16}$$

Using equation (5) for N perturbation frequencies

$$\mathrm{e}^{\pm\mathrm{i}\sum_{j=1}^N\varphi_j\cos(\omega_jt+\phi_j)}=\prod_{j=1}^N\sum_{n_j=-\infty}^{+\infty}J_{n_j}(\varphi_j)\mathrm{e}^{\mathrm{i}n_j\left(\omega_jt+\phi_j\pm\frac{\pi}{2}\right)},\tag{17}$$

equation (16) can be rewritten, yielding

$$\begin{aligned}
&\langle\!\langle f(y+u,\,t+\tau)f(y,\,t)\rangle\!\rangle_{y,t} = f_0^2 + \lim_{T\to\infty}\frac{f_0^2}{T}\frac{K^2}{4}\\
&\cdot\Bigg(\mathrm{e}^{-\mathrm{i}ku}\int_0^T\prod_{j=1}^{N}\sum_{n_j,m_j}\underbrace{J_{n_j}(\varphi_j)J_{m_j}(\varphi_j)\mathrm{e}^{\mathrm{i}m_j\omega_j\tau}\mathrm{e}^{\mathrm{i}\left[n_j\left(\phi_j+\frac{\pi}{2}\right)+m_j\left(\phi_j-\frac{\pi}{2}\right)\right]}}_{=A^{+}_{n_j,m_j}}\cdot\mathrm{e}^{\mathrm{i}(n_j+m_j)\omega_j t}\,\mathrm{d}t\\
&+\mathrm{e}^{\mathrm{i}ku}\int_0^T\prod_{j=1}^{N}\sum_{n_j,m_j}\underbrace{J_{n_j}(\varphi_j)\,J_{m_j}(\varphi_j)\mathrm{e}^{\mathrm{i}m_j\omega_j\tau}\mathrm{e}^{\mathrm{i}\left[n_j\left(\phi_j-\frac{\pi}{2}\right)+m_j\left(\phi_j+\frac{\pi}{2}\right)\right]}}_{=A^{-}_{n_j,m_j}}\cdot\mathrm{e}^{\mathrm{i}(n_j+m_j)\omega_j t}\,\mathrm{d}t\Bigg)\\
&=f_0^2+\lim_{T\to\infty}\frac{f_0^2}{T}\frac{K^2}{4}\\
&\cdot\Bigg(\mathrm{e}^{-\mathrm{i}ku}\int_0^T\sum_{n_1,m_1}\cdots\sum_{n_N,m_N}A^{+}_{n_1,m_1}\cdots A^{+}_{n_N,m_N}\cdot\mathrm{e}^{\mathrm{i}(n_1+m_1)\omega_1 t}\cdots\mathrm{e}^{\mathrm{i}(n_N+m_N)\omega_N t}\,\mathrm{d}t\\
&+\mathrm{e}^{\mathrm{i}ku}\int_0^T\sum_{n_1,m_1}\cdots\sum_{n_N,m_N}A^{-}_{n_1,m_1}\cdots A^{-}_{n_N,m_N}\cdot\mathrm{e}^{\mathrm{i}(n_1+m_1)\omega_1 t}\cdots\mathrm{e}^{\mathrm{i}(n_N+m_N)\omega_N t}\,\mathrm{d}t\Bigg)\\
&=f_0^2+f_0^2\frac{K^2}{4}\\
&\cdot\Bigg(\mathrm{e}^{-\mathrm{i}ku}\sum_{n_1,m_1}\cdots\sum_{n_N,m_N}A^{+}_{n_1,m_1}\cdots A^{+}_{n_N,m_N}\cdot\lim_{T\to\infty}\frac{1}{T}\int_0^T\mathrm{e}^{\mathrm{i}\sum_{j=1}^{N}(n_j+m_j)\omega_j t}\,\mathrm{d}t\\
&+\mathrm{e}^{\mathrm{i}ku}\sum_{n_1,m_1}\cdots\sum_{n_N,m_N}A^{-}_{n_1,m_1}\cdots A^{-}_{n_N,m_N}\cdot\lim_{T\to\infty}\frac{1}{T}\int_0^T\mathrm{e}^{\mathrm{i}\sum_{j=1}^{N}(n_j+m_j)\omega_j t}\,\mathrm{d}t\Bigg).
\end{aligned}\tag{18}$$

A closer look to the time integral reveals, that it can only become zero or one

$$\lim_{T\to\infty}\frac{1}{T}\int_0^T\mathrm{e}^{\mathrm{i}\sum_{j=1}^{N}(n_j+m_j)\omega_j t}\,\mathrm{d}t=\begin{cases}1 & \text{if }\sum_{j=1}^{N}(n_j+m_j)\omega_j=0\\ 0 & \text{else}\end{cases}.\tag{19}$$

This reduces the $2N$ sums in equation (18) to a (single) sum over all integer multiplets $\{n_j,\,m_j\}\in\mathbb{Z},\,j=1\,\ldots\,N$ for which the constraint

$$\sum_{j=1}^{N}(n_j+m_j)\omega_j=0\tag{20}$$

is fulfilled. Here it shall be noted, that for a finite acquisition time T, the constraint has to be changed to

$$\left|\sum_{j=1}^{N}(n_j+m_j)\omega_j\right|<2\pi/T,\tag{21}$$

because the minimal resolvable frequency is defined by the measurement time via $1/T$. In the following, however, it is assumed that $T\to\infty$ and therefore equation (20) is used for the calculations and discussions. Trivially, equation (20) is satisfied for all integer multiplets with $n_j=-m_j$. However, depending on the specific values of ω_j, the constraint might be fulfilled by additional integer multiplets $\{n_j,\,m_j\}$ with $n_j\neq-m_j$. The constraint from equation (20) can be expressed mathematically by introducing a function c

$$c:\mathbb{Z}^N\times\mathbb{Z}^N\longrightarrow\mathbb{R},\quad(n_{j=1\ldots N},\,m_{j=1\ldots N})\longmapsto\sum_{j=1}^{N}(n_j+m_j)\omega_j,\tag{22}$$

with the kernel of c ($\ker(c)$) being the set of all integer multiplets $\{n_j,\,m_j\}\in\mathbb{Z},\,j=1\,\ldots\,N$ for which $c(n_{j=1\ldots N},\,m_{j=1\ldots N})=0$ and therefore the constraint in equation (20) is fulfilled. Using this definition, equation (18) simplifies to

$$\langle\!\langle f(y+u,\,t+\tau)f(y,\,t)\rangle\!\rangle_{y,t} = f_0^2 + f_0^2\frac{K^2}{4} \cdot\left(\mathrm{e}^{-\mathrm{i}ku}\sum_{\substack{\{n_j,m_j\}\in\ker(c)\\ j=1\ldots N}}\prod_{j=1}^{N} A^{+}_{n_j,m_j} + \mathrm{e}^{\mathrm{i}ku}\sum_{\substack{\{n_j,m_j\}\in\ker(c)\\ j=1\ldots N}}\prod_{j=1}^{N} A^{-}_{n_j,m_j}\right). \tag{23}$$

Using the result of equations (13) and (23), the second-order correlation function in equation (9) now becomes

$$g^{(2)}(u,\,\tau) = 1 + \frac{K^2}{4}(\mathrm{e}^{-\mathrm{i}ku}A_+ + \mathrm{e}^{\mathrm{i}ku}A_-), \tag{24}$$

with

$$A_\pm = \sum_{\substack{\{n_j,m_j\}\in\ker(c)\\ j=1\ldots N}}\prod_{j=1}^{N} J_{n_j}(\varphi_j)J_{m_j}(\varphi_j)\mathrm{e}^{\mathrm{i}m_j\omega_j\tau}\chi^{\pm}_{n_j,m_j} \tag{25}$$

$$\chi^{\pm}_{n_j,m_j} = \mathrm{e}^{\mathrm{i}\left[n_j\left(\phi_j\pm\frac{\pi}{2}\right)+m_j\left(\phi_j\mp\frac{\pi}{2}\right)\right]}. \tag{26}$$

To calculate a more descriptive representation of the correlation function and to demonstrate, that $g^{(2)}(u,\,\tau)\in\mathbb{R}$, equations (24)–(26) can be further rewritten in terms of real and imaginary parts

$$\begin{aligned} g^{(2)}(u,\,\tau) &= 1 + \frac{K^2}{4}\sum_{\substack{\{n_j,m_j\}\in\ker(c)\\ j=1\ldots N}}\tilde{B}_{\{n_j,m_j\}}(\varphi_j)\mathrm{e}^{\mathrm{i}\left(\sum_{j=1}^{N}m_j\omega_j\tau+\sum_{j=1}^{N}\phi_j(m_j+n_j)\right)}\\ &\cdot\left[\mathrm{e}^{-\mathrm{i}\left(ku+\frac{\pi}{2}\sum_{j=1}^{N}(m_j-n_j)\right)} + \mathrm{e}^{\mathrm{i}\left(ku+\frac{\pi}{2}\sum_{j=1}^{N}(m_j-n_j)\right)}\right]\\ &= 1 + \frac{K^2}{2}\sum_{\substack{\{n_j,m_j\}\in\ker(c)\\ j=1\ldots N}}\tilde{B}_{\{n_j,m_j\}}(\varphi_j)\cos(ku+\tilde{\varphi}_{\{n_j,m_j\}})\\ &\cdot\left[\cos\left(\sum_{j=1}^{N}m_j\omega_j\tau+\Phi_{\{n_j,m_j\}}\right)+\mathrm{i}\cdot\sin\left(\sum_{j=1}^{N}m_j\omega_j\tau+\Phi_{\{n_j,m_j\}}\right)\right], \end{aligned} \tag{27}$$

with the product of the Bessel functions

$$\tilde{B}_{\{n_j,m_j\}}(\varphi_j) := \prod_{j=1}^{N} J_{n_j}(\varphi_j)J_{m_j}(\varphi_j). \tag{28}$$

The spatial correlation phase $\tilde{\varphi}_{\{n_j,m_j\}}$ and temporal phase $\Phi_{\{n_j,m_j\}}$ in equation (27) are given by

$$\tilde{\varphi}_{\{n_j,m_j\}} := \frac{\pi}{2}\sum_{j=1}^{N}(m_j-n_j), \quad \Phi_{\{n_j,m_j\}} := \sum_{j=1}^{N}\phi_j(m_j+n_j). \tag{29}$$

If the constraint in equation (20) is fulfilled for a multiplet $\{n_j,\,m_j\}$, it is also satisfied for $-\{n_j,\,m_j\}$. With $\tilde{B}_{-\{n_j,m_j\}}(\varphi_j) = (-1)^{\sum_j(n_j+m_j)}\tilde{B}_{\{n_j,m_j\}}(\varphi_j)$, $\tilde{\varphi}_{-\{n_j,m_j\}} = -\tilde{\varphi}_{\{n_j,m_j\}}$ and $\Phi_{-\{n_j,m_j\}} = -\Phi_{\{n_j,m_j\}}$, it can be shown, that the addend with $-\{n_j,\,m_j\}$ of the sum in equation (27) is complex conjugated to the addend with $\{n_j,\,m_j\}$. The addend of the zero multiplet $\{0,\,0\}$ is purely real valued. Therefore, the imaginary part vanishes after summing up all addends and equation (27) becomes real

$$g^{(2)}(u,\,\tau) = 1 + \frac{K^2}{2}\sum_{\substack{\{n_j,m_j\}\in\ker(c)\\ j=1\ldots N}}A_{\{n_j,m_j\}}(\tau,\,\Phi_{\{n_j,m_j\}})\cos(ku+\tilde{\varphi}_{\{n_j,m_j\}}), \tag{30}$$

with the amplitude

$$A_{\{n_j,m_j\}}(\tau,\,\Phi_{\{n_j,m_j\}}) = \tilde{B}_{\{n_j,m_j\}}(\varphi_j)\cdot\cos\left(\sum_{j=1}^{N}m_j\omega_j\tau+\Phi_{\{n_j,m_j\}}\right). \tag{31}$$

Here, the sum has to be taken over all integer multiplets $\{n_j,\,m_j\}\in\ker(c)$, $j=1\ \ldots\ N$ fulfilling the constraint in equation (20). In principle, the constraint is satisfied for an infinite number of multiplets each with their own contribution to the correlation function given by

$$a_{\{n_j,m_j\}}(u,\,\tau) = A_{\{n_j,m_j\}}(\tau,\,\Phi_{\{n_j,m_j\}})\cos(ku+\tilde{\varphi}_{\{n_j,m_j\}}). \tag{32}$$

However, contributions with large values of $\{n_j,\ m_j\}$ are suppressed, because the Bessel function (equation (28)) strongly decays for $m_j > \varphi_j$ [62]. This limits the number of multiplets that have to be taken into account for the correlation analysis. The contribution to $g^{(2)}(u,\ \tau)$ of each multiplet addend $a_{\{n_j,m_j\}}(u,\ \tau)$ shows a periodic modulation in the correlation length u with the same spatial periodicity $\lambda = 2\pi/k$ as the unperturbed interference pattern, but shifted in u-direction by the spatial correlation phase $\tilde{\varphi}_{\{n_j,m_j\}}$. The amplitude $A_{\{n_j,m_j\}}(\tau,\ \Phi_{\{n_j,m_j\}})$ (equation (31)) of each multiplet addend $a_{\{n_j,m_j\}}(u,\ \tau)$ depends on the correlation time τ and the specific perturbation characteristics. It shows a periodic structure in τ with the periodicity determined by the frequency component $\sum_{j=1}^{N} m_j\omega_j$ with the coefficients $\{n_j,\ m_j\} \in \ker(c)$. This periodic structure is shifted in τ-direction by the temporal phase $\Phi_{\{n_j,m_j\}}$. The amplitude of the modulation in τ-direction is given by the peak phase deviations φ_j, via the product of the Bessel functions in equation (28).

After summing up all addends $a_{\{n_j,m_j\}}(u,\ \tau)$, the resulting correlation function (equation (30)) shows the same spatial periodicity λ. The overall amplitude is equal to 1 only at certain correlation times τ given by the involved perturbation frequencies (see section 2.4). At these temporal positions, the contrast of the correlation function is $K^2/2$ and therefore directly linked to the contrast of the unperturbed interference pattern K. For all other correlation times, the contrast of the correlation function is $<K^2/2$. It has to be noted, that the maximum contrast of the correlation function is $K^2/2$ and therefore a factor of $K/2$ lower than the contrast K of the unperturbed interference pattern.

The overall amplitude of the resulting correlation function includes the perturbation frequencies ω_j, their harmonic frequencies as well as their differences and sums (intermodulation terms). All frequency components are given by the argument of the cosine $\sum_{j=1}^{N} m_j\omega_j$ in equation (31). Approximately, the maximum frequency component per perturbation frequency included in the correlation function is given by $m_{j,\max}\omega_j$, with $m_{j,\max} \approx \varphi_j$, as larger frequency components are suppressed due to the strong decay of the Bessel function in equation (28) for $m_j > \varphi_j$. Therefore, the maximum frequency component of all perturbation frequencies included in the correlation function is approximately given by $\max\{\varphi_j\omega_j\}$.

2.3. Approximate solution for the second-order correlation function

In the following, an approximate solution for the correlation function is deduced, by taking into account only the trivial solution to the constraint in equation (20). These are the multiplets with $n_j = -m_j$, which typically give the main contribution to the correlation function. Using $\Phi_{\{-m_j,m_j\}} = 0$, $\tilde{\varphi}_{\{-m_j,m_j\}} = \pi\sum_{j=1}^{N} m_j$ and $J_{-m_j}(\varphi_j) = (-1)^{m_j}J_{m_j}(\varphi_j)$, equations (30) and (31) become

$$g^{(2)}(u,\ \tau) = 1 + \frac{K^2}{2} \cdot \sum_{\substack{\{-m_j,m_j\}\in\ker(c)\\ j=1\ldots N}} \left(\prod_{j=1}^{N} J_{m_j}(\varphi_j)^2\right) \cos\left(\sum_{j=1}^{N} m_j\omega_j\tau\right) \underbrace{(-1)^{\sum_{j=1}^{N} m_j} \cos\left(ku + \pi\sum_{j=1}^{N} m_j\right)}_{=\cos(ku)}. \tag{33}$$

With $\cos(\sum_{j=1}^{N} m_j\omega_j\tau) = \frac{1}{2}(e^{i\sum_{j=1}^{N} m_j\omega_j\tau} + e^{-i\sum_{j=1}^{N} m_j\omega_j\tau})$ and $e^{i\sum_{j=1}^{N} m_j\omega_j\tau} = \prod_{j=1}^{N} e^{im_j\omega_j\tau}$, the approximate second-order correlation function yields

$$g^{(2)}(u,\ \tau) = 1 + \frac{K^2}{2} \cdot A(\tau)\cos(ku), \tag{34}$$

with the time-dependent amplitude

$$\begin{aligned} A(\tau) &= \prod_{j=1}^{N} \left(\sum_{m_j=-\infty}^{\infty} J_{m_j}(\varphi_j)^2 \cos(m_j\omega_j\tau)\right) \\ &= \prod_{j=1}^{N} \left(J_0(\varphi_j)^2 + 2 \cdot \sum_{m_j=1}^{\infty} J_{m_j}(\varphi_j)^2 \cos(m_j\omega_j\tau)\right). \end{aligned} \tag{35}$$

Similar to the explicit solution of the correlation function in equations (30) and (31), the spatial modulation of the approximate solution is given by the spatial periodicity λ of the unperturbed interference pattern. The approximate solution is independent of the spatial correlation phases $\tilde{\varphi}_{\{n_j,m_j\}}$ and temporal phases $\Phi_{\{n_j,m_j\}}$ (equation (29)). Therefore, the addends are not phase shifted with respect to each other in u- and τ-direction.

Usually, the approximate correlation function in equation (34) can be used for the description of multifrequency perturbations. However, in the case of few perturbation frequencies, that are multiples of each other, the constraint in equation (20) is additionally fulfilled for $n_j \neq -m_j$ and the explicit solution of the correlation function in equation (30) has to be applied. In the case of a single perturbation frequency, the constraint of equation (20) is only satisfied for $n_1 = -m_1$. Thus, the explicit and approximate solution of the

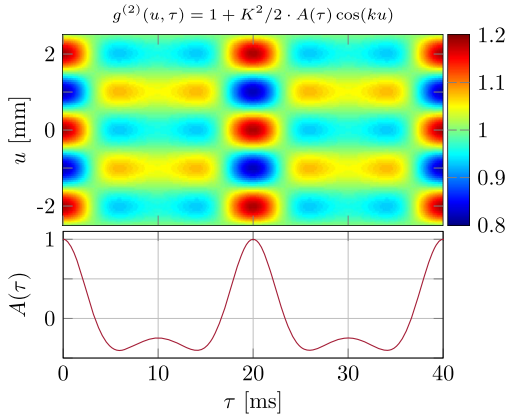

Figure 2. Top: correlation function of an interference pattern with $K = 0.6$, $\lambda = 2$ mm and a perturbation consisting of $\omega_1/2\pi = 50$ Hz, $\varphi_1 = 0.76\ \pi$ calculated with equations (34) and (35) for $N = 1$. Bottom: correlation amplitude depending on the correlation time τ and the perturbation parameters resulting from equation (35). It has its maximum value of 1 at the temporal coordinates $\tau = M_\tau \cdot 2\pi/\omega_1 = M_\tau \cdot 20$ ms, with $M_\tau \in \mathbb{N}_0$.

correlation function are identical. This demonstrates that it depends on the specific perturbation spectrum if either the explicit or approximate solution has to be applied to describe the experimental correlation function correctly.

2.4. Determination of contrast and spatial periodicity

The determination of the contrast K and spatial periodicity λ from the correlation function shall be discussed now. Both can only be correctly obtained at certain correlation times. As mentioned in sections 2.2 and 2.3, the explicit and approximate solution of the correlation function show a periodic modulation in u-direction having the same periodicity λ as the unperturbed interference pattern. The overall amplitude of this modulation (after summing up all multiplet addends) depends on the correlation time τ resulting from the specific perturbation spectrum for both correlation functions (equations (30) and (34)). Its maximum value of 1 is achieved at $\tau = M_\tau \tau_s$, $M_\tau \in \mathbb{N}_0$, with the superperiod $\tau_s = 2\pi/\omega_{\mathrm{gcd}}$ given by the reciprocal value of the greatest common divisor of all perturbation frequencies $\gcd(\omega_1, \ldots, \omega_N) = \omega_{\mathrm{gcd}}$. For each frequency ω_j there is an integer $s_j \in \mathbb{N}$ for which $\omega_{\mathrm{gcd}} = \omega_j/s_j$. At the temporal positions $\tau = M_\tau \tau_s$, only the addends with $n_j = -m_j$ sum up to a maximum value of 1, because then the addends in equation (30) are not phase shifted in u- and τ-direction with respect to each other. The sum of the addends with $n_j \neq -m_j$ is equal to zero at these temporal positions. Therefore, the exact and approximate solution are identical at correlation times $\tau = M_\tau \tau_s$. Using equations (34) and (35), the correlation function then becomes

$$g^{(2)}(u, M_\tau \tau_s) = 1 + \frac{K^2}{2}\cos(ku) \cdot \prod_{j=1}^{N} \underbrace{\left(\sum_{m_j=-\infty}^{\infty} J_{m_j}(\varphi_j)^2 \underbrace{\cos(2\pi M_\tau m_j s_j)}_{=1} \right)}_{=1}$$
$$= 1 + \frac{K^2}{2}\cos(ku), \tag{36}$$

which is suitable to obtain the contrast K and pattern periodicity $\lambda = 2\pi/k$ of the unperturbed interference pattern. If there is no greatest common divisor ω_{gcd}, the superperiod τ_s is infinite and the only position, where the amplitudes have a maximum value of 1, is at $\tau = 0$. Therefore, the determination of the contrast and spatial periodicity using equation (36) can always be applied to the correlation function at the correlation time of $\tau = 0$.

2.5. Correlation function of single- and two-frequency perturbations

The properties of the explicit and approximate correlation function, discussed in sections 2.2 and 2.3, are illustrated below for single- and two-frequency perturbations. The commonalities and differences of both solutions are pointed out.

In the case of one perturbation frequency ω_1 ($N = 1$), the constraint in equation (20) is only fulfilled for $n_1 = -m_1$. Thus, the explicit and approximate solution are identical. A correlation function of an interference pattern with $K = 0.6$, $\lambda = 2$ mm, a perturbation frequency $\omega_1/2\pi = 50$ Hz and a peak phase deviation $\varphi_1 = 0.76\ \pi$ is calculated according to equations (34) and (35) for $N = 1$ and plotted in figure 2 at the top,

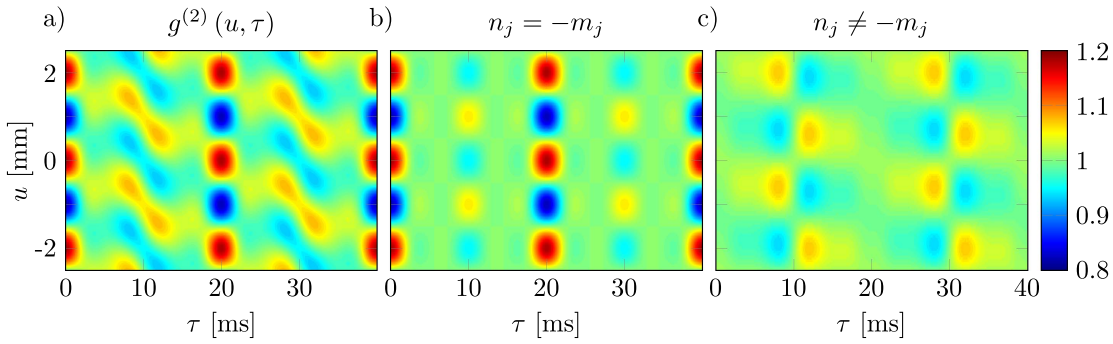

Figure 3. (a) Second-order correlation function $g^{(2)}(u, \tau)$ of an interference pattern with a contrast of $K = 0.6$, a spatial periodicity $\lambda = 2$ mm perturbed with two frequencies $\omega_1/2\pi = 50$ Hz, $\varphi_1 = 0.5\,\pi$, $\phi_1 = 0.25\,\pi$ and $\omega_2/2\pi = 100$ Hz, $\varphi_2 = 0.5\,\pi$, $\phi_2 = -0.25\,\pi$ calculated according to equations (30) and (31). (b) Approximate solution calculated with equations (34) and (35) including only the $n_j = -m_j$ terms. (c) Difference between explicit and approximate solution solely given by the terms with $n_j \neq -m_j$.

showing a clear periodic structure in the correlation length u and time τ. As seen from equation (34), the spatial periodicity of the unperturbed interference pattern is recovered in the correlation function as modulation along u. At each τ, however, the contrast is reduced to $K^2/2 \cdot A(\tau)$. As seen from equation (35) and figure 2 at the bottom, the amplitude $A(\tau)$ reaches its maximum at correlation times that are multiples of the perturbation time period $2\pi/\omega_1 = 20$ ms. Here, $A(\tau)$ becomes 1 and the contrast in the correlation function $K^2/2$ is directly linked to the contrast of the unperturbed interference pattern. According to equation (7) and figure 1, the integrated interference pattern would be completely 'washed-out' for these perturbation parameters. Using correlation theory, however, the contrast and spatial periodicity can be unveiled as described in section 2.4.

In the case of perturbation frequencies, that are multiples of each other, the explicit solution of the correlation function has to be used. This shall be demonstrated for two frequencies with $\omega_2 = 2\omega_1$. Here, equation (20) becomes $(n_1 + m_1) = -2(n_2 + m_2)$ and the constraint is satisfied not only for integer multiplets with $n_{1/2} = -m_{1/2}$, but also for $n_{1/2} \neq -m_{1/2}$, as $\{n_1, m_1, n_2, m_2\} = \{1, 1, -1, 0\}$. These terms lead to additional contributions to the explicit correlation function in equation (30), causing a spatial and temporal phase shift due to the not vanishing phases $\tilde{\varphi}_{\{n_j,m_j\}}$ and $\Phi_{\{n_j,m_j\}}$ (equation (29)). Therefore, the approximate solution of equation (34) is not suitable, and the explicit solution has to be used. In figure 3(a), a second-order correlation function calculated with the explicit solution (equations (30) and (31)) is shown for an interference pattern with a contrast of $K = 0.6$ and a spatial periodicity $\lambda = 2$ mm perturbed with $\omega_1/2\pi = 50$ Hz, $\varphi_1 = 0.5\,\pi$, $\phi_1 = 0.25\,\pi$ and $\omega_2/2\pi = 100$ Hz, $\varphi_2 = 0.5\,\pi$, $\phi_2 = -0.25\,\pi$. The approximate solution (equations (34) and (35)) including only the $n_j = -m_j$ terms can be seen in figure 3(b) and differs clearly from the exact solution in (a). Both correlation functions, figures 3(a) and (b), show a periodic modulation in u-direction having the same periodicity λ as the unperturbed interference pattern. The superperiod $\tau_s = 2\pi/\omega_{\text{gcd}} = 20$ ms can be identified in both correlation functions originating from the greatest common divisor of the involved perturbation frequencies $\omega_{\text{gcd}}/2\pi = 50$ Hz. At correlation times, which are multiples of this superperiod, the explicit and approximate correlation function are identical and the amplitudes achieve their maximum value of 1 (see section 2.4). The difference between the exact and approximate solution, which is solely given due to the terms with $n_j \neq -m_j$, is illustrated in figure 3(c). Its contribution to the correlation function in figure 3(a) leads to the correlation time dependent phase shift of the pattern in u-direction originating from the spatial correlation phases $\tilde{\varphi}_{\{n_j,m_j\}}$ and temporal phases $\Phi_{\{n_j,m_j\}}$.

2.6. Transition between explicit and approximate solution

As discussed in section 2.3, the explicit and approximate solution (equations (30) and (34)) are identical in the case of one perturbation frequency ($N = 1$) and also in the case of numerous frequencies ω_j, that are not multiples of each other. A common scenario, when both solutions differ from each other, is the case when the frequencies are multiples of each other, e.g. for N perturbation frequencies $\omega_j = M_j\omega_1$ with $j = 2 \ldots N$, $M_j \in \mathbb{N}\backslash\{0, 1\}$ and $M_2 < \ldots < M_N$. Here, it shall be shown, that also in this case the approximate solution might be suitable to describe the correlation function.

The explicit solution turns into the approximate, if the largest contributing addend in equation (30) for $n_j \neq -m_j$ is small compared to the largest addend with $n_j = -m_j$. The amplitudes of all addends are given by the peak phase deviations φ_j, via the product of the Bessel functions in equation (28). The maximum value of the

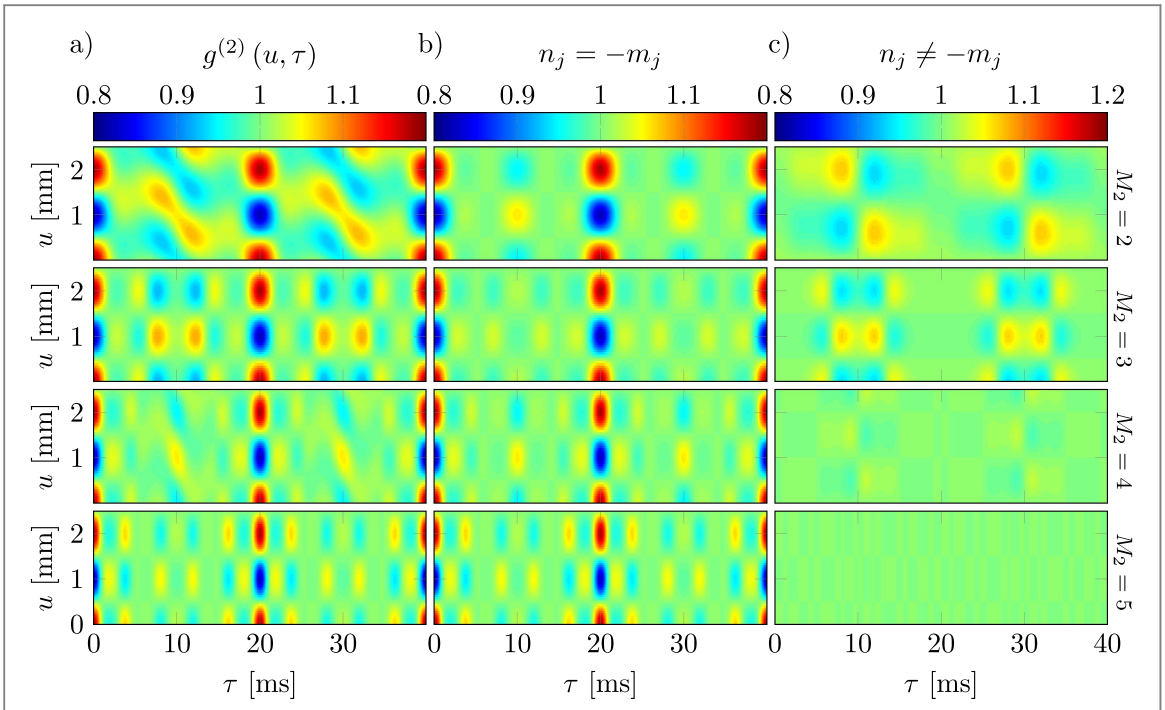

Figure 4. (a) Shown is a perturbation consisting of two frequencies with $\omega_1/2\pi = 50$ Hz, $\varphi_1 = 0.5\,\pi$, $\phi_1 = 0.25\,\pi$ and $\omega_2 = M_2\omega_1$, $M_2 \in \{2, 3, 4, 5\}$ with $\varphi_2 = 0.5\,\pi$, $\phi_2 = -0.25\,\pi$ as calculated according to equation (30). (b) Approximate solution of the second-order correlation function calculated with equation (34). (c) Difference between explicit and approximate solution given by the terms with $n_j \neq -m_j$. The structure in (c) is almost vanished for $M_2 = 4$ and disappeared for $M_2 = 5$. At this transition point, the correlation functions in (a) and (b) are identical and the approximate solution is suitable for the analysis.

Bessel function $J_m(\varphi)$ is approximately achieved, if the order is $m \approx \varphi - 1$ for $\varphi \geqslant 1$ and $m = 0$ otherwise. Therefore, the amplitude of the largest addend with $n_j = -m_j$ is given by

$$\tilde{B}_{\{n_j=-m_j\}}(\varphi_j) \approx \prod_{j=1}^{N} J_{\varphi_j-1}(\varphi_j)^2. \tag{37}$$

Using equation (20), the constraint for the integer multiplets $\{n_j,\ m_j\} \in \ker(c)$ can be written as

$$(n_1 + m_1) = -\sum_{j=2}^{N} M_j(n_j + m_j). \tag{38}$$

This constraint is generally satisfied for the multiplet with $n_j \neq -m_j$, resulting in the largest contributing integer multiplet

$$\{n_1,\ m_1,\ n_2,\ m_2,\ n_3,\ m_3,\ \ldots,\ n_N,\ m_N\} = \left\{\frac{M_2}{2},\ \frac{M_2}{2},\ -(m_2+1),\ m_2,\ -m_3,\ m_3,\ \ldots,\ -m_N,\ m_N\right\}. \tag{39}$$

Using this multiplet and $m \approx \varphi - 1$ for the order of the Bessel function, the amplitude (equation (28)) of the largest addend with $n_j \neq -m_j$ contributing to the correlation function is

$$\tilde{B}_{\{n_j\neq-m_j\}}(\varphi_j) \approx J_{\frac{M_2}{2}}(\varphi_1)^2 J_{-\varphi_2}(\varphi_2) J_{\varphi_2-1}(\varphi_2) \prod_{j=3}^{N} J_{\varphi_j-1}(\varphi_j)^2. \tag{40}$$

Here, the variable factor $J_{\frac{M_2}{2}}(\varphi_1)^2$ is given by $M_2 = \omega_2/\omega_1$ and determines the value of $\tilde{B}_{\{n_j\neq-m_j\}}(\varphi_j)$. The ratio of equations (37) and (40) is

$$\frac{\tilde{B}_{\{n_j\neq-m_j\}}(\varphi_j)}{\tilde{B}_{\{n_j=-m_j\}}(\varphi_j)} = \frac{J_{\frac{M_2}{2}}(\varphi_1)^2 J_{-\varphi_2}(\varphi_2)}{J_{\varphi_1-1}(\varphi_1)^2 J_{\varphi_2-1}(\varphi_2)}. \tag{41}$$

A closer look to the Bessel function unveils that $J_{\frac{M_2}{2}}(\varphi_1)^2$ decays rapidly for $M_2/2 > \varphi_1$, which can be seen with the asymptotic form of the Bessel function for $0 < \varphi_1 \ll \sqrt{n+1}$ [62]

$$J_n(\varphi_1) \approx \frac{1}{\Gamma(n+1)}\left(\frac{\varphi_1}{2}\right)^n, \tag{42}$$

with $\Gamma(n+1) = n!$ denoting the gamma function. Therefore, the explicit solution approaches rapidly to the approximate solution, once $M_2 > 2\varphi_1$.

Figure 4 shows an example for a two frequency perturbation with $M_2 = \omega_2/\omega_1 = \{2, 3, 4, 5\}$. For $\varphi_1 = 0.5\,\pi$, the explicit solution should closely approach the approximate once $M_2 > 2\varphi_1 \approx 3$, as can be seen in figure 4. For $M_2 = 4$, the structure in figure 4(c) is almost vanished. In this case, the leading term of equation (40) is about seven times smaller than $\tilde{B}_{\{n_j=-m_j\}}(\varphi_j)$ in equation (37). The structure in figure 4(c) disappears for $M_2 = 5$. Here, $\tilde{B}_{\{n_j\neq-m_j\}}(\varphi_j)$ is twenty-four times smaller than $\tilde{B}_{\{n_j=-m_j\}}(\varphi_j)$ and has a negligible contribution to the correlation function. Therefore, the correlation functions in figures 4(a) and (b) for $M_2 = 5$ are identical, proving the approximate solution to be suitable for the correlation analysis.

2.7. Amplitude spectrum of the second-order correlation function

As it might be difficult to identify the involved perturbation frequencies from the correlation function (see figure 3), the amplitude spectrum of the correlation function can be calculated and used for the determination of the perturbation characteristics [54]. This is possible, as the Fourier transform of the correlation function equals the power spectrum of the perturbed measurement signal according to the Wiener–Khintchine theorem [56, 57]. Therefore, the applied perturbation frequencies can be identified in the amplitude spectrum of $g^{(2)}(u, \tau)$. To determine the frequency components and their amplitudes, the temporal Fourier transform $\mathcal{F}(g^{(2)}(u, \tau))(u, \omega) = \frac{1}{\sqrt{2\pi}}\int_{-\infty}^{\infty} g^{(2)}(u, \tau)\mathrm{e}^{\mathrm{i}\omega\tau}\mathrm{d}\tau$ of equation (30) is calculated

$$\mathcal{F}(g^{(2)}(u, \tau))(u, \omega) = \sqrt{2\pi}\,\delta(\omega) + \frac{K^2}{2} \cdot \sum_{\substack{\{n_j,m_j\}\in\ker(c)\\ j=1\ldots N}} \mathcal{F}(A_{\{n_j,m_j\}}(\tau, \Phi_{\{n_j,m_j\}}))(\omega) \cdot \cos(ku + \tilde{\varphi}_{\{n_j,m_j\}}), \tag{43}$$

with the Fourier transformed amplitude of equation (31)

$$\begin{aligned}
&\mathcal{F}(A_{\{n_j,m_j\}}(\tau, \Phi_{\{n_j,m_j\}}))(\omega)\\
&= \frac{\tilde{B}_{\{n_j,m_j\}}(\varphi_j)}{2\sqrt{2\pi}}\left(\mathrm{e}^{-\mathrm{i}\Phi_{\{n_j,m_j\}}}\int_{-\infty}^{\infty}\mathrm{e}^{\mathrm{i}(\omega-\sum_{j=1}^{N}m_j\omega_j)\tau}\,\mathrm{d}\tau + \mathrm{e}^{\mathrm{i}\Phi_{\{n_j,m_j\}}}\int_{-\infty}^{\infty}\mathrm{e}^{\mathrm{i}(\omega+\sum_{j=1}^{N}m_j\omega_j)\tau}\,\mathrm{d}\tau\right)\\
&= \frac{\sqrt{2\pi}\,\tilde{B}_{\{n_j,m_j\}}(\varphi_j)}{2}\left[\mathrm{e}^{-\mathrm{i}\Phi_{\{n_j,m_j\}}}\delta\left(\omega - \sum_{j=1}^{N}m_j\omega_j\right) + \mathrm{e}^{\mathrm{i}\Phi_{\{n_j,m_j\}}}\delta\left(\omega + \sum_{j=1}^{N}m_j\omega_j\right)\right].
\end{aligned} \tag{44}$$

Using $\mathrm{e}^{\pm\mathrm{i}\Phi_{\{n_j,m_j\}}} = \cos(\Phi_{\{n_j,m_j\}}) \pm \mathrm{i}\cdot\sin(\Phi_{\{n_j,m_j\}})$ and $\omega_{\{m_j\}} := \sum_{j=1}^{N} m_j\omega_j$, the amplitude in equation (44) results in

$$\begin{aligned}
\mathcal{F}(A_{\{n_j,m_j\}}(\tau, \Phi_{\{n_j,m_j\}}))(\omega) &= \sqrt{2\pi}\,\tilde{B}_{\{n_j,m_j\}}(\varphi_j)\\
&\cdot(\cos(\Phi_{\{n_j,m_j\}})(\delta(\omega + \omega_{\{m_j\}}) + \delta(\omega - \omega_{\{m_j\}}))\\
&+ \mathrm{i}\cdot\sin(\Phi_{\{n_j,m_j\}})(\delta(\omega + \omega_{\{m_j\}}) - \delta(\omega - \omega_{\{m_j\}}))),
\end{aligned} \tag{45}$$

where $\omega_{\{m_j\}}$ are the frequency components and $\delta(\omega)$ the Dirac delta function. The resulting amplitude spectrum $|\mathcal{F}(g^{(2)}(u, \tau))(u, \omega)|$ calculated from equations (43) and (45) is given by

$$\begin{aligned}
\frac{1}{2\pi}|\mathcal{F}(g^{(2)}(u, \tau))(u, \omega)|^2 &= \delta(\omega)^2\\
&+ 2\cdot\left(\frac{K^2}{2}\sum_{\substack{\{n_j,m_j\}\in\ker(c)\\ j=1\ldots N}}\tilde{B}_{\{n_j,m_j\}}(\varphi_j)\cdot\cos(ku + \tilde{\varphi}_{\{n_j,m_j\}})\right.\\
&\left.\cdot\left(\cos\left(\Phi_{\{n_j,m_j\}} - \frac{\pi}{4}\right)\delta(\omega + \omega_{\{m_j\}}) + \cos\left(\Phi_{\{n_j,m_j\}} + \frac{\pi}{4}\right)\delta(\omega - \omega_{\{m_j\}})\right)\right)^2.
\end{aligned} \tag{46}$$

As for the explicit correlation function in equation (30), the sum in equation (46) is taken over the integer multiplets $\{n_j, m_j\} \in \ker(c)$, $j = 1 \ldots N$ resulting from the constraint in equation (20). Each addend shows a periodic structure in the correlation length u with the same spatial periodicity λ as the unperturbed interference pattern, but shifted in u-direction by the spatial correlation phase $\tilde{\varphi}_{\{n_j,m_j\}}$ (equation (29)). The amplitude of this modulation depends on the peak phase deviation φ_j, via the product of the Bessel functions in equation (28) modified by the cosine of the temporal phase $\Phi_{\{n_j,m_j\}}$ (equation (29)). The frequency position of the modulation is given by the frequency component $\omega_{\{m_j\}} := \sum_{j=1}^{N} m_j\omega_j$ with the coefficients $\{n_j, m_j\} \in \ker(c)$. The summed up amplitude spectrum contains all frequency components up to a maximum frequency $\max\{\varphi_j\omega_j\}$ resulting from the strong decay of the Bessel function as discussed for the explicit solution of the correlation function (equation (30)).

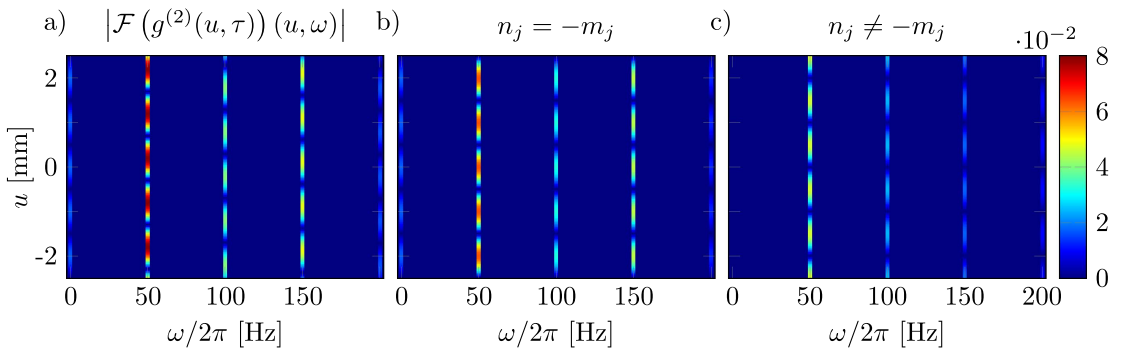

Figure 5. (a) Amplitude spectrum $|\mathcal{F}(g^{(2)}(u,\tau))(u,\omega)|$ of a perturbation with $\omega_1/2\pi = 50$ Hz, $\varphi_1 = 0.5\,\pi$, $\phi_1 = 0.25\,\pi$ and $\omega_2/2\pi = 100$ Hz, $\varphi_2 = 0.5\,\pi$, $\phi_2 = -0.25\,\pi$ calculated according to equation (46). (b) Approximate solution of the amplitude spectrum calculated using equation (47). (c) Contribution of the addends with $n_j \neq -m_j$ to the amplitude spectrum in (a).

The amplitude spectrum of the approximate second-order correlation function in equation (34) is calculated from equation (46) using $n_j = -m_j$ and reads

$$\frac{1}{2\pi}\,|\mathcal{F}(g^{(2)}(u,\tau))(u,\omega)|^2 = \delta(\omega)^2 + \left(\frac{K^2}{2}\cos(ku)\sum_{\substack{\{-m_j,m_j\}\in\ker(c)\\ j=1\ldots N}}\left(\prod_{j=1}^{N} J_{m_j}(\varphi_j)^2\right)\cdot\left(\delta(\omega+\omega_{\{m_j\}})+\delta(\omega-\omega_{\{m_j\}})\right)\right)^2. \tag{47}$$

As with the approximate solution, also the amplitude spectrum is independent from the spatial correlation phases $\tilde{\varphi}_{\{n_j,m_j\}}$ and temporal phases $\Phi_{\{n_j,m_j\}}$. Therefore, the spatial periodicity in the amplitude spectrum is directly given by the periodicity of the unperturbed interference pattern. The amplitude of the modulation in u-direction is now solely given by the peak phase deviations φ_j, via the square of the Bessel functions.

The amplitude spectrum corresponding to the second-order correlation function of the two frequency perturbation shown in figure 3(a) is calculated according to equation (46) and plotted in figure 5(a) for positive frequency components. The amplitude spectrum of the approximate solution of equation (47) is plotted in figure 5(b). In figure 5(c), the contribution of the addends with $n_j \neq -m_j$ to the explicit solution is shown. For each frequency component, given by $m_1\omega_1 + m_2\omega_2$ with $\{n_1, m_1, n_2, m_2\} \in \ker(c)$, the modulation of the unperturbed interference pattern with the periodicity λ can be identified in the spatial direction u. In figure 5(c), the phase shift of the interference pattern in the spatial direction is caused by the spatial phases $\tilde{\varphi}_{\{n_j,m_j\}}$. In figure 5(b), the interference pattern is not shifted in the spatial direction u and the amplitudes of the involved frequency components only depend on the peak phase deviations φ_j via the square of the Bessel functions in equation (47). As for the transition between the explicit and approximate correlation function discussed in section 2.6, the amplitude spectrum of the explicit correlation function (equation (46)) turns into the approximate solution (equation (47)), if the largest contributing addend in equation (40) is small compared to equation (37).

2.8. Determination of perturbation characteristics

The identification of unknown perturbation frequencies from the correlation function is difficult, because the structure of the correlation function does not reveal the frequencies directly (see figure 3). The amplitude spectrum offers a better access to the frequency components included in the correlation function. In [54], a numerical algorithm is described, which allows to identify unknown perturbation frequencies. After the determination of the perturbation frequencies ω_j, either the explicit (equation (46)) or approximate solution (equation (47)) is applied, depending on the specific perturbation spectrum (see end of sections 2.3 and 2.6), to obtain the corresponding peak phase deviations φ_j and phases ϕ_j. The latter are not uniquely determined, as the correlation function is invariant under phase transformations. However, it is possible to identify the original phases by the reconstruction of the unperturbed interference pattern with the obtained perturbation frequencies and amplitudes.

2.8.1. Invariance of the correlation function

As discussed in section 2.4, the contrast and pattern periodicity of the unperturbed interference pattern can be unveiled from the second-order correlation function. Using the amplitude spectrum, also the perturbation frequencies, amplitudes and phases can be determined (section 2.7). However, the perturbation phases can not be uniquely obtained. For a single perturbation frequency, for instance, the phase information is completely lost in the correlation function. However, for larger numbers of perturbation frequencies ($N > 1$), the phase informations are not completely lost. For $N > 1$, only relative phase information can be unveiled. In this context, it is useful to understand under which phase transformation $\phi_j \rightarrow \phi_j'$ the correlation function stays invariant.

As only time and position differences between particle events are taken into account, the second-order correlation function is invariant under position shifts $y \rightarrow y + y_0$ and time transformations $t \rightarrow t + t_0$. Using equations (1) and (2) such a time transformation and position shift equals transformations

$$y \rightarrow y + y_0 \quad \widehat{=} \quad \varphi(t) \rightarrow \varphi(t) + k y_0, \tag{48}$$

$$t \rightarrow t + t_0 \quad \widehat{=} \quad \phi_j \rightarrow \phi_j + \omega_j t_0. \tag{49}$$

Furthermore, the correlation function is invariant under simultaneous time and space reversal: $t \rightarrow -t$, $y \rightarrow -y$, because only time and space differences are taken into account. According to equations (1) and (2), this transformation equals a phase transformation

$$t \rightarrow -t, y \rightarrow -y \quad \widehat{=} \quad \phi_j \rightarrow -\phi_j + \pi. \tag{50}$$

Hence, under above phase transformations (equations (49) and (50)) the correlation function stays unchanged.

Exemplary, the invariance is calculated for a perturbation with two frequencies ($N = 2$) and phases ϕ_1 and ϕ_2. According to equation (49), the correlation function is invariant for following phase transformations

$$\hat{\phi}_1 = \phi_1 + \omega_1 t_0, \quad \hat{\phi}_2 = \phi_2 + \omega_2 t_0. \tag{51}$$

Eliminating t_0 yields

$$\hat{\phi}_2 = \frac{\omega_2}{\omega_1}\hat{\phi}_1 + \left(\phi_2 - \frac{\omega_2}{\omega_1}\phi_1\right). \tag{52}$$

Every phase duplet $\{\hat{\phi}_1, \hat{\phi}_2\}$ described by this equation, yields the same correlation function as the original phase duplet $\{\phi_1, \phi_2\}$. Therefore, the absolute phases ϕ_1 and ϕ_2 can not be uniquely determined by the correlation analysis. A second set of phase duplets $\{\tilde{\phi}_1, \tilde{\phi}_2\}$ with identical correlation functions can be found after evaluating the phase transformation for time and space reversal from equation (50)

$$\tilde{\phi}_1 = -\hat{\phi}_1 + \pi, \quad \tilde{\phi}_2 = -\hat{\phi}_2 + \pi, \tag{53}$$

yielding together with equation (52)

$$\tilde{\phi}_2 = \frac{\omega_2}{\omega_1}\tilde{\phi}_1 + \left(\frac{\omega_2}{\omega_1}\phi_1 - \phi_2 + \pi\left(1 - \frac{\omega_2}{\omega_1}\right)\right). \tag{54}$$

As result, there are two linear equations (equations (52) and (54)), that describe the same correlation function. It is thus not possible to determine the original phases ϕ_1 and ϕ_2 from the correlation analysis.

2.8.2. Determination of perturbation phases

Although the original phases ϕ_j can not be determined by the correlation analysis, the identification is possible by the reconstruction of the unperturbed interference pattern using the obtained perturbation parameters ω_j and φ_j [54]

$$y_{i,\mathrm{new}} = y_i - \frac{\lambda}{2\pi}\varphi(t_i) = y_i - \frac{\lambda}{2\pi}\sum_{j=1}^{N}\varphi_j \cos(\omega_j t_i + \phi_j), \tag{55}$$

with the spatial coordinate of the reconstructed interference pattern $y_{i,\mathrm{new}}$, the time-dependent perturbation $\varphi(t_i)$ (equation (2)) and y_i, t_i the spatial and temporal coordinate of particle i forming the perturbed interference pattern. The phases ϕ_j are varied until the maximum contrast of the reconstructed interference pattern is achieved. Using equations (52) or (54) in the reconstruction process, the free parameter space for the phases ϕ_j can be reduced by one-dimension.

3. Numerical second-order correlation function

In this chapter, the characteristics of the numerical second-order correlation function used for the evaluation of the experimental data are analyzed in detail. First, the numerical correlation function is derived and investigated how the discretization affects the obtained parameters as contrast and perturbation amplitude. A theoretical description of the influence on the correlation analysis and the effect of noise is presented. This theory is numerically cross-checked by simulations of single-particle interference. Afterwards, the possibility to use the correlation analysis for broad-band frequency noise is demonstrated by a simulation with a Gaussian distributed noise. At the end of this chapter, the application limits of the second-order correlation theory are discussed.

3.1. Correlation function for discrete signals

So far, the correlation function has been calculated from the analytic probability distribution of particle impacts at the detector. In reality, however, the detector yields a discrete signal of particle impacts for a finite acquisition time T. The corresponding second-order correlation function $g^{(2)}(u, \tau)$ is thus extracted from this detector signal $f(y, t)$ consisting of N particle arrival times t_i and coordinates y_i, $(i = 1 \ldots N)$

$$f(y, t) = \sum_{i=1}^{N} \delta(y - y_i)\delta(t - t_i). \tag{56}$$

Here, δ denotes the Dirac delta function, which assures normalization of $f(y, t)$

$$\int_{-\infty}^{\infty}\int_{-\infty}^{\infty} f(y, t)\mathrm{d}y\mathrm{d}t = N. \tag{57}$$

The approximation of the particle impacts in the detection plane by the Dirac delta function is suitable as the pulse width at the detector is much smaller than the mean time distance between particle impacts. Using this definition of the detector signal, the correlation function is calculated according to equation (9). As before, the denominator is calculated first

$$\begin{aligned}\langle\!\langle f(y + u, t + \tau)\rangle\!\rangle_{y,t} &= \frac{1}{TY}\int_0^T \int_{-Y/2}^{Y/2} \sum_{j=1}^{N} \delta(y + u - y_j)\delta(t + \tau - t_j)\mathrm{d}y\mathrm{d}t \\ &= \frac{1}{TY}\sum_{j=1}^{N} \underbrace{\int_0^T \delta(t - t_j + \tau)\mathrm{d}t}_{=1} \underbrace{\int_{-Y/2}^{Y/2} \delta(y - y_j + u)\mathrm{d}y}_{=1} \\ &= \frac{1}{TY}\sum_{j=1}^{N} 1 = \frac{N}{TY},\end{aligned} \tag{58}$$

with the acquisition time T and length Y. The second term in the denominator can be determined from equation (58) for $u = 0$ and $\tau = 0$, yielding $\langle\!\langle f(y, t)\rangle\!\rangle_{y,t} = N/TY$. Using equation (56), the numerator in equation (9) becomes

$$\begin{aligned}&\langle\!\langle f(y + u, t + \tau)f(y, t)\rangle\!\rangle_{y,t} \\ &= \frac{1}{TY}\int_0^T \int_{-Y/2}^{Y/2} \sum_{i,j=1}^{N} \delta(y + u - y_j)\delta(t + \tau - t_j)\delta(y - y_i)\delta(t - t_i)\mathrm{d}y\mathrm{d}t \\ &= \frac{1}{TY}\sum_{i,j=1}^{N} \underbrace{\int_0^T \delta(t + \tau - t_j)\delta(t - t_i)\mathrm{d}t}_{=\delta(\tau + t_i - t_j)} \underbrace{\int_{-Y/2}^{Y/2} \delta(y + u - y_j)\delta(y - y_i)\mathrm{d}y}_{=\delta(u + y_i - y_j)} \\ &= \frac{1}{TY}\sum_{i,j=1}^{N} \delta(\tau + t_i - t_j)\delta(u + y_i - y_j).\end{aligned} \tag{59}$$

With the results of equations (58) and (59), the discrete second-order correlation function is given by

$$\begin{aligned}g^{(2)}(u, \tau) &= \frac{\langle\!\langle f(y + u, t + \tau)f(y, t)\rangle\!\rangle_{y,t}}{\langle\!\langle f(y + u, t + \tau)\rangle\!\rangle_{y,t}\langle\!\langle f(y, t)\rangle\!\rangle_{y,t}} \\ &= \frac{TY}{N^2}\sum_{i,j=1}^{N} \delta(\tau + t_i - t_j)\delta(u + y_i - y_j).\end{aligned} \tag{60}$$

To achieve a proper correlation function, which can be compared with the analytic theory, it is necessary to implement a temporal and spatial discretization step size $\Delta\tau$ and Δu in equation (60), yielding

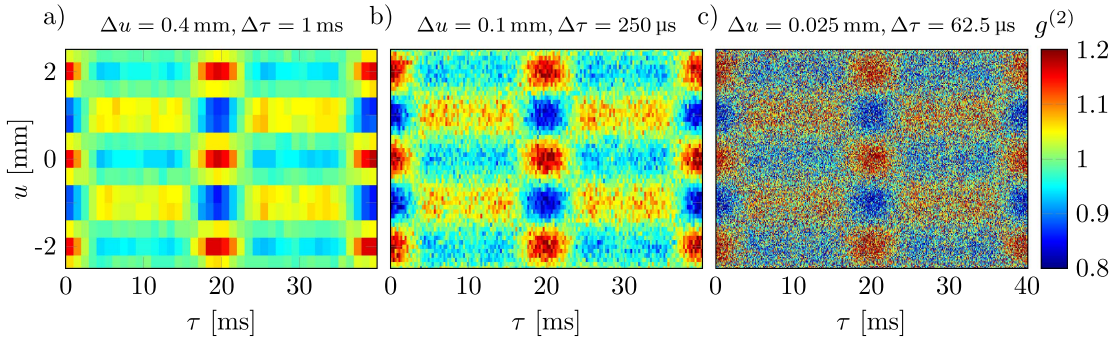

Figure 6. Correlation functions with different temporal and spatial discretization step sizes Δu and $\Delta\tau$ extracted according to equation (62) from a single-particle simulation of an interference pattern with a contrast $K = 0.6$ and a spatial periodicity $\lambda = 2$ mm perturbed with $\omega_1/2\pi = 50$ Hz and $\varphi_1 = 0.75\,\pi$. (a) The structure is 'smeared out', because the discretization step size is too large. (b) Compared to (a), the structure is clearly visible, but the noise increases with smaller Δu and $\Delta\tau$. (c) For even smaller discretization step size, the noise grows larger.

$$g^{(2)}(u,\tau) = \frac{TY}{N^2}\frac{1}{\Delta\tau\Delta u}\underbrace{\int_{\tau-\frac{\Delta\tau}{2}}^{\tau+\frac{\Delta\tau}{2}}\int_{u-\frac{\Delta u}{2}}^{u+\frac{\Delta u}{2}}\sum_{i,j=1}^{N}\delta(\tau+t_i-t_j)\delta(u+y_i-y_j)\mathrm{d}u\mathrm{d}\tau}_{=N_{u,\tau}}$$
$$= \frac{TY}{N^2\Delta\tau\Delta u}N_{u,\tau}, \tag{61}$$

with $N_{u,\tau}$ denoting the number of particle pairs (i,j) with distances $(y_i - y_j) \in [u - \Delta u/2,\ u + \Delta u/2]$ and time separations $(t_i - t_j) \in [\tau - \Delta\tau/2,\ \tau + \Delta\tau/2]$.

Due to the finite acquisition time T and length Y, the probability to detect particle impacts with large temporal and spatial differences is reduced by a factor of $(1 - \tau/T)$ and $(1 - |u|/Y)$, respectively. Therefore, the number $N_{u,\tau}$ in equation (61) has to be corrected for this effect, resulting in

$$g^{(2)}(u,\tau) = \frac{TY}{N^2\Delta\tau\Delta u}\frac{N_{u,\tau}}{\left(1-\frac{\tau}{T}\right)\left(1-\frac{|u|}{Y}\right)}. \tag{62}$$

As with the analytic correlation function, the numerical correlation function in equation (62) is normalized to one.

Three correlation functions with different spatial and temporal discretization step sizes are illustrated in figure 6. They are extracted using equation (62) from a single-particle simulation of an interference pattern (section 3.3) with a contrast $K = 0.6$ and a spatial periodicity $\lambda = 2$ mm perturbed with $\omega_1/2\pi = 50$ Hz and $\varphi_1 = 0.75\,\pi$. If Δu and $\Delta\tau$ are too large, the structure in the correlation function gets 'smeared out' as can be seen in figure 6(a). In contrast, the structure is clearly visible in figure 6(b). However, the noise in the correlation function increases compared to figure 6(a). This noise grows larger for even smaller discretization step size as seen in figure 6(c). Therefore, it is necessary to understand the effects of discretization and choose Δu and $\Delta\tau$ in an appropriate way.

3.2. Discretization effects

In this section, the effects of the discretization step size on the correlation analysis and noise in the correlation function are analyzed. Therefore, the influence on the contrast and peak phase deviation due to the discretization of the correlation function is derived for one perturbation frequency. The theory reveals how the spatial and temporal discretization step size have to be chosen. Afterwards, a theoretical description for the noise in the correlation function and the corresponding amplitude spectrum is derived. Thereby, an optimum spatial discretization step size is found, resulting in a maximum signal-to-noise ratio. At the end, an estimation of the smallest detectable peak phase deviation is given.

3.2.1. Influence on correlation analysis

To study the influence of the spatial and temporal discretization step size Δu and $\Delta\tau$, the analytic solution from equation (34) is used. For simplicity, only one perturbation frequency ω_1 is taken into account. Discretizing the correlation function into temporal and spatial intervals $\Delta\tau$ and Δu, then yields

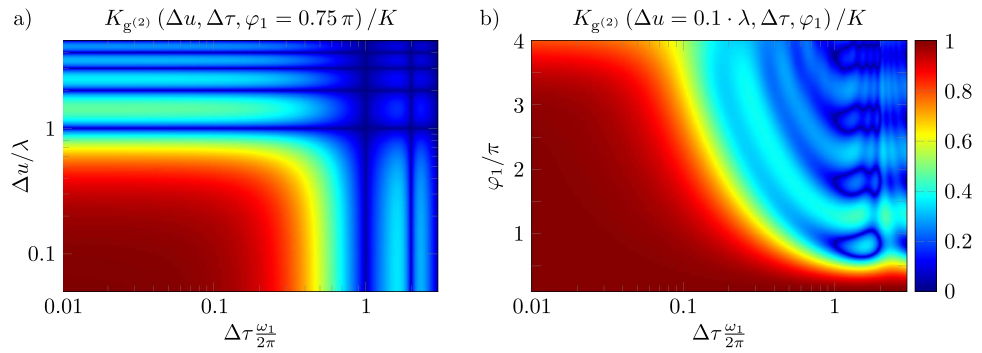

Figure 7. (a) Dependence of the extracted contrast $K_{g^{(2)}}(\Delta u,\ \Delta\tau,\ \varphi_1 = 0.75\ \pi)/K$ on the spatial and temporal discretization step size Δu and $\Delta\tau$ for one perturbation frequency ω_1 with a peak phase deviation of $\varphi_1 = 0.75\ \pi$. (b) Dependence of $K_{g^{(2)}}(\Delta u = 0.1\cdot\lambda,\ \Delta\tau,\ \varphi_1)/K$ on the temporal discretization $\Delta\tau$ and peak phase deviation φ_1 for $\Delta u/\lambda = 0.1$.

$$\begin{aligned} g^{(2)}(u,\ \tau)_{\Delta u,\Delta\tau} &= \frac{1}{\Delta\tau\Delta u}\int_{u-\frac{\Delta u}{2}}^{u+\frac{\Delta u}{2}}\int_{\tau-\frac{\Delta\tau}{2}}^{\tau+\frac{\Delta\tau}{2}} g^{(2)}(u,\ \tau)\mathrm{d}\tau\mathrm{d}u \\ &= 1 + \frac{K^2}{2}\frac{1}{\Delta u}\int_{u-\frac{\Delta u}{2}}^{u+\frac{\Delta u}{2}}\cos(ku)\mathrm{d}u \cdot \sum_{m_1=-\infty}^{\infty} J_{m_1}(\varphi_1)^2\frac{1}{\Delta\tau}\int_{\tau-\frac{\Delta\tau}{2}}^{\tau+\frac{\Delta\tau}{2}}\cos(m_1\omega_1\tau)\mathrm{d}\tau \\ &= 1 + \frac{K^2}{2}\cdot A(\tau)_{\Delta\tau}\,\mathrm{sinc}\left(k\frac{\Delta u}{2}\right)\cos(ku), \end{aligned} \tag{63}$$

with the sinc-function $\mathrm{sinc}(x) = \sin(x)/x$ and the amplitude

$$A(\tau)_{\Delta\tau} = \sum_{m_1=-\infty}^{\infty} J_{m_1}(\varphi_1)^2\cdot\mathrm{sinc}\left(m_1\omega_1\frac{\Delta\tau}{2}\right)\cos(m_1\omega_1\tau). \tag{64}$$

For $\Delta u = 0$ and $\Delta\tau = 0$, equations (63) and (64) yield the analytic solution of the correlation function in equations (34) and (35) for $N = 1$.

As discussed in section 2.4, the contrast K and spatial periodicity λ of the unperturbed interference pattern are determined from the correlation function at $\tau = 0$ (equation (36)). For this correlation time, equations (63) and (64) become

$$g^{(2)}(u,\ 0)_{\Delta u,\Delta\tau} = 1 + \frac{K^2}{2}\cdot A(0)_{\Delta\tau}\,\mathrm{sinc}\left(k\frac{\Delta u}{2}\right)\cos(ku), \tag{65}$$

with

$$A(0)_{\Delta\tau} = \sum_{m_1=-\infty}^{\infty} J_{m_1}(\varphi_1)^2\cdot\mathrm{sinc}\left(m_1\omega_1\frac{\Delta\tau}{2}\right). \tag{66}$$

Thus, the spatial periodicity $\lambda = 2\pi/k$ is not influenced by the discretization step size, but the extracted contrast $K_{g^{(2)}}$ is modified to

$$K_{g^{(2)}}(\Delta u,\ \Delta\tau,\ \varphi_1) = K\cdot\sqrt{\left|A(0)_{\Delta\tau}\cdot\mathrm{sinc}\left(k\frac{\Delta u}{2}\right)\right|}. \tag{67}$$

This contrast is zero for multiples of $\Delta\tau = 2\pi/\omega_1$ and $\Delta u = \lambda$, because the sinc-function is zero for this values. For $\Delta\tau \to 0$ and $\Delta u \to 0$, the sinc-functions in equations (66) and (67) approach to 1. Full contrast K is only achieved for $\Delta u = \Delta\tau = 0$. The dependence of the extracted contrast $K_{g^{(2)}}$ on $\Delta\tau$ and Δu is illustrated in figure 7(a) for a peak phase deviation of $\varphi_1 = 0.75\ \pi$. The dependence of the extracted contrast on the temporal discretization step size $\Delta\tau$ and the peak phase deviation φ_1 is shown in figure 7(b) for $\Delta u/\lambda = 0.1$.

To determine the perturbation frequency ω_1 and corresponding peak phase deviation φ_1 from the correlation function, the analytic amplitude spectrum of equation (47) is used. For discrete signals, the amplitude spectrum also depends on Δu and $\Delta\tau$. This dependence is calculated from equations (63) and (64) with a temporal Fourier transformation, yielding

$$\frac{1}{2\pi}\left|\mathcal{F}\left(g^{(2)}(u,\tau)_{\Delta u,\Delta\tau}\right)(u,\omega)\right|^2 = \delta(\omega)^2 + \left(\frac{K^2}{2}\mathrm{sinc}\left(k\frac{\Delta u}{2}\right)\cos(ku)\right.$$
$$\left.\cdot \sum_{m_1=-\infty}^{\infty} J_{m_1}(\varphi_1)^2 \cdot \mathrm{sinc}\left(m_1\omega_1\frac{\Delta\tau}{2}\right)\left(\delta(\omega + m_1\omega_1) + \delta(\omega - m_1\omega_1)\right)\right)^2, \tag{68}$$

with the frequency components $\pm m_1\omega_1$. Comparing equation (68) with the analytic solution in equation (47) for $N = 1$, it can be seen, that the frequency components $\pm m_1\omega_1$ are not changed, but their amplitudes $J_{m_1}(\varphi_1)^2$ are modified in equation (68) due to the spatial and temporal discretization. This dependence is calculated for the amplitude of the fundamental frequency component in equation (68) with $m_1 = 1$ and $u = 0$, resulting in

$$\frac{1}{\sqrt{2\pi}}\left|\mathcal{F}\left(g^{(2)}(0,\tau)_{\Delta u,\Delta\tau}\right)(0,\omega_{\{m_1=1\}})\right| = \frac{K^2}{2}J_1(\bar{\varphi}_1)^2, \tag{69}$$

with the modified amplitude $J_1(\bar{\varphi}_1)^2$ of the fundamental frequency component ω_1 depending on Δu and $\Delta\tau$

$$J_1(\bar{\varphi}_1)^2 = \mathrm{sinc}\left(k\frac{\Delta u}{2}\right)\mathrm{sinc}\left(\omega_1\frac{\Delta\tau}{2}\right)\cdot J_1(\varphi_1)^2. \tag{70}$$

Here, the amplitude of the fundamental frequency component $J_1(\varphi_1)^2$ is reduced by the factor of $\mathrm{sinc}\left(k\frac{\Delta u}{2}\right)\mathrm{sinc}\left(\omega_1\frac{\Delta\tau}{2}\right)$, which needs to be taken into account for the determination of φ_1. Therefore, the peak phase deviation $\bar{\varphi}_1$ extracted from the amplitude spectrum of the correlation function also depends on the discretization step size via the square of the Bessel function. For $\Delta u \to 0$ and $\Delta\tau \to 0$, equation (69) results in $K^2/2 \cdot J_1(\varphi_1)^2$ yielding the correct peak phase deviation φ_1.

3.2.2. Influence of noise

As discussed in section 3.1, a real experiment requires the correlation function to be derived from a finite number of detection events. More precisely, it is calculated from the number of correlated particle pairs $N_{u,\tau}$ within a given correlation window $\Delta\tau$ and Δu. Due to the statistical nature of the particles, $N_{u,\tau}$ is subject to Poissonian noise, which is transferred onto the correlation function and the corresponding amplitude spectrum. In principle, this limits the signal-to-noise ratio and the minimum detectable perturbation amplitude.

In the following section, this effect is estimated and optimal settings for the discretization step size are found. Therefore, all fluctuating variables X are described by their corresponding mean values $\langle X\rangle$ and variances σ_X^2, with σ_X being the standard deviation

$$\sigma_X^2 = \langle (X - \langle X\rangle)^2\rangle = \langle X^2\rangle - \langle X\rangle^2 . \tag{71}$$

For simplicity reasons the analysis is restricted to correlation times $\tau \ll T$ and positions $u \ll Y$. With the correlation function from equation (62) being normalized to 1, it can be found

$$g^{(2)}(u,\tau) = \frac{N_{u,\tau}}{\langle N_{u,\tau}\rangle} \quad \text{with} \quad \langle N_{u,\tau}\rangle = \frac{N^2\Delta\tau\Delta u}{TY}. \tag{72}$$

The expected standard deviation can then be calculated yielding

$$\sigma^2_{g^{(2)}} = \langle g^{(2)}(u,\tau)^2\rangle - \langle g^{(2)}(u,\tau)\rangle^2 = \frac{\langle N_{u,\tau}^2\rangle}{\langle N_{u,\tau}\rangle^2} - 1. \tag{73}$$

With $N_{u,\tau}$ following a Poissonian distribution, variance and mean value are directly linked

$$\sigma^2_{N_{u,\tau}} = \langle N_{u,\tau}^2\rangle - \langle N_{u,\tau}\rangle^2 = \langle N_{u,\tau}\rangle, \tag{74}$$

yielding

$$\sigma^2_{g^{(2)}} = \frac{1}{\langle N_{u,\tau}\rangle} = \frac{TY}{N^2\Delta\tau\Delta u} = \frac{N_\tau N_u}{N^2}. \tag{75}$$

As expected, the variance (noise) of the correlation function depends on the total number of detected particles and the number of bins $N_\tau = T/\Delta\tau$ and $N_u = Y/\Delta u$ in the temporal and spatial direction.

Before calculating, how the noise in the correlation function transfers onto its amplitude spectrum, the correlation function is split in two parts: the first part $g^{(2)}_{\mathrm{id}}$ describing the ideal correlation function, as expected in the limit of infinite detection events and the second part f describing the noise only

$$g^{(2)}(\tau) = g^{(2)}_{\mathrm{id}}(\tau) + f(\tau). \tag{76}$$

Obviously, mean values and standard deviations of these functions are given to

$$\langle g^{(2)}_{\mathrm{id}}\rangle = \langle g^{(2)}\rangle,\ \sigma_{g^{(2)}_{\mathrm{id}}} = 0 \quad \text{and} \quad \langle f(\tau)\rangle = 0,\ \sigma_f = \sigma_{g^{(2)}}. \tag{77}$$

Following this description, the amplitude spectrum of the correlation function reads

$$|\mathcal{G}(\omega)| = |\mathcal{G}_{\mathrm{id}}(\omega) + \mathcal{F}(\omega)| \approx |\mathcal{G}_{\mathrm{id}}(\omega)| + |\mathcal{F}(\omega)|, \tag{78}$$

with $\mathcal{G}$ and $\mathcal{F}$ denoting the discrete Fourier transforms of the time discrete signals $g^{(2)}$ and f

$$\mathcal{F}(\omega) = \frac{1}{\tau_{\max}} \int_0^{\tau_{\max}} f(\tau) \mathrm{e}^{\mathrm{i}\omega\tau} \mathrm{d}\tau = \frac{\Delta\tau}{\tau_{\max}} \sum_{n=1}^{N} f_n \mathrm{e}^{\mathrm{i}\omega t_n}. \tag{79}$$

Here, $\tau_{\max}$ denotes the maximum correlation time up to which the correlation function is evaluated. The noise in the spectrum is thus solely included in $|\mathcal{F}(\omega)|$. Using Parsival's theorem [63] together with $N_{\tau_{\max}} = \tau_{\max}/\Delta\tau$, it can be found

$$\langle |\mathcal{F}(\omega)|^2 \rangle = \frac{\sigma_f^2}{N_{\tau_{\max}}} \quad \text{and} \quad \langle |\mathcal{F}(\omega)| \rangle^2 = \frac{\pi}{4} \frac{\sigma_f^2}{N_{\tau_{\max}}} \tag{80}$$

and thus a direct link between the noise in the power spectrum and the noise in the correlation function (equation (75))

$$\sigma^2_{|\mathcal{F}(\omega)|} = \left(1 - \frac{\pi}{4}\right) \frac{\sigma^2_{g^{(2)}}}{N_{\tau_{\max}}} = \left(1 - \frac{\pi}{4}\right) \frac{N_u}{N^2} \frac{T}{\tau_{\max}}. \tag{81}$$

The signal-to-noise ratio $\mathrm{SNR}(\Delta u, \Delta\tau)$ of the amplitude spectrum used for the determination of the peak phase deviation φ_1 can be calculated with equations (69), (70) and (81) yielding

$$\begin{aligned} \mathrm{SNR}(\Delta u, \Delta\tau) &= \frac{\frac{1}{\sqrt{2\pi}} |\mathcal{F}(g^{(2)}(0, \tau)_{\Delta u, \Delta\tau})(0, \omega_{\{m_1=1\}})|}{\sigma_{|\mathcal{F}(\omega)|}} \\ &= \frac{K^2 J_1(\varphi_1)^2}{\sqrt{\left(1 - \frac{\pi}{4}\right) 2k}} \frac{\sin\left(k\frac{\Delta u}{2}\right)}{\left(k\frac{\Delta u}{2}\right)^{\frac{1}{2}}} \mathrm{sinc}\left(\omega_1 \frac{\Delta\tau}{2}\right) \cdot \frac{N\sqrt{\tau_{\max}/T}}{\sqrt{Y}} \\ &= \alpha \cdot \frac{\sin\left(k\frac{\Delta u}{2}\right)}{\left(k\frac{\Delta u}{2}\right)^{\frac{1}{2}}} \mathrm{sinc}\left(\omega_1 \frac{\Delta\tau}{2}\right), \end{aligned} \tag{82}$$

with

$$\alpha = 0.6089 \cdot K^2 J_1(\varphi_1)^2 \cdot \frac{N\sqrt{\tau_{\max}/T}}{\sqrt{Y/\lambda}}. \tag{83}$$

For $\Delta\tau \to 0$, the sinc-function approaches to 1 and the signal-to-noise ratio only depends on the spatial discretization step size Δu. The function $f\left(k\frac{\Delta u}{2}\right) = \sin\left(k\frac{\Delta u}{2}\right) \Big/ \left(k\frac{\Delta u}{2}\right)^{\frac{1}{2}}$ has a global maximum at the position $k\frac{\Delta u_{\mathrm{opt}}}{2} = 1.1656$ with the maximum value of $f\left(k\frac{\Delta u_{\mathrm{opt}}}{2}\right) = 0.8512$. Hence, the optimum spatial discretization step size, leading to a maximum of the signal-to-noise ratio, becomes

$$\Delta u_{\mathrm{opt}} = 0.371 \cdot \lambda. \tag{84}$$

The signal-to-noise ratio calculated with equation (82) is plotted in figure 8 for different spatial and temporal discretization step sizes. The optimum spatial discretization step size is clearly visible at $\Delta u/\lambda = 0.371$. From equations (82) and (83), the optimum signal-to-noise ratio is deduced for $\Delta u_{\mathrm{opt}} = 0.371 \cdot \lambda$ and $\Delta\tau \to 0$

$$\mathrm{SNR}_{\mathrm{opt}}(\Delta u_{\mathrm{opt}} = 0.371 \cdot \lambda, \Delta\tau \to 0) = 0.5183 \cdot K^2 J_1(\varphi_1)^2 \cdot \frac{N\sqrt{\tau_{\max}/T}}{\sqrt{Y/\lambda}}. \tag{85}$$

A lower limit for the identification of small peak phase deviations $\varphi_1 \ll 1$ can be derived from equation (85) by setting $\mathrm{SNR}_{\mathrm{opt}}$ equal to 1. This sets the threshold at which the noise and signal have equal amplitude. With $J_1(\varphi_1)^2 \approx \varphi_1^2/4$ and equation (85), this yields

$$\varphi_{1,\min} = 0.8842\,\pi \cdot \frac{(Y/\lambda)^{\frac{1}{4}}}{K N^{\frac{1}{2}} (\tau_{\max}/T)^{\frac{1}{4}}}. \tag{86}$$

For the measurement of small peak phase deviations it is thus favorable to have an interference pattern with large contrast K and pattern periodicity λ. Furthermore, a large number of particles N decreases the minimum detectable peak phase deviation.

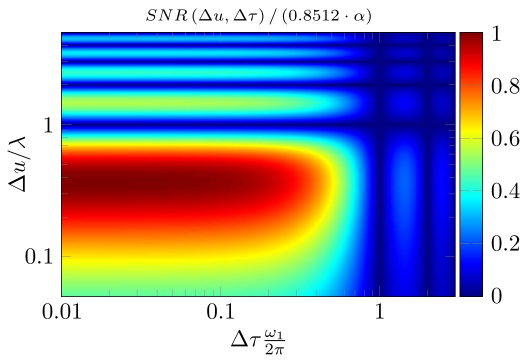

Figure 8. Signal-to-noise ratio calculated with equation (82) and normalized to α (equation (83)) and $f\left(k\frac{\Delta u_{\text{opt}}}{2}\right) = 0.8512$. The optimum spatial discretization can be identified at $\Delta u/\lambda = 0.371$.

3.3. Simulations of single-particle interference

To numerically cross-check the theoretical calculations in section 3.2, a set of N particles with temporal and spatial coordinates (t_i, y_i), $i = 1 \ldots N$ have been simulated. Therefore, time and position coordinates are generated according to the corresponding distribution functions using the acceptance-rejection method [64]. For the temporal coordinates, the probability distribution of time differences $\Delta t_i = t_{i+1} - t_i$ between successive events is used, which for Poisson statistics is given by [65]

$$p(\Delta t) = \mathrm{e}^{-cr\cdot\Delta t}. \tag{87}$$

Here, $cr = N/T$ denotes the mean count rate. Following this distribution function, a set of $N - 1$ time differences Δt_i, $i = 1 \ldots N - 1$ is generated. Starting with the first event at $t_1 = 0$, the time steps for successive events are given by

$$t_j = \sum_{i=1}^{j-1} \Delta t_i. \tag{88}$$

After having generated all time coordinates t_i, the corresponding spatial coordinates y_i are created according to the probability distribution

$$p(y, t_i) = 1 + K\cos(ky + \varphi(t_i)), \tag{89}$$

with the time-dependent perturbation $\varphi(t_i)$ from equation (2). This results in a full set of time and position coordinates.

Such a simulation has been made for an interference pattern with a contrast of $K = 0.6$, a spatial periodicity of $\lambda = 2$ mm and a single frequency perturbation $\varphi(t)$ with $\omega_1/2\pi = 50$ Hz and $\varphi_1 = 0.4\,\pi$. With an acquisition time of $T = 39.05$ s and length $Y = 20$ mm, 1.95×10^5 particles have been simulated. This parameters have been chosen in accordance to typical experimental parameters [54]. The correlation function was extracted from the simulated data according to equation (62) for different spatial discretization step sizes (Δu), a temporal discretization step size ($\Delta\tau = 0.2$ ms) and a maximum correlation time of $\tau_{\max} = 1$ s. The temporal discretization step size is chosen to ensure that it does not reduce the signal-to-noise ratio (see figure 8 for $\Delta\tau\frac{\omega_1}{2\pi} = 0.01$). Three correlation functions for different spatial discretization step sizes Δu are illustrated in figure 9. The cut line at $u = 0$ mm plotted below each correlation function shows that the signal decreases for increasing Δu from figures 9(a)–(c). Therefore, the structure in the correlation function is 'smeared out'. Additionally, the noise decreases for a larger spatial discretization step size, because the mean particle number increases (equation (75)). The relation between this two effects leads to an optimum $\Delta u_{\text{opt}} = 0.371 \cdot \lambda$ (equation (84)) that provides a maximum of the signal-to-noise ratio (see equation (85)), which is illustrated in figure 9(b).

As the correlation functions in figure 9, many correlation functions with different spatial discretisation step sizes ranging from $\Delta u = 0.009\lambda$ to $\Delta u = 2\lambda$ are extracted from the above simulation according to equation (62). For each correlation function, the amplitude spectrum was calculated at the spatial position $u = 0$ mm using a numerical Fourier transformation. The signal height of the peak at the 50 Hz position and the standard deviation of the noise were determined in each spectrum. The result for the extracted signal height is plotted in figure 10(a) (blue dots). The standard deviation of the noise is shown in 10(b) and the signal-to-noise ratio in figure 10(c). The theoretical curve in figure 10(a) (red solid line) was calculated using equation (69) with the parameters of the simulation. For $\Delta u/\lambda > 0.1$, the signal height is significantly reduced, because the structure in the correlation functions begins to 'smear out' (see figure 9(b)) until it is totally vanished for

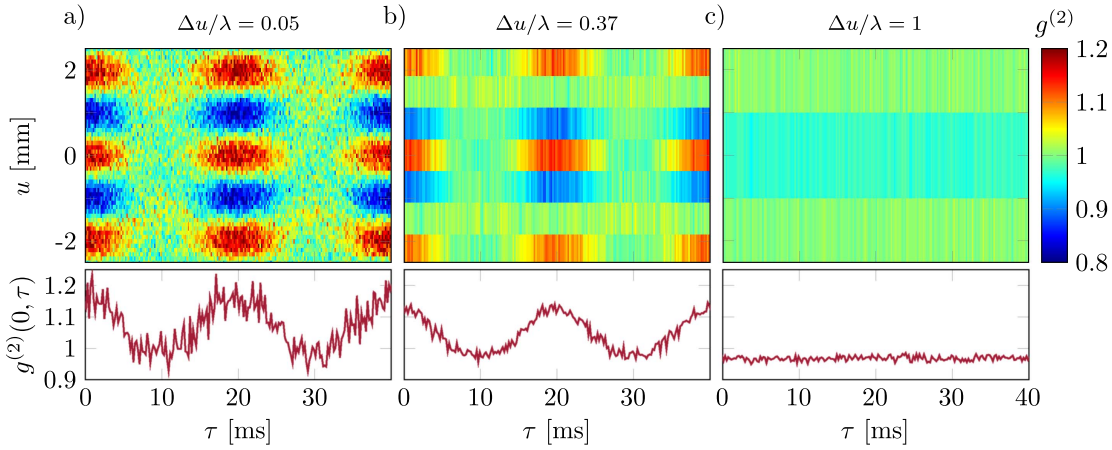

Figure 9. Three correlation functions for different spatial $\Delta u/\lambda$ and a fixed temporal discretization step size $\Delta\tau\omega_1/2\pi = 0.01$. They are extracted from a single-particle simulation of an interference pattern with $K = 0.6$ and $\lambda = 2$ mm perturbed with $\omega_1/2\pi = 50$ Hz and $\varphi_1 = 0.4\,\pi$ used in equation (89). The spatial discretization step size is increased from (a) to (c). Below each correlation function, the cut line at the spatial position $u = 0$ mm is plotted which is used for the calculation of the amplitude spectrum. The signal decreases for increasing discretization step size and therefore, the structure of the correlation function is 'smeared out' until it is vanished in (c). On the other hand, the noise decreases for larger $\Delta u/\lambda$ resulting in a maximum signal-to-noise ratio at $\Delta u/\lambda = 0.37$ which is illustrated in (b).

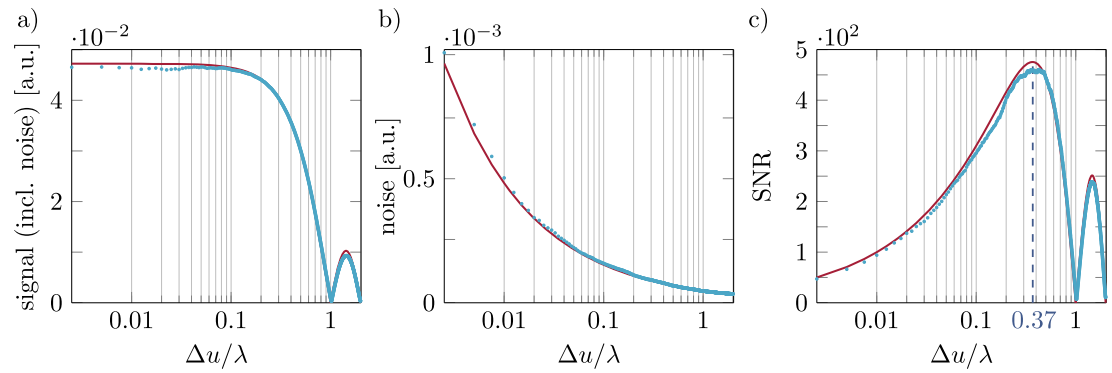

Figure 10. (a) Signal height of the peak at the 50 Hz position in the amplitude spectrum of the correlation function (blue dots). The solid red line indicates the theoretical signal height calculated with equation (69). (b) The standard deviation of the noise determined from the amplitude spectrum. The theoretical curve was evaluated using equation (81). (c) The signal-to-noise ratio of the data points in (a) and (b) shows a good agreement to the theory calculated according to equations (82) and (83). The optimum spatial discretization can be identified at $\Delta u_{\mathrm{opt}}/\lambda = 0.37$.

$\Delta u/\lambda = 1$ (see figure 9(c)). The theoretical curve in figure 10(b) is evaluated with equation (81) indicating that the noise is reduced for larger $\Delta u/\lambda$ due to the increasing mean particle number $\langle N_{u,\tau}\rangle$ in equation (75). The theoretical signal-to-noise ratio in figure 10(c) is calculated according to equations (82) and (83) illustrating the predicted optimum at $\Delta u_{\mathrm{opt}}/\lambda = 0.37$. The corresponding correlation function is shown in figure 9(b). The minimum detectable peak phase deviation in equation (86) can be calculated with the above values and yields $\varphi_{1,\mathrm{min}} = 1.49 \times 10^{-2}\,\pi$.

3.4. Correlation analysis of broad-band frequency noise

To demonstrate the possibility, using the correlation analysis to describe not only single perturbation frequencies but also broad-band noise spectra, the following single-particle simulation has been made. The temporal coordinates t_i of the particles are generated in the same way as described in section 3.3. The perturbation caused by a broad-band frequency noise is given by the corresponding amplitude spectrum $\hat{\varphi}(\omega_j)$ and phase spectrum $\hat{\Phi}(\omega_j)$. This is different to the former simulation, where the time-dependent perturbation $\varphi(t_i)$ was given by equation (2). With the amplitude and phase spectrum, the time-dependent perturbation $\varphi(t_i)$ for the temporal coordinate t_i can be calculated using a discrete Fourier transformation

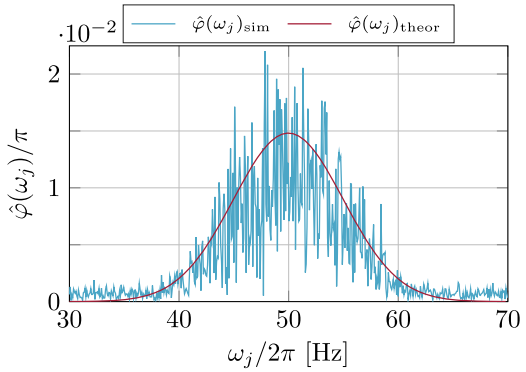

Figure 11. The blue solid line indicates the amplitude spectrum $\hat{\varphi}(\omega_j)_{\mathrm{sim}}$. It is calculated with a numerical Fourier transformation from the time-dependent perturbation $\varphi(t_i)$ (equation (90)) used for the simulation in equation (89). Theoretical amplitude spectrum $\hat{\varphi}(\omega_j)_{\mathrm{theor}}$ (red solid line) resulting from the fit of equation (92) to the correlation function extracted from the simulated data. The determined characteristics of the Gaussian distributed noise in equation (91) are $\varphi_0 = (1.48 \pm 0.02) \times 10^{-2}\,\pi$, $\omega_0/2\pi = (49.97 \pm 0.11)$ Hz and $\sigma_\omega/2\pi = (5.01 \pm 0.11)$ Hz.

$$\varphi(t_i) = \frac{1}{\sqrt{2\pi}\,N_\omega} \sum_{j=1}^{N_\omega} \hat{\varphi}(\omega_j)\, \mathrm{e}^{\mathrm{i}\hat{\Phi}(\omega_j)} \mathrm{e}^{-\mathrm{i}\omega_j t_i}, \tag{90}$$

with the number of frequencies in the spectrum N_ω. The spatial coordinate y_i is determined as before according to the probability distribution (equation (89)) with the calculated phase shift of equation (90). For the simulation demonstrated here, a Gaussian distributed noise spectrum with uncorrelated phases is applied. The discrete amplitude spectrum is thus given by

$$\hat{\varphi}(\omega_j) = \varphi_0 \cdot \mathrm{e}^{-\frac{1}{2}\left(\frac{\omega_j - \omega_0}{\sigma_\omega}\right)^2} \tag{91}$$

and the phase spectrum $\hat{\Phi}(\omega_j)$ is randomly distributed between $-\pi$ and π. Here, φ_0 denotes the maximum peak phase deviation, ω_0 the central frequency and σ_ω the frequency standard deviation (band width).

An interference pattern consisting of 5×10^5 particles acquired in 100 s with a contrast of $K = 0.6$ and a spatial periodicity $\lambda = 2$ mm was perturbed by a Gaussian distributed noise according to equation (91) with $\varphi_0 = 2 \times 10^{-2}\,\pi$, $\omega_0/2\pi = 50$ Hz and $\sigma_\omega/2\pi = 5$ Hz. The frequency spectrum used for the simulation ranges from 30 to 70 Hz with a resolution of 1 mHz. After the simulation, the amplitude spectrum $\hat{\varphi}(\omega_j)_{\mathrm{sim}}$ of the created time-dependent perturbation (equation (90)) is calculated using a numerical Fourier transformation and plotted in figure 11 (blue solid line). The noise on the Gaussian distribution originates from the finite acquisition time and the randomly chosen phases.

The correlation function of the simulated interference pattern is extracted according to equation (62) with a spatial and temporal discretization of $\Delta u = 67\ \mu$m and $\Delta\tau = 1$ ms, that were chosen to have a good signal in the correlation function. In figure 12(a), the resulting correlation function $g^{(2)}(u, \tau)_{\mathrm{sim}}$ is shown. The contrast $K_{g^{(2)}} = 0.587 \pm 0.003$ and spatial periodicity $\lambda_{g^{(2)}} = (1.996 \pm 0.001)$ mm are determined by fitting equation (36) to the correlation function at the temporal position $\tau = 0$ ms (see section 2.4). The superperiod of $\tau_s = 20$ ms belongs to the central frequency of 50 Hz. The contrast of the correlation function decays on timescales of $\tau \propto 2\pi/\sigma_\omega$. In figure 12(a), the contrast is almost vanished for $\tau > 85$ ms. This point is shifted to higher correlation times for smaller σ_ω until the single frequency case with $\omega_1/2\pi = 50$ Hz is reached. For larger σ_ω, more frequency components with random phases contribute to the perturbation and the resulting time-dependent perturbation $\varphi(t_i)$ becomes more uncorrelated between two time stamps. Therefore, the corresponding particles are also uncorrelated and the contrast in the correlation function vanishes for shorter correlation times until it is completely lost.

To determine the characteristics of the Gaussian distributed noise (φ_0, ω_0 and σ_ω), equations (34) and (35) are used together with the amplitude spectrum of the applied perturbation $\hat{\varphi}(\omega_j)$ in equation (91) as argument of the Bessel function

$$g^{(2)}(u, \tau) = 1 + \frac{K^2_{g^{(2)}}}{2} \cos\left(\frac{2\pi}{\lambda_{g^{(2)}}} u\right) \cdot \prod_{j=1}^{N_\omega} \left(\sum_{m_j=-\infty}^{\infty} J_{m_j}(\hat{\varphi}(\omega_j))^2 \cos(m_j \omega_j \tau) \right). \tag{92}$$

The approximate correlation function can be used for the theoretical description of broad-band frequency noise as long as the number of involved frequencies is large enough, so that the constraint in equation (20) is only fulfilled for $n_j = -m_j$. The contrast $K_{g^{(2)}}$ and spatial periodicity $\lambda_{g^{(2)}}$ extracted according to section 2.4 are fixed parameters for the fit to the correlation function of the simulation in figure 12(a). The fit parameters are φ_0, ω_0

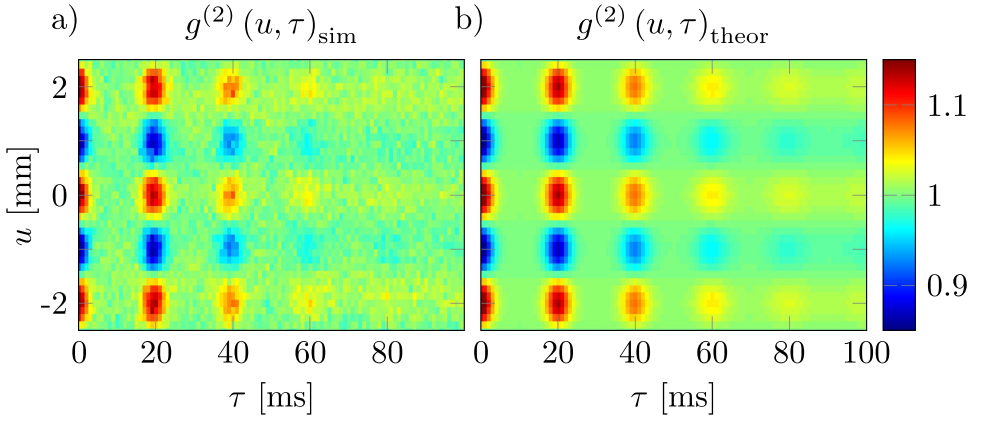

Figure 12. (a) Correlation function of an interference pattern with $K = 0.6$ and $\lambda = 2$ mm perturbed by a Gaussian distributed noise according to equation (91) with $\varphi_0 = 2 \times 10^{-2}\,\pi$, $\omega_0/2\pi = 50$ Hz, $\sigma_\omega/2\pi = 5$ Hz and a frequency resolution of 1 mHz. The superperiod of $\tau_s = 20$ ms belongs to the central frequency of 50 Hz. With the full width at half maximum (FWHM) of the applied noise spectrum being FWHM $= 2\sqrt{2\ln(2)}\,\sigma_\omega \approx 2\pi \times 11.8$ Hz, the contrast in the correlation function vanishes on a timescale $\tau = 2\pi/\mathrm{FWHM} \approx 85$ ms. (b) Theoretical correlation function resulting from the fit with equation (92). Here, the argument of the Bessel function is given by the discrete amplitude spectrum in equation (91).

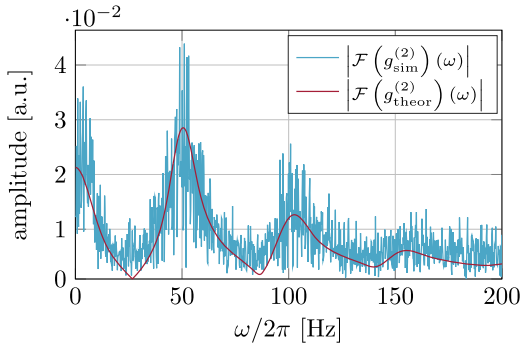

Figure 13. Amplitude spectra of the simulated (blue solid line) and theoretical correlation function (red solid line) determined from the numerical Fourier transformation calculated at $u = 0$ mm.

and σ_ω in the discrete amplitude spectrum of the Gaussian distributed noise (equation (91)). The resulting theoretical correlation function $g^{(2)}(u, \tau)_{\mathrm{theor}}$ is illustrated in figure 12(b) and shows a good agreement with the correlation function of the simulation. The corresponding amplitude spectrum $\hat{\varphi}(\omega_j)_{\mathrm{theor}}$ resulting from the fitted theoretical correlation function is plotted in figure 11 (red solid line). It is also in good agreement with the amplitude spectrum of the applied perturbation (blue solid line). The determined characteristics of the Gaussian distributed noise in equation (91) are $\varphi_0 = (1.48 \pm 0.02) \times 10^{-2}\,\pi$, $\omega_0/2\pi = (49.97 \pm 0.11)$ Hz and $\sigma_\omega/2\pi = (5.01 \pm 0.11)$ Hz, which are in good agreement with the original values.

In figure 13, the amplitude spectra of the simulated and theoretical correlation function, $|\mathcal{F}(g^{(2)}(0, \tau)_{\mathrm{sim}})(0, \omega)|$ (blue solid line) and $|\mathcal{F}(g^{(2)}(0, \tau)_{\mathrm{theor}})(0, \omega)|$ (red solid line), are plotted. Both are calculated with a numerical Fourier transformation at $u = 0$ mm with a frequency resolution of 100 mHz. The theoretical amplitude spectrum agrees well with the simulation. The theoretical description of the amplitude spectrum of the correlation function is given by equation (47) for $u = 0$ mm and positive frequencies using the amplitude spectrum of the perturbation in equation (91) as argument of the Bessel function

$$\frac{1}{2\pi}\,|\mathcal{F}(g^{(2)}(0,\tau))(0,\omega)|^2 = \delta(\omega)^2 + \left(\frac{K^2_{g^{(2)}}}{2} \sum_{\substack{\{-m_j,m_j\}\in\ker(c)\\ j=1\ldots N_\omega}} \left(\prod_{j=1}^{N_\omega} J_{m_j}(\hat{\varphi}(\omega_j))^2\right) \cdot \delta(\omega - \omega_{\{m_j\}})\right)^2. \tag{93}$$

The broad frequency distribution around 50 Hz originates from the fundamental frequencies of the applied perturbation. They are represented in equation (93) by the first order of the Bessel function ($m_j = 1$). The distributions around 0 and 100 Hz are generated by the sum and difference frequencies (intermodulation terms) of the perturbation frequencies. Additionally, the distribution around 150 Hz originates from the sum of three frequency components of the applied perturbation.

If the properties of the applied perturbation are not known *a priori*, the amplitude spectrum can be used to get a reference to the shape and frequency characteristics, because they are included in the spectrum. In figure 13, the central frequency of 50 Hz can be identified at the position of the maximum frequency distribution in the amplitude spectrum and used as starting value for the theoretical fit function (equation (92)). If the central frequency of the perturbation would have been 100 Hz, for example, the distribution around 50 Hz would not be present in the spectrum. The frequency standard deviation of the frequency distribution around 50 Hz is broadened because of additional terms in equation (93), that do not correspond to the fundamental perturbation frequencies ($m_j = 1$). However, it can be used as maximum frequency standard deviation for the theoretical fit function. The applied perturbation spectrum can be identified, if the frequency distributions contained in the resulting amplitude spectrum are separated. They can overlap, if the amplitudes of the perturbation spectrum are large or for very broad spectra.

3.5. Application limits of the second-order correlation analysis

The second-order correlation analysis can not be applied under all conditions. Especially, the possibility to determine the perturbation frequency and amplitude is crucial. Therefore, the limits of the applicability of the second-order correlation analysis shall be pointed out.

If the time of flight t_{tof}, that the particles spend in the area of perturbation, is much shorter than the cycle time of the oscillation ($t_{\mathrm{tof}} \ll 2\pi/\omega_1$) each particle probes the perturbation $\mathcal{A}(t) = \mathcal{A}_1 \cos(\omega_1 t + \phi_1)$ at a constant time, yielding a phase shift

$$\varphi(t) \sim \mathcal{A}(t) \cdot t_{\mathrm{tof}} = \underbrace{\mathcal{A}_1 t_{\mathrm{tof}}}_{\varphi_1} \cos(\omega_1 t + \phi_1). \tag{94}$$

If, however, the time of flight is comparable to the cycle time of the perturbation or even larger, the particle experiences a temporal changing perturbation on its way through the area of dephasing, resulting in a phase shift

$$\varphi(t) \sim \int_t^{t+t_{\mathrm{tof}}} \mathcal{A}(t)\mathrm{d}t = \underbrace{\mathcal{A}_1 t_{\mathrm{tof}}}_{\varphi_1} \operatorname{sinc}\left(\frac{\omega_1 t_{\mathrm{tof}}}{2}\right) \cos(\omega_1 t + \bar{\phi}_1) = \breve{\varphi}_1 \cos(\omega_1 t + \bar{\phi}_1). \tag{95}$$

Therefore, the total phase shift $\breve{\varphi}_1$ is reduced as compared to φ_1 and vanishes for $\omega_1 = 2\pi N/t_{\mathrm{tof}}$, with $N \in \mathbb{N}$, and in the limit $\omega_1 \to \infty$. In these cases, the perturbation characteristics can not be obtained using the correlation analysis.

In general, the second-order correlation theory can be used for periodic oscillations, even if the average particle count rate is lower than the perturbation frequency, because of the infinite coherence of such a perturbation. Due to the strong decay of the Bessel function $J_{m_j}(\varphi_j)$, the highest order per perturbation frequency contributing to the correlation function is $m_{j,\max} \approx \varphi_j$. Therefore, the maximum frequency component of all perturbation frequencies included in the correlation function is given by $\max(\varphi_j \omega_j)$, which arises from the argument of the cosine in equations (31) and (35). For slow and random perturbations with a high peak phase deviation this product sets a lower limit for the average particle count rate to get a good agreement between experiment and theory.

4. Conclusion

Single-particle interferometry is an outstanding instrument in the field of quantum physics and sensor applications. Due to the high sensitivity of interferometers, they are susceptible to dephasing effects originating from electromagnetic oscillations [52, 53], mechanical vibrations [54] or temperature drifts. Compared to decoherence, dephasing is a collective shift of the particle wave function and the contrast is only reduced in the temporally integrated interference pattern. Therefore, dephasing can in principle be reversed. Using second-order correlation theory, the wave properties can be identified and the perturbation characteristics can be determined. This was demonstrated experimentally in former publications for electromagnetic perturbations [52, 53] and mechanical vibrations [54]. This paper provides the theoretical fundament for those articles and other future applications in various fields of single-particle interferometry. It gives a detailed description of the analytic solution to the second-order correlation function and its numerical application.

We presented the full analytic derivation of our two-dimensional second-order correlation theory for multifrequency perturbations. The difference between the explicit and approximate solution was discussed and areas of validity were investigated. The amplitude spectra of both solutions, that are used for the identification of the perturbation characteristics [54], have been calculated. We provided the numerical solution of the correlation function and investigated the dependence of the extracted contrast and perturbation amplitude on the discretization step size. The influence of noise on the correlation function and corresponding amplitude spectrum was investigated and an optimum spatial discretization step size was provided to achieve a maximum

signal-to-noise ratio, which was used in a previous publication [60] for the identification of the electrical network frequency. The validity of our calculations could be demonstrated with a single-particle simulation of a perturbed interference pattern evaluated for different spatial discretization step sizes. The possibility to analyze broad-band frequency noise was shown using a simulated interference pattern perturbed by Gaussian distributed noise.

Our method is a powerful tool for the proof of single-particle interferences, even if they are vanished in the spatial signal. Especially for mobile interferometers or experiments in perturbing environments, the requirements for vibrational damping and electromagnetic shielding can be reduced. Furthermore, it is suitable to analyze the characteristics of multifrequency perturbations and broad-band noise. Therefore, it has possible sensor applications, which was demonstrated for mechanical vibrations in an electron interferometer [54]. It can be used in principle in every interferometer generating a spatial interference pattern on a detector with high spatial and temporal single-particle resolution. This makes our method applicable in a wide range of experiments.

Acknowledgments

We gratefully acknowledge support from the DFG through the SFB TRR21 and the Emmy Noether program STI 615/1-1. AR acknowledges support from the Evangelisches Studienwerk eV Villigst. The authors thank N Kerker and A Pooch for helpful discussions.

References

[1] Cronin A D, Schmiedmayer J and Pritchard D E 2009 *Rev. Mod. Phys.* **81** 1051
[2] Carnal O and Mlynek J 1991 *Phys. Rev. Lett.* **66** 2689
[3] Keith D W, Ekstrom C R, Turchette Q A and Pritchard D E 1991 *Phys. Rev. Lett.* **66** 2693
[4] Margalit Y, Zhou Z, Machluf S, Rohrlich D, Japha Y and Folman R 2015 *Science* **349** 1205
[5] Arndt M and Brand C 2015 *Science* **349** 1168
[6] Gustavson T L, Bouyer P and Kasevich M A 1997 *Phys. Rev. Lett.* **78** 2046
[7] Peters A, Chung K Y and Chu S 1999 *Nature* **400** 849
[8] Grisenti R E, Schöllkopf W, Toennies J P, Hegerfeldt G C, Köhler T and Stoll M 2000 *Phys. Rev. Lett.* **85** 2284
[9] Brezger B, Hackermüller L, Uttenthaler S, Petschinka J, Arndt M and Zeilinger A 2002 *Phys. Rev. Lett.* **88** 100404
[10] Gerlich S, Eibenberger S, Tomandl M, Nimmrichter S, Hornberger K, Fagan P J, Tüxen J, Mayor M and Arndt M 2011 *Nat. Commun.* **2** 263
[11] Arndt M and Hornberger K 2014 *Nat. Phys.* **10** 271
[12] Haslinger P, Dörre N, Geyer P, Rodewald J, Nimmrichter S and Arndt M 2013 *Nat. Phys.* **9** 144
[13] Zurek W H 2003 *Rev. Mod. Phys.* **75** 715
[14] Hackermüller L, Hornberger K, Brezger B, Zeilinger A and Arndt M 2004 *Nature* **427** 711
[15] Hornberger K, Uttenthaler S, Brezger B, Hackermüller L, Arndt M and Zeilinger A 2003 *Phys. Rev. Lett.* **90** 160401
[16] Rauch H, Treimer W and Bonse U 1974 *Phys. Lett.* A **47** 369
[17] Colella R, Overhauser A W and Werner S A 1975 *Phys. Rev. Lett.* **34** 1472
[18] Hasselbach F 2010 *Rep. Prog. Phys.* **73** 016101
[19] Hasselbach F and Maier U 1999 *Quantum Coherence and Decoherence—Proc. ISQM-Tokyo 98* ed Y A Ono and K Fujikawa (Amsterdam: Elsevier) p 299
[20] Maier U 1997 *Doctoral Thesis* University of Tübingen
[21] Kuo H S, Hwang I S, Fu T Y, Lin Y C, Chang C C and Tsong T T 2006 *Japan. J. Appl. Phys.* **45** 8972
[22] Ehberger D, Hammer J, Eisele M, Krüger M, Noe J, Högele A and Hommelhoff P 2015 *Phys. Rev. Lett.* **114** 227601
[23] Hommelhoff P, Kealhofer C and Kasevich M A 2006 *Phys. Rev. Lett.* **97** 247402
[24] Hasselbach F 1988 *Z. Phys.* B **71** 443
[25] Hammer J, Hoffrogge J, Heinrich S and Hommelhoff P 2014 *Phys. Rev. Appl.* **2** 044015
[26] Schütz G, Rembold A, Pooch A, Meier S, Schneeweiss P, Rauschenbeutel A, Günther A, Chang W T, Hwang I S and Stibor A 2014 *Ultramicroscopy* **141** 9
[27] Chang C C, Kuo H S, Hwang I S and Tsong T T 2009 *Nanotechnology* **20** 115401
[28] Cho B, Ichimura T, Shimizu R and Oshima C 2004 *Phys. Rev. Lett.* **92** 246103
[29] Jagutzki O, Mergel V, Ullmann-Pfleger K, Spielberger L, Spillmann U, Dörner R and Schmidt-Böcking H 2001 *Nucl. Instrum. Methods Phys. Res.* A **477** 244
[30] Aharonov Y and Bohm D 1959 *Phys. Rev.* **115** 485
[31] Batelaan H and Tonomura A 2009 *Phys. Today* **62** 38
[32] Schütz G, Rembold A, Pooch A, Prochel H and Stibor A 2015 *Ultramicroscopy* **158** 65
[33] Sonnentag P and Hasselbach F 2007 *Phys. Rev. Lett.* **98** 200402
[34] Scheel S and Buhmann S Y 2012 *Phys. Rev.* A **85** 030101(R)
[35] Putnam W P and Yanik M F 2009 *Phys. Rev.* A **80** 040902(R)
[36] Kruit P *et al* 2016 *Ultramicroscopy* **164** 31–45
[37] Grattan L S and Meggitt B T (ed) 2013 *Optical Fiber Sensor Technology: Fundamentals* (Berlin: Springer)
[38] Abbott B P *et al* 2016 *Phys. Rev. Lett.* **116** 061102
[39] Graham P W, Hogan J M, Kasevich M A and Rajendran S 2013 *Phys. Rev. Lett.* **110** 171102
[40] Hanbury Brown R and Twiss R Q 1956 *Nature* **177** 27
[41] Glauber R J 1963 *Phys. Rev.* **130** 2529

[42] Kiesel H, Renz A and Hasselbach F 2002 *Nature* **418** 392
[43] Schellekens M, Hoppeler R, Perrin A, Gomes J V, Boiron D, Aspect A and Westbrook C I 2005 *Science* **310** 648
[44] Foellmi C 2009 *Astron. Astrophys.* **507** 1719
[45] Simon J, Bakr W S, Ma R, Tai M E, Preiss P M and Greiner M 2011 *Nature* **472** 307
[46] Agakishiev G *et al* 2011 *Eur. Phys. J.* A **47** 63
[47] Öttl A, Ritter S, Köhl M and Esslinger T 2005 *Phys. Rev. Lett.* **95** 090404
[48] Federsel P, Rogulj C, Menold T, Darázs Z, Domokos P, Günther A and Fortágh J 2017 *Phys. Rev.* A **95** 043603
[49] Grondalski J, Alsing P M and Deutsch I H 1999 *Opt. Express* **5** 249
[50] Altman E, Demler E and Lukin M D 2004 *Phys. Rev.* A **70** 013603
[51] Fölling S, Gerbier F, Widera A, Mandel O, Gericke T and Bloch I 2005 *Nature* **434** 481
[52] Rembold A, Schütz G, Chang W T, Stefanov A, Pooch A, Hwang I S, Günther A and Stibor A 2014 *Phys. Rev.* A **89** 033635
[53] Günther A, Rembold A, Schütz G and Stibor A 2015 *Phys. Rev.* A **92** 053607
[54] Rembold A, Schütz G, Röpke R, Chang W T, Hwang I S, Günther A and Stibor A 2017 *New J. Phys.* **19** 033009
[55] Möllenstedt G and Düker H 1956 *Z. Phys.* A **145** 377
[56] Wiener N 1930 *Acta Math.* **55** 117–258
[57] Khintchine A 1934 *Math. Ann.* **109** 604
[58] Siegmund O H, Vallerga J V, Tremsin A S, Mcphate J and Feller B 2007 *Nucl. Instrum. Methods Phys. Res.* A **576** 178
[59] Zhou X, Ranitovic P, Hogle C W, Eland J H D, Kapteyn H C and Murnane M M 2012 *Nat. Phys.* **8** 232
[60] Pooch A, Seidling M, Layer M, Rembold A and Stibor A 2017 *Appl. Phys. Lett.* **110** 223108
[61] Hasselbach F and Nicklaus M 1993 *Phys. Rev.* A **48** 143
[62] Abramowitz M and Stegun I A 1964 *Handbook of Mathematical Functions* vol 55 (New York: Dover Publications) p 360
[63] Arfken G B and Weber H J 2005 *Mathematical Methods for Physicists* (Oxford: Elsevier)
[64] Casella G, Robert C P and Wells M T 2004 Generalized accept-reject sampling schemes *Lecture Notes-Monograph Series* 45, pp 342–7 (www.jstor.org/stable/4356322)
[65] Haight F A 1967 *Handbook of the Poisson distribution* (New York: Wiley)

Publication 2

A. Rembold, G. Schütz, W. T. Chang, A. Stefanov, A. Pooch, I. S. Hwang, A. Günther, and A. Stibor,
Correction of dephasing oscillations in matter-wave interferometry,
Physical Review A **89**, 033635 (2014).

Correction of dephasing oscillations in matter-wave interferometry

A. Rembold,[1] G. Schütz,[1] W. T. Chang,[2] A. Stefanov,[3] A. Pooch,[1] I. S. Hwang,[2] A. Günther,[4,*] and A. Stibor[1,†]

[1]*Institute of Physics and Center for Collective Quantum Phenomena in LISA*$^+$*, University of Tübingen, Auf der Morgenstelle 15, 72076 Tübingen, Germany*

[2]*Institute of Physics, Academia Sinica, Nankang, Taipei 11529, Taiwan, Republic of China*

[3]*Institute of Applied Physics, University of Bern, 3012 Bern, Switzerland*

[4]*Institute of Physics and Center for Collective Quantum Phenomena in LISA*$^+$*, University of Tübingen, Auf der Morgenstelle 14, 72076 Tübingen, Germany*

(Received 16 January 2014; published 31 March 2014; publisher error corrected 2 April 2014)

Vibrations, electromagnetic oscillations, and temperature drifts are among the main reasons for dephasing in matter-wave interferometry. Sophisticated interferometry experiments, e.g., with ions or heavy molecules, often require integration times of several minutes due to the low source intensity or the high velocity selection. Here we present a scheme to suppress the influence of such dephasing mechanisms—especially in the low-frequency regime—by analyzing temporal and spatial particle correlations available in modern detectors. Such correlations can reveal interference properties that would otherwise be washed out due to dephasing by external oscillating signals. The method is shown experimentally in a biprism electron interferometer where a perturbing oscillation is artificially introduced by a periodically varying magnetic field. We provide a full theoretical description of the particle correlations where the perturbing frequency and amplitude can be revealed from the disturbed interferogram. The original spatial fringe pattern without the perturbation can thereby be restored. The technique can be applied to lower the general noise requirements in matter-wave interferometers. It allows for the optimization of electromagnetic shielding and decreases the efforts for vibrational or temperature stabilization.

DOI: 10.1103/PhysRevA.89.033635 PACS number(s): 03.75.Dg, 41.85.−p, 07.77.Ka

I. INTRODUCTION

Matter-wave interferometers with electrons [1–4], atoms [5,6], neutrons [7,8], molecules [9,10], or ions [4,11,12] are all extremely sensitive to dephasing mechanisms. Thereby, the phase of each single-particle wave is shifted relative to the detector by a temporal varying process. Integrating the individual interference patterns with such alternating phase shifts leads to a loss of contrast, even if full coherence is still maintained in the system. However, if the time-dependent phase shift were known, the dephasing could be corrected and full contrast could be recovered. Decoherence, on the other hand, causes a loss of contrast on the single-particle level, which cannot be corrected for.

The origin of dephasing mechanisms can be quite different, such as mechanical vibrations [13], temperature drifts, or, especially important in the case of charged-particle interferometers, electromagnetic oscillations. While high-frequency perturbations can be efficiently suppressed via vibrational isolation systems, electric filters, and mu-metal shieldings, low-frequency components become dominant. They can only be partially addressed by, e.g., using complex shielding schemes, low noise beam guiding electronics, and filtering of the 50 Hz oscillation of the electric network. Moreover, the beam emission center might drift in position, as has been observed for conventional field ionization sources such as "supertips" [14], which was a major obstacle in the first realization of ion interferometry [4,11,12]. The suppression of low-frequency oscillations is therefore of major importance for the realization of stable particle interferometers. It is, for instance, a substantial challenge for the realization of sophisticated ion interference experiments [4,11,12], e.g., in the context of Aharonov-Bohm physics [15,16], where long signal integration times are necessary.

In this article, we describe a method to significantly decrease the influence of low-frequency oscillations by including temporal and spatial particle correlations in the data analysis. The method is demonstrated experimentally using an electron interferometer, where a modern delay line detector [17] provides not only spatial information about the particle impact but also high temporal resolution. This makes them superior to commonly used multichannel plates (MCPs) in conjunction with a fluorescence screen, which does not allow for high-precision time and position measurements. We show that, even after strong dephasing oscillations, the interference pattern can be recovered via correlation analysis. Therefore, we provide a full theory, which takes into account spatial and temporal correlations of all particle pairs. In principle, this method can be used for all periodic dephasing oscillations in the low-frequency regime below the particle count rate. Our method is thus of special importance in matter-wave experiments where temperature drifts or mechanical oscillations from the environment, such as the building, the cooling system, or the vacuum pumps, tend to wash out the interference pattern. For periodic perturbations, our procedure can determine the frequency and amplitude of the dephasing signal and completely restore the spatial fringe pattern. The capability to identify the origin of dephasing is helpful for the design of further shielding or filtering in a matter-wave interferometer.

II. EXPERIMENT

We demonstrate the correlation analysis using a biprism electron interferometer. It was originally constructed by Hasselbach *et al.* [4,11,12] and modified with a new beam

*a.guenther@uni-tuebingen.de
†alexander.stibor@uni-tuebingen.de

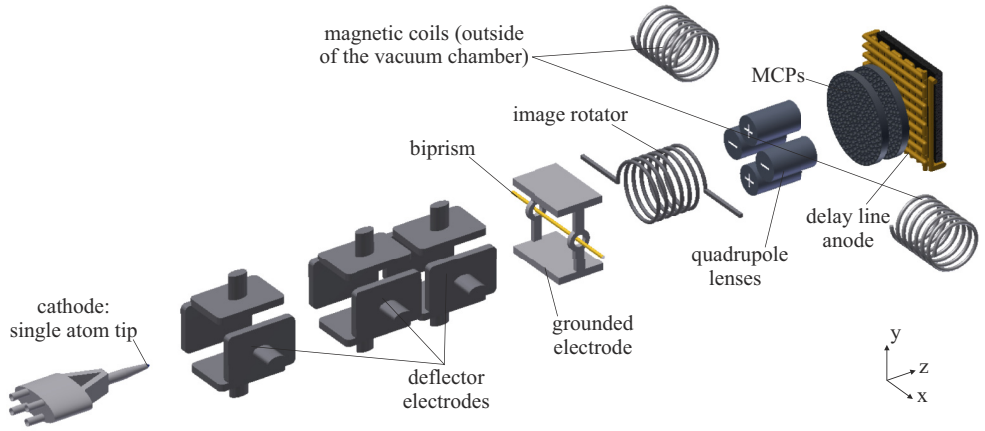

FIG. 1. (Color online) In-vacuum setup of the electron biprism interferometer, which is a modified version of the one described in [4,11,12] (not to scale). An electron beam is field emitted from a single-atom tip [18,19] and adjusted by deflector electrodes toward the optical axis. The electron matter waves are coherently separated and recombined by an electrostatic biprism [1]. The resulting interference pattern is magnified by quadrupole lenses and detected in a delay line detector [17]. It can be artificially disturbed by a time-varying field originating from two magnetic coils, which are placed outside the vacuum chamber. A mu-metal shield (not shown) is placed between the in-vacuum setup and the magnetic coils.

source and a new detector. Figure 1 shows a sketch of the in-vacuum setup. It consists of an iridium-covered tungsten (111) single-atom tip [18,19] that acts as a field emitter for a highly coherent electron beam. The field emission voltage was set to -1.53 kV. The vacuum pressure in the setup was 5×10^{-9} mbar. The beam adjustment toward the optical axis of the setup is performed by using three deflector electrodes. Each one consists of four metal plates pairwise on opposite potentials to deflect the beam in the horizontal (x) and vertical (y) direction. The tip illuminates a fine gold-coated biprism glass fiber that is oriented along x and has a diameter of $\sim$400 nm [20]. It is positioned between two grounded plates to coherently split and recombine the electron matter wave [1]. Setting the biprism on a positive potential of a few volts, the partial waves overlap and create an interference pattern parallel to the direction of the biprism fiber. For imaging purposes, this interference pattern is expanded along y using a quadrupole lens. A magnetic coil directly after the biprism is used as an image rotator to align the fringes to the quadrupole lens. The electron signal is amplified by a double-stage multichannel plate and detected by a delay line anode. The signal is recorded and analyzed by a computer. The whole in-vacuum setup is surrounded by a mu-metal shield, primarily damping high-frequency electromagnetic perturbations.

Essential for our method of dephasing removal is the delay line detector. In biprism interferometry, interference patterns are typically detected using a MCP in conjunction with a fluorescent phosphor screen, which is then digitalized with a CCD camera. This allowed a moderate spatial resolution, restricted by the channel diameters of the MCP's, but only a rather limited temporal detection that is dependent on the long fluorescence decay time of the phosphor screen. With the delay line anode, single electrons can be detected with a spatial resolution below 100 μm and a time accuracy below 1 ns. The dead time between two individual pulses is 310 ns, limiting the detectable count rate to the MHz regime. An incoming amplified electron pulse hits the delay line anode, consisting of two meandering wires oriented perpendicular to each other (x and y directions), and it induces a charge pulse in both directions of each wire. By measuring the time delay between those pulses at the wire endings, the spatial position and time of impact can be determined [17].

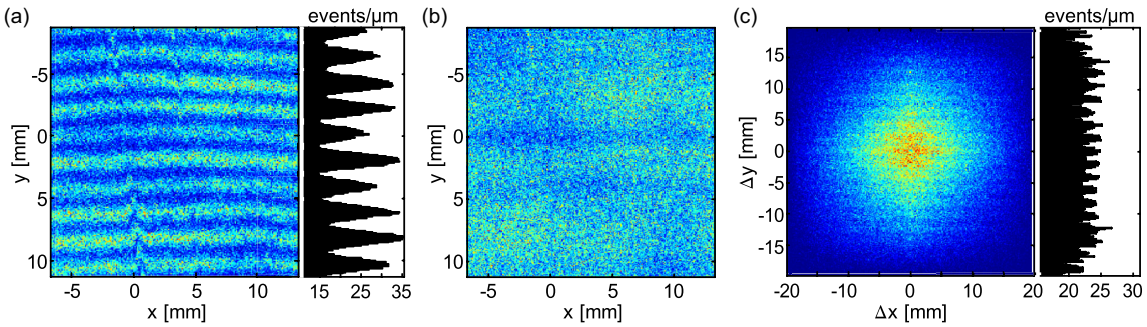

FIG. 2. (Color online) (a) Electron biprism interference pattern and corresponding integrated line profile recorded with the setup of Fig. 1. (b) The same interference pattern after the introduction of a periodic 50 Hz magnetic-field oscillation with a dc amplitude of 2π. The fringes are completely washed out. (c) Histogram and integrated line profile of spatial distances Δx and Δy between temporal adjacent events. They clearly show correlations in the position of two consecutive events, revealing the existence of an interference pattern even after perturbation. The integrated line profile has been corrected by a factor $(1 - |\Delta y|/Y)^{-1}$ to correct for the finite pattern width of $Y = 20$ mm.

Figure 2(a) shows an interference pattern, as detected with the delay line detector, after a total number of about 5×10^5 electrons recorded in about 100 s. This corresponds to a particle count rate of ∼5 kHz. The distance between two fringes in the interferogram is ∼2 mm and the contrast amounts to about 35%. To demonstrate our method, we artificially add a periodic dephasing in the form of an oscillating magnetic field. It is created by two external magnetic coils positioned outside the vacuum chamber and the mu-metal shield (see Fig. 1). The magnetic-field lines are oriented in the x direction applying a force on the electrons in the y direction normal to the interference fringes and parallel to the detection plane. This causes a periodic shift of the interference pattern, reducing the overall fringe contrast of the time-integrated pattern. Using a function generator, the frequency and amplitude of this disturbance can be tuned.

We disturbed the interference pattern of Fig. 2(a) with a 50 Hz oscillation. The amplitude was set such that it moved the pattern by ± 2 mm when a static current was applied to the coils. For oscillating currents, however, this amplitude is reduced due to the mu-metal shield around the in-vacuum setup of the interferometer. We thus expect a peak phase shift of the interferogram below 2π. The resulting image with again $\sim 5 \times 10^5$ events is illustrated in Fig. 2(b) and clearly shows a washed-out pattern where the contrast decreased to almost zero.

As our detector provides a list of coordinates and impact times of all consecutive incidents, we correlate each electron with its subsequent temporal neighbor by determining their spatial distance in the x and y directions $(\Delta x, \Delta y)$. The relative commonness of these distances is plotted in Fig. 2(c). As can be seen, the periodic pattern is revealed, a distinct evidence for matter-wave interferometry even in the presence of strong dephasing. For better visualization, Fig. 2(c) includes the integrated line profile (corrected by the finite pattern width), which clearly shows a periodic modulation on the length scale of the original fringe pattern.

III. THEORY

To gain more information about the disturbed interference pattern, we apply a full correlation analysis on the data by including correlations not only between temporally adjacent particles, but also between all possible particle pairs. For the theoretical description of particle correlations in a periodically disturbed interference pattern, the probability distribution $f(y,t)$ of particle impacts at the detector is of major importance:

$$f(y,t) = f_0(1 + K\cos[ky + \varphi(t)]) \quad \text{with} \quad \varphi(t) = \varphi_0 \cos(\omega t). \tag{1}$$

At each time t, the distribution function is normalized via f_0 and characterized by its spatial periodicity $\lambda = 2\pi/k$, contrast K, and phase φ. The time dependence of φ causes a periodic phase shift of the probability distribution, with φ_0 being the peak phase deviation and $\omega = 2\pi\nu$ the frequency of the phase disturbance. The corresponding interference pattern observed at the detector is given by the time-averaged probability distribution

$$\lim_{T\to\infty} \frac{1}{T} \int_0^T f(y,t)dt = f_0(1 + K\, J_0(\varphi_0)\cos(ky)), \tag{2}$$

with J_0 being the zero-order Bessel function of the first kind. Depending on the strength of the phase deviation, the visible contrast is thus reduced by a factor of $J_0(\varphi_0)$, leading to vanishing interference fringes for large φ_0.

If the detector allows for spatial and temporal information on the particle arrival, a correlation analysis can be used to retain information of the undisturbed interference pattern and the phase disturbance. Starting from Eq. (1), the second-order correlation function reads

$$g^{(2)}(u,\tau) = \frac{\langle\langle f(y+u,t+\tau) f(y,t)\rangle\rangle_{y,t}}{\langle\langle f(y+u,t+\tau)\rangle\rangle_{y,t}\langle\langle f(y,t)\rangle\rangle_{y,t}}, \tag{3}$$

where $\langle\langle\cdot\rangle\rangle_{y,t}$ denotes the average over position and time,

$$\langle\langle f(y,t)\rangle\rangle_{y,t} = \lim_{Y,T\to\infty} \frac{1}{TY} \int_0^T \int_{-Y/2}^{Y/2} f(y,t)\, dy\, dt. \tag{4}$$

In the limit of large acquisition times $T \gg 2\pi/\omega$ and lengths $Y \gg \lambda$, the integrals can be solved and the correlation function becomes

$$g^{(2)}(u,\tau) = 1 + A(\tau)\cos(ku) \tag{5}$$

with

$$A(\tau) = \frac{1}{2}K^2 \sum_{n=-\infty}^{\infty} J_n(\varphi_0)^2\, e^{-in\omega\tau} \tag{6}$$

$$= \frac{1}{2}K^2 J_0(\varphi_0)^2 + K^2 \sum_{n=1}^{\infty} J_n(\varphi_0)^2 \cos(n\omega\tau). \tag{7}$$

Centered around 1, the second-order correlation function of the disturbed interference pattern thus shows a periodic modulation in the spatial distance u between two detection events with the same periodicity as the undisturbed interference pattern. The amplitude of this modulation, however, depends on the correlation time τ. In the frequency domain, $A(\tau)$ can be decomposed to a superposition of sidebands at discrete frequencies $n\omega$ $(n \in \mathbb{Z})$ with strengths given by the peak phase deviation and the Bessel functions $J_n(\varphi_0)$.

Figure 3 shows the two-dimensional correlation function and the amplitude $|A(\tau)|$ for different peak phase deviations. As illustrated in Fig. 3(a), without modulation (undisturbed interference pattern) only J_0 remains nonzero and $A = 0.5$ K^2. The correlation function thus becomes independent of τ and resembles the original interference pattern [Fig. 2(a)]. For small but nonzero φ_0, the first-order Bessel function J_1 comes into play causing a sinusoidal modulation of A at frequency ω [Fig. 3(b)]. As φ_0 increases further, more and more higher-order Bessel functions have to be taken into account, adding higher harmonic modulations to A. However, maximal spatial contrast 0.5 K^2 is only recovered at multiples of $\tau = 1/\nu$, where all higher harmonics constructively interfere [Figs. 3(c) and 3(d)]. Independent of the peak phase deviation, the correlation analysis thus reveals the frequency of the

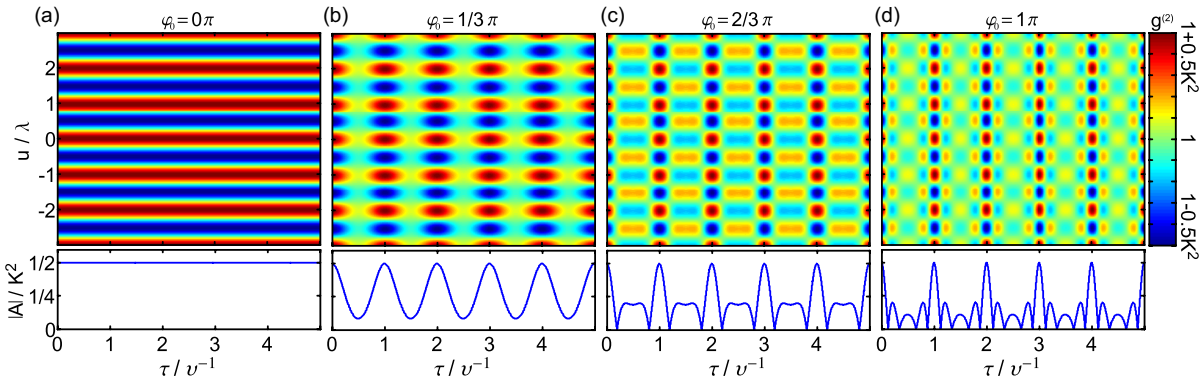

FIG. 3. (Color online) Two-dimensional correlation functions $g^{(2)}(u,\tau)$ of disturbed interference patterns as a function of the spatial (u) and temporal (τ) distance between two detection events. The axes are normalized to the spatial periodicity (λ) and the perturbation period (υ^{-1}). The plots visualize the results of Eq. (5) for different peak phase deviations φ_0 of (a) 0π, (b) $1/3\pi$, (c) $2/3\pi$, and (d) 1π. The absolute value of $A(\tau)$ normalized to the contrast K^2 is shown below each plot.

phase disturbance and the spatial frequency of the underlying interference pattern.

Before the correlation theory can be applied on our measurements, the second-order correlation function needs to be extracted from the detector signal. This signal is given by the position y_i and time t_i of all particle events $i = 1,\ldots,N$. Following Eq. (3), the correlation function is basically determined by the number $N_{u,\tau}$ of particle pairs (i,j) with $(t_i - t_j) \in [\tau,\tau+\Delta\tau]$ and $(y_i - y_j) \in [u,u+\Delta u]$,

$$g^{(2)}(u,\tau) = \frac{TY}{N^2\Delta\tau\,\Delta u}\,\frac{N_{u,\tau}}{\left(1-\frac{\tau}{T}\right)\left(1-\frac{|u|}{Y}\right)} \tag{8}$$

with normalization factor TY/N^2 and discretization step size $\Delta\tau$ and Δu. The additional factor $[(1-\tau T^{-1})(1-|u|Y^{-1})]^{-1}$ corrects $N_{u,\tau}$ for the finite acquisition time T and length Y because large time and position differences will be less likely to be observed.

IV. RESULTS

To apply the theory to the outcome of our electron biprism experiment, we extracted the $g^{(2)}(u,\tau)$ function according to Eq. (8) from the raw data corresponding to Fig. 2(b). The result is shown in Fig. 4(a). As described in Sec. III, the periodicity of this pattern in u and τ is an apparent sign of matter-wave interference that can be observed even in experimental conditions with significant periodic dephasing perturbations.

Using the theoretical expression of Eqs. (5)–(7), we fitted the data in Fig. 4(a). The fit and the remaining residuum are shown in Figs. 4(b) and 4(c), respectively. They reveal all parameters describing the interferogram and the perturbation. The fitted parameters are $\nu = 49.996$ (± 0.018) Hz for the dephasing frequency, $K = 34.5$ (± 0.2)% for the interference contrast, $\lambda = 2.089$ (± 0.001) mm for the spatial period of the interference pattern, and $\varphi_0 = 0.802$ (± 0.004) π for the peak phase deviation. These values are in excellent agreement with the properties of the unperturbed interference pattern ($K \approx 35\%$, $\lambda \approx 2$ mm) and the applied disturbance frequency ($\nu = 50$ Hz). Only the peak phase deviation shows a discrepancy to its dc value of $\varphi_0 = 2\pi$, which is due to the mu-metal shield between the interferometer and the dephasing coils. As expected, this shield damps the amplitude of external field oscillations.

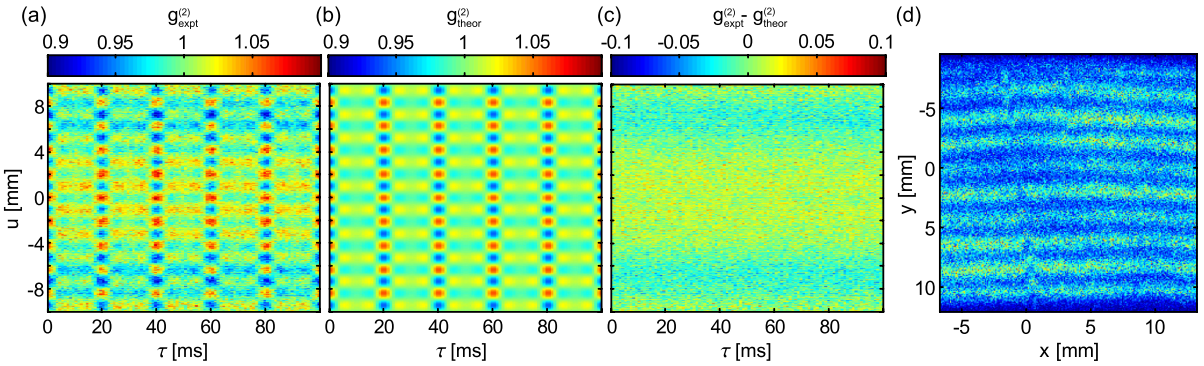

FIG. 4. (Color online) (a) Experimentally determined two-dimensional correlation function $g^{(2)}(u,\tau)$, extracted according to Eq. (8) from the detector signal of the disturbed interference pattern in Fig. 2(b). (b) Fit of the pattern in (a) with the theoretical expression in Eqs. (5)–(7). (c) The residual of theoretical and experimental data. The remaining periodic structure might be related to diffraction at the biprism. (d) Reconstruction of the original undisturbed interference pattern from the strongly disturbed data of Fig. 2(b) using the extracted fitting parameters.

The lack of any substructure in the residual plot [Fig. 4(c)] shows that our correlation model is well suited to describe the experimental data. The residuum shows only a weak remaining structure on the length scale of ∼7 mm, which is probably due to diffraction on both edges of the biprism.

We demonstrated that it is possible to extract the unknown frequency and amplitude of periodic, single-frequency dephasing oscillations from the perturbed interference pattern even if no interference fringes are visible in the spatially integrated image [Fig. 2(b)]. With the obtained parameters and the spatial and temporal coordinates of the events, we are able to reverse the perturbation. This can be done by shifting each event back to its original, undisturbed coordinate according to the determined information,

$$y_{\text{new}} = y - \frac{\lambda}{2\pi}\varphi_0 \cos(\omega t + \phi). \tag{9}$$

The only parameter we do not obtain from the fit is the starting phase of the perturbation ϕ. We extract it by varying the starting phase between 0 and 2π until the maximal contrast of the resulting interference pattern is achieved. Figure 4(d) shows the reconstructed interference pattern. It agrees well with the experimentally undisturbed pattern of Fig. 2(a). Even small structures such as the local phase shifts by charged dust particles on the biprism can be reconstructed.

V. CONCLUSION

Sensitive and accurate matter-wave interference experiments are susceptible to dephasing perturbations that wash out the interference pattern and decrease the contrast [13]. The dephasing can be due to electromagnetic oscillations, electrical network oscillations, temperature drifts, or mechanical vibrations. Usually major efforts to shield or damp these setups are required to suppress these perturbations.

We have presented a method to effectively decrease dephasing effects by including temporal and spatial correlations between the detected particles in the analysis of an interference signal. The full correlation analysis reveals the fringe pattern even in the presence of oscillating perturbations, while conventional methods that rely only on spatial signal accumulation are not able to verify matter-wave interference. The analysis can be applied whenever the frequency of the perturbing signal is significantly lower than the average incident rate on the detector. This condition is well met for most interference experiments since signal rates of several kHz and perturbations below a few hundred Hz are common. Besides information on the perturbation, our method can be used to retain the undisturbed interference pattern.

Our method has potential applications in any kind of charged and neutral particle interferometer where a detector with a high spatial as well as temporal resolution is used. Nowadays, such detectors are available for electrons [17], ions [17], neutrons [21], and neutral atoms [22]. The technique is of general importance for the analysis of dephasing perturbations in matter-wave interferometry, and it allows to optimize shielding and damping installations. It decreases the requirements for vibrational stabilization, temperature stabilization, and filtering of low-frequency perturbations from electronic instruments.

ACKNOWLEDGMENTS

This work was supported by the Deutsche Forschungsgemeinschaft (DFG, German Research Foundation) through the Emmy Noether program STI 615/1-1. A.R. acknowledges support from the Evangelisches Studienwerk e.V. Villigst, W.T.C., and I.S.H. from the Academia Sinica project AS-102-TP-A01, A.Ste. acknowledges the support from the Swiss National Science Foundation and A.G. from the DFG SFB TRR21. The authors thank P. Federsel, H. Prochel, and F. Hasselbach for helpful discussions.

[1] G. Möllenstedt and H. Düker, Z. Phys. **145**, 377 (1956).
[2] H. Kiesel, A. Renz, and F. Hasselbach, Nature (London) **418**, 392 (2002).
[3] F. Hasselbach, Z. Phys. B **71**, 443 (1988).
[4] F. Hasselbach, Rep. Prog. Phys. **73**, 016101 (2010).
[5] O. Carnal and J. Mlynek, Phys. Rev. Lett. **66**, 2689 (1991).
[6] D. W. Keith, C. R. Ekstrom, Q. A. Turchette, and D. E. Pritchard, Phys. Rev. Lett. **66**, 2693 (1991).
[7] H. Rauch, W. Treimer, and U. Bonse, Phys. Lett. A **47**, 369 (1974).
[8] R. Colella, A. W. Overhauser, and S. A. Werner, Phys. Rev. Lett. **34**, 1472 (1975).
[9] B. Brezger, L. Hackermüller, S. Uttenthaler, J. Petschinka, M. Arndt, and A. Zeilinger, Phys. Rev. Lett. **88**, 100404 (2002).
[10] R. E. Grisenti, W. Schöllkopf, J. P. Toennies, G. C. Hegerfeldt, T. Köhler, and M. Stoll, Phys. Rev. Lett. **85**, 2284 (2000).
[11] F. Hasselbach and U. Maier, *Quantum Coherence and Decoherence, Proceedings of ISQM-Tokyo 98*, edited by Y. A. Ono and K. Fujikawa (Elsevier, Amsterdam, 1999), p. 299.
[12] U. Maier, Ph.D. thesis, Faculty of Physics, University of Tübingen, 1997.
[13] A. Stibor, K. Hornberger, L. Hackermüller, A. Zeilinger, and M. Arndt, Laser Phys. **15**, 10 (2005).
[14] S. Kalbitzer and A. Knoblauch, Appl. Phys. A **78**, 269 (2004).
[15] H. Batelaan and A. Tonomura, Phys. Today **62**(9), 38 (2009).
[16] M. P. Silverman, Phys. Lett. A **182**, 323 (1993).
[17] O. Jagutzki, V. Mergel, K. Ullmann-Pfleger, L. Spielberger, U. Spillmann, R. Dörner, and H. Schmidt-Böcking, Nucl. Instrum. Methods Phys. Res. A **477**, 244 (2002).
[18] H. S. Kuo, I. S. Hwang, T. Y. Fu, Y. C. Lin, C. C. Chang, and T. T. Tsong, Jpn. J. Appl. Phys. **45**, 8972 (2006).
[19] H. S. Kuo, I. S. Hwang, T. Y. Fu, Y. H. Lu, C. Y. Lin, and T. T. Tsong, Appl. Phys. Lett. **92**, 063106 (2008).
[20] F. Warken, A. Rauschenbeutel, and T. Bartholomäus, Photonics Spectra **42**(3), 73 (2008).
[21] O. H. Siegmund, J. V. Vallerga, A. S. Tremsin, J. Mcphate, and B. Feller, Nucl. Instrum. Methods Phys. Res. A **576**, 178 (2007).
[22] M. Schellekens, R. Hoppeler, A. Perrin, J. Viana Gomes, D. Boiron, A. Aspect, and C. I. Westbrook, Science **310**, 648 (2005).

Publication 3

A. Günther, A. Rembold, G. Schütz, and A. Stibor,
Multifrequency perturbations in matter-wave interferometry,
Physical Review A **92**, 053607 (2015).

PHYSICAL REVIEW A **92**, 053607 (2015)

Multifrequency perturbations in matter-wave interferometry

A. Günther,[1,*] A. Rembold,[2] G. Schütz,[2] and A. Stibor[2,†]
[1]*Institute of Physics and Center for Collective Quantum Phenomena in LISA⁺, University of Tübingen, Auf der Morgenstelle 14, 72076 Tübingen, Germany*
[2]*Institute of Physics and Center for Collective Quantum Phenomena in LISA⁺, University of Tübingen, Auf der Morgenstelle 15, 72076 Tübingen, Germany*
(Received 27 August 2015; published 9 November 2015)

High-contrast matter-wave interferometry is essential in various fundamental quantum mechanical experiments as well as for technical applications. Thereby, contrast and sensitivity are typically reduced by decoherence and dephasing effects. While decoherence accounts for a general loss of quantum information in a system due to entanglement with the environment, dephasing is due to collective time-dependent external phase shifts, which can be related to temperature drifts, mechanical vibrations, and electromagnetic oscillations. In contrast to decoherence, dephasing can, in principle, be reversed. Here, we demonstrate in experiment and theory a method for the analysis and reduction of the influence of dephasing noise and perturbations consisting of several external frequencies in an electron interferometer. This technique uses the high spatial and temporal resolution of a delay-line detector to reveal and remove dephasing perturbations by second-order correlation analysis. It allows matter-wave experiments under perturbing laboratory conditions and can be applied, in principle, to electron, atom, ion, neutron, and molecule interferometers.

DOI: 10.1103/PhysRevA.92.053607 PACS number(s): 03.75.Dg, 41.85.−p, 03.65.Ta

I. INTRODUCTION

Matter-wave interferometers accomplish an outstanding sensitivity for high-precision measurements. This has been shown in various fields, e.g., by the measurement of inertial forces [1,2], gravitational acceleration [3], and atomic or molecular polarizabilities [4,5]. As a consequence of this high sensitivity, interferometers are also susceptible to external perturbations and noise that dephase the matter wave. Typical dephasing sources are temperature drifts, mechanical vibrations, and electromagnetic oscillations. These influences result in a "washing-out" of the interference fringes. This generally reduces the interference contrast [6] and is especially an obstacle in precision phase measurements such as in Aharonov-Bohm physics [7,8]. Dephasing also needs to be prevented in decoherence studies, where the transition from quantum to classical behavior is analyzed through the contrast loss in matter-wave interferometers [9–11]. Decoherence destroys the phase relation between two beam paths by interaction with the environment, whereas dephasing is due to a collective time-dependent phase shift of the wave functions. Both reduce the contrast and need to be distinguished to study experimentally the theory of decoherence [12]. The knowledge of decoherence mechanisms is of importance to achieve long coherence times in a variety of hybrid quantum devices in the community to date [13–18].

Certainly, isolating, damping, or shielding of interferometers reduces the dephasing influences. However, in a perturbing environment this often cannot be achieved efficiently in a broad frequency range. In addition, for some applications such as mobile interferometric devices [19], the perturbation sources and therefore the shielding requirements change between experimental runs.

In this article we present a general method to reveal dephasing and reduce the influence of external multifrequency perturbations and noise by second-order correlation analysis of an interference pattern. The technique can in principle be applied in all matter-wave interferometers, where the detector has a high spatial and temporal resolution. Such detectors are available for electrons [20], ions [20], neutrons [21], and neutral atoms [22]. Perturbation frequencies and amplitudes can then be revealed after data acquisition is completed.

Recently, we demonstrated [23] that the influence of a single perturbation frequency can be isolated and removed and the complete spatial interference pattern recovered. All parameters such as the contrast, pattern periodicity, perturbation frequency, and amplitude can be extracted from the perturbed interference data. This is useful to eliminate a distinct electromagnetic oscillation such as 50-Hz noise from the electric network or a vibration from a rotating vacuum pump.

In this article we enhance this method towards several frequencies with different amplitudes, which dephase the interference pattern at once. We provide a detailed theoretical description of the multifrequency case, for which we calculate an exact solution for the second-order correlation function. While the theory holds for an arbitrary number of discrete perturbation frequencies, it requires increasing computational power. However, an approximate solution can be found, which is used to extend the theory to arbitrary noise spectra with a high-frequency cutoff. Such noise is often found in typical laboratory situations, where several low-frequency noise sources disturb the interference pattern at the same time. Here, the relative phases of the frequency components do not influence the correlation function and the approximate solution is applicable.

We demonstrate our method by the application of an electron matter-wave interferometer in combination with a delay-line detector. Using an external magnetic field, we introduce artificial multifrequency perturbations, which we analyze

*a.guenther@uni-tuebingen.de
†alexander.stibor@uni-tuebingen.de

on the basis of the "washed-out" interference pattern. In detail, we demonstrate two- and three-frequency perturbations, including the special case where the frequencies are multiples of each other. The influence of broad-band noise is investigated by using a perturbation spectrum with a cutoff frequency of 150 Hz. For all scenarios, the measured particle correlations are compared to our theory.

II. THEORY

Recently, we demonstrated a full correlation analysis for a single-frequency perturbation of a matter-wave interference pattern in an interferometer [23]. In the following we discuss the general case and extend the correlation analysis to multiple perturbation frequencies and broad-band noise.

Similarly as before, we start with the probability distribution $f(y,t)$ of particle impacts at the detector:

$$f(y,t) = f_0(1 + K\cos(ky + \varphi(t))). \tag{1}$$

Here K denotes the contrast, $k = 2\pi/\lambda$ is the wave number of the unperturbed interference pattern with spatial periodicity λ, and f_0 assures normalization. The perturbation is mediated via the time-dependent phase shift $\varphi(t)$, which we assume to be the superposition of N discrete harmonic frequencies,

$$\varphi(t) = \sum_{j=1}^{N} \varphi_j \cos(\omega_j t + \phi_j). \tag{2}$$

Thereby φ_j and ϕ_j denote the peak phase deviation and the perturbation phase at the frequency component ω_j. These perturbations will typically lead to a washout of the time-averaged interference pattern at the detector.

To regain information about the unperturbed interference pattern, the spatial and temporal information on the particles arriving at the detector is recorded and evaluated by correlation analysis. Using Eq. (1), the second-order correlation function reads

$$g^{(2)}(u,\tau) = \frac{\langle\langle f(y+u,t+\tau)f(y,t)\rangle\rangle_{y,t}}{\langle\langle f(y+u,t+\tau)\rangle\rangle_{y,t}\langle\langle f(y,t)\rangle\rangle_{y,t}}, \tag{3}$$

with $\langle\langle\cdot\rangle\rangle_{y,t}$ denoting the average over position and time,

$$\langle\langle f(y,t)\rangle\rangle_{y,t} = \lim_{Y,T\to\infty} \frac{1}{TY}\int_0^T \int_{-Y/2}^{Y/2} f(y,t)\,dy\,dt. \tag{4}$$

In the limit of large acquisition times $T \gg 2\pi/\omega_j$ and lengths $Y \gg 1/k$, Eq. (3) can be solved analytically, yielding

$$g^{(2)}(u,\tau) = 1 + \frac{1}{4}K^2[e^{-iku}A_+ + e^{iku}A_-], \tag{5}$$

with

$$A_\pm = \prod_{j=1}^{N} \sum_{n_j,m_j} J_{n_j}(\varphi_j)J_{m_j}(\varphi_j)e^{im_j\omega_j\tau}\chi^{\pm}_{n_j,m_j}, \tag{6}$$

$$\chi^{\pm}_{n_j,m_j} = e^{i[n_j(\phi_j\pm\frac{\pi}{2})+m_j(\phi_j\mp\frac{\pi}{2})]}, \tag{7}$$

where J_n denote the Bessel functions of first kind and the sum in Eq. (6) has to be taken over all integer duplets, $\{n_j,m_j\} \in \mathbb{Z}, j = 1\ldots N$, for which

$$\sum_j (n_j + m_j)\omega_j = 0 \tag{8}$$

is fulfilled. Although in principle this makes for an infinite number of addends, the contribution of integer duplets $\{n_j,m_j\} > \varphi_j$ to $A_\pm$ is suppressed due to the strong decay of the Bessel functions.

For multiple perturbation frequencies ω_j and broad-band noise spectra, the constraint from Eq. (8) usually requires $m_j = -n_j$ for all $j = 1\ldots N$. With $\chi^{\pm}_{n_j,-n_j} = (-1)^{n_j}$, this results in a correlation function

$$g^{(2)}(u,\tau) = 1 + A(\tau)\cos(ku), \tag{9}$$

with

$$A(\tau) = \frac{1}{2}K^2\prod_{j=1}^{N} \underbrace{\sum_{n_j=-\infty}^{\infty} J_{n_j}(\varphi_j)^2 e^{-in_j\omega_j\tau}}_{J_0(\varphi_j)^2+2\sum_{n_j=1}^{\infty}J_{n_j}(\varphi_j)^2\cos(n_j\omega_j\tau)}. \tag{10}$$

The correlation function for multiple dephasing oscillations will thus show a periodic modulation in the spatial distance u between two detection events. It has the same periodicity as the undisturbed interference pattern. Therefore, it can prove matter-wave interference in a situation where the periodic pattern would be "washed out" after signal integration. The amplitude $A(\tau)$ of this modulation, however, depends on the correlation time τ and is given by the specific perturbation spectrum. The function $A(\tau)$ includes a superposition of sidebands at discrete frequencies $n_j\omega_j$ ($n_j \in \mathbb{Z}$). Their strengths are defined by the peak phase deviation φ_j via the Bessel functions $J_{n_j}(\varphi_j)$. Due to $n_{j,\max} \approx \varphi_j$ (for $n_j > \varphi_j : J_{n_j}(\varphi_j) \to 0$) the highest sidebands appear at frequencies $\varphi_j\omega_j$, setting a lower bound to the particle detection rate, in order to get a good agreement between the experimental and the theoretical correlation function. The maximal modulation amplitude of $0.5K^2$ is achieved at correlation time $\tau = 0$ with

$$g^{(2)}(u,0) = 1 + \tfrac{1}{2}K^2\cos(ku), \tag{11}$$

which is ideally suited to determine the contrast K and pattern periodicity $\lambda = 2\pi/k$ of the unperturbed interference pattern.

While for $N = 1$, the results from Eqs. (9) and (10) coincide with our previous result found for single-frequency perturbations [23], special care must be taken for small numbers of perturbation frequencies which are multiples of each others. In this case the constraint from Eq. (8) might be fulfilled for integers $m_j \neq -n_j$, leading to additional terms in Eq. (10). This can be easily seen in the two-frequency case, with $\omega_2 = 2\omega_1$, where Eq. (8) is solved not only for $m_{1/2} = -n_{1/2}$, but for all multiplets with $n_1 + m_1 = -2(n_2 + m_2)$, such as $\{n_1,m_1,n_2,m_2\} = \{2,2,-1,-1\}$. Following Eqs. (5)–(7), additional terms appear in the correlation function, with $\chi^{\pm}_{n_j,m_j} \neq \pm 1$, thus introducing a phase shift into the correlation pattern, which depends on the correlation time and the perturbation phases ϕ_j. The correlation function then cannot be described by the simple form of Eqs. (9) and (10) but must be calculated via Eqs. (5)–(7).

Similar effects may arise for larger numbers of perturbation frequencies, but the contributions of these parts become more

and more negligible with respect to the main correlation component described by Eqs. (9) and (10).

Examples of all of the above scenarios are given in Sec. IV.

We note that the correlation function is insensitive to the absolute time t, as it involves only time differences between particle impacts at the detector. The correlation function thus must be invariant under time transformation $t \to t - t_0$, which, according to Eq. (2), can be seen as phase transformations,

$$\phi_j \to \phi_j - \omega_j t_0. \tag{12}$$

As expected, the correlation function from Eqs. (5)–(7) is invariant under these transformations.

III. EXPERIMENT

To demonstrate our method we use an electron biprism interferometer and analyze interference patterns that were subject to multifrequency perturbations. The experimental setup is equal to the one used for the single-frequency correlation analysis and is described elsewhere [23–27]. A coherent beam of electrons is field emitted from a single-atom tip cathode [28,29] and guided towards an electrostatic biprism wire. Being on a positive potential it separates and recombines the matter wave, leading to an interference pattern [30]. After magnification the interferogram is amplified by two multichannel plates and detected by a delay-line detector with a high spatial and temporal resolution [20]. The whole setup is in an UHV chamber at a pressure of 1.4×10^{-10} mbar. The beam path inside the chamber is shielded by a μ-metal tube.

For the course of this paper, we artificially disturb the pattern with several superposed oscillating magnetic fields. They are generated by two external magnetic coils in a Helmholtz configuration positioned around the vacuum chamber. The frequencies are introduced by a frequency generator. The oscillating magnetic field shifts the interference pattern perpendicular to the fringes and the integrated pattern gets washed out.

Extraction of the second-order correlation function from the detector signal data was performed according to the same procedure as described in [23]. From the detector we get the position y_i and the time t_i of all particle events $i = 1 \ldots M$. We then determine the number $M_{u,\tau}$ of particle pairs (i,j) with $(y_i - y_j) \in [u, u + \Delta u]$ and $(t_i - t_j) \in [\tau, \tau + \Delta\tau]$, yielding the correlation function

$$g^{(2)}(u,\tau) = \frac{TY}{M^2 \Delta\tau \Delta u} \frac{M_{u,\tau}}{\left(1 - \frac{\tau}{T}\right)\left(1 - \frac{|u|}{Y}\right)}. \tag{13}$$

Here, $\Delta\tau$ and Δu denote the discretization step size in correlation time and position, respectively. TY/M^2 is a normalization factor and $[(1 - \tau/T)(1 - |u|/Y)]^{-1}$ corrects $M_{u,\tau}$ for the finite acquisition time T and length Y.

Before applying multifrequency perturbations, the μ-metal shielding has to be characterized, as it causes a frequency-dependent damping of the externally applied fields. This is done by applying a single-frequency perturbation via the external coils, with the perturbation frequency stepwise increased from 0 to 500 Hz. For each measurement the same oscillation amplitude was applied to the coils and an electron interferogram was recorded. The peak phase deviation of the perturbation in the individual interference pattern was extracted by fitting the correlation theory from Eqs. (9) and (10), for the single-frequency case ($N = 1$), to the measured particle correlations. The resulting phase deviations $\varphi_1(\omega)$ were compared to the phase shift for a constant magnetic field $\varphi_1(0)$, which can be extracted from the 0-Hz measurement. The normalized frequency-dependent transmission of the μ-metal shield is then given by $\varphi_1(\omega)/\varphi_1(0)$ and shown in Fig. 1 together with an appropriate fit function.

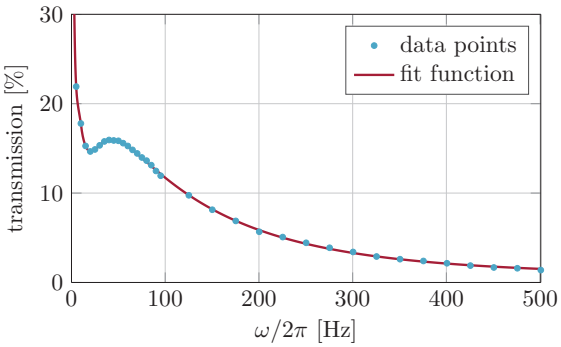

FIG. 1. (Color online) Frequency-dependent transmission of the μ-metal shield around the beam path. Data were obtained by applying single-frequency perturbations between 0 and 500 Hz to the interferogram. Each point corresponds to the correlation analysis of a disturbed interference pattern where the extracted perturbation amplitude has been set in relation to the phase shift at constant magnetic field (0 Hz). The curve has been fitted by an appropriate function.

IV. RESULTS

For the experimental verification of our multifrequency correlation theory we investigate different perturbation scenarios. Starting with two and three perturbation frequencies, we also analyze a full perturbation noise spectrum. For all measurements an interference pattern with 7×10^5 counts was recorded in about 22 s. For each of these measurements the contrast and pattern periodicity are obtained by fitting $g^{(2)}(u,0)$ according to Eq. (11). All data sets are then fitted by either the exact solution [Eqs. (5)–(7)] or the approximate one [Eqs. (9) and (10)]. For practical reasons the perturbation frequencies ω_j have been fixed during this fit. However, the same fit function results if the frequencies are fitted together with the other parameters. In this case, the condition from Eq. (8) has to be weakened to $|\sum_j (n_j + m_j)\omega_j| < \epsilon$ with sufficiently small ϵ.

In the first measurement the interference pattern was perturbed by two superposed magnetic oscillations, at $\omega_1 = 2\pi \times 6$ Hz and $\omega_2 = 2\pi \times 40$ Hz. Using Eq. (13), we then extracted the second-order correlation function $g^{(2)}_{\text{expt}}(u,\tau)$ from these data, which is shown in the upper panel in Fig. 2. The theoretical correlation function $g^{(2)}_{\text{theor}}(u,\tau)$, in the lower panel in Fig. 2, was fitted to the experimental data according to Eqs. (5)–(7) with $N = 2$ and shows a good agreement with the experiment. From the theoretical fit we extracted the contrast $K = 62.9\%$, the pattern periodicity $\lambda = 2.08$ mm, and the peak phase deviations $\varphi_1 = 1.34\pi$ and $\varphi_2 = 0.93\pi$. The phases ϕ_1 and ϕ_2 have no influence on the resulting theoretical

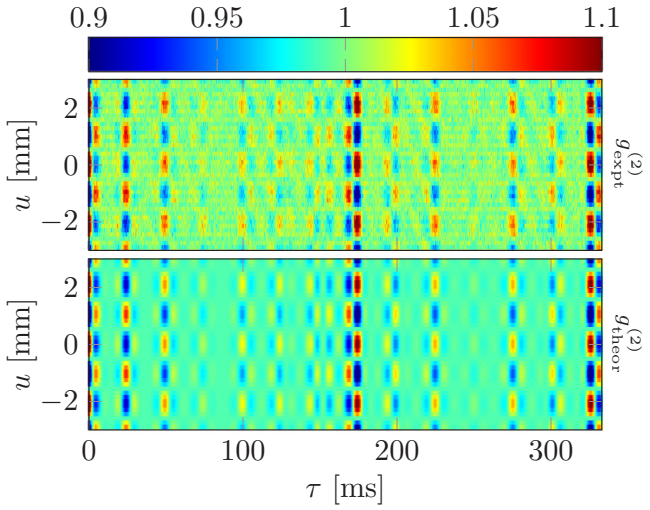

FIG. 2. (Color online) Top: Experimental correlation function $g^{(2)}_{\mathrm{expt}}(u,\tau)$ at two perturbation frequencies: $\omega_1 = 2\pi \times 6$ Hz and $\omega_2 = 2\pi \times 40$ Hz. Bottom: Theoretical fit according to Eqs. (5)–(7) with $N = 2$.

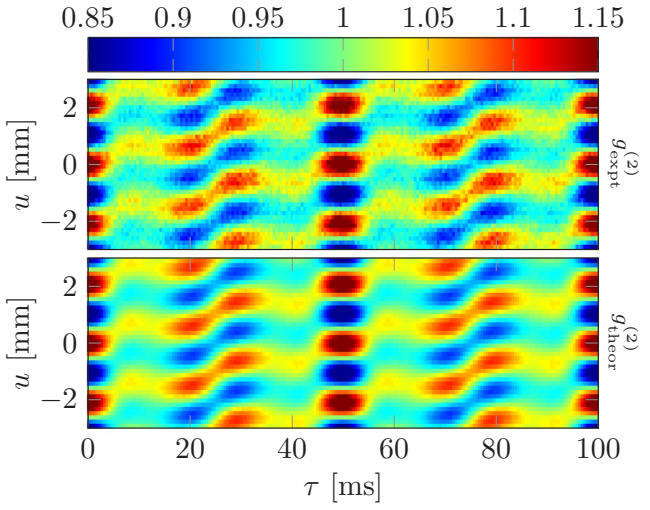

FIG. 4. (Color online) Top: Electron interference measurement at two perturbation frequencies that are multiples of each other: $\omega_1 = 2\pi \times 20$ Hz and $\omega_2 = 2\pi \times 40$ Hz. Bottom: The exact solution from Eqs. (5)–(7) with $N = 2$ was fitted to the experimental correlation data, showing a good agreement.

function in Fig. 2, because the constraint from Eq. (8) is only fulfilled for $m_j = -n_j$ and therefore Eq. (7) becomes $\chi^{\pm}_{n_j,-n_j} = (-1)^{n_j}$. In this case we also could have used Eqs. (9) and (10) to fit the experimental data, yielding the same result.

With the parameters obtained from the theoretical fit it is possible to recalculate the interference pattern from the perturbed one in Fig. 3(a). To get the unperturbed interference pattern we have to calculate the new positions y_{new} according to the extracted perturbation frequencies ω_j and peak phase deviations φ_j,

$$y_{\mathrm{new}} = y - \frac{\lambda}{2\pi} \sum_{j=1}^{N} \varphi_j \cos(\omega_j t + \phi_j), \tag{14}$$

with the particle positions of the perturbed pattern y, pattern periodicity λ, and phases of the perturbations ϕ_j. As the

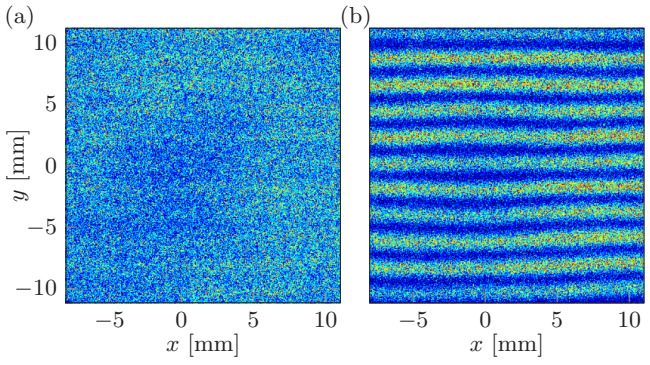

FIG. 3. (Color online) (a) Electron interference pattern perturbed at two frequencies, $\omega_1 = 2\pi \times 6$ Hz and $\omega_2 = 2\pi \times 40$ Hz. The remaining contrast is $K = 6.4\%$. (b) Recalculated interference pattern where the dephasing could be corrected by the presented correlation analysis together with Eq. (14) for $N = 2$. The contrast of the reconstructed pattern is $K = 62.4\%$.

phases could not be obtained from the correlation analysis, they have to be varied to find the maximum contrast of the interference pattern. For our measurement we found $\phi_1 = -0.33\pi$ and $\phi_2 = -0.63\pi$. The resulting back-calculated interference pattern is shown in Fig. 3(b). In the dephased pattern only the small contrast of 6.4% can be adumbrated. After recalculating the new particle positions the interference pattern is clearly visible and the contrast is significantly higher, amounting to 62.4%, which is in good agreement with the value extracted from the correlation analysis.

In the second experiment the correlation function was studied for the case of two perturbation frequencies that are multiples of each other. At $\omega_1 = 2\pi \times 20$ Hz and $\omega_2 = 2\pi \times 40$ Hz the resulting correlation pattern is shown in Fig. 4. As discussed in the theory section, the constraint from Eq. (8) is now not only fulfilled for $m_{1/2} = -n_{1/2}$. Thus additional terms appear in the correlation function, which result in a phase shift of the correlation pattern depending on the correlation time τ and the perturbation phases ϕ_j. This phase shift is clearly seen in the correlation pattern of Fig. 4. In this case the full theory from Eqs. (5)–(7) is required to fit the experimental data, as the correlation time-dependent phase shifts are not included in the approximate solution from Eqs. (9) and (10). The fit is shown in the lower panel in Fig. 4 and agrees well with the experiment. From the fit we extract the contrast $K = 62.9\%$, the pattern periodicity $\lambda = 2.08$ mm, the peak phase deviations $\varphi_1 = 0.50\pi$ and $\varphi_2 = 0.52\pi$, and the phases $\phi_1 = -0.21\pi$ and $\phi_2 = 0.24\pi$. According to Eq. (12), the fit function remains unchanged under the transformation $\phi_1 \to \phi_1 - \omega_1 t_0$ and $\phi_2 \to \phi_2 - \omega_2 t_0$, which leaves the parameter t_0 undetermined. It can be obtained by maximizing the contrast in the back-calculated interference pattern [see Eq. (14)].

Also, the case of three superposed perturbation frequencies was studied and compared to our theoretical approach. The outcome of a corresponding electron interference experiment

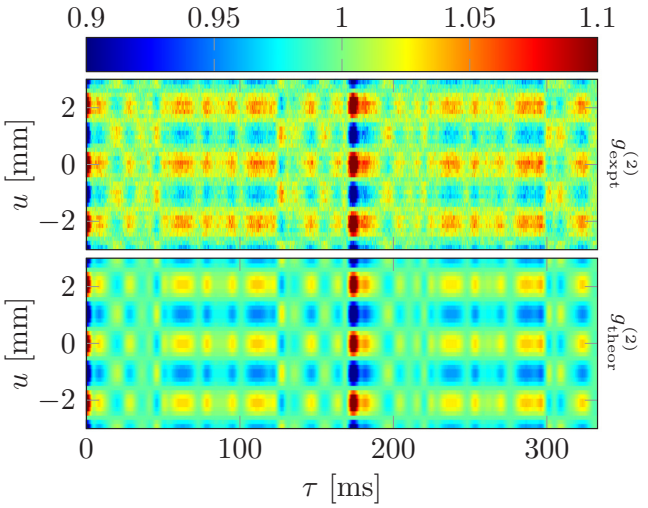

FIG. 5. (Color online) Top: Measurement with three perturbation frequencies: $\omega_1 = 2\pi \times 6$ Hz, $\omega_2 = 2\pi \times 23$ Hz, and $\omega_3 = 2\pi \times 40$ Hz. Bottom: Fit, from Eqs. (5)–(7) with $N = 3$, to the experimental correlation data.

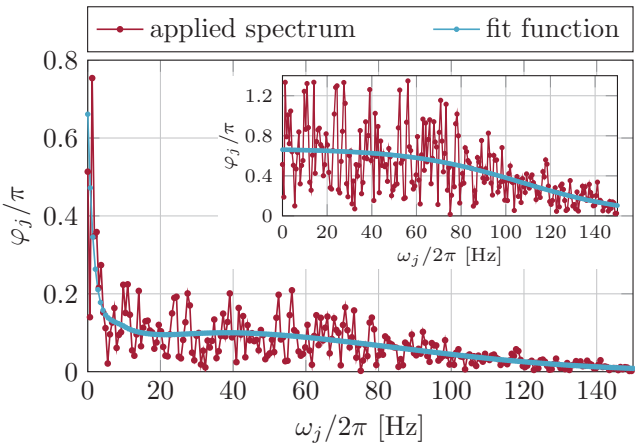

FIG. 6. (Color online) Applied perturbation spectrum [thin solid (red) line with circles] at the position of the electrons together with an appropriate fit function [thin solid (blue) line with circles], which was used to calculate the theoretical correlation function in Fig. 7, according to Eqs. (9) and (10). The spectrum originates from the externally applied noise spectrum (see inset) and the frequency-dependent damping of the μ-metal shield (see Fig. 1).

is shown in the upper panel in Fig. 5. Here, the frequencies $\omega_1 = 2\pi \times 6$ Hz, $\omega_2 = 2\pi \times 23$ Hz, and $\omega_3 = 2\pi \times 40$ Hz have been applied. For fitting these data we use the exact solution from Eqs. (5)–(7) for three frequencies, because the constraint from Eq. (8) is fulfilled for many multiplets $\{n_j, m_j\}$, with $m_j \neq -n_j$. As for the case of two frequencies that are multiples of each other (Fig. 4), this leads to additional terms in the correlation function. The result of the fit is shown in the lower panel in Fig. 5, yielding the contrast $K = 61.3\%$, the pattern periodicity $\lambda = 2.08$ mm, the peak phase deviations $\varphi_1 = 0.76\pi$, $\varphi_2 = 1.01\pi$, and $\varphi_3 = 0.52\pi$, and the phases $\phi_1 = 0.01\pi$, $\phi_2 = 1.01\pi$, and $\phi_3 = 0.01\pi$. Similarly as before, these phases are undetermined with respect to the invariant transformation from Eq. (12). With the exact solution a good agreement between theory and experiment can be achieved.

In the last experiment we investigate a perturbation consisting of a broad frequency spectrum. This should simulate typical noise from a laboratory environment originating from electric or magnetic devices or mechanical vibrations. We introduced a perturbation noise spectrum from 0 Hz up to a cutoff frequency at 150 Hz to the magnetic coils. A part of the time signal of the applied perturbation spectrum was measured while integrating the signal at the detector. The amplitude spectrum of this time signal together with an appropriate fit function [thin solid (blue) line with circles], is shown in the inset in Fig. 6. From this we deduce the perturbation spectrum at the position of the particles by using the transmission characteristic of the μ-metal shield from Fig. 1. The resulting spectrum is shown in Fig. 6 together with the attenuated fit function [thin solid (blue) line with circles], which is used to calculate the theoretical correlation function according to Eqs. (9) and (10). In this case it is possible to use the approximate solution for the correlation function, because the perturbation consists of a large number of frequencies and uncorrelated phases. Figure 7 shows the measured data together with the theoretical correlation function, from which we deduce the contrast of the interference pattern $K = 63.4\%$ and the pattern periodicity $\lambda = 2.16$ mm. Again, the experimental and theoretical correlation functions agree well.

V. CONCLUSION

Matter-wave interference experiments appear in various fields of experimental quantum physics for atoms [31],

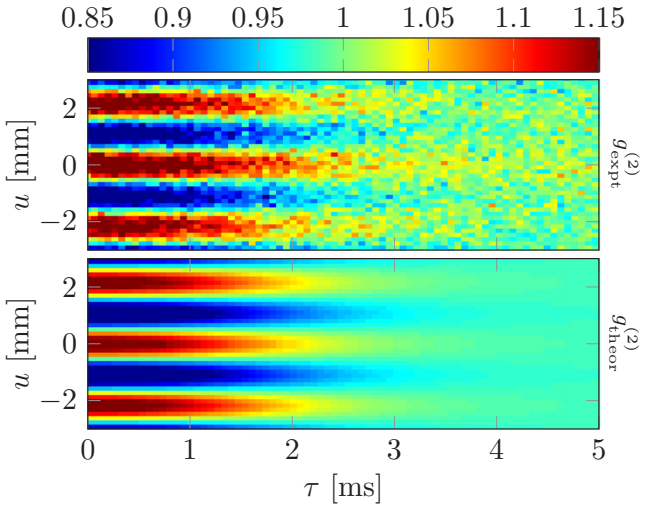

FIG. 7. (Color online) Correlation analysis of an interference pattern that was perturbed by a broad-band noise spectrum with a cutoff frequency at 150 Hz. This simulates a perturbing laboratory environment. Top: Correlation function $g^{(2)}_{\mathrm{expt}}(u,\tau)$ as obtained from the measurement. Bottom: Theoretical correlation function calculated from the fit function in Fig. 6 [thin solid (blue) line with circles], according to Eqs. (9) and (10).

molecules [32], neutrons [33], electrons [25], and ions [26]. Most of these approaches have a spatial resolution for the interference pattern but not a temporal one. Therefore, these kind of setups are susceptible to dephasing effects. Oscillations from electromagnetic sources, temperature drifts, or mechanical vibrations decrease the contrast or totally "wash out" the interference fringes. For this reason good shielding and damping is required.

However, the technological progress allows for particle detectors with a high spatial and temporal resolution. In this paper we have demonstrated that the additional temporal information can be used to determine and decrease the effect of dephasing significantly even if the interferometer is under the influence of a multifrequency perturbation and broad-band noise. We have presented a theoretical approach that uses second-order correlation theory to analyze an interference pattern disturbed by a spectrum of various frequencies with different amplitudes and phases. Thereby, the specific composition of the perturbation frequencies is relevant. It determines whether the exact solution is needed or an approximate solution, requiring less computational effort, is sufficient.

Our method was verified experimentally by electron interference patterns that were artificially perturbed and washed out by several superposed frequencies. The resulting correlation data for two- and three-frequency perturbations and a perturbation noise spectrum matched well with our theoretical description. We demonstrated the reconstruction of the unperturbed interference pattern with the information obtained about the perturbation frequencies and amplitudes.

For periodic perturbations the method can be applied also for average particle count rates lower than the perturbation frequency because of the infinite "phase memory" of such a perturbation. For very slow and random drifts with a high peak phase deviation, the count rate of the particles has to be higher than the product of the frequency and peak phase deviation of the perturbation, as mentioned in Sec. II. This requirement is fulfilled for most interferometry experiments, where a count rate of several kilohertz and perturbation frequencies of a few hundred hertz are common. The information obtained from our analysis allows for the optimization of damping and shielding installations. Our technique has potential application for (mobile) interferometers in a noisy environment and in sensor technology. The susceptibility of electron interferometers may be used for the construction of a sensor with a high sensitivity for electromagnetic and vibrational frequencies. The resolution of such a device would presumably be limited only by the count rate of the particles and the distance of the interference fringes. The sensitivity can be increased by using heavier particles, such as ions, or a larger beam path separation [34].

Our method identifies and analyzes multifrequency perturbations and noise in interferometric measurements. It is applicable for a broad variety of matter-wave interferometers, where a reduction of dephasing and proof of the wave nature of particles are required in a noisy environment with multifrequency perturbations.

ACKNOWLEDGMENTS

The authors thank A. Pooch and R. Röpke for helpful discussions. This work was supported by the Deutsche Forschungsgemeinschaft (DFG; German Research Foundation) through the Emmy Noether program STI 615/1-1. A.G. acknowledges support from DFG SFB TRR21, and A.R. from Evangelisches Studienwerk e.V. Villigst.

[1] T. L. Gustavson, P. Bouyer, and M. A. Kasevich, Phys. Rev. Lett. **78**, 2046 (1997).
[2] F. Hasselbach and M. Nicklaus, Phys. Rev. A **48**, 143 (1993).
[3] A. Peters, K. Y. Chung, and S. Chu, Nature **400**, 849 (1999).
[4] C. R. Ekstrom, J. Schmiedmayer, M. S. Chapman, T. D. Hammond, and D. E. Pritchard, Phys. Rev. A **51**, 3883 (1995).
[5] M. Berninger, A. Stefanov, S. Deachapunya, and M. Arndt, Phys. Rev. A **76**, 013607 (2007).
[6] A. Stibor, K. Hornberger, L. Hackermüller, A. Zeilinger, and M. Arndt, Laser Phys. **15**, 10 (2005).
[7] Y. Aharonov and D. Bohm, Phys. Rev. **115**, 485 (1959).
[8] G. Schütz, A. Rembold, A. Pooch, H. Prochel, and A. Stibor, Ultramicroscopy **158**, 65 (2015).
[9] L. Hackermüller, K. Hornberger, B. Brezger, A. Zeilinger, and M. Arndt, Nature **427**, 711 (2004).
[10] K. Hornberger, S. Uttenthaler, B. Brezger, L. Hackermüller, M. Arndt, and A. Zeilinger, Phys. Rev. Lett. **90**, 160401 (2003).
[11] P. Sonnentag and F. Hasselbach, Phys. Rev. Lett. **98**, 200402 (2007).
[12] W. H. Zurek, Rev. Mod. Phys. **75**, 715 (2003).
[13] M. Wallquist, K. Hammerer, P. Rabl, M. Lukin, and P. Zoller, Phys. Scripta T **137**, 014001 (2009).
[14] J. Chan, T. P. M. Alegre, A. H. Safavi-Naeini, J. T. Hill, A. Krause, S. Gröblacher, M. Aspelmeyer, and O. Painter, Nature **478**, 89 (2011).
[15] D. Hunger, S. Camerer, T. W. Hänsch, D. König, J. P. Kotthaus, J. Reichel, and P. Treutlein, Phys. Rev. Lett. **104**, 143002 (2010).
[16] G. Sagué, E. Vetsch, W. Alt, D. Meschede, and A. Rauschenbeutel, Phys. Rev. Lett. **99**, 163602 (2007).
[17] A. André, D. DeMille, J. M. Doyle, M. D. Lukin, S. E. Maxwell, P. Rabl, R. J. Schoelkopf, and P. Zoller, Nature Physics **2**, 636 (2006).
[18] M. Gierling, P. Schneeweiss, G. Visanescu, P. Federsel, M. Häffner, D. P. Kern, T. E. Judd, A. Günther, and J. Fortágh, Nature Nanotechnol. **6**, 446 (2011).
[19] M. Hauth, C. Freier, V. Schkolnik, A. Senger, M. Schmidt, and A. Peters, Appl. Phys. B **113**, 49 (2013).
[20] O. Jagutzki, V. Mergel, K. Ullmann-Pfleger, L. Spielberger, U. Spillmann, R. Dörner, and H. Schmidt-Böcking, Nucl. Instr. Meth. Phys. Res. A **477**, 244 (2002).
[21] O. H. Siegmund, J. V. Vallerga, A. S. Tremsin, J. Mcphate, and B. Feller, Nucl. Instr. Meth. Phys. Res. A **576**, 178 (2007).

[22] M. Schellekens, R. Hoppeler, A. Perrin, J. Viana Gomes, D. Boiron, A. Aspect, and C. I. Westbrook, Science **310**, 648 (2005).

[23] A. Rembold, G. Schütz, W. T. Chang, A. Stefanov, A. Pooch, I. S. Hwang, A. Günther, and A. Stibor, Phys. Rev. A **89**, 033635 (2014).

[24] G. Schütz, A. Rembold, A. Pooch, S. Meier, P. Schneeweiss, A. Rauschenbeutel, A. Günther, W. T. Chang, I. S. Hwang, and A. Stibor, Ultramicroscopy **141**, 9 (2014).

[25] F. Hasselbach, Rep. Prog. Phys. **73**, 016101 (2010).

[26] F. Hasselbach and U. Maier, in *Quantum Coherence and Decoherence—ISQM Tokyo 98: Proceedings of the 6th International Symposium on Foundations of Quantum Mechanics in the Light of New Technology, Saitama, Japan, August 24–27, 1998*, edited by Y. A. Ono and K. Fujikawa (Elsevier, Amsterdam, 1999), p. 299.

[27] U. Maier, Dissertation, University of Tübingen, 1997.

[28] H. S. Kuo, I. S. Hwang, T. Y. Fu, Y. C. Lin, C. C. Chang, and T. T. Tsong, Japan. J. Appl. Phys. **45**, 8972 (2006).

[29] H. S. Kuo, I. S. Hwang, T. Y. Fu, Y. H. Lu, C. Y. Lin, and T. T. Tsong, Appl. Phys. Lett. **92**, 063106 (2008).

[30] G. Möllenstedt and H. Düker, Z. Phys. A Hadron Nucl. **145**, 377 (1956).

[31] M. R. Andrews, C. G. Townsend, H.-J. Miesner, D. S. Durfee, D. M. Kurn, and W. Ketterle, Science **275**, 637 (1997).

[32] B. Brezger, L. Hackermüller, S. Uttenthaler, J. Petschinka, M. Arndt, and A. Zeilinger, Phys. Rev. Lett. **88**, 100404 (2002).

[33] H. Rauch and S. A. Werner, *Neutron Interferometry: Lessons in Experimental Quantum Mechanics, Wave-Particle Duality, and Entanglement*, Vol. 12 (Oxford University Press, New York, 2015).

[34] J. F. Clauser, Physica B **151**, 262 (1988).

Publication 4

A. Rembold, G. Schütz, R. Röpke, W. T. Chang, I. S. Hwang, A. Günther, and A. Stibor,
Vibrational dephasing in matter-wave interferometers,
New Journal of Physics **19**, 033009 (2017).

New Journal of Physics
The open access journal at the forefront of physics

Deutsche Physikalische Gesellschaft DPG
IOP Institute of Physics

Published in partnership with: Deutsche Physikalische Gesellschaft and the Institute of Physics

OPEN ACCESS

RECEIVED
17 August 2016

REVISED
27 January 2017

ACCEPTED FOR PUBLICATION
15 February 2017

PUBLISHED
6 March 2017

PAPER

Vibrational dephasing in matter-wave interferometers

A Rembold[1], G Schütz[1], R Röpke[1], W T Chang[2], I S Hwang[2], A Günther[3] and A Stibor[1,4]

[1] Institute of Physics and Center for Collective Quantum Phenomena in LISA$^+$, University of Tübingen, Auf der Morgenstelle 15, D-72076 Tübingen, Germany
[2] Institute of Physics, Academia Sinica, Nankang, Taipei 11529, Taiwan, Republic of China
[3] Institute of Physics and Center for Collective Quantum Phenomena in LISA$^+$, University of Tübingen, Auf der Morgenstelle 14, D-72076 Tübingen, Germany
[4] Author to whom any correspondence should be addressed.

E-mail: a.guenther@uni-tuebingen.de **and** alexander.stibor@uni-tuebingen.de

Keywords: matter-wave interferometry, dephasing, vibration, correlation analysis, sensor technology, spectrum analysis

Abstract

Matter-wave interferometry is a highly sensitive tool to measure small perturbations in a quantum system. This property allows the creation of precision sensors for dephasing mechanisms such as mechanical vibrations. They are a challenge for phase measurements under perturbing conditions that cannot be perfectly decoupled from the interferometer, e.g. for mobile interferometric devices or vibrations with a broad frequency range. Here, we demonstrate a method based on second-order correlation theory in combination with Fourier analysis, to use an electron interferometer as a sensor that precisely characterizes the mechanical vibration spectrum of the interferometer. Using the high spatial and temporal single-particle resolution of a delay line detector, the data allows to reveal the original contrast and spatial periodicity of the interference pattern from 'washed-out' matter-wave interferograms that have been vibrationally disturbed in the frequency region between 100 and 1000 Hz. Other than with electromagnetic dephasing, due to excitations of higher harmonics and additional frequencies induced from the environment, the parts in the setup oscillate with frequencies that can be different to the applied ones. The developed numerical search algorithm is capable to determine those unknown oscillations and corresponding amplitudes. The technique can identify vibrational dephasing and decrease damping and shielding requirements in electron, ion, neutron, atom and molecule interferometers that generate a spatial fringe pattern on the detector plane.

1. Introduction

The high phase sensitivity of interferometric sensors is the basis for their broad implementation in technical [1] as well as in fundamental applications [2, 3]. Recent developments in matter-wave interferometry indicate the wide applicability in various fields of quantum physics. Such interferometers are used for interferometry with large organic molecules [4], to test the limits of quantum mechanical superpositions [5], for interference on optical ionization gratings in the time domain [6], for the measurement of inertial forces [7, 8], to determine gravitational acceleration [9] or with coherent particles prepared as self-interfering clocks [10, 11].

Interferometers are also highly sensitive towards mechanical vibrations [12]. Such perturbations dephase the matter-wave and decrease the interference contrast. This is in particular critical for precision experiments in a perturbing environment. Vibrational dephasing has been analyzed and decreased in several related fields of research e.g. for a continuous beam of thermal atoms in a Mach–Zehnder interferometer [13]. In precision interferometric measurements with ultracold atoms, such as for gravity [14] or inertial effects [15], the vibrations induce an arbitrary phase shift for each interfering particle pulse. Usually, the atoms have a large time of flight in the setup and therefore an elaborated active and passive vibration damping is required [16]. The vibrational phase shifts can be compensated e.g. with the signal of a low noise seismometer attached to the beam mirror [17] or by simultaneous operation of a pair of conjugate atom interferometers [18, 19]. Vibrational noise is also one of the main challenges to achieve a higher accuracy in measurements concerning the equivalence principle [20, 21] since

it is impossible to distinguish between the gravitational acceleration and a perturbing movement of the setup. For precise tests of the weak equivalence principle, the differential phase between dual-species atom interferometers can be extracted using a mechanical accelerometer to measure the vibration-induced phase and to reconstruct the interference contrast [22]. Dephasing noise reduction has also applications to increase current frequency standards for atomic clocks. By a phase lock of a classical oscillator to an atomic superposition state, based on repeated coherence-preserving measurements and phase corrections, an atomic clock can be operated beyond the limit set by the local oscillator noise [23]. Furthermore, the laser noise in the stability between different optical clocks can be decreased, allowing probe times longer than the coherence of the laser in the time domain [24].

It is also important to identify dephasing in experiments to study the theory of decoherence [25, 26]. Thereby, the gradual loss of interference contrast due to entanglement of the quantum superposition state of the matter-wave with the environment is measured [27–29] and needs to be distinguished from the contrast loss originating from dephasing. Such mechanisms also significantly disturb sensitive phase measurements, as necessary in Aharonov–Bohm physics [30–33].

Recently, we demonstrated in theory and experiment a method to reestablish an electron interference pattern disturbed by known single [34] and multifrequency [35] electromagnetic perturbations using second-order correlation analysis [36]. Thereby, the technique is based on the high spatial and temporal resolution of a delay line detector [37] for single-particle events. In this article, we demonstrate that this method can be applied on vibrational dephasing and be extended to perform spectroscopy of unknown dephasing perturbation frequencies from a 'washed-out' interference pattern. We present a precise characterization of the mechanical resonance spectrum of our electron interferometer after applying vibrational dephasing perturbations. In contrast to previous measurements with electromagnetic disturbances, the actual perturbation frequencies can vary from the applied ones due to possible excitations of higher harmonics in the setup and additional perturbation frequencies originating from the environment. Therefore, a numerical search algorithm has been developed to identify the unknown perturbation frequencies and corresponding amplitudes. As for electromagnetic oscillations, it is again possible to fully correct the dephasing by our correlation method, reestablishing interferograms with a high contrast. Furthermore, the influence of temporal binning of the measurement data is analyzed in detail.

The mechanical dephasing perturbations were artificially applied in a biprism electron interferometer by a speaker and piezo element in a frequency range between 100 and 1000 Hz. This kind of frequencies occur in typical lab situations when acoustic noise, vibrations from the building, the cooling system or the vacuum pumps decrease the interference contrast and therefore 'wash-out' the matter-wave interferogram. Because of the complexity of the system with several mechanical resonances, the contributing perturbation frequencies are not known *a priori*. Therefore, our numerical search algorithm was developed, combining the second-order correlation theory with a Fourier analysis. According to the Wiener–Khintchine theorem [38, 39], the Fourier transform of the correlation function equals the power spectrum of the perturbed measurement signal. This is used in our method to identify the perturbation frequencies and amplitudes that have contributed to the dephasing of the interference pattern. With these values it is possible to reconstruct the original undisturbed pattern. The contrast of the unperturbed interference pattern could be recovered in the whole frequency range. Our technique allows to reveal the matter-wave nature of particles under conditions in which usual spatial integration of an interference pattern would be inapplicable.

The method has potential applications to restore the contrast for interferometers in perturbing environments that cannot be satisfactorily decoupled by damping or shielding in a broad frequency range. In case, the time that the particles need to cross the interferometer is significantly smaller than the cycle duration of the perturbation, our technique can reveal the spectrum of vibrational and electromagnetic frequencies and amplitudes in all interferometers that generate a spatial fringe pattern on a detector with a high spatial and temporal single-particle resolution. Such detectors exist for electrons [37], ions [37], neutrons [40], atoms [41] and molecules [42]. The technique is therefore also a helpful tool to design optimal active and passive damping structures for a specific setup.

2. Theory

To calculate the two-dimensional second-order correlation function $g^{(2)}(u, \tau)$, we start with the probability distribution $f(y, t)$ of the particle impacts at the detector

$$f(y, t) = f_0(1 + K_0 \cos(ky + \varphi(t))), \tag{1}$$

where K_0 is the unperturbed contrast, $k = 2\pi/\lambda$ the wave number of the unperturbed interference pattern, with λ the spatial periodicity, and the normalization factor f_0. The interference pattern is perturbed by the time-dependent phase shift $\varphi(t)$, which consists of a superposition of N frequencies ω_j

$$\varphi(t) = \sum_{j=1}^{N} \varphi_j \cos(\omega_j t + \phi_j). \tag{2}$$

Here φ_j and ϕ_j denote the peak phase deviation and phase of the perturbation frequency ω_j respectively. This phase shift leads to a washout of the integrated interference pattern at the detector [34, 35], yielding

$$\begin{aligned}\lim_{T\to\infty} \frac{1}{T}\int_0^T f(y, t)\,\mathrm{d}t &= f_0 + \lim_{T\to\infty} \frac{f_0 K_0}{2T}\left(\mathrm{e}^{\mathrm{i}ky}\int_0^T \mathrm{e}^{\mathrm{i}\varphi_1 \cos(\omega_1 t+\phi_1)}\,\mathrm{d}t + \text{c.c.}\right)\\ &= f_0(1 + K_0\, J_0(\varphi_1)\cos(ky))\end{aligned} \tag{3}$$

for $N = 1$. Here, $\mathrm{e}^{\pm\mathrm{i}\varphi_1 \cos(\omega_1 t+\phi_1)} = \sum_{n_1=-\infty}^{+\infty} J_{n_1}(\varphi_1)\mathrm{e}^{\mathrm{i}n_1\left(\omega_1 t+\phi_1\pm\frac{\pi}{2}\right)}$ was used. The limit of the time integral is equal to one only for $n_1 = 0$ and zero otherwise. The contrast in the 'washed-out' interference pattern is thus reduced by a factor of $J_0(\varphi_1) \approx 1 - \varphi_1^2/4$ for small peak phase deviations $\varphi_1 < 1$.

According to [34, 35] the second-order correlation function is calculated and the explicit correlation function for N perturbation frequencies ω_j becomes

$$g^{(2)}(u, \tau) = 1 + \frac{1}{2}K_0^2 \sum_{\substack{\{n_j,m_j\}\in\mathbb{Z}\\ j=1\ldots N}} A_{\{n_j,m_j\}}(\tau, \Phi_{\{n_j,m_j\}})\cos(ku + \tilde{\varphi}_{\{n_j,m_j\}}), \tag{4}$$

with

$$A_{\{n_j,m_j\}}(\tau, \Phi_{\{n_j,m_j\}}) = \tilde{B}_{\{n_j,m_j\}}(\varphi_j) \cdot \cos\left(\sum_{j=1}^{N} m_j\omega_j\tau + \Phi_{\{n_j,m_j\}}\right). \tag{5}$$

The sum in equation (4) has to be taken over all integer multiplets $\{n_j, m_j\} \in \mathbb{Z},\ j = 1 \ldots N$, for which the following constraint is fulfilled [35]

$$\sum_{j=1}^{N}(n_j + m_j)\omega_j = 0. \tag{6}$$

For a finite acquisition time T, the constraint in equation (6) has to be modified to $\left|\sum_{j=1}^{N}(n_j + m_j)\omega_j\right| < 2\pi/T$, as $1/T$ defines the minimal resolvable frequency. In principle an infinite number of integer multiplets fulfill this constraint, but the contribution to the sum is suppressed due to the strong decay of the Bessel functions of first kind J_n in

$$\tilde{B}_{\{n_j,m_j\}}(\varphi_j) := \prod_{j=1}^{N} J_{n_j}(\varphi_j)J_{m_j}(\varphi_j). \tag{7}$$

The spatial correlation phase $\tilde{\varphi}_{\{n_j,m_j\}}$ and temporal phase $\Phi_{\{n_j,m_j\}}$ in equations (4) and (5) are given by

$$\begin{aligned}\tilde{\varphi}_{\{n_j,m_j\}} &:= \frac{\pi}{2}\sum_{j=1}^{N}(m_j - n_j),\\ \Phi_{\{n_j,m_j\}} &:= \sum_{j=1}^{N}\phi_j(m_j + n_j).\end{aligned} \tag{8}$$

If the constraint in equation (6) is satisfied only for $n_j = -m_j$ ($j = 1 \ldots N$), the temporal phase $\Phi_{\{-m_j,m_j\}}$ in equation (8) becomes zero and $\tilde{\varphi}_{\{-m_j,m_j\}} = \pi\sum_{j=1}^{N} m_j$. Together with $J_{-m_j}(\varphi_j) = (-1)^{m_j}J_{m_j}(\varphi_j)$ equation (4) then simplifies, yielding the approximate correlation function [35]

$$g^{(2)}(u, \tau) = 1 + A(\tau)\cos(ku), \tag{9}$$

with

$$A(\tau) = \frac{1}{2}K_0^2 \prod_{j=1}^{N}\sum_{m_j=-\infty}^{\infty} J_{m_j}(\varphi_j)^2\cos(m_j\omega_j\tau). \tag{10}$$

More details to the differentiation and applicability of the explicit and approximate correlation theory can be found in [35].

The correlation functions in equations (4) and (9) show a periodic modulation in the spatial distance u, with the same periodicity λ as in the unperturbed interference pattern. The amplitudes $A_{\{n_j,m_j\}}(\tau, \Phi_{\{n_j,m_j\}})$ and $A(\tau)$ of this modulation result from the specific perturbation spectrum. The maximum of $0.5K_0^2$ is achieved at $\tau = 0$, where only the addends with $n_j = -m_j$ contribute to the correlation function and therefore equation (4) is equal to equation (9), resulting in [34, 35]

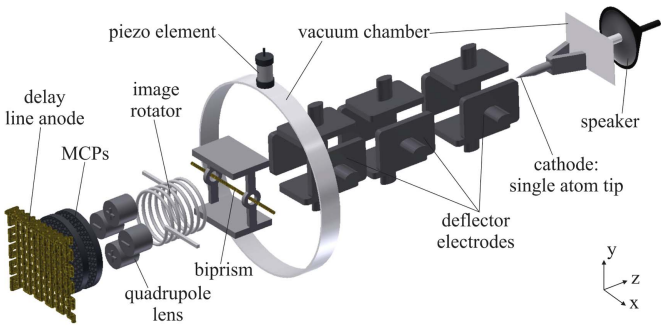

Figure 1. Sketch of the experimental setup for the measurement of vibrational dephasing in an electron biprism interferometer. An electron beam is emitted by a single atom tip cathode and aligned by deflection electrodes. After separation by a charged biprism fiber, the partial matter-waves are superposed and form an interference pattern that can be tilted by an image rotator parallel to the *x*-direction of the quadrupole lens. The magnified pattern is detected by two multi-channelplates (MCPs) in combination with a delay line anode. To demonstrate the technique for identifying perturbation frequencies of mechanical vibrations and correcting the reduction of contrast, vibrations were artificially introduced by a speaker and a piezo element mounted outside on the vacuum chamber.

$$g^{(2)}(u,\,0) = 1 + \frac{1}{2}K_0^2\cos(ku), \tag{11}$$

which is appropriate to obtain the contrast of the unperturbed interference pattern K_0 and the spatial periodicity $\lambda = 2\pi/k$. Therefore, it is possible to proof matter-wave interference, although the periodic pattern would be 'washed-out' after integration of the signal.

The function $A_{\{n_j,m_j\}}(\tau,\,\Phi_{\{n_j,m_j\}})$ in equation (5) contains a superposition of harmonics, intermodulation terms (sums and differences) of the perturbation frequencies at discrete values of $\sum_{j=1}^{N} m_j\omega_j$, with the coefficient $m_j \in \mathbb{Z}$ resulting from the constraint in equation (6). Their amplitudes are given by the peak phase deviations φ_j via the product of the Bessel functions in equation (7). The highest contributing frequency component appears at roughly $\sum_{j=1}^{N} m_{j,\max}\omega_j$, with $m_{j,\max} \approx \varphi_j$. For higher orders $m_j > \varphi_j$, the Bessel function decays strongly and the frequency component disappears. To get the positions of the frequencies and the corresponding amplitudes, the amplitude spectrum $|\mathcal{F}(g^{(2)}(u,\,\tau))(u,\,\omega)|$ of equation (4) for the positive frequency region is calculated to

$$\frac{1}{2\pi}\,|\mathcal{F}(g^{(2)}(u,\,\tau))(u,\,\omega)|^2 = \delta(\omega)^2 + 2\cdot\left[\frac{1}{2}K_0^2\sum_{\substack{\{n_j,m_j\}\in\mathbb{Z}\\ j=1\ldots N}}\tilde{B}_{\{n_j,m_j\}}(\varphi_j)\right.$$
$$\left.\cdot\,\delta(\omega-\omega_{\{m_j\}})\cdot\cos\left(\Phi_{\{n_j,m_j\}}+\frac{\pi}{4}\right)\cos(ku+\tilde{\varphi}_{\{n_j,m_j\}})\right]^2, \tag{12}$$

with the Dirac delta function $\delta(\omega)$ and the frequency components $\omega_{\{m_j\}} := \sum_{j=1}^{N} m_j\omega_j$.

The amplitude spectrum of the correlation function is used to identify the perturbation frequencies ω_j, peak phase deviations φ_j and phases ϕ_j of the applied perturbation.

3. Experiment

We demonstrate the identification of vibrational dephasing in an electron biprism interferometer [43]. The experimental setup is illustrated in figure 1 and described elsewhere [44–47]. A coherent electron beam is field emitted by a single atom tip source [48, 49]. The beam is adjusted by electrostatic deflection electrodes towards a 400 nm-thick biprism fiber that is coated with gold-palladium [44]. It is positioned between two grounded electrodes and acts as a coherent beam splitter for the electron matter-wave [43]. By the application of a positive voltage the two separated beam paths get deflected towards each other creating a matter-wave interference pattern with a period of a few hundred nanometers. The quadrupole lens expands the pattern by a factor of several thousand which is then projected on a delay line detector. Using the image rotator the pattern is aligned parallel to the *x*-direction. The detector amplifies the single electron events by two multi-channelplates and detects them with high spatial and temporal resolution [37]. The individual components are mounted on two ceramic rods to prevent temperature drifts and provide electrical insulation. The whole system is installed within

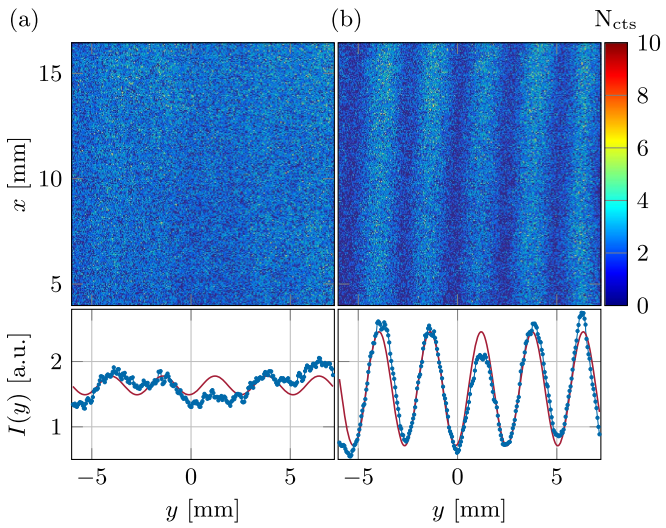

Figure 2. (a) Electron interference pattern perturbed with an excitation frequency of $\omega_0/2\pi = 540$ Hz. The averaged interference pattern (blue dots) and the fitted model function in equation (13) (red solid line) are presented below. (b) With the obtained parameters from the correlation analysis and subsequent optimization the unperturbed interference pattern can be reconstructed.

an ultrahigh vacuum chamber at a pressure of 4.5×10^{-10} mbar. To avoid perturbations it is mounted on an air-damped optical table and shielded against electromagnetic radiation.

For the demonstration of dephasing identification and frequency analysis, the electron interferences are artificially disturbed by mechanical vibrations from a speaker in the frequency range between 100 and 320 Hz and a piezo element in the range between 330 and 1000 Hz. Both are mounted outside on the vacuum-chamber. The speaker was attached behind the cathode generating vibrations along the z-direction (see figure 1), with a direct connection to the vacuum chamber. The piezo element mounted on the vacuum chamber produced vibrations in the y-direction. Both are controlled by a frequency generator with a resolution of 1 μHz and an accuracy of $\pm$10 ppm on the set frequency value.

Only a single excitation frequency is applied at once. At each frequency an interference pattern with $(1.95 \pm 0.02) \times 10^5$ electrons (at a count rate of (2.0 ± 0.5) kHz for the speaker measurement and (11 ± 2) kHz for the piezo measurement) is accumulated and the temporal and spatial information for each particle is recorded. Stepwise, the frequency is increased and a new interference pattern is acquired. This way, the complete spectral response of the interferometer was measured. The electron energy for each measurement was 1.45 keV which results in a velocity of 2.26×10^7 m s^{-1}. The flight time of the electrons from the tip to the delay line detector amounts 26 ns.

4. Data analysis

We will demonstrate exemplarily our method to analyze an electron interference pattern perturbed by a mechanical vibration with the excitation frequency of $\omega_0/2\pi = 540$ Hz, which is introduced by a piezo element.

For each electron that reaches the detector the spatial positions (x_i, y_i) and the arrival time t_i is recorded. The histogram for the integrated signal is shown in figure 2(a). To determine the contrast of the perturbed interference pattern K_{pert} and spatial periodicity λ_{pert}, the histogram is averaged along the x-direction and fitted with a model function

$$I(y) = I_0(1 + K\cos(ky)), \tag{13}$$

with the mean intensity I_0, contrast K and wave number $k = 2\pi/\lambda$. The result is plotted below the histogram in figure 2(a), yielding a contrast $K_{\mathrm{pert}} = (8.8 \pm 1.6)\%$ and a spatial periodicity $\lambda_{\mathrm{pert}} = (2.62 \pm 0.06)$ mm. Here, the errors indicate the 95% confidence interval of the fit.

To extract the two-dimensional correlation function $g^{(2)}(u, \tau)$, a histogram $N_{u,\tau}$ of all particle pair distances $(y_i - y_j)$ and time differences $(t_i - t_j)$ is generated and properly normalized [34]

$$g^{(2)}(u, \tau) = \frac{TY}{N^2 \Delta\tau \Delta u} \frac{N_{u,\tau}}{\left(1 - \frac{\tau}{T}\right)\left(1 - \frac{|u|}{Y}\right)}. \tag{14}$$

Here, T and Y describe the acquisition time and spatial length and $\Delta\tau$, Δu the histogram bin size. The factor $[(1 - \tau/T)(1 - |u|/Y)]^{-1}$ corrects $N_{u,\tau}$ for the finite acquisition time and spatial length. The correlation function is normalized such that $\langle g^{(2)}(u, \tau)\rangle = 1$.

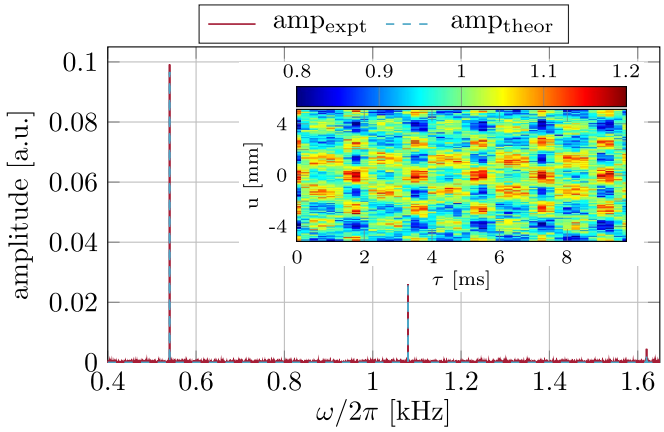

Figure 3. Amplitude spectrum of the $\omega_0/2\pi = 540$ Hz measurement (solid red line), as calculated from the correlation function (see inset) via a discrete Fourier transformation at $u = N_u \lambda_{g^{(2)}}/2$. After identifying the fundamental perturbation frequency of $\omega_1/2\pi = (540.0 \pm 0.05)$ Hz equation (12) is fitted to the spectrum (dashed blue line) and the peak phase deviation $\varphi_1 = (0.5725 \pm 0.0015)\,\pi$ is obtained.

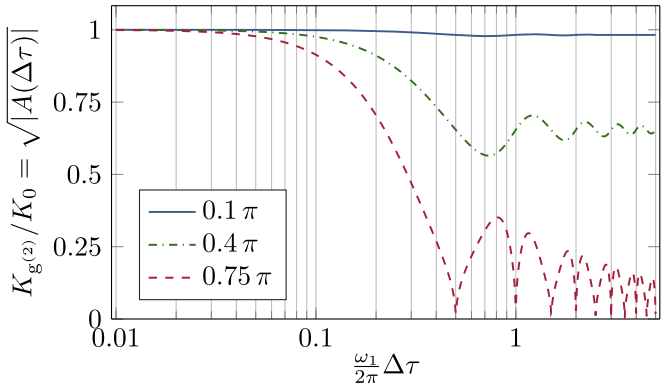

Figure 4. Contrast reduction due to temporal binning for three different peak phase deviations 0.1 π, 0.4 π and 0.75 π (blue solid line, green chain line and red dashed line). The curves are calculated according to equation (15).

The resulting correlation function for $\Delta u = 90$ μm and $\Delta\tau = 50$ μs is shown in the inset of figure 3. The spatial periodicity of the unperturbed interference pattern can be seen in u-direction. The periodicity in τ-direction is $2\pi/\omega_1 = 1.9$ ms. The contrast of the unperturbed interference pattern is extracted at $\tau = 0$ by fitting equation (11) to the data. The results are $K_{g^{(2)}} = (58.5 \pm 3.2)\%$ and $\lambda_{g^{(2)}} = (2.60 \pm 0.02)$ mm. The extracted contrast, however, depends on the temporal binning $\Delta\tau$ of the correlation function. Following equation (9), the bin averaged correlation function at $\tau = 0$ and $N = 1$ becomes

$$\frac{1}{\Delta\tau}\int_0^{\Delta\tau} g^{(2)}(u,\tau)\mathrm{d}\tau = 1 + \frac{1}{2}K_0^2 \cdot A(\Delta\tau)\cos(ku), \tag{15}$$

with

$$A(\Delta\tau) = \sum_{m_1=-\infty}^{\infty} J_{m_1}(\varphi_1)^2 \cdot \frac{\sin(m_1\omega_1\Delta\tau)}{m_1\omega_1\Delta\tau}.$$

The extracted contrast $K_{g^{(2)}}$ is thus modified by the amplitude $A(\Delta\tau)$, reaching K_0 only in the limit $\Delta\tau \to 0$. Figure 4 shows the expected contrast reduction $K_{g^{(2)}}/K_0 = \sqrt{|A(\Delta\tau)|}$ due to temporal binning, for a single perturbation frequency ω_1 and three different peak phase deviations φ_j ranging from 0.1 π to 0.75 π. At these modulation strengths a binning of $\Delta\tau < 0.08 \cdot 2\pi/\omega_1$ is sufficient to extract the unperturbed contrast with 95% accuracy.

After having determined contrast and spatial periodicity of the unperturbed interference pattern, the perturbation frequency needs to be identified. This is done by calculating the temporal amplitude spectrum of the correlation function via a discrete Fourier transformation for every value $u = N_u \lambda_{g^{(2)}}/2$ with $N_u \in \mathbb{Z}$ and subsequent averaging. Following equation (12), the resulting spectrum contains all frequency components

$\omega_{\{m_1\}}$, as can be seen in figure 3 for the 540 Hz measurement (red solid line). Three peaks can be identified, that correspond to the fundamental frequency and harmonics at discrete frequencies $m_1\omega_1$, $m_1 \in \{1, 2, 3\}$ in equation (12). The amplitudes are given by the Bessel functions of the peak phase deviation and the contrast of the unperturbed interference pattern $\frac{1}{2}K_0^2 J_{m_1}(\varphi_1)^2$.

For more than one perturbation frequency ω_j, the spectrum consists not only of the fundamental frequencies and harmonics, but also of intermodulation terms. Therefore, it is difficult to identify the fundamental frequencies. For the determination of the correct perturbation frequencies a search algorithm has been developed which is described below and illustrated in figure 5. The algorithm will be discussed exemplary on a two-frequency perturbation with $\omega_1/2\pi = 6$ Hz, $\varphi_1 = 0.6\ \pi$, $\phi_1 = 0\ \pi$ and $\omega_2/2\pi = 40$ Hz, $\varphi_2 = 0.5\ \pi$, $\phi_2 = 0\ \pi$. This results in an amplitude spectrum of the correlation function as shown in figure 5 top left (red solid line). First, the frequency positions ω_{expt} of all peaks above the mean noise level in the experimental amplitude spectrum are identified and stored in a list $\{\omega_{\text{expt}}\}$. For the example shown in figure 5, this list is $\{\omega_{\text{expt}}\}/2\pi = \{6, 12, 18, 22, \ldots, 98\}$. The next step is the creation of a 'search list' of possible perturbation frequencies from the experimental spectrum $\{\omega_{s,N=1}\} = \{\omega_{\text{expt}}\}$ (single frequency case). Here, $\{\omega_{s,N=j}\}_i$ is the list-element i containing j frequencies. The total number of elements in $\{\omega_{s,N=j}\}$ is N_{ω_s}. The search algorithm starts with the single frequency case ($j = 1$) and uses the first element $i = 1$ of $\{\omega_{s,N=1}\}$. In the example, this is $\{\omega_{s,N=1}\}_1/2\pi = 6$ Hz. It is used as perturbation frequency ω_1 in equation (12) to calculate the positions of the frequency components ω_{theor} in the theoretical amplitude spectrum. The resulting positions are stored in the list $\{\omega_{\text{theor}}\}_i$ with $i = 1$. For the perturbation frequency of 6 Hz this list is $\{\omega_{\text{theor}}\}_1/2\pi = \{6, 12, 18, 24, \ldots, 96\}$. By comparing the frequency components in the theoretical and experimental spectrum, $\{\omega_{\text{theor}}\}_i$ and $\{\omega_{\text{expt}}\}$, the degree of congruence M_ω is determined. This indicates how many frequencies in the experimental spectrum coincide with those in the theoretical, compared to $N_{\omega_{\text{expt}}}$, the total number of frequencies stored in $\{\omega_{\text{expt}}\}$. In the example, three frequency positions coincide, $\{6, 12, 18\}$, and $N_{\omega_{\text{expt}}} = 17$. This results in a degree of congruence of $M_\omega = 17.6\%$. The value of M_ω determines which of the next three cases is fulfilled. If $M_\omega \geqslant 80\%$, the element $\{\omega_{s,N=1}\}_1$ is stored in the list of resulting perturbation frequencies $\{\omega_{\text{res}}\}$. The element $\{\omega_{s,N=1}\}_1$ is not taken into account for the next steps, if $M_\omega \leqslant 10\%$. For $10\% < M_\omega < 80\%$, the element is stored in a list of possible perturbation frequencies $\{\omega_{\text{p}}\}$. The third case is fulfilled for the element $\{\omega_{s,N=1}\}_1/2\pi = 6$ Hz. Then, the next element ($i = i + 1$) in the list $\{\omega_{s,N=1}\}$, $\{\omega_{s,N=1}\}_2/2\pi = 12$ Hz, is taken for the calculation of $\{\omega_{\text{theor}}\}_i$ and the determination of the degree of congruence M_ω. This loop (indicated by the blue arrows and boxes in figure 5) continues until the last element in $\{\omega_{s,N=1}\}$ was used ($i = N_{\omega_s}$). For the example in figure 5, the list of possible perturbation frequencies is $\{\omega_{\text{p}}\}/2\pi = \{6, 12, 18, 24, \ldots, 92\}$. The last element in $\{\omega_{s,N=1}\}$, 98 Hz, is missing because it fulfilled the second case. If no element has satisfied the first case ($M_\omega \geqslant 80\%$), then $\{\omega_{\text{res}}\}$ is empty and a new list $\{\omega_{\text{u}}\}$ is created containing all unique frequencies included in $\{\omega_{\text{p}}\}$. In the single frequency case it is trivial because $\{\omega_{\text{u}}\} = \{\omega_{\text{p}}\}$. As example, for two frequencies per element in $\{\omega_{\text{p}}\}/2\pi = \{\{7, 13\}, \{7, 19\}, \{13, 41\}\}$ the list of unique frequencies would be $\{\omega_{\text{u}}\}/2\pi = \{7, 13, 19, 41\}$. Using $\{\omega_{\text{u}}\}$, all possible combinations of $j = j + 1$ frequencies are calculated and a new search list $\{\omega_{s,N=2}\}/2\pi = \{\{6, 12\}, \{6, 18\}, \{6, 22\}, \ldots, \{86, 92\}\}$ is created. Afterwards, the search algorithm starts with the first element ($i = 1$) in $\{\omega_{s,N=2}\}$. This loop which increases the number of frequencies ($j = j + 1$) is indicated in figure 5 with green arrows and boxes. Then, all elements i in $\{\omega_{s,N=2}\}$ are probed by the search algorithm in the same way as described above for the single frequency case. On the left side of figure 5, the three cases are illustrated with different lists of frequency components $\{\omega_{\text{theor}}\}_i$ (blue solid line) together with $\{\omega_{\text{expt}}\}$ (red solid line). The first case was calculated for $\{\omega_{s,N=2}\}_i/2\pi = \{6\text{ Hz}, 40\text{ Hz}\}$, the second for $\{\omega_{s,N=2}\}_i/2\pi = \{58\text{ Hz}, 74\text{ Hz}\}$ and the third for $\{\omega_{s,N=2}\}_i/2\pi = \{18\text{ Hz}, 62\text{ Hz}\}$. A very good match between theory and experiment can be seen for the first case. If the algorithm has stored one element in $\{\omega_{\text{res}}\}$ it is used as perturbation frequencies for the fit of equation (12) to the experimental spectrum. Thereby, the extracted contrast $K_{g^{(2)}}$, spatial periodicity $\lambda_{g^{(2)}}$ and the perturbation frequencies ω_j are fixed parameters for the determination of the peak phase deviation φ_j and phases ϕ_j. If the list of resulting perturbation frequencies $\{\omega_{\text{res}}\}$ contains more than one element, a theoretical spectrum is fitted to the experimental data with each element of $\{\omega_{\text{res}}\}$ in the same way as described above for one element. The best matching theoretical spectrum determines the perturbation frequencies ω_j and parameters φ_j and ϕ_j. At the bottom of figure 5 the theoretical spectrum (dashed blue line) for the resulting perturbation frequencies $\omega_1/2\pi = 6$ Hz and $\omega_2/2\pi = 40$ Hz can be seen. The algorithm identifies the perturbation frequencies ω_j with a probability of about 90% for $N = 3$ and 70% for $N = 4$.

With the exemplary measurement from figures 2 and 3, the above described algorithm yields a single perturbation frequency $\omega_1/2\pi = (540.0 \pm 0.05)$ Hz. After identification of the perturbation frequencies, equation (12) is used to fit the peak phase deviation φ_j to the amplitude spectrum, as shown in figure 3 (dashed blue line). The resulting peak phase deviation is $\varphi_1 = (0.5725 \pm 0.0015)\ \pi$. The main error in the determination of the perturbation parameters ω_j, φ_j and ϕ_j originates from the frequency resolution in the

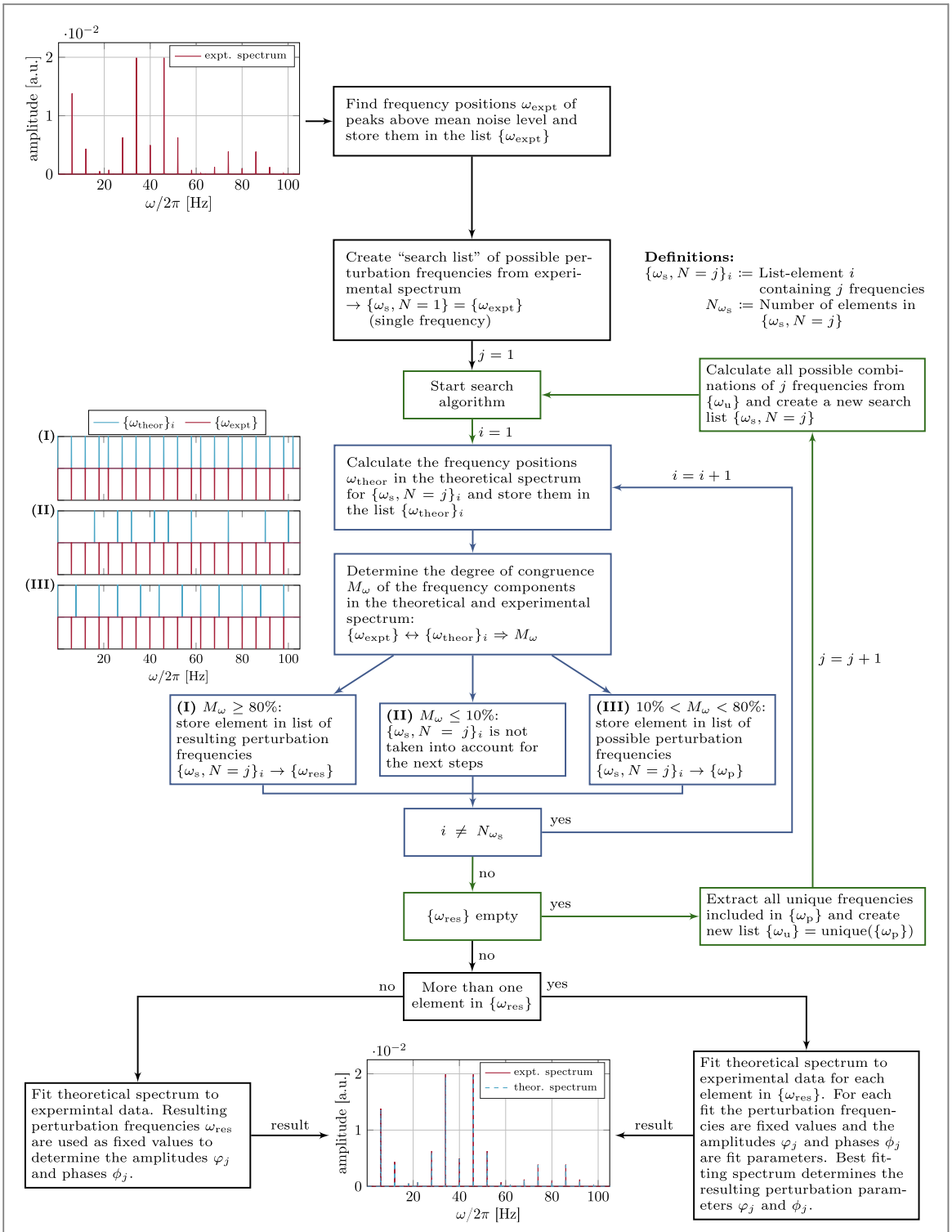

Figure 5. Search algorithm for the identification of perturbation frequencies using the temporal amplitude spectrum of the correlation function.

numerical amplitude spectrum. This was set to 100 mHz to reduce the computing time, especially for the search algorithm.

With the obtained values from the correlation analysis, it is possible to reconstruct the interference pattern from the perturbed one in figure 2(a). To get the reconstructed pattern the new particle coordinates $y_{i,\mathrm{new}}$ have to be calculated according to the extracted perturbation frequencies ω_j and peak phase deviations φ_j [35]

$$y_{i,\mathrm{new}} = y_i - \frac{\lambda}{2\pi}\varphi(t_i) = y_i - \frac{\lambda}{2\pi}\sum_{j=1}^{N}\varphi_j \cos(\omega_j t_i + \phi_j), \tag{16}$$

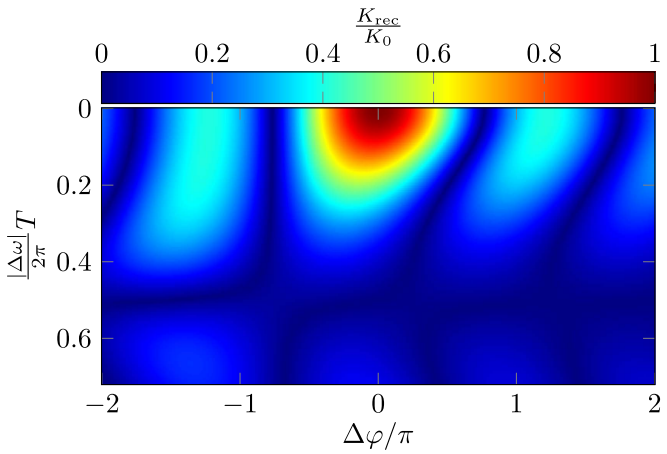

Figure 6. Resulting contrast reduction $K_{rec}(|\Delta\omega|,\ \Delta\varphi,\ \Delta\phi)/K_0$, as calculated for different deviations $\frac{|\Delta\omega|}{2\pi}T$ and $\Delta\varphi$ at $\Delta\phi = 0\ \pi$. The diagram applies for all integration times T.

where $\varphi(t_i)$ is the time-dependent phase shift in equation (2) and y_i, t_i are the spatial and temporal particle coordinates of the perturbed interference pattern. To determine the contrast of the reconstructed pattern, a two-dimensional histogram is calculated with $y_{i,new}$, averaged along the x-direction and fitted using equation (13). To maximize the resulting contrast the perturbation frequencies ω_j, the peak phase deviations φ_j and phases ϕ_j are optimized by varying their values in a narrow window around the values extracted from the correlation analysis. For the exemplary measurement, this optimization results in $\omega_1/2\pi = 539.994$ Hz, $\varphi_1 = 0.66\ \pi$ and $\phi_1 = 0.59\ \pi$. The reconstructed interference pattern, which can be seen in figure 2(b), reveals a contrast $K_{rec} = (55.5 \pm 2.8)\%$ and pattern periodicity $\lambda_{rec} = (2.57 \pm 0.01)$ mm. Both are determined similarly as for the perturbed interference pattern with equation (13). The result for the reconstructed contrast is in good agreement with the contrast obtained from the correlation analysis $K_{g^{(2)}} = (58.5 \pm 3.2)\%$.

The contrast in the reconstructed interference pattern depends strongly on the extracted perturbation values. Only, if the exact values of the perturbation (ω_j, φ_j and ϕ_j) are used in equation (16), the reconstructed contrast K_{rec} is equal to the one of the unperturbed interference pattern K_0. For values with a deviation from the exact values $K_{rec}(|\Delta\omega|,\ \Delta\varphi,\ \Delta\phi)$ is reduced.

In equation (13) the model function yields the contrast K_0, if the reconstructed coordinates are equal to the coordinates of the unperturbed interference pattern y_0. The maximum contrast is obtained at positions, where $ky_0 = 2\pi M$ for $y_0 = M\lambda$ with $M \in \mathbb{Z}$, resulting in $K_{rec} = K_0\cos(2\pi M)$. If not the exact perturbation parameters are used in equation (16), the coordinates of the unperturbed interference pattern are not correctly determined and a phase factor $\Delta\tilde{\varphi}$ remains, that depends on the deviations $|\Delta\omega|$, $\Delta\varphi$ and $\Delta\phi$. This factor reduces the contrast of the reconstructed interference pattern $K_{rec}(|\Delta\omega|,\ \Delta\varphi,\ \Delta\phi) = K_0\cos(2\pi M + \Delta\tilde{\varphi})$. By integration over the acquisition time T a theoretical description for one perturbation frequency can be found and reads

$$K_{rec}(|\Delta\omega|,\ \Delta\varphi,\ \Delta\phi) = \frac{K_0}{T}\int_0^T \cos\left(2\pi M + \varphi_1\cos(\omega_1 t + \phi_1)\right. \\ \left. - (\varphi_1 + \Delta\varphi)\cos\left((\omega_1 + |\Delta\omega|)t + (\phi_1 + \Delta\phi)\right)\right)\mathrm{d}t. \tag{17}$$

Figure 6 shows the resulting contrast reduction $K_{rec}(|\Delta\omega|,\ \Delta\varphi,\ \Delta\phi)/K_0$ as function of the relevant parameters $\frac{|\Delta\omega|}{2\pi}T$ and $\Delta\varphi$ for $\Delta\phi = 0\ \pi$. The result is independent of ω_1, ϕ_1 and T as long as $T \gg \frac{2\pi}{\omega_1}$, i.e. the measurement time is much larger than the cycle duration of the perturbation. For the three cases, where two of three deviations are equal to zero and one is small, approximate solutions can be found

$$K_{rec}(|\Delta\omega|,\ 0,\ 0) \approx K_0 \cdot \mathrm{e}^{-\frac{1}{2}\left(\frac{\pi}{8}|\Delta\omega|T\varphi_1\right)^2} \approx K_0\left(1 - \frac{1}{2}\left(\frac{\pi}{8}|\Delta\omega|T\varphi_1\right)^2\right) \\ K_{rec}(0,\ \Delta\varphi,\ 0) \approx K_0 \cdot |J_0(\Delta\varphi)| \approx K_0\left|\left(1 - \frac{\Delta\varphi^2}{4}\right)\right| \\ K_{rec}(0,\ 0,\ \Delta\phi) \approx K_0 \cdot |J_0(\Delta\phi\cdot\varphi_1)| \approx K_0\left|\left(1 - \frac{\Delta\phi^2}{4}\varphi_1^2\right)\right|. \tag{18}$$

Knowing the landscape of figure 6, it is possible to optimize the reconstruction of the interference pattern. At the position of $K_{rec} = K_0$ also the values of the perturbation are correctly determined. Above theory has been demonstrated for one perturbation frequency, but can be applied also in the case of numerous frequencies,

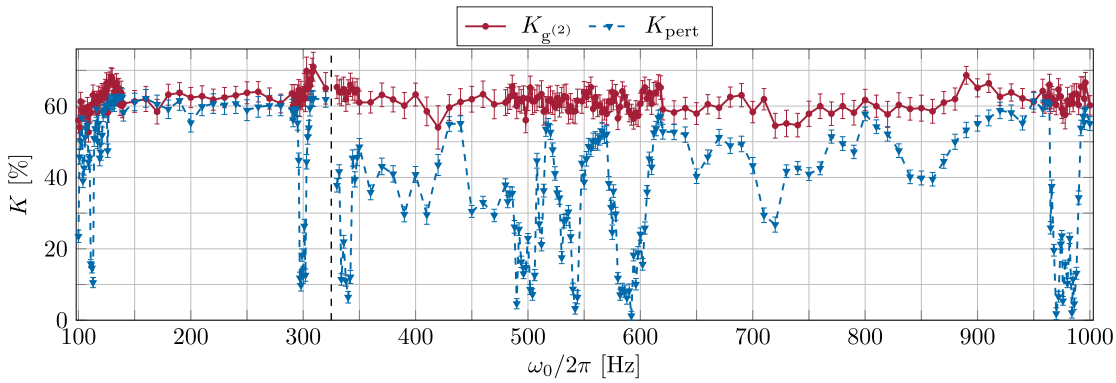

Figure 7. Contrast $K_{g^{(2)}}$ (red dots with solid line) of the speaker and piezo measurements resulting from the correlation analysis using equation (11) for $\tau = 0$ and the contrast of the perturbed interference pattern K_{pert} (blue triangles with dashed line) obtained by fitting equation (13) to the averaged histogram. The two measurement sets are separated by the black dashed vertical line at 325 Hz. The averaged contrast $K_{g^{(2)}}$ over the complete measurement with the speaker is (62.5 ± 3.4)% and the mean error of the individual fit is ±3.0%. For the piezo measurement the result is (61.3 ± 2.7)% with the mean error ±3.2%. The averaged spatial periodicity for the speaker measurement is $\lambda_{g^{(2)}} = (2.62 \pm 0.04)$ mm with the mean error of each fit ±0.02 mm and $\lambda_{pert} = (2.60 \pm 0.04)$ mm with the mean error of ±0.05 mm. For the piezo measurement the results are $\lambda_{g^{(2)}} = (2.65 \pm 0.05)$ mm with ±0.02 mm and $\lambda_{pert} = (2.65 \pm 0.04)$ mm with ±0.03 mm.

because in equation (16) the perturbations are independent of each other and therefore can be recalculated successively. For each reconstruction step the resulting contrast gets larger, until it reaches K_0.

For the exemplary measurement with 540 Hz, the acquisition time was $T = 19.2$ s. Using equation (18) with $\varphi_1 = 0.66\,\pi$, $\Delta\varphi = 0$, $\Delta\phi = 0$ and $\Delta\omega/2\pi = 5$ mHz, the reconstructed contrast is reduced to $K_{rec} = 0.88 \cdot K_0$. For the reconstruction of the unperturbed interference pattern with equation (16), a frequency accuracy of ±1 mHz is required for the optimization process to reveal the reconstructed contrast with less than 1% deviation from K_0.

5. Results

The following measurements will demonstrate the extraction of the unperturbed interference pattern contrast K_0 in the presence of dephasing. Additionally, we will determine the vibrational response spectrum of the interferometer, including the possibility to reconstruct the unperturbed interference pattern.

From the measurements with the speaker (excitation frequency $\omega_0/2\pi$ from 100 to 320 Hz) and the piezo ($\omega_0/2\pi$ from 330 to 1000 Hz) the correlation function is extracted according to equation (14). For each measurement the correlation function is calculated with a spatial discretization of $\Delta u = 90\ \mu$m and a temporal of $\Delta\tau = 200\ \mu$s for the speaker and $\Delta\tau = 50\ \mu$s for the piezo measurement. The maximum correlation time is $\tau = 10$ s. As discussed in section 4, the contrast of the perturbed interference pattern K_{pert} is determined by using equation (13). From the correlation function at $\tau = 0$ (equation (11)), the corresponding contrast of the unperturbed interference pattern $K_{g^{(2)}}$ is extracted. The results for the speaker and piezo measurement are shown in figure 7. The data for K_{pert} show clear resonance structures at discrete frequencies. At these resonances, the contrast of the integrated interference image vanishes almost completely. However, the correlation analysis reveals the full contrast of the unperturbed interference pattern over the full spectral range.

Following section 4, the amplitude spectrum of the correlation function is calculated and the involved perturbation frequencies ω_j and corresponding peak phase deviations φ_j are identified by the described algorithm. The resulting response spectrum for the speaker measurement with excitation frequencies of $\omega_0/2\pi$ from 100 to 320 Hz is shown in figure 8. The red solid line, plotted in the frequency-plane, denotes the positions of the fundamental frequency, where ω_j is equal to ω_0. By comparison of the positions of large amplitudes φ_j on this line with the positions of the reduced contrast K_{pert} in figure 7, a good agreement can be seen, according to equation (3). The maximum peak phase deviation in the complete spectrum is $\varphi_j = 0.99\ \pi$ at $\omega_j/2\pi = 112$ Hz. The blue chain lines in the frequency-plane represent higher harmonics of ω_0. For a given harmonic excitation at ω_0 and a linear response of the interferometer, the response spectrum should include only the excitation frequency. However, due to anharmonicities in the excitation process and possible nonlinear response of the complex interferometer setup, the response spectrum may include higher harmonics. Especially in the region of 100 to 140 Hz this behavior can be observed. The green horizontal dashed lines show constant frequencies at 150 and 300 Hz that are independent of the excitation frequency, probably originating from the electrical network frequency at 50 Hz.

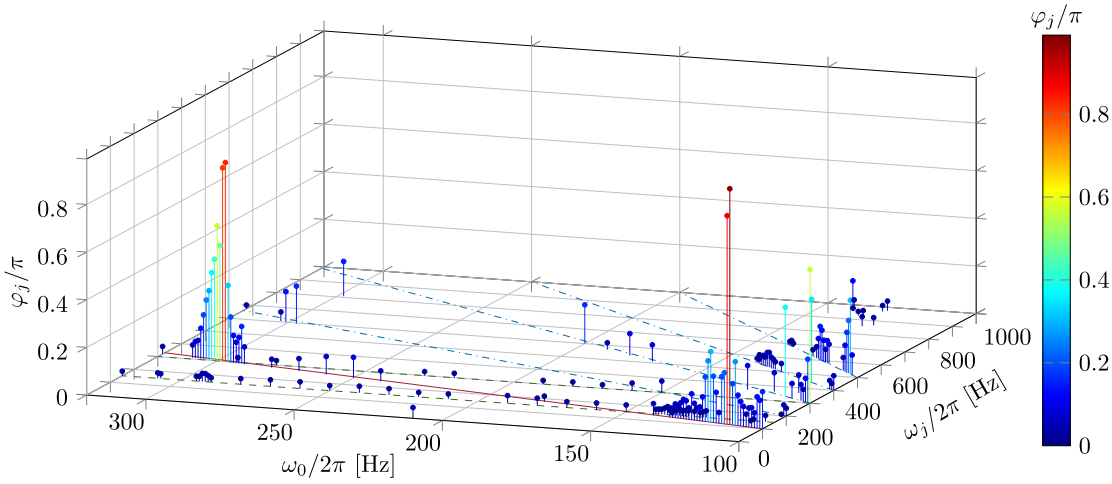

Figure 8. Response spectrum of the interferometer as extracted from the speaker measurement. The red solid line in the frequency-plane shows the fundamental frequency, where ω_j is equal to ω_0. The blue chain lines represent the higher harmonics of ω_0. The green horizontal dashed lines indicate constant frequencies at 150 and 300 Hz.

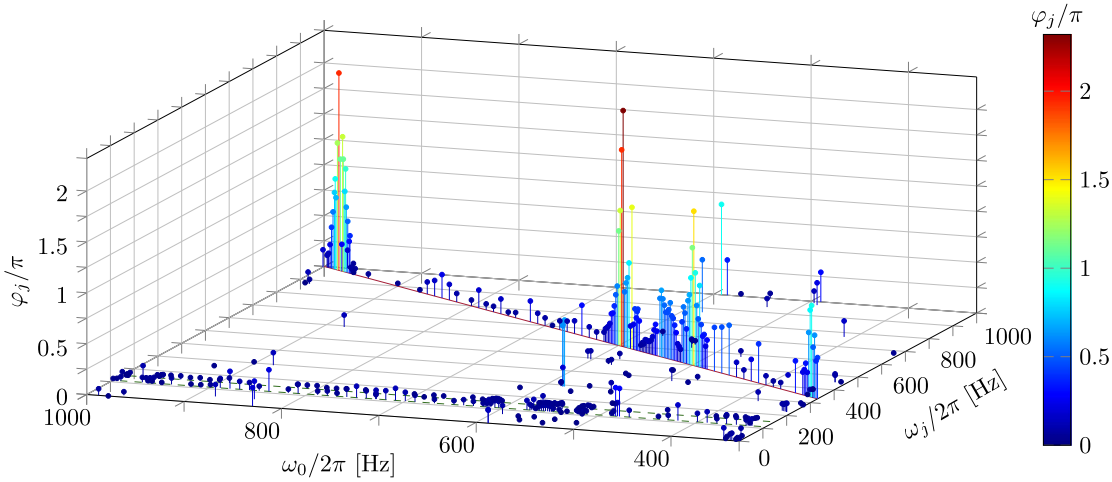

Figure 9. Response spectrum of the piezo measurement. The red solid line shows the fundamental frequency of ω_0. The green horizontal dashed lines are constant frequencies at 111.4 and 150 Hz.

The results of the piezo measurement with $\omega_0/2\pi$ from 330 to 1000 Hz are shown in figure 9. Again, the positions of large peak phase deviations φ_j agree well with the positions of reduced contrast K_{pert} in figure 7, according to equation (3). The maximum value in this spectrum is $\varphi_j = 2.32\ \pi$ at $\omega_j/2\pi = 594$ Hz. The green horizontal dashed lines of constant frequencies are at 111.4 and 150 Hz. The origin of the first one could be a vibration in the laboratory. The latter is likely a harmonic frequency of the electrical network.

Comparing the two spectra in figures 8 and 9 it can be seen, that the resulting peak phase deviations of the speaker measurement are below the values extracted from the piezo measurement. One reason could be, that the excitation of the speaker is directed along the interferometer axis (z-direction, figure 1), whereas the piezo excitation is oriented along the direction of interference (y-direction). The piezo excitation will thus have a stronger influence on the dephasing of the interference pattern. Another difference between the two spectra are the positions of constant frequencies indicated by the green horizontal lines. This difference could probably originate from the excitation direction mentioned above and the fact that the two measurements have been made at different days. Therefore, a change of the environmental conditions could be possible.

Calculating the spatial periodicity of the electron interference pattern before the magnification through the quadrupole lens, allows to determine the spatial perturbation amplitude. The measurements have been made with an electron emission voltage of 1.45 kV and a voltage of 0.3 V at the biprism, yielding an interference pattern with the unmagnified spatial periodicity of $\lambda = 880$ nm [43]. With this value and the resulting peak phase deviations φ_j, the spatial perturbation amplitude A can be calculated via $A(\varphi_j) = \lambda\frac{\varphi_j}{2\pi}$. The resulting

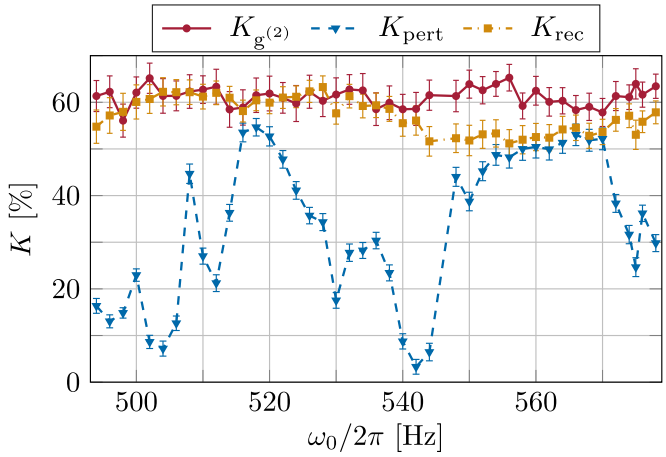

Figure 10. Contrast obtained from the correlation analysis $K_{g^{(2)}}$ (red dots with solid line), contrast of the perturbed interference pattern K_{pert} (blue triangles with dashed line) and contrast of the reconstructed interference pattern K_{rec} (yellow squares with chain line) for different excitation frequencies ω_0. To calculate K_{rec} equation (16) is used to maximize the contrast by varying the perturbation parameters. $K_{g^{(2)}}$ represents the upper limit for K_{rec}.

amplitudes are in the range of 6 nm ($\varphi_1 = 0.014\ \pi$ at $\omega_1/2\pi = 111.4$ Hz) up to 1.021 μm ($\varphi_1 = 2.320\ \pi$ at $\omega_1/2\pi = 594$ Hz). Here we assume, that the perturbation occurs before the magnification of the interference pattern through the quadrupole lens. In principle it is possible to increase the sensitivity for measuring perturbation amplitudes by reducing the spatial periodicity. This can be achieved by decreasing the acceleration voltage or increasing the biprism voltage.

With the obtained values from the correlation analysis, the unperturbed interference pattern can be reconstructed from the experimental data with equation (16). In addition, the accuracy in identifying the perturbation frequencies ω_j and peak phase deviations φ_j can be increased by maximizing the contrast of the reconstructed pattern K_{rec}. The result is plotted in figure 10 for the region from 494 to 578 Hz of the piezo measurement. Over the whole range the contrast of the reconstructed interference pattern K_{rec} is significantly larger than the contrast of the perturbed one K_{pert} and close to the contrast $K_{g^{(2)}}$ of the unperturbed interference pattern, which marks an upper limit for the contrast of the reconstructed pattern.

6. Conclusion

Due to the technological progress for single-particle detection with high spatial and temporal resolution, it is possible to prove matter-wave interference by second-order correlation analysis, although the integrated interference structure vanishes by vibrational dephasing. Furthermore, the involved perturbation frequencies and amplitudes can be identified. In this paper we have demonstrated theoretically and experimentally, how this can be performed using the additional information about the particle impact time t_i and position y_i. Our method can in principle be applied in various interferometric experiments equipped with such a detector. It has major potential for applications in sensor technology for vibrational as well as electromagnetic perturbations [34, 35].

By introducing vibrations artificially to our biprism electron interferometer, we have disturbed the integrated interference pattern. The degree of disturbance depends on the response of the interferometer to this excitation frequency. With our method the matter-wave characteristics, contrast and spatial periodicity, were extracted for the whole excitation spectrum from 100 to 1000 Hz. By calculating the amplitude spectrum of the correlation function, it is possible to identify the perturbation frequencies using our numerical search algorithm. With the obtained frequencies, the theoretical function was fitted to the experimental spectrum to determine the perturbation amplitudes and phases. By applying our method to all measurements, a response spectrum of the interferometer was created. With the possibility to reconstruct the unperturbed interference pattern, the accuracy of the parameters obtained from the correlation analysis could be increased.

We have demonstrated, that our method is not only a tool to prove matter-wave interferences even if they are invisible in the integrated picture, but has also possible sensor applications for the identification of perturbation frequencies and amplitudes originating from the environment. The interferometer could be used for the analysis of external perturbations, if its response spectrum is known. On the other hand, it is possible to apply a defined external perturbation source to map the response spectrum of the interferometer. With the knowledge of the vibrational as well as electromagnetic response spectrum of an interferometer, the mechanical decoupling from

the environment and electromagnetic shielding can be optimized for the specific application. Additionally, perturbation sources can be identified and eliminated.

Acknowledgments

This work was supported by the Deutsche Forschungsgemeinschaft (DFG, German Research Foundation) through the Emmy Noether program STI 615/1-1. AG acknowledges support from the DFG SFB TRR21, and AR from the Evangelisches Studienwerk eV Villigst. The authors thank N Kerker and A Pooch for helpful discussions.

References

[1] Grattan L S and Meggitt B T (ed) 2000 *Optical Fiber Sensor Technology: Fundamentals* (New York: Springer Science & Business Media)
[2] Abbott B P *et al* 2016 *Phys. Rev. Lett.* **116** 061102
[3] Graham P W, Hogan J M, Kasevich M A and Rajendran S 2013 *Phys. Rev. Lett.* **110** 171102
[4] Gerlich S, Eibenberger S, Tomandl M, Nimmrichter S, Hornberger K, Fagan P J, Tüxen J, Mayor M and Arndt M 2011 *Nat. Commun.* **2** 263
[5] Arndt M and Hornberger K 2014 *Nat. Phys.* **10** 271
[6] Haslinger P, Dörre N, Geyer P, Rodewald J, Nimmrichter S and Arndt M 2013 *Nat. Phys.* **9** 144
[7] Gustavson T L, Bouyer P and Kasevich M A 1997 *Phys. Rev. Lett.* **78** 2046
[8] Hasselbach F and Nicklaus M 1993 *Phys. Rev.* A **48** 143
[9] Peters A, Chung K Y and Chu S 1999 *Nature* **400** 849
[10] Margalit Y, Zhou Z, Machluf S, Rohrlich D, Japha Y and Folman R 2015 *Science* **349** 1205
[11] Arndt M and Brand C 2015 *Science* **349** 1168
[12] Stibor A, Hornberger K, Hackermüller L, Zeilinger A and Arndt M 2005 *Laser Phys.* **15** 10
[13] Miffre A, Jacquey M, Büchner M, Trénec G and Vigué J 2006 *Appl. Phys.* B **84** 617
[14] Hauth M, Freier C, Schkolnik V, Senger A, Schmidt M and Peters A 2013 *Appl. Phys.* B **113** 49
[15] Geiger R *et al* 2011 *Nat. Commun.* **2** 474
[16] Hensley J M, Peters A and Chu S 1999 *Rev. Sci. Instrum.* **70** 2735
[17] Gouët L, Mehlstäubler T E, Kim J, Merlet S, Clairon A, Landragin A and Pereira dos Santos F 2008 *Appl. Phys.* B **92** 133
[18] Chiow S W, Herrmann S, Chu S and Müller H 2009 *Phys. Rev. Lett.* **103** 050402
[19] Chiow S-W, Kovachy T, Chien H-C and Kasevich M A 2011 *Phys. Rev. Lett.* **107** 130403
[20] Fray S, Alvarez Diez C, Hänsch T W and Weitz M 2004 *Phys. Rev. Lett.* **93** 240404
[21] Chen X, Zhong J, Song H, Zhu L, Wang J and Zhan M 2014 *Phys. Rev.* A **90** 023609
[22] Barrett B, Antoni-Micollier L, Chichet L, Battelier B, Gominet P-A, Bertoldi A, Bouyer P and Landragin A 2015 *New J. Phys.* **17** 085010
[23] Kohlhaas R, Bertoldi A, Cantin E, Aspect A, Landragin A and Bouyer P 2015 *Phys. Rev.* X **5** 021011
[24] Hume D B and Leibrandt D R 2016 *Phys. Rev.* A **93** 032138
[25] Zurek W H 2003 *Rev. Mod. Phys.* **75** 715
[26] Pikovski I, Zych M, Costa F and Brukner Č 2015 *Nat. Phys.* **11** 668
[27] Hackermüller L, Hornberger K, Brezger B, Zeilinger A and Arndt M 2004 *Nature* **427** 711
[28] Hornberger K, Uttenthaler S, Brezger B, Hackermüller L, Arndt M and Zeilinger A 2003 *Phys. Rev. Lett.* **90** 160401
[29] Sonnentag P and Hasselbach F 2007 *Phys. Rev. Lett.* **98** 200402
[30] Aharonov Y and Bohm D 1959 *Phys. Rev.* **115** 485
[31] Batelaan H and Tonomura A 2009 *Phys. Today* **62** 38
[32] Schmid H 1997 *Doctoral Thesis* University of Tübingen
[33] Schütz G, Rembold A, Pooch A, Prochel H and Stibor A 2015 *Ultramicroscopy* **158** 65
[34] Rembold A, Schütz G, Chang W T, Stefanov A, Pooch A, Hwang I S, Günther A and Stibor A 2014 *Phys. Rev.* A **89** 033635
[35] Günther A, Rembold A, Schütz G and Stibor A 2015 *Phys. Rev.* A **92** 053607
[36] Fölling S, Gerbier F, Widera A, Mandel O, Gericke T and Bloch I 2005 *Nature* **434** 481
[37] Jagutzki O, Mergel V, Ullmann-Pfleger K, Spielberger L, Spillmann U, Dörner R and Schmidt-Böcking H 2001 *Nucl. Instrum. Methods Phys. Res.* A **477** 244
[38] Wiener N 1930 *Acta Math.* **55** 117–258
[39] Khintchine A 1934 *Math. Ann.* **109** 604–15
[40] Siegmund O H, Vallerga J V, Tremsin A S, Mcphate J and Feller B 2007 *Nucl. Instrum. Methods Phys. Res.* A **576** 178
[41] Schellekens M, Hoppeler R, Perrin A, Viana Gomes J, Boiron D, Aspect A and Westbrook C I 2005 *Science* **310** 648
[42] Zhou X, Ranitovic P, Hogle C W, Eland J H D, Kapteyn H C and Murnane M M 2012 *Nat. Phys.* **8** 232
[43] Möllenstedt G and Düker H 1956 *Z. Phys.* A **145** 377
[44] Schütz G, Rembold A, Pooch A, Meier S, Schneeweiss P, Rauschenbeutel A, Günther A, Chang W T, Hwang I S and Stibor A 2014 *Ultramicroscopy* **141** 9
[45] Hasselbach F 2010 *Rep. Prog. Phys.* **73** 016101
[46] Hasselbach F and Maier U 1999 *Quantum Coherence and Decoherence—Proc. ISQM-Tokyo 98* ed Y A Ono and K Fujikawa (Amsterdam: Elsevier) p 299
[47] Maier U 1997 *Doctoral Thesis* University of Tübingen
[48] Kuo H S, Hwang I S, Fu T Y, Lin Y C, Chang C C and Tsong T T 2006 *Japan. J. Appl. Phys.* **45** 8972
[49] Kuo H S, Hwang I S, Fu T Y, Lu Y H, Lin C Y and Tsong T T 2008 *Appl. Phys. Lett.* **92** 063106